

**CURRENT ENGINEERING  
METHODS APPLIED TO THE  
DESIGN OF MIMO ANTENNA  
SYSTEMS**

BY

**ASIM GHALIB**

A Dissertation Presented to the  
DEANSHIP OF GRADUATE STUDIES

**KING FAHD UNIVERSITY OF PETROLEUM & MINERALS**

DHAHRAN, SAUDI ARABIA

In Partial Fulfillment of the  
Requirements for the Degree of

**DOCTOR OF PHILOSOPHY**

In

**ELECTRICAL ENGINEERING**

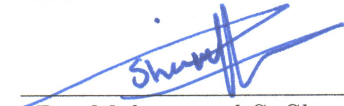
APRIL 2018

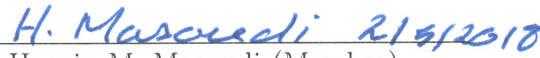
KING FAHD UNIVERSITY OF PETROLEUM & MINERALS  
DHAHRAN 31261, SAUDI ARABIA

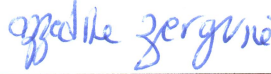
DEANSHIP OF GRADUATE STUDIES


This dissertation, written by **ASIM GHALIB** under the direction of his thesis adviser and approved by his thesis committee, has been presented to and accepted by the Dean of Graduate Studies, in partial fulfillment of the requirements for the degree of **DOCTOR OF PHILOSOPHY IN ELECTRICAL ENGINEERING**.

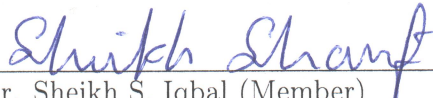
Dissertation Committee

 2 May 2018  
Dr. Mohammad S. Sharawi (Adviser)

 21/5/2018  
Dr. Husain M. Masoudi (Member)


 2 May 2018  
Dr. Azzedine Zerguine (Member)

 2 MAY 2018  
Dr. Khurram K. Qureshi (Member)

  
Dr. Sheikh S. Iqbal (Member)



Dr. Ali A. Al-Shaikhi  
Department Chairman

  
Dr. Salam A. Zummo  
Dean of Graduate Studies

Date

3/5/17





©Asim Ghalib  
2018

*Indeed, in the creation of the heavens and earth, and the alternation of the night and the day, and the [great] ships which sail through the sea with that which benefits people, and what Allah has sent down from the heavens of rain, giving life thereby to the earth after its lifelessness and dispersing therein every [kind of] moving creature, and [His] directing of the winds and the clouds controlled between the heaven and the earth are signs for a people who use reason.*

THE GLORIOUS QURAN, 2:164

*To Ghalib Shah and Jamila, my parents whom are my greatest  
support and inspiration.*

*To Dr. Adnan Ghalib, my brother for his tremendous encouragement  
and support.*

*To Dr. Aneela and Bushra, my sisters, Zonerah and Muneeba, my  
nieces, you brought unprecedented joy in my life.*

*I could not do this without your support*



# ACKNOWLEDGMENTS

First and foremost, I would like to thank the Almighty Allah (the One and the Only Creator of everything), the most Gracious and the most Merciful. All praise be to Allah for his guidance and limitless blessings. I have always found sustenance and motivation in Him even in the most difficult of times.

During my PhD studies, I have met and interacted with several people who helped me in many ways. I would like to sincerely thank each and everyone of them. First and foremost, I would like to wholeheartedly thank my supervisor, Prof. Mohammad S. Sharawi, for the patient guidance, encouragement and advice he has provided throughout my time as his student. I have been extremely lucky to have a supervisor who cared so much about my work, and who responded to my questions and queries so promptly. He always made sure that I was never short of anything that is required in my research work. His mentorship and guidance will serve as a life experience and a beacon for my future.

I would also like to extend my gratitude towards my committee members Prof. Husain M. Masoudi, Prof. Azzedine Zerguine, Dr. Khurram K. Qureshi and Dr. Sheikh S. Iqbal for their encouragement, insightful comments and hard questions.

I would like to thank the Deanship of Graduate studies for the stipend during my PhD studies and the Deanship of Scientific Research for funding the projects I worked on. I would like to thank the chairman of the electrical engineering (EE) department Dr. Ali Ahmad Al-Shaikhi for all his support.

I would like to extend my gratitude to all Antenna and Microwave Structures Design Laboratory (AMSDL) group members especially Muhammad Ikram, Dr. Rifaqat Hussain, Sagar and Syed Shahan. I would also like to thank all faculty members of EE department for the excellent course work that was conducted during my PhD.

I would like to acknowledge my colleagues who made my time at KFUPM enjoyable and whose advice and support was invaluable. I would especially like to thank Saifullah Shafiq, Farhan Sayal, Dr. Waqas Afzal, Dr. Hussain Ali, Dr. Naveed Iqbal, Jalal khan and Sanaullah Shafiq for the wonderful tea sessions we spent together and their kind advices.

I am also grateful to Dr. Farman Ali and Dr. Sheraz khan for their constant encouragement. Their support was indispensable during this journey.

Lastly, I would like to acknowledge my family for their constant support. Thank you so much. This thesis is for you.

# TABLE OF CONTENTS

<b>ACKNOWLEDGEMENT</b>	<b>iv</b>
<b>LIST OF TABLES</b>	<b>x</b>
<b>LIST OF FIGURES</b>	<b>xii</b>
<b>LIST OF SYMBOLS</b>	<b>xxiii</b>
<b>LIST OF ABBREVIATIONS</b>	<b>xxiv</b>
<b>ABSTRACT (ENGLISH)</b>	<b>xxvi</b>
<b>ABSTRACT (ARABIC)</b>	<b>xxix</b>
<b>CHAPTER 1 INTRODUCTION</b>	<b>1</b>
1.1 Motivation . . . . .	6
1.2 Problem Statement . . . . .	7
1.3 Work Contributions . . . . .	9
1.4 Dissertation Overview . . . . .	11
<b>CHAPTER 2 BACKGROUND</b>	<b>13</b>
2.1 Theory Of Characteristic Modes . . . . .	13
2.1.1 Mathematical Formulation . . . . .	14
2.1.2 Modal Significance . . . . .	19
2.1.3 Characteristic Angle . . . . .	20
2.1.4 Reactive Loading . . . . .	21



2.1.5	Computer Simulation Technology (CST) . . . . .	22
2.2	The Antenna Current Green's Function (ACGF) . . . . .	23
2.3	Characteristic Basis Function (CBF) . . . . .	26
2.4	Substrate Integrated Waveguide (SIW) Technology . . . . .	30
<b>CHAPTER 3 LITERATURE REVIEW</b>		<b>32</b>
3.1	Cross-Correlation Green Function . . . . .	32
3.2	TCM . . . . .	36
3.2.1	BW Enhancement . . . . .	36
3.2.2	Correlation Coefficient . . . . .	41
3.2.3	Reconfigurability . . . . .	42
3.2.4	Slot Antennas . . . . .	50
3.2.5	Isolation Enhancement . . . . .	52
3.3	SIW . . . . .	56
3.3.1	Polarization . . . . .	60
3.3.2	Beam Scanning . . . . .	61
3.3.3	Slot Antenna Arrays . . . . .	63
3.4	Summary . . . . .	64
<b>CHAPTER 4 FREQUENCY RECONFIGURABILITY AND SLOT CURRENT MODES USING TCM</b>		<b>66</b>
4.1	Slot Effect on Chassis Modes . . . . .	69
4.1.1	Slot Mode Generation . . . . .	69
4.1.2	Slot Shape Effects on Chassis modes . . . . .	77
4.2	Antenna System Design . . . . .	83
4.2.1	Simulation and Measurement Results . . . . .	85
4.2.2	MIMO Antenna Scattering Parameters . . . . .	86
4.2.3	MIMO Antenna Gain Patterns . . . . .	89
4.2.4	MIMO Antenna Characterization . . . . .	91
4.3	Circular Slot (Single/MIMO) Antenna TCM Analysis . . . . .	93
4.4	Reconfigurability using TCM . . . . .	98

4.5	Conclusions . . . . .	106
<b>CHAPTER 5 ISOLATION ENHANCEMENT BETWEEN MIMO</b>		
<b>ANTENNAS USING TCM</b>		<b>108</b>
5.1	Antenna Design And Analysis Cases . . . . .	112
5.1.1	PIFA based 4-element MIMO Antenna Design . . . . .	113
5.1.2	Monopole Based 4-element MIMO Design . . . . .	117
5.2	Defected Ground Structure Analysis . . . . .	119
5.2.1	PIFA based MIMO Design . . . . .	119
5.2.2	Monopole Based MIMO Design . . . . .	129
5.2.3	Wire Monopole 2-element MIMO Design . . . . .	135
5.2.4	Systematic Approach to isolation enhancement in MIMO antennas . . . . .	136
5.3	MIMO Antenna Parameter Evaluation . . . . .	142
5.3.1	PIFA Based MIMO Design . . . . .	142
5.3.2	Monopole Based MIMO Design . . . . .	143
5.4	Conclusions . . . . .	145
<b>CHAPTER 6 EFFECT OF PRACTICAL ANTENNA ON CHAS-</b>		
<b>SIS CURRENT MODES</b>		<b>147</b>
6.1	Analysis Process . . . . .	149
6.1.1	Design 1 . . . . .	149
6.1.2	Design 2 . . . . .	156
6.1.3	Design 3 . . . . .	156
6.1.4	Design 4 . . . . .	158
6.2	Conclusions . . . . .	160
<b>CHAPTER 7 A NEW CURRENT MODE FOR PRACTICAL AN-</b>		
<b>TENNAS</b>		<b>161</b>
7.1	Analysis Process . . . . .	162
7.2	Effect on Chassis Modes . . . . .	164

7.3	Antenna Mode Generation . . . . .	169
7.4	Antenna Mode Excitation . . . . .	170
7.5	Conclusion . . . . .	172
<b>CHAPTER 8 SIW BASED MIMO ANTENNA</b>		<b>173</b>
8.1	Analysis Process . . . . .	174
8.1.1	Genetic Algorithm . . . . .	175
8.1.2	Antenna 1 (tilt of $10^0$ ) . . . . .	176
8.1.3	Antenna 1 (tilt of $-10^0$ ) . . . . .	181
8.1.4	Antenna 2 (tilt of $35^0$ ) . . . . .	184
8.1.5	4 element MIMO . . . . .	191
<b>CHAPTER 9 CONCLUSIONS &amp; FUTURE WORK</b>		<b>198</b>
9.1	Conclusions . . . . .	198
9.2	Future Work . . . . .	201
<b>APPENDICES</b>		<b>204</b>
<b>APPENDIX A DERIVATION OF THE ACGF</b>		<b>204</b>
A.1	Wilcox Expansion . . . . .	206
A.2	Multipole Expansion . . . . .	209
A.3	Weyl Expansion . . . . .	211
A.4	ACGF . . . . .	213
<b>APPENDIX B COMPUTER SIMULATION TECHNOLOGY (CST)</b>		<b>216</b>
<b>REFERENCES</b>		<b>222</b>
<b>VITAE</b>		<b>258</b>
<b>LIST OF PUBLICATIONS</b>		<b>259</b>



# LIST OF TABLES

1.1	Market forecast for the number of wireless mobile devices [2]. All values are in millions. . . . .	6
4.1	MS curve comparison of circular slot when introduced at the center and corner of the chassis. . . . .	77
4.2	MS curve comparison of different slot shapes when introduced at the center and corner of a chassis ( $120 \times 60mm^2$ ) in the presence of a RO4350 substrate. . . . .	82
4.3	Comparison between the proposed antenna and other works. . . . .	92
4.4	Simulated and measured ECC . . . . .	93
4.5	Comparison of MS curves to observe the effect of multiple slots on chassis modes. WB refers to whole BW, which is from 1 to 4 GHz. . . . .	100
4.6	Comparison of MS plots for reconfigurability analysis of first 7 modes analyzed at their respective resonance frequencies. . . . .	104
5.1	Isolation enhancement comparison with previous works . . . . .	141
5.2	Measured ECC( $\rho_e$ ) . All frequencies are in GHz . . . . .	143
5.3	Measured ECC( $\rho_e$ ) . All frequencies are in GHz . . . . .	146
6.1	Effect of chassis reduction on the resonance and BW . . . . .	153
7.1	Comparison of MS curves to observe the effect of the antenna on the chassis modes. . . . .	166

8.1 The offset and location of the slots on the top conductor of the SIW  
in Figure 8.3, for a tilt of 10 degrees in the beam. All numbers are  
in mm. . . . . 180

8.2 The offset and location of the slots on the top conductor of the SIW  
for a tilt of 35 degrees in the beam. All numbers are in mm. . . . 187

# LIST OF FIGURES

1.1	Calculating Radiated Field from Sources. . . . .	3
2.1	Eigen Values variation with frequency for a dipole of length 0.5 m and wire diameter of 1 mm [23]. . . . .	18
2.2	Modal Significance associated with the first four characteristic modes (or eigen values) for a dipole of length 0.5 m and wire diameter of 1 mm [23]. . . . .	20
2.3	Characteristic angle associated with the first four characteristic modes (or eigen values) for a dipole of length 0.5 m and wire diameter of 1 mm [23]. . . . .	21
2.4	Transmission and Reception of the antenna divided into three modes [19]. . . . .	24
2.5	CBF application on antenna (a) Surface of a geometry divided into 16 blocks, (b) Extended blocks introduction in the geometry [42,43].	28
2.6	SIW technology (a) SIW resemblance to Metallic Rectangular waveguide and (b) Basic SIW antenna Geometry [48]. . . . .	31
3.1	Literature Survey . . . . .	33
3.2	TCM used for BW enhancement Literature Review . . . . .	37
3.3	(a) Antenna geometry, (b) characteristic currents of mode 1 (left) and mode 4 (right) at 850 MHz [73]. . . . .	38
3.4	PIFA designs where (a) shows the PIFA with the ground plane, (b) zoomed element, (c) second PIFA design with different feeding and shorting location (c) third PIFA design [84]. . . . .	39



3.5	TCM used for Reconfigurability, Literature Review . . . . .	43
3.6	PIFA Antenna, where (a) Front view. (b) Side view. (c) Back view [115]. . . . .	45
3.7	Characteristic modes excitation, (a) First 3 Modes characteristic modes current distribution patterns, (b) ICE's location for the excitation of 3 modes, and (c) CCE's location for the excitation of 3 modes [124]. . . . .	48
3.8	Geometry Modification of chassis to introduce (a) Inductive Coupled Elements (b) Capacitive Coupled Elements [124]. . . . .	49
3.9	Feed Network for the selective excitation of modes [125]. . . . .	50
3.10	TCM used for Isolation Enhancement, Literature Review . . . . .	53
3.11	Double resonant SIW antenna [200]. . . . .	58
3.12	Double resonant SIW antenna [202]. . . . .	59
3.13	SIW based Beam-scanning based on scheme used . . . . .	62
3.14	16x16 planar slot array [226]. . . . .	64
4.1	Current distribution of the first 10 modes of the chassis at 3.182 GHz, where (a) Mode 1 (b) Mode 2 (c) Mode 3 (d) Mode 4 (e) Mode 5 (f) Mode 6 (g) Mode 7 (h) Mode 8 (i) Mode 9 (j) Mode 10. . . . .	71
4.2	Current distribution of first 10 modes of a circular slot of radius 15 mm at the center of the chassis at 3.182 GHz, where (a)-(j) represents Mode 1 to 11 respectively. . . . .	71
4.3	Modal Significance curves: (a) Ground plane or chassis, (b) Circular slot at center having radius of 15 mm, (c) Circular slot at center having radius of 20 mm, (d) Circular slot at center having radius of 30 mm, (e) Circular slot at corner having radius of 20 mm, (f) Circular slot at corner having radius of 30 mm . . . . .	75

4.4	(1)-(4) represents the first four modes of (a) Chassis (b) Circular slot of radius 15 mm at center of chassis (c) Circular slot of radius 15 mm at both edges of chassis (d) Circular slot of radius 15 mm at both edges of chassis with continuous current flow. . . . .	76
4.5	Current distribution of the first 11 modes of the chassis, where (a)-(k) represents Mode 1 to 11 respectively. . . . .	78
4.6	The rows represent mode 2, 5 and 9 respectively, where (a) Circular slot (b) Triangular slot (c) Rectangular slot (d) Square slot. . . .	79
4.7	Proposed slot MIMO antenna system (a) Top layer (b) GND plane (c) Fabricated model top layer (d) Fabricated model GND plane- All dimensions are in millimeters (mm). . . . .	84
4.8	(a) Detailed view of proposed design (b) Biasing circuitry. . . . .	84
4.9	(a) $ s_{11} $ and $ s_{22} $ -simulated (b) $ s_{11} $ and $ s_{22} $ -measured (c) $ s_{11} $ simulated and measured (d) $ s_{22} $ -simulated and measured (e) $ s_{12} $ -simulated (f) $ s_{12} $ - measured (g) $ s_{13} $ -simulated (h) $ s_{13} $ - measured. . . . .	88
4.10	Surface current distribution at 1.820 GHz (a) Top view (b) Bottom view. . . . .	90
4.11	Measured and simulated normalized radiation patterns at 1.86 GHz ( $E_{total}$ ) (a) ( $\theta$ -cuts) Ant-1 and Ant-2 at $\phi = 0^\circ$ (b) ( $\phi$ -cuts) Ant-1 and Ant-2 at $\theta = 90^\circ$ (c) ( $\theta$ -cuts) Ant-3 and Ant-4 at $\phi = 0^\circ$ (d) ( $\phi$ -cuts) Ant-3 and Ant-4 at $\theta = 90^\circ$ (e) Radiation pattern measurement setup. . . . .	90
4.12	Current distribution of the first 11 modes of single circular slot antenna when introduced on chassis, where (a) Mode 1 (b) Mode 2 (c) Mode 3 (d) Mode 4 (e) Mode 5 (f) Mode 6 (g) Mode 7 (h) Mode 8 (i) Mode 9 (j) Mode 10 (k) Mode 11. . . . .	94
4.13	Current distribution of the first 11 modes of 2-element circular slot antenna when introduced on chassis, where (a) Mode 1 (b) Mode 2 (c) Mode 3 (d) Mode 4 (e) Mode 5 (f) Mode 6 (g) Mode 7 (h) Mode 8 (i) Mode 9 (j) Mode 10 (k) Mode 11. . . . .	95

4.14	Current distribution of the first 11 modes of 4-element circular slot antenna when introduced on chassis, where (a) Mode 1 (b) Mode 2 (c) Mode 3 (d) Mode 4 (e) Mode 5 (f) Mode 6 (g) Mode 7 (h) Mode 8 (i) Mode 9 (j) Mode 10 (k) Mode 11. . . . .	98
4.15	Modal Significance curves: (a) Ground plane or chassis, (b) Single circular slot antenna, (c) 2-element circular slot antenna, (d) 4-element circular slot antenna. . . . .	99
4.16	Modal Significance curves: (a) Single Circular slot antenna with 2.0 pF capacitor, (b) Single Circular slot antenna with 5.0 pF capacitor, (c) 4-element MIMO Circular slot antenna with 2.0 pF capacitor, (d) 4-element MIMO Circular slot antenna with 5.0 pF capacitor. . . . .	102
5.1	Current distribution of the first six modes of the chassis in the presence of an FR-4 substrate at 2.20 GHz, where (a)-(f) represents mode 1 to 6 respectively. . . . .	114
5.2	Modal Significance curves of the ground plane or chassis. . . . .	114
5.3	Geometry of the 4-element MIMO PIFA deisgn (a) top view, (b) bottom view with DGS, all dimensions are in mm (c) fabricated prototype top view, (d) fabricated prototype bottom view with DGS, (e) measured reflection coefficient without DGS, (f) measured isolation without DGS. . . . .	116
5.4	3D view of single element (a) PIFA, (b) monopole. . . . .	117
5.5	Current distribution of the first six modes of the 4-element MIMO PIFA in the presence of an FR-4 substrate at 2.20 GHz, where (a)-(f) represents mode 1 to 6 respectively. . . . .	118
5.6	Modal significance curves of the 4-element PIFA based MIMO in the presence of the FR-4 substrate. . . . .	118

5.7	Geometry of the 4-element MIMO PIFA design (a) top view, (b) bottom view with DGS, all dimensions are in mm (c) fabricated prototype top view, (d) fabricated prototype bottom view with DGS, (e) measured reflection coefficient without DGS, (f) measured isolation without DGS. . . . .	120
5.8	Current distribution of the first six modes of the 4-element MIMO monopole in the presence of an FR-4 substrate at 2.20 GHz, where (a)-(f) represents mode 1 to 6 respectively. . . . .	121
5.9	Modal significance curves of the 4-element MIMO monopole in the presence of FR-4 substrate. . . . .	121
5.10	Current distribution on the surface of the 4 element MIMO PIFA antenna at 2.2 GHz when all antenna's are excited (a) without any DGS, (b) DGS between Ant-1 and 3. . . . .	123
5.11	Current distribution of the first six modes of the 4-element PIFA like MIMO in the presence of the DGS at 2.20 GHz, where (a)-(f) represents the mode 1 to 6 respectively. . . . .	126
5.12	Modal significance curves of the 4-element PIFA like MIMO in the presence of DGS. . . . .	126
5.13	Current distribution of the first six modes of the 4-element MIMO PIFA in the presence of two DGS at 2.20 GHz, where (a)-(f) represents mode 1 to 6 respectively. . . . .	128
5.14	Modal significance curves of the 4-element MIMO in the presence of two DGS. The vertical blue lines represent the impedance BW. . . . .	128
5.15	4-element PIFA design, (a) measured reflection coefficient with DGS, (b) measured isolation curve with DGS, (c) current distribution without DGS when Ant-1 is excited, (d) current distribution with DGS when Ant-1 is excited. . . . .	130
5.16	Current distribution on the surface of the 4-element MIMO monopole antenna and chassis at 2.2 GHz when all antennas are excited. . . . .	131

5.17	Current distribution of the first six modes of the 4-element Monopole based MIMO in the presence of DGS at 2.20 GHz, where (a)-(f) represents mode 1 to 6 respectively. . . . .	132
5.18	Modal significance curves of the 4-element MIMO Monopole in the presence of FR-4 substrate in the presence of DGS. The vertical blue lines represent the impedance BW. . . . .	133
5.19	4-element Monopole design, (a) measured reflection coefficient with DGS, (b) measured isolation curve with DGS, (c) current distribution without DGS when Ant-1 is excited, (d) current distribution with DGS when Ant-1 is excited. . . . .	134
5.20	2-element wire monopole design, (a) reflection coefficient, (b) coupling coefficient, (c) modal significance curves of the 2-element MIMO wire monopole (no DGS), and (d) modal significance curves of the 2-element MIMO wire monopole in the presence of DGS. . . . .	137
5.21	Block diagram of the proposed isolation enhanced TCM based method using DGS . . . . .	139
5.22	Radiation pattern measurement setup (a) 4-element MIMO PIFA (b) 4-element MIMO Monopole. . . . .	143
5.23	PIFA-based MIMO antenna measured and simulated normalized radiation patterns at 2.20 GHz ( $E_{total}$ ) (a) ( $\phi$ cut) Ant 1 and 2 at $\theta = 90$ , (b) ( $\theta$ cut) Ant 1 and 2 at $\phi = 90$ , (c) ( $\phi$ cut) Ant 3 and 4 at $\theta = 90$ , (b) ( $\theta$ cut) Ant 3 and 4 at $\phi = 90$ . . . . .	144
5.24	Measured Gain and efficiency curves for (a) 4-element MIMO PIFA, (b) 4-element MIMO Monopole. . . . .	144
5.25	Monopole-based MIMO antenna measured and simulated normalized radiation patterns at 2.20 GHz ( $E_{total}$ ) (a) ( $\phi$ cut) Ant 1 and 2 at $\theta = 90$ , (b) ( $\theta$ cut) Ant 1 and 2 at $\phi = 0$ , (c) ( $\phi$ cut) Ant 3 and 4 at $\theta = 90$ , (b) ( $\theta$ cut) Ant 3 and 4 at $\phi = 0$ . . . . .	145

6.1	Design Geometries, (a) Antenna element on mobile chassis (b) Design 1, PIFA antenna resonating at 2.2 GHz, (c) Design 2, Monopole antenna resonating at 2.2 GHz, (d) Design 3, PIFA antenna resonating at 0.93 GHz and (e) Design 4, Monopole antenna resonating at 0.95 GHz. SP and FP represents the shorting point and the feeding point respectively. All dimensions are in mm. . . . .	150
6.2	CM Current distribution, where (a)-(f) represents mode 1 to 6 of (1) Ground plane/chassis, (2) Design 1, PIFA, (3) Design 2, Monopole. Red arrows show the location as well as the direction of the maximum current of a mode. . . . .	151
6.3	Reflection Coefficient Curves for (a) Design 1, (b) Design 2, (c) Design 3 and Design 4. C1 to C10 refers to chassis size reduction by 0%, 16%, 30%, 44%, 56%, 64%, 75%, 83%, 90% and 94%, respectively.	153
6.4	Modal Significance curves (a) Chassis ( $120 \times 60mm^2$ ), (b) Design 1, (c) Design 2, (d) 90% reduced chassis ( $40 \times 20mm^2$ ), (e) Design 1 on 90% reduced chassis, (f) Design 2 on 90% reduced chassis. . .	155
6.5	CM Current distribution, where (a)-(f) represents mode 1 to 6 of (1) 90% reduced Chassis, (2) Design 1 on 90% reduced Chassis, (3) Design 2 on 90% reduced Chassis. . . . .	157
6.6	Modal Significance curves (a) Chassis ( $120 \times 60mm^2$ ), (b) Design 3, (c) Design 4. . . . .	159
7.1	Design geometries, where (a) Antenna element on chassis showing different locations for the placement of the antenna. L1, L2 and L3 refers to the placement of the antenna at the corner, middle of the short edge and middle of long edge respectively, (b) Design 1, PIFA, (c) Design 2, Monopole and (d) Design 3, Loop antenna. SP and FP represents the shorting point and the feeding point respectively. All the dimensions are in mm. . . . .	163
7.2	Reflection Coefficient curves for the three antennas. . . . .	164

7.3	Eigenvalues of the first six characteristic modes (J1-J6) of chassis 120×60 mm <sup>2</sup> . . . . .	165
7.4	CM current distribution, where (a)-(f) represents the mode 1 to 6 and (g) represents the newly generated mode of (1) Ground plane, (2) Design 1, PIFA located at the corner of the chassis, (3) Design 2, Monopole located at the corner of the chassis, (4) Design 3, Loop antenna located at the corner of the chassis, (5) Design 1, PIFA located at the middle of the shorter edge and (6) Design 1, PIFA located at the middle of the longer edge. . . . .	167
7.5	Modal Significance curves (a) Chassis (120×60 mm <sup>2</sup> ), (b) Design 1, PIFA, (c) Design 2, Monopole, (d) Loop antenna, (e) Design 1, PIFA located at width (shorter edge) center, (f) PIFA located at longitudinal (longer edge) center. . . . .	168
7.6	MS curve of the new antenna mode. D1 to D3 refers to the PIFA, Monopole and Loop antenna respectively. LC and WC refers to the cases when the antenna is placed at the center of the long arm, and short arm respectively. . . . .	171
8.1	Genetic Algorithm (GA) flow chart. . . . .	177
8.2	The desired normalized radiation pattern and the GA algorithm based optimized radiation pattern for a $\theta$ cut at $\phi = 270^0$ . . . . .	178
8.3	Design geometries, where (a) Top view showing the locations of different slots on the top conductors and (b) bottom view. All the dimensions are in mm. . . . .	179
8.4	Reflection coefficient of the SIW antenna in Figure 8.3. . . . .	180
8.5	The 3D radiation pattern showing a tilt of 10 degrees at different frequency band where, (a) 28.75 GHz, (b) 29 GHz, (c) 30 GHz and (d) 31.5 GHz . . . . .	181
8.6	Normalized radiation pattern showing a tilt of 10 degrees at differ- ent frequency bands for a $\theta$ cut at $\phi = 270^0$ . . . . .	182

8.7	Normalized radiation pattern showing a tilt of 10 degrees at different frequency bands for a $\theta$ cut at $\phi = 270^0$ , limited between $0^0 \leq \theta \leq 180^0$ . . . . .	182
8.8	The 3D radiation pattern showing a tilt of $-10$ degrees at different frequency band where, (a) 28.75 GHz, (b) 29 GHz, (c) 30 GHz and (d) 31.5 GHz . . . . .	183
8.9	Normalized radiation pattern showing a tilt of $-10$ degrees at different frequency bands for a $\theta$ cut at $\phi = 270^0$ . . . . .	184
8.10	Normalized radiation pattern showing a tilt of $-10$ degrees at different frequency bands for a $\theta$ cut at $\phi = 270^0$ . . . . .	185
8.11	The desired normalized radiation pattern and the GA algorithm based optimized radiation pattern for a 14 element slot SIW with a $\theta$ cut at $\phi = 270^0$ . . . . .	185
8.12	Design geometries, where (a) Top view showing the locations of different slots on the top conductors and (b) bottom view. All the dimensions are in mm. . . . .	186
8.13	Reflection coefficient of antenna. . . . .	188
8.14	Normalized radiation pattern showing a tilt of 35 degrees at different frequency bands for a $\theta$ cut at $\phi = 270^0$ . . . . .	189
8.15	Normalized radiation pattern showing a tilt of 35 degrees at different frequency bands for a $\theta$ cut at $\phi = 270^0$ . . . . .	189
8.16	Normalized radiation pattern showing a tilt of $-35$ degrees at different frequency bands for a $\theta$ cut at $\phi = 270^0$ . . . . .	190
8.17	Normalized radiation pattern showing a tilt of $-35$ degrees at different frequency bands for a $\theta$ cut at $\phi = 270^0$ . . . . .	190
8.18	Design geometry of 4 element MIMO case, where (a) Top view showing the 4 antenna array and (b) bottom view. All the dimensions are in mm. . . . .	192
8.19	Reflection coefficient of 4 element MIMO. . . . .	193
8.20	Isolation enhancement of 4 element MIMO. . . . .	193



8.21	Normalized radiation pattern showing a tilt of -10 degrees at different frequency bands for a $\theta$ cut at $\phi = 270^0$ by antenna element 1. . . . .	194
8.22	Normalized radiation pattern showing a tilt of -10 degrees at different frequency bands for a $\theta$ cut at $\phi = 270^0$ by antenna element 1. . . . .	194
8.23	Normalized radiation pattern showing a tilt of 30 degrees at different frequency bands for a $\theta$ cut at $\phi = 270^0$ by antenna element 2. . . . .	195
8.24	Normalized radiation pattern showing a tilt of 30 degrees at different frequency bands for a $\theta$ cut at $\phi = 270^0$ by antenna element 2. . . . .	195
8.25	Normalized radiation pattern showing a tilt of -30 degrees at different frequency bands for a $\theta$ cut at $\phi = 270^0$ by antenna element 2. . . . .	196
8.26	Normalized radiation pattern showing a tilt of -30 degrees at different frequency bands for a $\theta$ cut at $\phi = 270^0$ by antenna element 2. . . . .	196
8.27	Normalized radiation pattern showing a tilt of 10 degrees at different frequency bands for a $\theta$ cut at $\phi = 270^0$ by antenna element 4. . . . .	197
8.28	Normalized radiation pattern showing a tilt of 10 degrees at different frequency bands for a $\theta$ cut at $\phi = 270^0$ by antenna element 4. . . . .	197
A.1	Regions around antenna. . . . .	206
A.2	Regions surrounding antenna. $R_o$ is referring to far field. $R_1, R_2, \dots, R_\infty$ refers to near field [21]. . . . .	207
B.1	CST design environment. A metallic chassis of $120 \times 60 \text{ mm}^2$ is shown.	218

B.2 CST design environment. Frequency BW on which the CM are  
need calculated. . . . . 219

B.3 CST design environment. Frequencies on which the user want to  
plot the currents or the far-field radiation pattern shall be entered. 219

B.4 CST design environment. Enter the number of modes. . . . . 220

B.5 CST design environment. Modal Significance curves. . . . . 220

B.6 CST design environment. Current distribution on the surface of  
the antenna for particular mode. . . . . 221

B.7 CST design environment. Far-field radiation pattern of the modes. 221

# LIST OF SYMBOLS

$\lambda$	: Wavelength
$f$	: frequency
$E$	: Electric field intensity
$H$	: Magnetic field intensity
$\mu_r$	: Relative permeability of the medium
$\mu_0$	: Permeability of free space
$\epsilon_r$	: Relative permittivity of the medium
$\epsilon_0$	: Permittivity of free space
$J$	: Electric current density
$M$	: Magnetic current density
$A$	: Magnetic vector potential
$F$	: Electric vector potential
$x^*$	: Complex conjugate of vector $x$
$Q$	: Modal quality factor
$\alpha_n$	: Characteristic angle
$\nabla$	: Gradient
$\nabla \cdot$	: Divergence
$\nabla^2$	: Laplacian
$J$	: Current density
$Z$	: Impedance matrix

# LIST OF ABBREVIATIONS

ACGF	:	Antenna current green function
AMSDL	:	Antenna and Microwave structure design lab
BW	:	Bandwidth
CA	:	Characteristic angle
CBF	:	characteristic basis function
CCE	:	Capacitive coupled element
CCGF	:	Cross-correlation green function
CMA	:	Characteristic modal analysis
CM	:	Characteristic mode
CST	:	Computer Simulation Technology
DGS	:	Defected ground structure
ECC	:	Envelope correlation coefficient
EFIE	:	Electric field integral equation
FBR	:	Front to back ratio
FEM	:	Finite element method
FTTD	:	Finite-difference time-domain method
FN	:	Feeding network
FSGF	:	Free space green function
GA	:	Genetic Algorithm

GND	:	Ground
HPBW	:	Half power bandwidth
HMSIW	:	Half mode substrate integrated waveguide
HSIW	:	Hollow substrate integrated waveguide
HFSS	:	High frequency Electromagnetic field simulation
ICE	:	Inductive coupled element
MIMO	:	Multiple-input-multiple-output
MoM	:	Method of Moments
MS	:	Modal significance
MN	:	Matching network
PD	:	Power divider
PS	:	Phase shifter
PIFA	:	Printed Inverted F-antenna
SIW	:	Substrate integrated waveguide
TCM	:	Theory of characteristic modes
UWB	:	Ultra wide-band antenna
VNA	:	Vector Network Analyzer
WLAN	:	Wireless local area network
WiMAX	:	Worldwide interoperability for microwave access
2D	:	Two dimensional
3D	:	Three dimensional

# THESIS ABSTRACT

**NAME:** Asim Ghalib  
**TITLE OF STUDY:** Current Engineering methods applied to the design of  
MIMO antenna systems  
**MAJOR FIELD:** Electrical Engineering  
**DATE OF DEGREE:** April 30, 2018

Fourth Generation (4G) and fifth Generation (5G) wireless communication devices will rely on multiple-input-multiple-output (MIMO) technology for providing enhanced data rates. Antenna design for MIMO systems is a challenging task in any communication system because it depends on past experience and thus lacks physical explanation and systematic design steps. Some recent theories like antenna current green function (ACGF), theory of characteristic modes (TCM) and characteristic basis function (CBF) were proposed to provide some insight. This work focuses on critically evaluating the feasibility of all these current engineering methods from a practical antenna design perspective and in particular in the context of printed MIMO antennas. ACGF, suffers from the issue that it relies on the current equation which is mathematically intractable for printed antennas. TCM

and CBF can be used for any antenna type because they rely on the Method of Moments (MoM).

With the help of TCM, it was found that the introduction of circular slots on a chassis does not generate any new modes. The presence of the slot modifies the chassis modes. Based on the size, shape and location of the slot different chassis modes are affected. The effect of multiple circular slots on the chassis modes was investigated for the first time. Based on our analysis, a miniaturized frequency agile annular slot-based MIMO antenna system was designed and analyzed for mobile sized phones. The antenna exhibits wide tuning range operation by covering several well known wireless standards. Using TCM analysis, the physical behavior behind frequency reconfigurability was also investigated.

A systematic method was developed with the help of TCM (current engineering) to predict whether the isolation can be enhanced between adjacent antenna elements. The behavior of defected ground structures (DGS) when added to antenna designs was also investigated. A properly designed DGS introduces currents opposite in direction to the original characteristic modes (CM) currents thus reducing mutual coupling. Using the proposed approach, isolation was improved on an average by 11 dB for three different antenna design types.

With the help of TCM, the use of the mobile chassis as the main radiating element for frequencies greater than 2 GHz is shown to be not practical nor realistic. For such frequencies, the antenna is the main radiating source. The effect of real antenna elements on rectangular chassis modes was also investigated. For

the first time, we showed that the presence of the antenna generates a completely new antenna mode (compared to chassis mode modifications in other existing works). The new antenna mode only depends on the shape of the antenna and is independent of the location of the antenna on the chassis (unlike chassis modes).

Two substrate integrated waveguide (SIW) antennas having a tilt of  $10^{\circ}$  and  $35^{\circ}$  (from broad side) with a side lobe level (SLL) of at least 7 dB operating over a wide frequencyband from 28.75 GHz to 31.2 GHz are presented in a MIMO configuration for future 5G handheld terminals. The antennas were optimized using genetic algorithm (GA) that determines the location of the slots based on predefined SLL and beam tilt.



## ملخص الرسالة

الاسم: عاصم غالب

عنوان الدراسة: تطبيق طرق هندسة التيار على تصميم أنظمة هوائيات MIMO

التخصص: الهندسة الكهربائية

تاريخ الدرجة: 30 نيسان 2018

أجهزة الاتصالات اللاسلكية للجيل الرابع 4G والجيل الخامس 5G سوف يعتمد على تكنولوجيا متعدد-المدخلات-متعدد-المخرجات MIMO لتوفير سرعة نقل بيانات محسنة. تصميم الهوائيات لأنظمة MIMO مهمة صعبة في أي نظام اتصالات لأنها تعتمد على الخبرة السابقة وبالتالي تفتقر إلى التفسير الفيزيائي وخطوات التصميم المنظمة. بعض النظريات الحديثة مثل الاقتران الأخضر لتيار الهوائي ACGF، نظرية الأوضاع المميزة TCM، واقتران الأساسات المميزة CBF تم عرضها لتبسيط بعض الضوء. هذا العمل يتركز على التقييم النقدي لجدوى جميع هذه الطرق لهندسة التيار من جهة تصميم الهوائيات العملي وتصميم هوائيات MIMO المطبوعة بالتحديد. ACGF، تعاني من معضلة أنها تعتمد على معادلة التيار التي يصعب استخراجها رياضياً من الهوائيات المطبوعة. TCM و CBF يمكن استخدامها لأي نوع هوائيات لأنها تعتمد على طريقة العزوم MoM.

بمساعدة TCM، تبين أن ظهور فتحات دائري بهيكل معدني لا ينتج أي أوضاع جديدة. ظهور الفتحة يعدل أوضاع الهيكل. اعتماداً على حجم وشكل وموقع الفتحة، أوضاع مختلفة تتأثر في الهيكل. تأثير فتحات دائرية متعددة في الهيكل تم استكشافه لأول مرة. اعتماداً على تحليلنا، تم تصميم وتحليل نظام هوائيات MIMO مصغر مبني على فتحات حلقة تعتمد على تحديد التردد بحجم أجهزة الهاتف. الهوائي يعرض تشغيل طيف واسع من الترددات المضبوطة من خلال تغطية العديد من معايير الاتصالات اللاسلكية المعروفة. باستخدام تحليل TCM، تم أيضاً استكشاف السلوك الفيزيائي خلف خاصية التحكم في التردد.

تم تطوير طريقة منظمة بمساعدة TCM (هندسة التيار) لتوقع إذا ما كان يمكن تحسين العزل بين عناصر الهوائيات المتجاورة. تم أيضاً استكشاف سلوك تركيبات التاريز الشقي DGS عند إضافتها لتصميمات الهوائيات. DGS المصممة بعناية تنتج تيارات تعاكس اتجاه تيارات الأوضاع المميزة CM الأصلية مما يعني تقليل التأثير المتبادل. باستخدام المقاربة المقترحة، تم تحسين العزل بمعدل 11 dB لثلاثة أنواع من تصميمات الهوائيات.

بمساعدة TCM، تم تبين أن استخدام الهيكل المعدني للهاتف كعنصر إشعاع رئيسي للترددات الأكبر من 2 GHz ليس عملي ولا واقعي. لتلك الترددات، الهوائي هو مصدر الإشعاع الرئيسي. تم أيضاً استكشاف تأثير عناصر الهوائيات الحقيقية على أوضاع الهيكل المستطيل الشكل. لأول مرة، أثبتنا أن تواجد الهوائي ينتج وضع جديد تماماً للهوائي (مقارنة بمجرد التعديلات على أوضاع الهيكل كما في الأعمال السابقة). الوضع الجديد للهوائي يعتمد فقط على شكل الهوائي وهو لا يعتمد على موقع الهوائي على الهيكل (على خلاف الحال في أوضاع الهيكل).

تم عرض تصميم هوائيين من نوع موجة الموجه المضمن في المادة SIW بزاوية ميلان 10 و 35 درجة (عن الاتجاه الأساسي) ومستوى إشعاع ثانوي (جانبي) SLL 7 dB على الأقل تعمل على نطاق ترددات واسع من 28.75 GHz لغاية 31.2 GHz وفق ضبط MIMO لأجهزة 5G اليدوية المستقبلية. تم تحسين الهوائي باستخدام خوارزمية الجينات GA التي تحدد موقع الفتحات اعتماداً على التحديد المسبق لكل من SLL وزاوية ميلان الإشعاع.

# CHAPTER 1

# INTRODUCTION

*“A good beginning makes a good end”*

---

LOUIS L'AMOUR

Significant advancements were achieved in the area of antenna design in recent years due to printed technology and the multitude of wireless standards and strict requirements of small mobile devices. The use of smart devices is increasing day by day, and it is predicted that by the end of 2020, around 50 billion devices will be connected to the Internet, where major portion of the devices will be connected wirelessly [1]. According to [2], by the end of 2018, more than 50 % of users will use smart phones or tablets for online activities while WIFI will be specified as the default connection for all non-mobile devices such as desk phones, desktops, projectors and conference rooms. The requirement of smart phones in 2017 was around 2.0 billions as compared to 2013, where it was 1.7 billions. It is expected that 5G will be launched by the end of 2021. 5G will provide 100 to 1000 times faster data rates as compared to 4G. Such High data rates can be achieved by

employing multiple-input-multiple-output (MIMO) systems and the use of wider bandwidths at the range of millimeter wave (mm-wave).

Beside the need of high data rates, there are other design constraints that an antenna designer needs to take care of such as compactness, small size, low profile, light weight and robustness of the design [3]. The antenna shall also provide broadband operation [4] or reconfigurable capability to address multiple bands [5]. Up to date, there are very limited general guidelines developed for some basic antenna designs [6, 7]. Even after following these guidelines, we still need to apply parametric sweeps in full wave software packages (computer aided design-CAD) like FEKO [8], HFSS [9] and CST [10] in order to get the desired response. The use of numerical and computational methods is also limited because of the huge amount of complexity involved [11–13]. The use of automatic optimization techniques such as Genetic Algorithms (GA) [14], particle-swarm optimization [15] and artificial neural networks [16] are very limited to specific applications and cannot be generalized because of different behavior and large amount of parameters that need to be optimized, other wise useful for specific applications.

Nowadays, antenna design depends alot on past experience and know-how. The designers do not look into the physics behind the antenna design process in alot of cases and only focus on the final output. Just on the basis of careful observations, they design antennas that fulfill the requirements needed, such as appropriate bandwidth (BW), highly miniaturized and high efficiency.

If the antenna current density has a closed form expression, we can easily

calculate the radiation patterns for a specific antenna. As shown in Figure 1.1, we can calculate the Electric and Magnetic potentials from the current density and then from these potentials, we can find out the radiation patterns of any antenna. If we have Electric ( $J$ ) and Magnetic ( $M$ ) sources then we can calculate the Magnetic ( $A$ ) and Electric ( $F$ ), vector potentials from (1.1) and (1.2), respectively [6], where  $\mu$  and  $\epsilon$  are the permeability and permittivity of the medium in which the wave is propagating and  $R$  represents the distance from the source to any observation point.  $k$  represents the propagation constant and is given by  $k = \omega\sqrt{\mu\epsilon}$ .

$$A = \frac{\mu}{4\pi} \iiint_V J \frac{e^{-jkR}}{R} dv' \quad (1.1)$$

$$F = \frac{\epsilon}{4\pi} \iiint_V M \frac{e^{-jkR}}{R} dv' \quad (1.2)$$

The Electric ( $E$ ) and Magnetic ( $H$ ) fields generated by the Electric source (Mag-

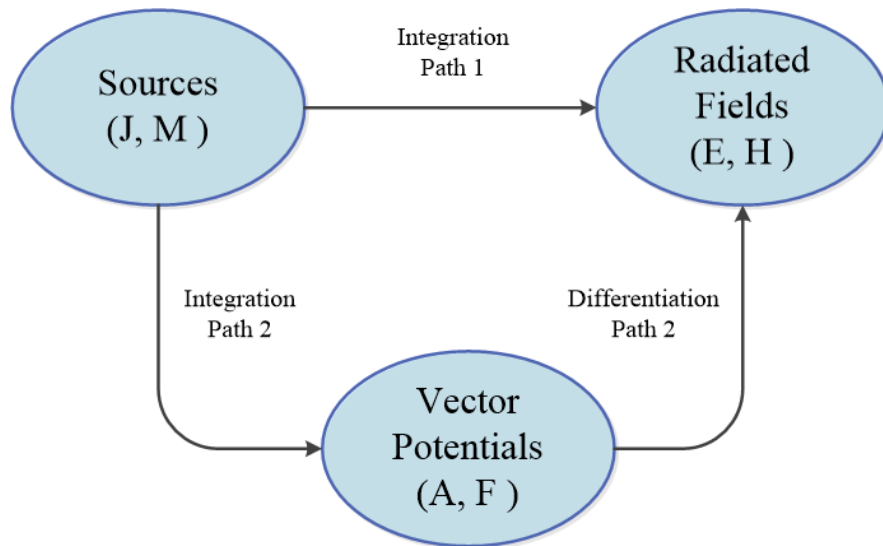


Figure 1.1: Calculating Radiated Field from Sources.

netic vector potential) are given (1.3), and (1.4). where  $\omega$  is the angular frequency

at which we want to find the  $E_A$  field at.

$$H_A = \frac{1}{\mu} \nabla \times A \quad (1.3)$$

$$E_A = -\nabla\phi_e - j\omega A = -j\omega A - j\frac{1}{\omega\mu\epsilon} \nabla(\nabla \cdot A) \quad (1.4)$$

Similarly, the electric and magnetic fields generated by the magnetic source (electric vector potential) are given by [6]

$$E_F = -\frac{1}{\epsilon} \nabla \times F \quad (1.5)$$

$$H_F = -\nabla\phi_m - j\omega F = -j\omega F - j\frac{1}{\omega\mu\epsilon} \nabla(\nabla \cdot F) \quad (1.6)$$

The total Fields are thus given by

$$E = E_A + E_F \quad (1.7)$$

$$H = H_A + H_F$$

For simple wire structures like monopole and dipole antennas, it is easy to calculate the closed form expressions for the antenna fields because the current distributions are well defined under ideal condition (i.e. free space without existence of a dielectric, lossless conductors and small feeding gaps). A problem arises when we are dealing with complex (i.e. printed) structures. It is very hard to get closed form expressions for the current distribution (if not impossible) and thus the fields cannot be obtained in closed form, but rather using numerical methods. That is

why less attention has been given to the calculation of the current density in a closed form fashion in the past.

Recently, some theories were developed such as theory of characteristic modes (TCM) [17], antenna current green function (ACGF) [34–39] and characteristic basis function (CBF) [42, 43] to explain the physical behavior of the antennas. Engineering the current in these methods lead to direct impact on the radiated fields and other antenna parameters. The objective of this work is to analyze these methods and to study whether these methods can be extended to real antenna designs with MIMO antenna system focus. For these three methods we need to identify their advantages and disadvantages. TCM will be used to analyze the behavior of MIMO antenna designs via current engineering. The size constraint of the MIMO antenna systems causes severe coupling between the antenna elements, and thus TCM will be also used to develop a systematic approach for isolation enhancement between the antenna elements via current control. It will be also used to explain the physics behind frequency reconfigurability in frequency agile antennas.

Since fields are directly coupled to the currents, this will be utilized to design substrate integrated waveguide (SIW) antennas via field engineering and optimization using GA for 5G MIMO enabled terminals. SIW's have the advantage of huge BW, high gain, low profile and ease of integration with planar structures.

## 1.1 Motivation

Table 1.1 presents the forecast in the demand of wireless devices. In 2015, around 2.9 billions devices were sold while in 2018 it is expected to sell 3.1 billions. We can observe that the demand of almost all the products increased. The number of wireless hand held devices had already exceeded the number of people on Earth.

Table 1.1: Market forecast for the number of wireless mobile devices [2]. All values are in millions.

Device Type	2015	2016	2017	2018
Ultramobiles (Premium)	45	57	73	90
PC Market (Laptops)	289	284	296	306
Ultramobiles (Basic and Utility)	195	188	188	194
Computing Devices Market	484	473	485	500
Mobile Phones	1917	1943	1983	2022
<b>Total Devices Market</b>	<b>2930</b>	<b>2945</b>	<b>3025</b>	<b>3112</b>

It is expected that 5G will be launched by the end of 2021. It will have features such as high data rates, higher system capacity, massive device connectivity, reduced latency, energy saving and cost reduction. Large BW can be achieved using millimeter wave bands. Antenna design will play a vital role in the performance of the system. Obviously MIMO antenna systems or massive MIMO antenna systems, will meet these requirements. Thus the design of such antennas for wireless devices according to 4G/5G standards has a lot of importance. Design requirements for MIMO antenna systems are low cost, compact size, low profile with acceptable amount of isolation between the antenna elements. Also, 4G and 5G antenna coexistence and integration is important.

Antennas are designed normally on the basis of practical experience and fine

tuned based on educated parametric sweeps in CAD tools. Systematic antenna design methods are almost non existent, and developing such methods can reduce design time and improve performance. Such methods will also predict, whether a particular performance can be achieved or not.

## 1.2 Problem Statement

The design of novel antennas with good radiation characteristics is an important requirement for the 4G/5G MIMO antenna designs. Printed antennas are the most widely used due to their ease of integration with other microwave electronics and within the wireless device. Even with current advancements in antenna design, there is no systematic procedure developed for the design of printed MIMO antennas in literature. The main problem is that, we do not have closed form expressions for the current distribution on the surface of the antenna in the first place. If we some how can control or know the current distribution on the surface of antenna and the ground plane, the design procedure can become more structured.

Recently, few methods (ACGF [19–22], TCM [23–25], CBF [42–44]) were developed, to provide physical explanation as well as some systematic design procedures. Although these methods have provided physical explanation to many problems they still need alot of improvement.

In this work, we are throughly analyzing these methods along with their feasibility in practical designs. After performing a comprehensive literature review,



the applicability and the extension of these methods to printed antenna designs is performed. TCM is then extensively used to design printed MIMO antennas systems and a systematic method for isolation enhancement is provided. Orthogonal patterns can be obtained from the characteristic modes that is why alot of research address pattern reconfigurability. As characteristic modes have no direct link with the frequency reconfigurability, only two research publications are present in the literature that used TCM without any systematic procedure to get the frequency reconfigurability for an antenna design via the use of reactive loading.

From a MIMO perspective, isolation is an important performance metric. Normally the compactness of the terminals may degrade the performance of MIMO systems due to high port and field coupling which affect the channel capacity, BW and efficiency of the system. Previously, TCM was used only to study the behavior of chassis to improve the isolation by 5 dB only. Normally for MIMO designs we need high isolation. Any systematic procedure, if developed with the help of TCM, that can enhance the isolation will be of great help to designers.

MM-wave band will be used in 5G to provide ultrahigh speeds due to the large available BW. The design of substrate integrated waveguide (SIW) arrays with current control can generate uncorrelated beams and is of high interest for mobile manufacturers. Thus, we provide a 5G mm-wave MIMO antenna solution utilizing pattern synthesis via field and current control using a genetic algorithm (GA) based optimization procedure.

The objectives of this work are;

- To critically evaluate ACGF, TCM and CBF current engineering methods in terms of their up-to-date work and applicability to printed MIMO antenna design. To evaluate whether these methods can help in antenna designing process or explain the antenna performance parameters.
- To design a MIMO circular slot antenna design covering frequency Band from 1.8 to 2.45 GHz with frequency reconfigurable and explain the physical mechanism of frequency reconfigurability from the perspective of TCM.
- To develop a systematic approach that can predict whether a DGS can enhance the isolation between MIMO antenna elements or not and to provide a physical explanation to the physical behaviour of DGS and explain its mechanism with the help of TCM.
- To design a 5G SIW MIMO based antenna system with optimized pattern synthesis using GA. The antenna system will work at 28 GHz and at least 2 GHz of BW with two arrays each behaving as a single MIMO antenna.

### 1.3 Work Contributions

The contributions of this work are summarized as follows;

1. A comprehensive investigation of the feasibility of ACGF, TCM and CBF current engineering methods in the design of printed MIMO antennas.
2. The design of a circular slot MIMO antenna system covering the frequency bands from 1.8 to 2.45 GHz with frequency reconfigurability capability and

explain for the first time the physical mechanism of frequency reconfigurability from the perspective of TCM. The average BW is 38 MHz. The measured maximum efficiency was 73% while the measured maximum gain was 2.43 dBi. The envelope correlation coefficient did not exceed 0.186 across the complete operating BW.

3. The development of a systematic approach that can predict whether a DGS can enhance the isolation between MIMO antenna elements or not and providing for the first time a physical explanation to the behavior of DGS with the help of TCM.
4. For frequencies greater than 1 GHz, we show for the first time that the antenna is the element responsible for the radiation and not the mobile chassis. So, the use of the chassis for frequencies greater than 1 GHz is unrealistic approach.
5. We show that the presence of the antenna generates a new mode. It depends on the antenna element geometry and not on the location of the antenna on the chassis.
6. The design of a novel 5G SIW based MIMO antenna system with optimized pattern synthesis using GA via engineering the currents. The antenna system works at 28 GHz with at least 3 GHz of BW and two arrays each behaving as a single MIMO antenna.

## 1.4 Dissertation Overview

The dissertation is divided into nine chapters. In chapter 2, an overview of the ACGF, TCM, CBF and SIW is provided. Parameters used to evaluate the performance of all these methods are discussed. In chapter 3, a comprehensive literature review of ACGF, TCM, CBF and SIW is conducted to show the contributions of this work.

In chapter 4, TCM is applied to study and have better understanding of the physical effect of slots when introduced in mobile chassis. Based on the analysis, a novel 4 element MIMO frequency reconfigurable slot antenna is proposed. The physical mechanism behind frequency reconfigurability is analyzed for the first time and explained using TCM.

In chapter 5, a systematic method for the isolation enhancement between MIMO antennas is presented. The method can predict whether with the help of DGS we can or we cannot improve the isolation. Using TCM, an explanation to the physical behavior of DGS is also provided. An average of 11 dB isolation enhancement was achieved when the systematic method was applied to different MIMO antenna systems.

In chapter 6, emphasis was made against the use of the chassis as the main radiator for frequencies greater than 2 GHz, which was normally done in the literature. It was shown that a 90 % reduction in the mobile chassis did not affect the antenna behaviour in terms of resonance. In chapter 7, it is shown that the presence of the antenna generates a new mode. As all the modes have current

maxima across the antenna element itself, the excitation of a single antenna mode with the existing available techniques is impossible.

In chapter 8, a GA is used to design a traveling wave SIW slot antenna operating at 28.5 GHz. The offset and the location of the slots are determined from the GA. Two single element designs are presented that are having a tilt of  $10^0$  and  $35^0$  from the broad side.

Chapter 9, summarizes the research work, gives conclusions and highlights the future work.

## CHAPTER 2

# BACKGROUND

*“Life can be only understood backwards; but it must be lived forwards”*

---

SOREN KIERKEGAARD

### 2.1 Theory Of Characteristic Modes

TCM was developed by Garbacz in 1968 by diagonalizing the scattering matrix for an arbitrary shape conducting object [17]. This theory was later modified by Harrington and Mautz in 1971 [18]. They obtained the characteristic modes by diagonalizing the Impedance matrix for an arbitrary shape conducting object. Characteristic modes gain importance because of their three important features [23–25, 29–32].

- The Modes obtained are real over the surface on which they exist.
- On the surface, modes are orthogonal with each other.

- The modes are obtained by diagonalizing the general impedance matrix for the surface.

### 2.1.1 Mathematical Formulation

Before giving a mathematical explanation to TCM, one thing should be made clear that characteristic modes are found for the object and are dependent on the shape of the object. Characteristic modes are totally independent of the excitation source. As explained in [33], TCM was developed by defining an operator that relates the current on the surface of a conducting object with the incident electric field ( $E_i$ ).

$$[L(J) - E^i]_{tan} = 0 \quad (2.1)$$

The subscript *tan* represents the tangential component while  $L(J)$  represents the intensity of the Electric field at any point in space due to the current density  $J$  on the surface of an antenna.

The characteristic current Modes for an arbitrary conducting object can be found according to [33],

$$[Z]I_n = (1 + j\lambda_n)[R]I_n \quad (2.2)$$

Where  $Z$  represents the impedance and  $Z = R + jX$ ,  $I_n$  represents the current eigen vector and  $1 + j\lambda_n$  represents the eigen value. Further simplification of (2.2) gives

$$[X]I_n = \lambda_n[R]I_n \quad (2.3)$$

It can be also represented as

$$[X]J_n = \lambda_n[R]J_n \quad (2.4)$$

Here  $J_n$  represents the current density eigen vector. From Reciprocity we know that, if  $Z$  is a linear symmetric operator then the Hermitian parts of  $Z$  ( $R$  and  $X$ ) will be also linear symmetric operators [23]. Thus we can conclude that the eigen values will be always real and we can assume that the eigen vectors will always be real and equiphasal.

The orthogonal properties of the eigen vector can be explained from the following relations following those in [33]. We know that the power radiated from any source can be represented by the equation as

$$P = I^*V = I^*RI = 1 \quad (2.5)$$

For our convenience, we have normalized the power radiated to be 1.

$$I_m^*[R]I_n = \delta_{mn} \quad (2.6)$$

Where  $\delta_{mn}$  represents Kronecher delta function. This means that all the eigen vectors are orthogonal to each other. Similarly,

$$I_m^*[X]I_n = \lambda_n\delta_{mn} \quad (2.7)$$



Summing (2.6) and (2.7) yields

$$I_m^*[Z]I_n = (1 + j\lambda_n)\delta_{mn} \quad (2.8)$$

The following equation's are also represented in eigen current density ( $J_n$ ) form as presented in [23] as,

$$J_m^*[R]J_n = \delta_{mn} \quad (2.9)$$

$$J_m^*[X]J_n = \lambda_n\delta_{mn} \quad (2.10)$$

$$J_m^*[Z]J_n = (1 + j\lambda_n)\delta_{mn} \quad (2.11)$$

Electric fields produced by these eigen currents are known as characteristic fields [18,23,33]. These Characteristic fields can be calculated as

$$E(J_n) = Z(J_n) = R(J_n) + jX(J_n) = R(J_n)(1 + j\lambda_n) \quad (2.12)$$

Based on eqs. (2.6) to (2.8) or eqs. (2.9) to (2.11), we can observe that due to the orthogonality property of eigen vectors, each characteristic mode or eigen vector radiates power independently. Due to this feature, total current on the surface of a conducting body can be expanded as

$$J = \sum_n \alpha_n J_n \quad (2.13)$$

where  $\alpha_n$  are the coefficients of the eigen current distribution, now putting (2.13)

in (2.1) we get

$$\sum_n [\alpha_n Z(J_n) - E^i]_{tan} = 0 \quad (2.14)$$

We multiply it by an eigen vector  $J_m$  we get

$$\sum_n \alpha_n \langle J_m, ZJ_n \rangle - \langle J_m, E^i \rangle = 0 \quad (2.15)$$

Due to the orthogonality property, we know that for  $m \neq n$ , the term  $\alpha_n \langle J_m, ZJ_n \rangle = 0$ . Only for  $m = n$  the term  $J_n ZJ_n = (1 + j\lambda_n)$  thus

$$\alpha_n (1 + j\lambda_n) = \langle J_m, E^i \rangle \quad (2.16)$$

The right hand term of (2.16) is called the modal excitation coefficient [23] and is represented by  $V_i$ , thus (2.16) can be written as

$$\alpha_n = \frac{V_{ni}}{(1 + j\lambda_n)} \quad (2.17)$$

Putting (2.17) in (2.13) we get,

$$J = \sum_n \frac{V_n^i J_n}{(1 + j\lambda_n)} \quad (2.18)$$

Equation (2.18) is of great importance.  $V_n^i$  represents the applied voltage magnitude and phase. The numerator of (2.18) decides which particular characteristic mode will be excited on the surface of the conductor. Remember that the eigen

value is of great importance because it decides whether the mode should radiate or store energy in Electrical or Magnetic forms. The frequencies for which the corresponding eigen value is zero are the resonance frequencies of the conducting object. For frequencies having positive eigen values, they mean that the object will not radiate effectively and will store energy in magnetic form. Similarly, negative eigen values mean that they will store energy in electric energy form. For a dipole of length 0.5m and diameter of 1 mm the first four eigen values associated with the first four characteristic modes are plotted in Figure 2.1. Note the resonance of the various modes. If the antenna is a  $\lambda/2$  dipole, its resonance is at 300 MHz.

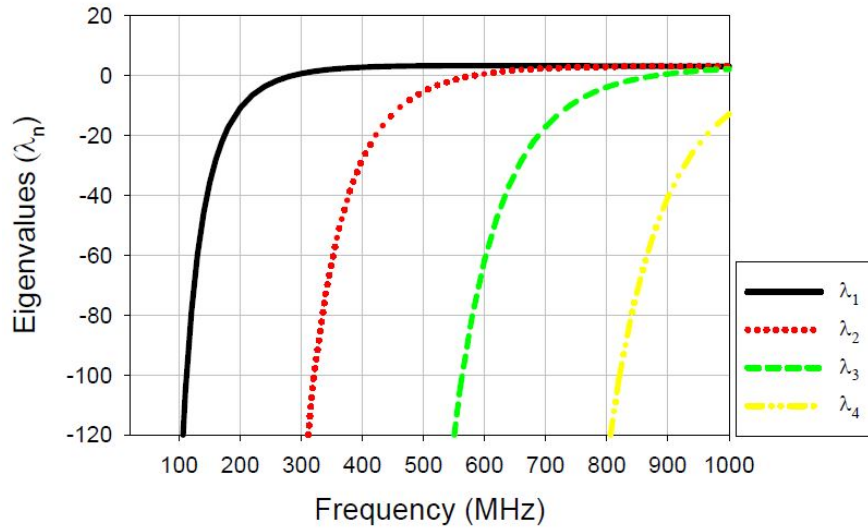


Figure 2.1: Eigen Values variation with frequency for a dipole of length 0.5 m and wire diameter of 1 mm [23].

### 2.1.2 Modal Significance

Modal Significance (MS) can be obtained by normalizing equation (2.18) as

$$MS_n = \left| \frac{1}{1 + j\lambda_n} \right| \quad (2.19)$$

MS depends on one parameter that is the eigen value, thus the MS gives us a physical insight of the behavior of a conducting object. It tells us about its resonance and radiating BW.

At the resonance frequency we know that  $\lambda_n = 0$  so  $MS = 1$ . The Half power bandwidth (HPBW) is the point, where  $MS = 0.707$  or  $MS = 1/\sqrt{2}$ . This value of HPBW is obtained for eigen values of  $\lambda_n = \pm 1$ . The HPBW can be calculated from Figure 2.2 using (2.20) as follows,

$$BW_n = \frac{f_u - f_L}{f_{res}} \quad (2.20)$$

The Modal Quality factor is also used to find out the radiating Bandwidth of the antenna. The Modal Quality Factor ( $Q_{rad,n}$ ) basically defines the sharpness of the resonance frequency and is inversely proportional to the BW, that is

$$Q_{rad,n} = \frac{1}{BW_n} \quad (2.21)$$

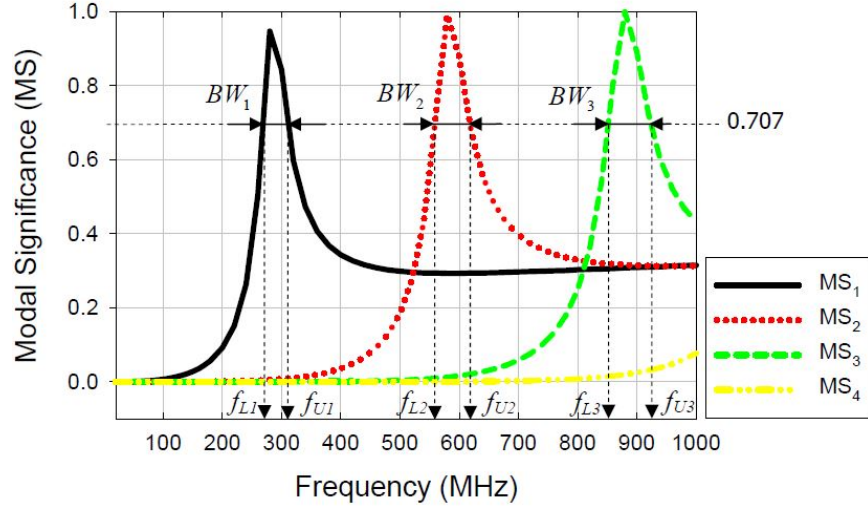


Figure 2.2: Modal Significance associated with the first four characteristic modes (or eigen values) for a dipole of length 0.5 m and wire diameter of 1 mm [23].

The Modal Quality factor can be also calculated as [23],

$$\left[ \omega \frac{dx}{d\omega} \right] [J_n] = Q_n [R] [J_n] \quad (2.22)$$

In terms of eigen values, the modal quality factor can be expressed as,

$$Q_{rad,n} = \frac{\omega d\lambda_n}{2 d\omega} \quad (2.23)$$

### 2.1.3 Characteristic Angle

The characteristic angle is the angle between the characteristic mode ( $J_n$ ) and the associated characteristic field. Mathematically, the characteristic angle can be expressed as

$$\alpha_n = 180^\circ - \tan^{-1}(\lambda_n) \quad (2.24)$$

The BW of an element can be also calculated from the characteristic angle plots as shown in Figure 2.3. At the resonance frequency  $\lambda_n = 0$ , thus the characteristic angle at resonance frequency will be equal to  $180^\circ$ . From equation (2.24) we know that, at the highest and lowest frequencies of a bandwidth, the maximum and minimum eigen values are  $\lambda_n = +1$  and  $-1$  respectively. For  $\lambda_n = +1$  the characteristic angle is  $135^\circ$  and for  $\lambda_n = -1$  the characteristic angle is  $225^\circ$ .

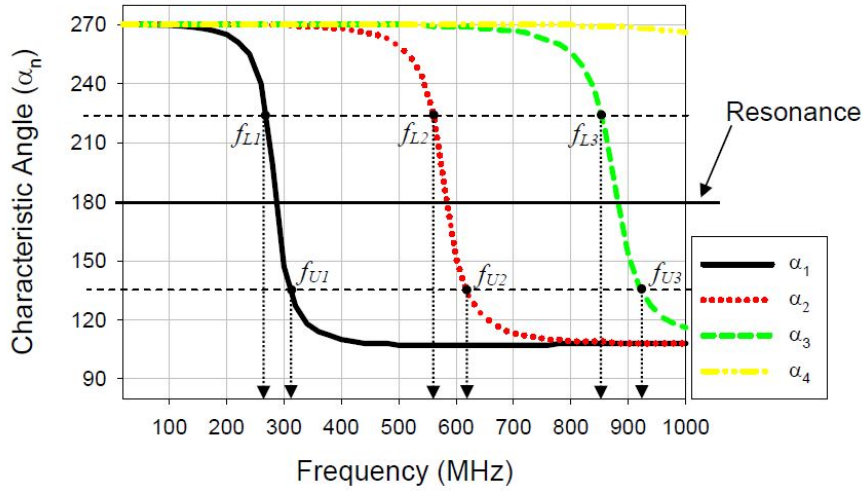


Figure 2.3: Characteristic angle associated with the first four characteristic modes (or eigen values) for a dipole of length 0.5 m and wire diameter of 1 mm [23].

### 2.1.4 Reactive Loading

We know that the basic equation for obtaining characteristic modes is (2.4) but for the sake of comparison we will repeat it over here.

$$[X]J_n = \lambda_n[R]J_n \quad (2.25)$$

Now if the surface of the conducting object is loaded with continuous reactive loads, the new characteristic modes can be expressed from the following equation.

$$[X_L + X]J_n = \lambda_n[R]J_n \quad (2.26)$$

Due to the addition of this continuous reactive load the characteristic modes of the conducting body will change. Characteristic modes will be affected in terms of resonance frequency and radiating BW.

### 2.1.5 Computer Simulation Technology (CST)

CST was used as the simulation tool to find the CM of any geometry [10]. CST is a simulation software that can solve a problem using many numerical approaches like finite element method (FEM), multilevel fast multipole method (MLFMM), method of moments (MoM) and shooting boundary ray (SBR) method. Depending upon the application, different solvers can be used. TCM analysis is offered by the integral equation solver as well as the Multilayer solver. For the case of TCM analysis for metallic structures i.e. in the absence of any dielectric material the integral equation solver is used. When ever we have multi layers geometry consisting of metal and dielectric layers then the Multilayer solver is used for TCM analysis.

## 2.2 The Antenna Current Green's Function (ACGF)

In signal processing the behavior of the system is represented by its impulse response, In the same way the behavior of an Electromagnetic system is represented by the Green's Function (GF) [34–39]. For an electromagnetic system if we know the GF we can calculate or predict the behavior of the system for any excitation.

By using the Wilcox and Weyl expansions (Section A.1) the fields behavior was studied from a perspective that has got much resemblance to reality. Section A.3, shows that the Electric field radiated by an antenna can be represented in terms of a GF. In [19] and [20], the new concept of ACGF was introduced. An Electromagnetic system was framed into three modes. Mode A, B and C. Mode A, deals with the antenna excitation by an external excitation source and shows how the current is induced into the antenna surface. Mode B relates the radiation pattern produced by the currents on the surface of antenna and, Mode C is linked with the receiving antenna, how currents are induced into antenna, from the fields present in the near field of the antenna. Mode A and B are linked with the transmitting antenna while mode C is linked with the receiving antenna. Collectively all these modes cover a transmission and reception process and is shown in the Figure 2.4.

As Mode A refers to the relation between the current excitation on the surface of antenna ( $J$ ) and the external Electric field ( $E^{ex}(r')$ ) applied at position  $r'$  in



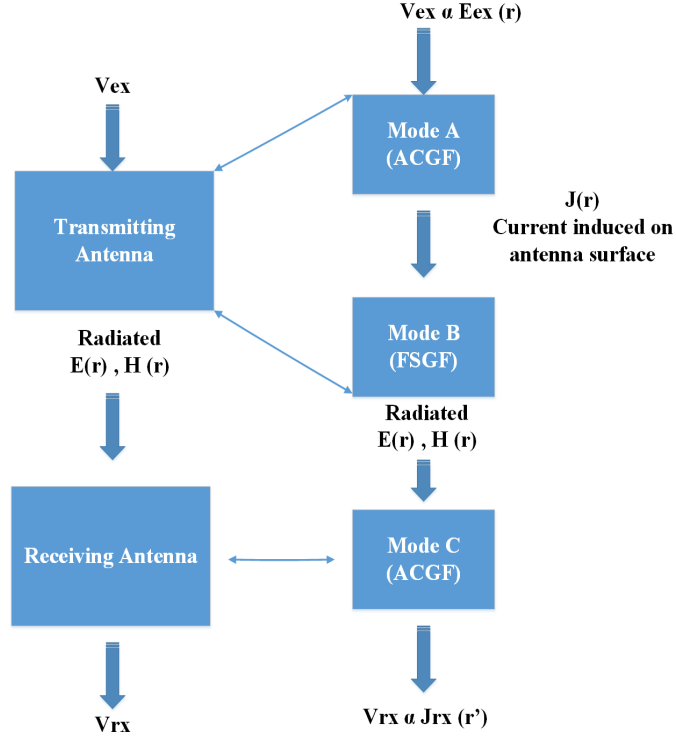


Figure 2.4: Transmission and Reception of the antenna divided into three modes [19].

space then the current induced in the antenna at point  $r$  will be given by

$$J(r) = \int_s F(r, r') ds' \cdot [\hat{n} \times E^{ex}(r')] \quad (2.27)$$

Here  $F(r, r')$  represents the ACGF. This current that is induced in the antenna will radiate fields in the external environment. After few mathematical manipulations, it was found that the fields radiated are related to the current density through free space green function (FSGF),

$$E(r) = \int_s G(r, r') ds' \cdot J(r') \quad (2.28)$$

Mode C, which is a receiving mode. Due to the linearity of the problem the current induced on the antenna by the surrounding electric field is also governed by another GF known as  $L(r, r'')$ . Mode C can be taken as similar to Mode A,

$$J_{rx}(r) = \int_s L(r, r') ds' \cdot E_{tr}(r') \quad (2.29)$$

Based on these formulations the system can be generalized. Now for any geometry if we know the excitation, based on the Green function we can calculate the current density that will be induced on the antenna surface, and from the current density we can calculate the vector potentials and finally the radiation pattern. The tangential component of the Electric field generated by the current on the surface of antenna can be written in terms of an electric field integral equation (EFIE) [37] as,

$$E_t^{ex}(r) = -i\omega\mu\hat{n} \times \int_s d_{s'} \left[ \hat{I} + \frac{1}{k_o^2} \nabla \nabla \cdot \right] \frac{e^{ik_o|r-r'|}}{4\pi|r-r'|} \cdot J(r) \quad (2.30)$$

In simplified form, (2.30) can be represented as

$$E_t^{ex}(r) = \mathcal{L}J(r) \quad (2.31)$$

Since  $\mathcal{L}$  is a linear operator, its inverse is possible, thus

$$J(r) = \mathcal{L}^{-1}E_t^{ex}(r). \quad (2.32)$$

(2.32) resembles (2.27), so for any impulse input the response will be the GF and

for this particular case it will be known as the ACGF. ACGF of mode A and C is a  $3D$  tensor and in terms of a  $3D$  coordinate system where  $\hat{x}_p = \hat{x}_1 + \hat{x}_2 + \hat{x}_3$ , it is given by,

$$F(r, r') = \sum_{p=1}^3 \sum_{q=1}^3 F_{x_p x_q}(r, r') \hat{x}_p \hat{x}_q \quad (2.33)$$

As antenna surfaces are normally in  $2D$  space, modes A and C can be simplified to a  $2D$  tensor. In both cases, only the tangential component of the electric field is active. Due to the farfield radiation pattern, mode  $B$  GF shall be represented by a  $3D$  tensor.

## 2.3 Characteristic Basis Function (CBF)

The normal practice to solve a method of moments (MoM) based problem is to use the Rao, Wilton and Glisson (RWG) basis functions. The discretization range using RWG approach is from  $\frac{\lambda}{10}$  to  $\frac{\lambda}{20}$ . This causes the object size electrically large and the MoM matrix increases in size very rapidly [42, 43].

CM are the natural modes as already discussed in section 2.1. CM are developed in the absence of excitation source. To overcome these problems, CBF were developed. The CBF method has a lot of advantages such as [42–46]

- It is a general technique and can be applied to any arbitrary design.
- CBF also accounts for mutual coupling between antenna elements in a design.
- CBF reduces the matrix size dimension of the impedance matrix by creat-

ing sub-blocks and solving them separately. The matrices created are well conditioned and sparse.

- Direct solvers can be used instead of iterative solvers.

The MoM equation for a general design is given by,

$$Z.J = V \tag{2.34}$$

where,  $Z$  represents the generalized impedance matrix of dimensions  $N \times N$ ,  $J$  represents the unknown eigen current distribution matrix and is of the dimension  $N \times 1$ , while  $V$  represents the excitation source, which is a known quantity. Thus (2.34) has  $N$  number of unknowns for which we need to solve. The complexity of the problem can be reduced, if the antenna is divided into  $M$  number of blocks. Let  $N_b$ , be the number of unknowns in each block. For a single block, (2.34) can be solved by exciting it via plane wave (PW) with different incident angles. Let say the total number of incident angles are  $N^{PWS} = N_\theta N_\phi$ . The measurements are taken deliberately overestimated so that the CBF should be invariant with respect to shape and size of the geometry under consideration.

To make CBF, count for coupling the idea of extended blocks was introduced. Figure 2.5(a) shows the blocking of any antenna to  $M$  number of block, here  $M$  is equal to 16 while Figure 2.5(b) shows the introduction of extended block on the antenna surface.

The extended block impedance matrix ( $Z_{ii}$ ) dimensions can be represented by  $N_{bc} \times N_{bc}$ .  $Z_{ii}$  can be extracted by s matrix segmentation procedure from

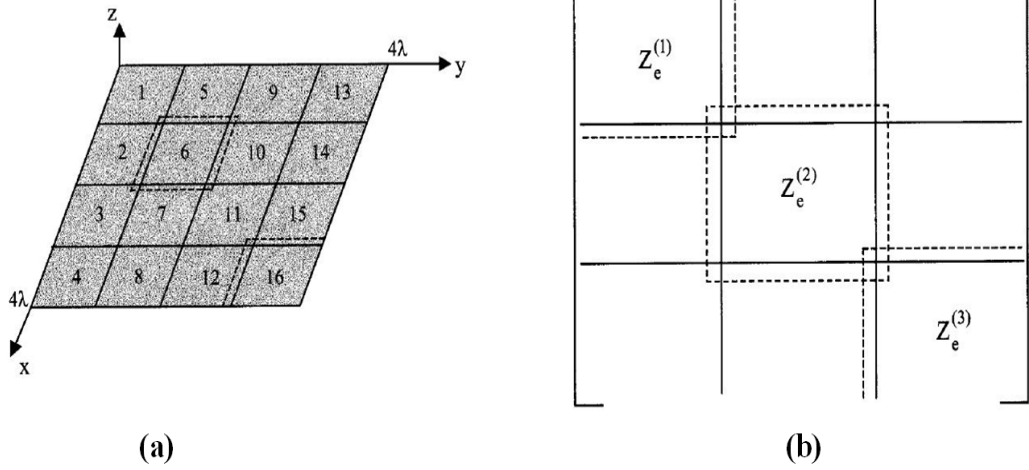


Figure 2.5: CBF application on antenna (a) Surface of a geometry divided into 16 blocks, (b) Extended blocks introduction in the geometry [42, 43].

the impedance matrix. When PW are impinged on the extended block from the ( $N^{PWS}$ ) incident angles, (2.34) can be written as

$$Z_{ii} \times J_{ii}^{CBF} = V_{ii}^{PWS} \quad (2.35)$$

The dimensions of  $J_{ii}^{CBF}$  is  $N_{bc} \times N^{PWS}$  while that of the applied voltage in the extended block region will be also  $N_{bc} \times N^{PWS}$ . If we compare (2.35) with (2.34), we can observe that the number of unknowns have been significantly reduced from  $N$  to  $N_{bc}$ . The size of the M block is manageable and user dependent, we can increase and decrease the size without any restriction. As the matrix dimension of (2.35) are smaller, we can solve them by using LU decomposition. Typically CBFs exceed the number of degrees of freedom (DoF) associated with the block and it is desirable to remove the redundancy by using singular value decomposition (SVD) method.

$$J_{ii}^{CBF} = UDV^t \quad (2.36)$$

where  $U$  and  $V$  are orthogonal matrices with dimensions of  $N_{bc} \times N^{PWS}$  and  $N^{PWS} \times N_{bc}$ .  $D$  is a diagonal matrix with dimensions  $N^{PWS} \times N^{PWS}$  and the elements of the matrix are singular values of  $J_{ii}$ . A new set of CBFs is constructed via SVD approach. For the sake of simplicity, all the blocks contain the same number of CBF after SVD. Assume,  $k$  represents the number of remaining or selected CBF and is smaller than  $N^{PWS}$ .

To get the solution for the whole design, we will construct KM primary basis functions.  $K$ , for each of the  $M$  block. The linear combination of the CBFs will be the solution to entire problem.

$$J = \sum_{k=1}^K \alpha_k^{(1)} \begin{bmatrix} [J_k^1] \\ 0 \\ \vdots \\ 0 \end{bmatrix} + \sum_{k=1}^K \alpha_k^{(2)} \begin{bmatrix} 0 \\ [J_k^2] \\ \vdots \\ 0 \end{bmatrix} + \cdots + \sum_{k=1}^K \alpha_k^{(M)} \begin{bmatrix} 0 \\ 0 \\ \vdots \\ [J_k^M] \end{bmatrix} \quad (2.37)$$

where,  $\alpha$  represents the weighting coefficient. The reason of all this analysis is to solve (2.34) with the least number of unknowns, after this whole procedure the number of unknowns have reduced to  $N = KM$ . The original matrix in (2.34) dimensions are reduced from  $N \times N$  to  $KM \times KM$ .

## 2.4 Substrate Integrated Waveguide (SIW) Technology

The deployment of mm-wave technology is essential for 5G technology. Huge BW, high gain and low profile are essential for mm-wave antennas. The idea of SIW to be used at mm wave, originated from the concept of cavity backed antennas (CBA) and slot antennas. The depth of a CBA is roughly quarter guided wavelength. The bulky volumes and big sizes make CBA not suitable for many practical applications. Thus SIW was introduced to overcome all these problems. SIW have small size, light weight, low cost, low profile and has the ability to be easily integrated with planar structures. Beside such features, SIW based antennas have the feature of high gain, high Front to Back (FBR) ratio and low cross polarization level like metallic waveguide ones [47–49]. Figure 2.6(a) shows a very basic SIW geometry. Substrates that are backed at top and bottom by metallic conductors and at the sides, via holes are used to direct the energy in one direction. The diameter as well as the distance between vias plays significant role in frequency adjustment as well as the leaky wave radiation mechanism. The width of the SIW determines the cutoff frequency of the fundamental mode. The BW provided is similar to a rectangular waveguide case but with a reduction factor of  $\epsilon_r^{-\frac{1}{2}}$  [47]. Figure 2.6(b) shows a slot based SIW antenna.

Like other techniques, SIW also suffers from three major losses which are conductor losses, dielectric losses and radiation losses due to energy leakage. The conductor losses and dielectric losses are similar to other technologies but they can

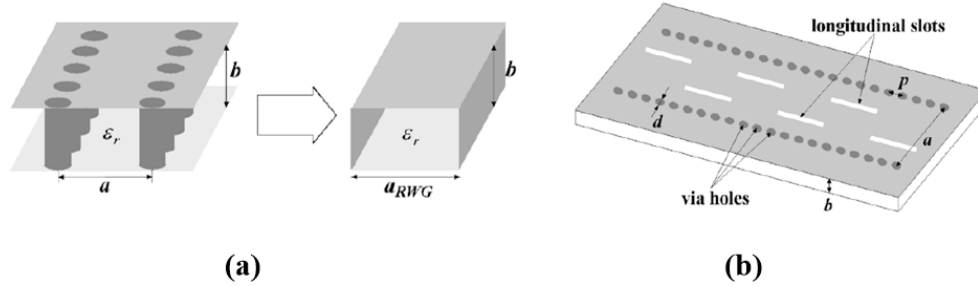


Figure 2.6: SIW technology (a) SIW resemblance to Metallic Rectangular waveguide and (b) Basic SIW antenna Geometry [48].

be reduced. Conductor losses can be reduced by increasing the substrate thickness. Dielectric losses can be reduced by selecting efficient dielectrics. Radiation losses can be minimized if the spacing to the diameter ratio of the vias is less than 2.5 [47].

Passive components such as filters and couplers were designed in SIW technology. Active circuits were also implemented as well as transition methods were used to excite SIW designs either through microstrip line or coplanar feeding [47]. To reduce the size of the SIW further, Half Modes Substrate integrated waveguide (HMSIW) were introduced [50, 51]. HMSIW reduced the size of SIW by cutting the SIW in half. The open edge (after cutting) acts as a radiator because the field can be radiated from the open slot.



## CHAPTER 3

# LITERATURE REVIEW

*“Research is to see what everybody else has seen, and to think what nobody else has  
thought”*

---

—ALBERT SZENT-GYÖRGI

A comprehensive literature review covering all the works conducted utilizing the ACGF, TCM and CBF was conducted to identify the contribution areas as well as examine their practical use. A literature review on SIW was also conducted to highlight the contribution of the work presented. The generic tree of the literature is shown in Figure 3.1. The detailed Literature review will be presented in the following sections.

### 3.1 Cross-Correlation Green Function

The envelope correlation coefficient ( $\rho_e$ ) is an important multiple-input-multiple-output (MIMO) parameter that can severely affect MIMO antenna system performance. It measures how much the antenna radiation patterns are isolated from

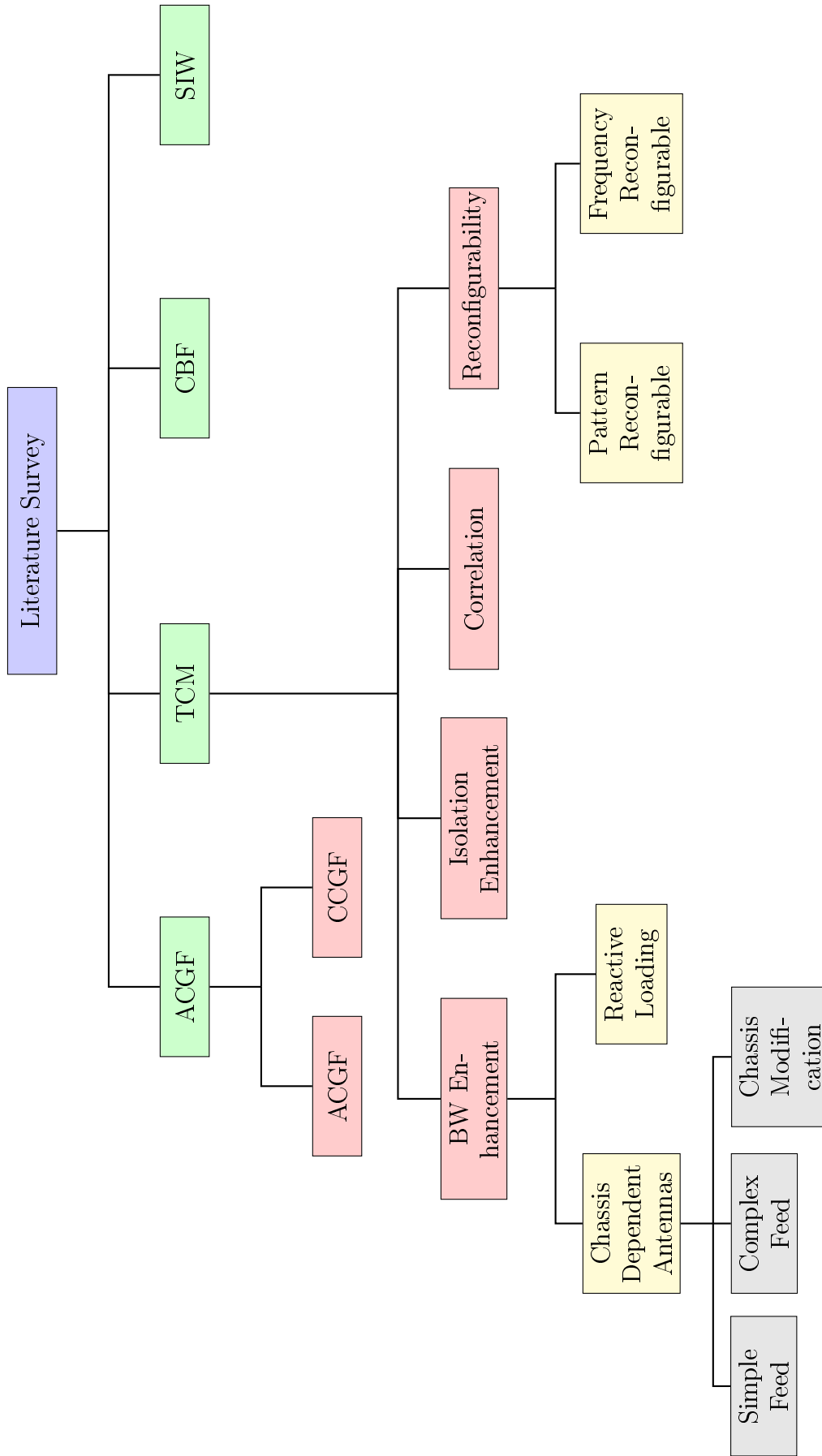


Figure 3.1: Literature Survey

each other.  $\rho_e$  values can be computed using the radiation patterns in an isotropic multi-path environment using [57]:

$$\rho_e = \frac{|\int \int_{4\pi} [\vec{F}_1(\theta, \varphi) * \vec{F}_2(\theta, \varphi) d\Omega]|^2}{\int \int_{4\pi} |\vec{F}_1(\theta, \varphi)|^2 d\Omega \int \int_{4\pi} |\vec{F}_2(\theta, \varphi)|^2 d\Omega} \quad (3.1)$$

where  $\vec{F}_i(\theta, \varphi)$  is the field radiation pattern of the antenna when port  $i$  is excited and  $*$  denotes the Hermitian product and  $d\Omega$  represents the solid angle. The square root of  $\rho_e$  is called the correlation coefficient ( $\rho$ ), given by,

$$\rho = \frac{|\iint_{4\pi} d\Omega E_1(\theta, \phi) \cdot E_2^*(\theta, \phi)|}{\sqrt{\iint_{4\pi} d\Omega |E_1(\theta, \phi)|^2} \sqrt{\iint_{4\pi} d\Omega |E_2(\theta, \phi)|^2}} \quad (3.2)$$

The Cross-correlation green function (CCGF) was introduced to relate  $\rho$  to the currents on the antenna surface [58–60]. After few mathematical derivations (3.2) can be written in terms of the CCGF as

$$\iint_{4\pi} d\Omega E_1(\hat{r}) \cdot E_2^*(\hat{r}) = \int_{V_1} d^3r' \int_{V_2} d^3r'' J_1(r') \cdot \bar{C}(r', r'') \cdot J_2^*(r'') \quad (3.3)$$

where  $J_1(r')$  represents the current on the surface of the antenna 1 placed at location  $r'$  and similarly  $J_2(r'')$  represents the current on the surface of antenna 2 placed at location  $r''$ .  $V_1$  and  $V_2$  represents the volumes of antenna 1 and 2 respectively. The  $\bar{C}(r', r'')$  represents the CCGF and is given by

$$\hat{C}(r', r'') = \int_{4\pi} d\Omega [\bar{I} - \hat{r}\hat{r}] e^{ik(r' - r'') \cdot \hat{r}} \quad (3.4)$$

$$\int_{4\pi} d\Omega | E_1(r') |^2 = \int_{V_1} d^3r' \int_{V_2} d^3r'' J_1(r') \cdot \bar{C}(r', r'') \cdot J_1^*(r'') \quad (3.5)$$

$$\int_{4\pi} d\Omega | E_2(r') |^2 = \int_{V_1} d^3r' \int_{V_2} d^3r'' J_2(r') \cdot \bar{C}(r', r'') \cdot J_2^*(r'') \quad (3.6)$$

Comparing CCGF with FSGF, it can be found that the CCGF integration is smooth and finite but at the same time both of them are shift invariant, that is they depend on the distance between the two sources. The study was tested on two infinitesimal dipoles, it was found that the minimum value for  $\rho$  can be achieved when both the dipoles lie on the same line and are positioned orthogonally. The study can be extended to dipoles having greater length than infinitesimal dipole case. The current distribution on the antenna was assumed to be summation of infinitesimal dipoles [59].

The main problem with this approach is that the possible current distribution that we will get as an output for  $\rho$  minimum case cannot be excited because for real designs we have a single excitation source. Genetic Algorithms (GA) were used to find the optimum locations to place the infinitesimal dipoles [58]. The mutual coupling estimate between antenna arrays was also addressed in [61, 62] utilizing near field theory and ACGF respectively. In [60], a full array electromagnetic operation is decomposed into a sum of interaction and isolation element operators. Perturbation series was used to expand the full array element operator and after few mathematical operations the effect of mutual coupling was estimated.

## 3.2 TCM

### 3.2.1 BW Enhancement

TCM has been used for BW enhancement purposes. The tree summarizes the literature review of TCM use for the BW enhancement, shown in Figure 3.2. The impedance bandwidth of the antenna in general can be improved in many ways, some of them are

- Pure excitation of a single wideband Characteristic mode.
- Excitation of multiple characteristic modes.
- Designing a matching network at the feeding terminal for the whole band of interest.
- Loading the antenna on its surface with reactive components such that the impedance at the input terminals remains in a desirable range for the whole band of interest.

A BW of 1 to 6 GHz on a 6 dB return loss scale was achieved by using the rectangular chassis as the main radiating element [63]. In [64] an antenna was designed by utilizing the mobile chassis. A feeding network was designed in [65–68] to excite chassis modes. A 2-port MIMO antenna system was designed for a laptop using its chassis with the help of TCM in the frequency range from 704 MHz to 960 MHz [69].

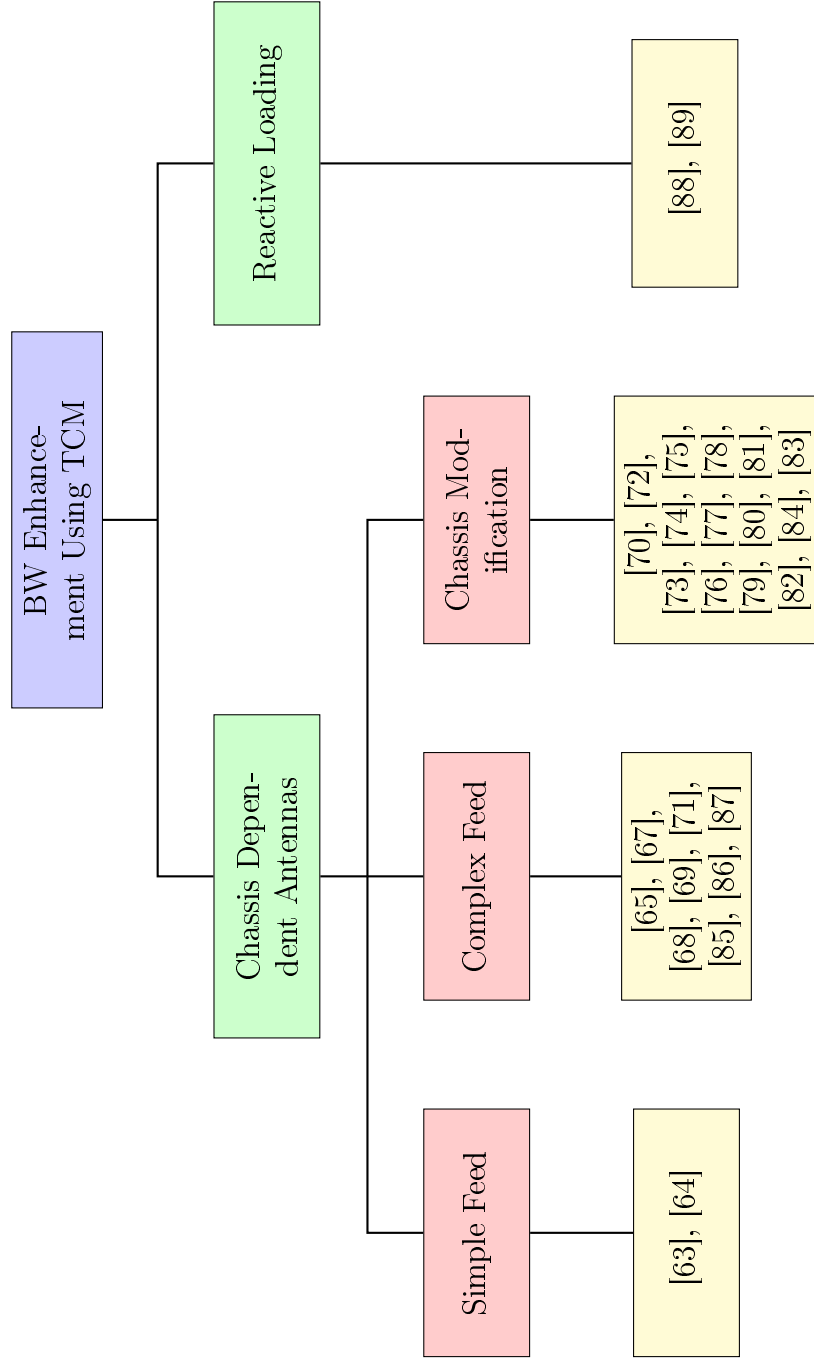


Figure 3.2: TCM used for BW enhancement Literature Review

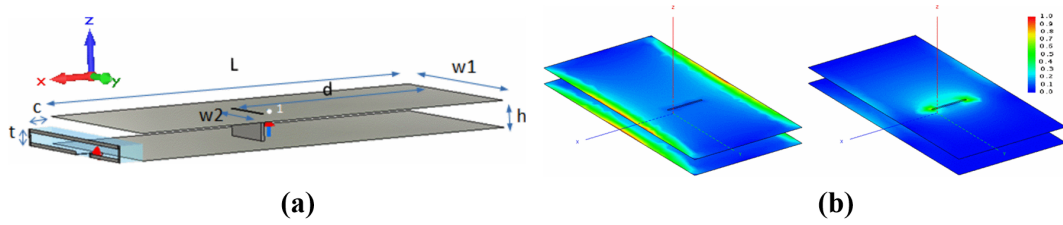


Figure 3.3: (a) Antenna geometry, (b) characteristic currents of mode 1 (left) and mode 4 (right) at 850 MHz [73].

Planar antennas can have their BW enhanced via geometrical changes [70,71]. In [72], a metallic strip was connected with the chassis to increase its BW. A rectangular metallic plate with  $130 \times 66 \text{ mm}^2$  area was connected in parallel with chassis and cause the antenna to resonate at 850 MHz [73]. There is only one mode for mobile chassis below 1 GHz so a metallic strip was connected across the chassis to create a new or lower the resonance frequency of mode (already existing mode) as shown in Figure 3.3. The modes can be excited by the use of single source. Both of the modes have got different current distribution at the chassis but the current maxima lies at the same location i.e. shorting post. To make the antenna as multi band, another two modes were excited at higher frequency band (1.3-2.0 GHz). Such excitation of 4 modes helps in making the antenna as multiband antenna [74–78].

In [79, 80], a planar monopole was modified to support the excitation of a single mode, such modification enhanced the BW of the antenna. In [82], it was demonstrated that the impedance BW of a monopole is extremely dependent on the feeding gap structure. A rectangular monopole feed via two feeding points provided optimum performance. In [83], it was demonstrated that beveling the

monopole along with shorting, significantly reduces the size of the antenna as well as improves its BW.

In [84], the main focus was on the effect of the ground plane, on the performance (in terms of BW) of a PIFA antenna. The effect of the ground plane was studied, ignoring the design of PIFA antenna. The paper demonstrated 4 different PIFA examples. 3 of the examples of PIFA elements used are shown in the Figure 3.4. TCM was applied such that the ground plane and the feeding gap were modeled while the PIFA element was replaced by an Infinite ground plane. The length of the ground plane was varied and it effected the BW. The BW of the antenna was varying when changing the length of the ground plane. The main reason behind the changing BW was the number of dominant modes available near the resonating frequency. For a particular length if we have a single dominant mode then we have small BW, but for another length if we have two dominant modes then our BW increases. It was also observed that a defected ground plane can alter the BW of the antenna as well.

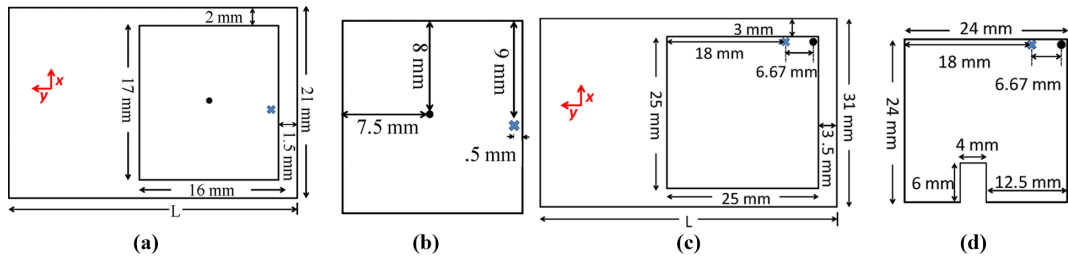


Figure 3.4: PIFA designs where (a) shows the PIFA with the ground plane, (b) zoomed element, (c) second PIFA design with different feeding and shorting location (c) third PIFA design [84].

The use of capacitive coupled element (CCE) enables simultaneous excitation



of modes while inductive coupling elements (ICE) provide an advantage of selective excitation of a mode. For Broad-band and multiband antennas, normally the aim is to excite as many modes as possible within the desired frequency range. CCE are best suited because they can be placed at common voltage maxima [85–87].

The impedance BW of the antenna can be also improved by reactive loading on the antenna surface. In [88] the antenna was loaded with reactance at different antenna points. The value of the reactances is measured by solving the eigenfunction problem at different frequency points and then the reactance (calculated) were loaded in the form of Foster and Non-Foster elements. In [89], the general current pattern on the surface of antenna is known for few antennas like dipole. To resonate the antenna at a different frequency, we need to excite the same current distribution on the surface of antenna at that particular frequency. A new method was proposed to come up with the desired current pattern on the surface of the antenna to resonate it at the desired frequency which was represented by a variable ( $Id_i$ ). Using TCM calculations for scatterers, the value of the reactances is calculated for the desired current distribution  $Id$ , When these reactances are installed on antenna surface the antenna resonates at the desired band of interest. For both papers [88,89] there is no systematic way to find the number of reactance ports needed as well as the location of these reactance on the antenna surface.

### 3.2.2 Correlation Coefficient

Correlation coefficient was defined in (5.1) and (3.2). The value of correlation depends on the following parameters [90].

1. Phase (Complex field)
2. Angular dependency (Shape of Pattern)
3. Polarization

For two antennas located on the same ground plane, the maximum cross correlation between them occurs if both of them are exciting same mode on the ground plane and minimum cross correlation occurs if both of the antennas excite modes that are out of phase with one another. If only one mode can be excited, then the location of the antennas shall be chosen such that the modal current distribution at the location of both antennas get out of phase [91]. In [92] it was demonstrated that the best position for placing the antenna on chassis is the point of maximum Electric field. Similarly in case of loop antennas the best positions are location of maxima of Magnetic field [93].

In [94], a 2-port MIMO antenna is presented. Two orthogonal modes of the chassis are excited via CCE's. Orthogonal mode excitation helps in providing highly uncorrelated radiation patterns. Similarly in [95], ICE's were used for the selective excitation of modes. In [96], from the known radiation pattern of a complex structure, a tool was developed to find out the modes from the farfield and then comparison was made based on the power radiated.

### 3.2.3 Reconfigurability

Reconfigurability is the property of the antenna system design that can switch either its frequency band of operation or the direction of radiation or the polarization. A detailed tree summarizing the literature review from the perspective of empirical design model (EDM) and TCM analysis is presented in Figure 3.5.

#### Pattern Reconfigurability from EDM

Two types of pattern reconfigurable antennas are reported in literature,

1. Fixed Beam Shape [97–99].
2. Variable Beam Shape [100–102]

In [97], a frequency and pattern reconfigurable antenna is presented, working at 2 frequency bands which are 3.7 GHz behaving as a patch antenna and at 6 GHz behaving as a broad side radiator. The total size of the antenna was  $25 \times 25 \text{ mm}^2$ . PIN diodes were used to make the antenna pattern reconfigurable in [98,99]. In [100,101] antennas were proposed that can work as omni-directional and directional in two different states. In [102], the beam was steered using RF switch. In [103], a  $2 \times 1$  dipole MIMO antenna with variable length was presented to achieve the reconfigurability using PIN diode. A fractal reconfigurable antenna was presented in [104]. In all these designs, the locations of reactive loading were optimized based on parametric sweeps.

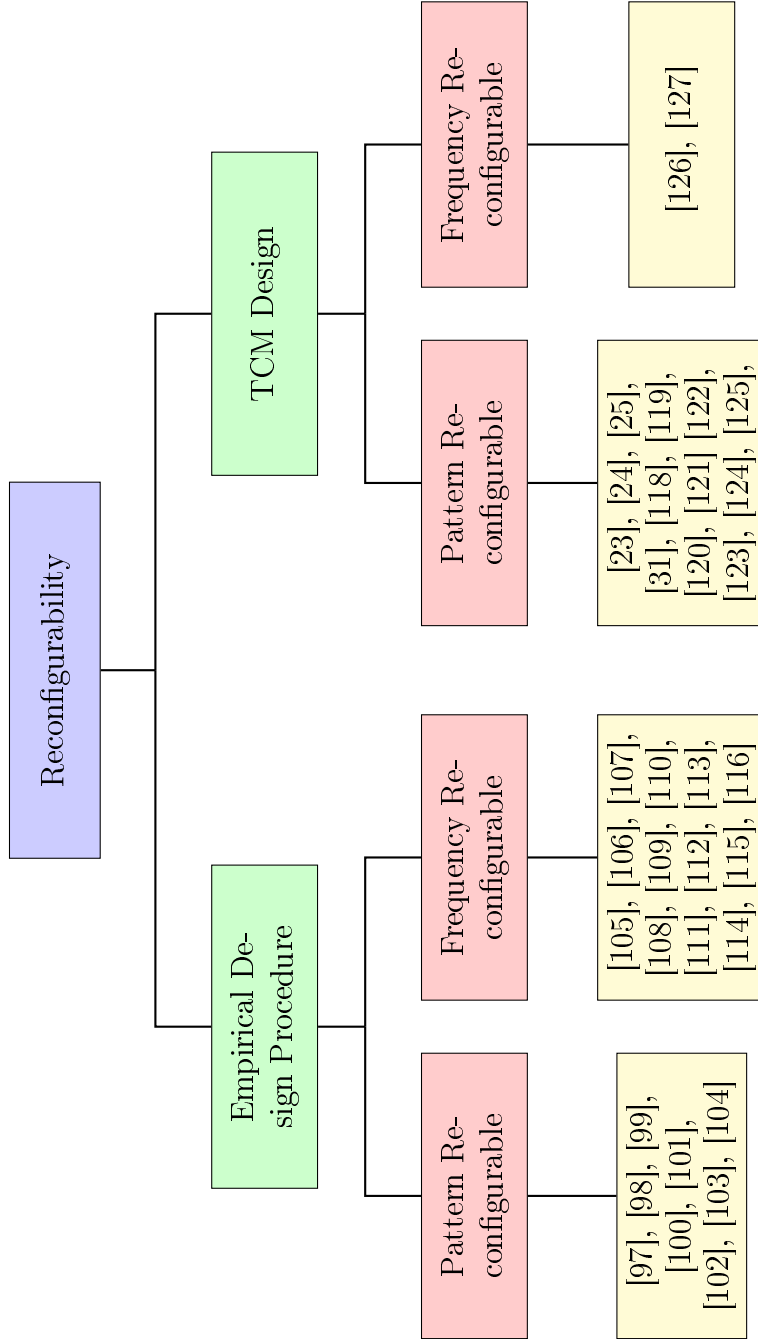


Figure 3.5: TCM used for Reconfigurability, Literature Review

## Frequency Reconfigurability from EDM

Frequency reconfigurable MIMO antenna systems combine the advantages of high throughput capability and several bands/standard coverage, that is why they are considered a good solution for next generation cognitive radio (CR) front-ends [105]. There is a need to switch the operating bands in CR platforms and hence frequency agile MIMO antennas are required to serve this purpose. Slot reconfigurable antennas are simple in structure and highly suitable to be easily integrated in CR platforms.

Several frequency reconfigurable slot based antennas appeared recently in literature. Single element antennas were presented in [106–113]. In [106], microstrip-fed based frequency reconfigurable half annular ring slot antenna was presented. The frequency bands covered were 2.43 GHz, 2.85 GHz, 3.42 GHz and 4.40 GHz. The half annular ring slot antenna had a radius of 12.5 mm on a ground (GND) plane size of  $50 \times 50$  mm<sup>2</sup>. In [107], a dual-band reconfigurable slot antenna was presented. The antenna was a combination of a folded slot with multiple strips branch edges loaded with lumped components. Varactor diodes were used for reconfigurability and it covered S-band applications at 2.45 GHz (WLAN) as well as 1.227/1.381/1.575 GHz (GPS). The antenna was designed on  $30 \times 70 \times 0.8$  mm<sup>3</sup> board.

Few MIMO slot based antennas were presented in [114, 115] while very few MIMO slot based frequency reconfigurable antennas appeared in literature. A compact 4-element MIMO slot antenna system was presented for ultra wideband

(UWB) applications in [114]. It covered the frequency band between 3.1 to 12 GHz. The MIMO antenna was realized on a board size of  $49 \times 25 \times 1.6 \text{ mm}^3$  with single element area of  $21 \times 8 \text{ mm}^2$ . In [115], 2-element F-shaped microstrip MIMO slot antenna for WLAN and WiMAX bands was presented. The antenna was tuned to operate at four different bands at center frequencies of 2.4 GHz, 3.5 GHz, 5.2 GHz, and 5.8 GHz. The board used was with dimensions  $33 \times 36 \times 1.524 \text{ mm}^3$ . The geometry of the antenna is shown in the Figure 3.6. None of the antennas in [114, 115] had frequency reconfigurability ability. In [116], a port reconfigurable MIMO slot antenna was presented that covered three frequency bands. (2.4, 5, 5.5 GHz). The overall antenna dimensions were  $46 \times 20 \times 1.6 \text{ mm}^3$ .

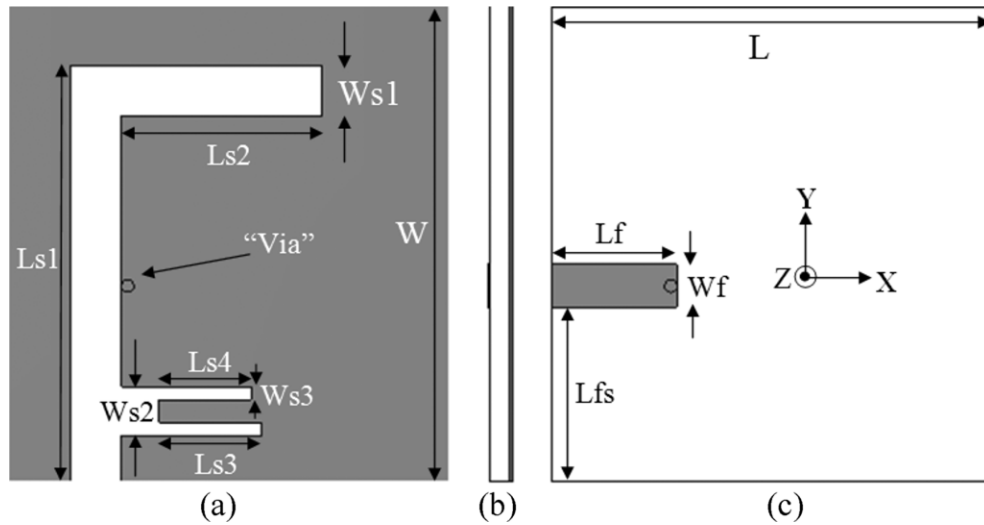


Figure 3.6: PIFA Antenna, where (a) Front view. (b) Side view. (c) Back view [115].

### Pattern Reconfigurability from TCM

Until now, frequency reconfigurability mechanism has not been explained with the help of TCM, although few researchers have revisited reconfigurability from

different perspectives. In [118], [119] parasitic elements were used to operate the antenna in a pattern reconfigurable fashion by using TCM. The value of the parasitic elements were chosen such that they cause the port coupling ( $Z_{12}$ ) zero. The problem was solved graphically and two results were obtained. The values obtained were such that they provide orthogonal like modes same as CM. It was demonstrated in [120] that coupled elements used for the excitation of the chassis modes, affects the chassis modes current distribution. In the presence of the coupled elements the characteristic modes shall be evaluated again.

Pattern reconfigurability was obtained for a 2 element design by non-degenerate modes whose resonance frequency were near to one another. 180 Hybrid decoupler was used for the excitation. When ports were excited in phase, one mode was excited on the surface of the antenna but when ports were excited out of phase, another mode was excited. In [121], a triangle is selected as an antenna element. Triangles have degenerate modes because of their geometry. The first two degenerate modes are selected for excitation. The two modes can be excited by placing the feeds at the two edges (sides) of the triangle. Both of the modes have orthogonal radiation patterns with respect to one another thus pattern reconfigurability was achieved.

In [31], [122] pattern reconfigurability was obtained by using pin diodes that connect a metallic strip to the chassis. Using TCM two modes were defined; the fundamental chassis mode and the bezel mode. In [23–25] pattern reconfigurability was obtained by using multiple sources to excite different modes of the antenna

chassis.

CM (eigen currents) for an antenna are orthogonal. The radiation patterns of the modes are orthogonal in nature. If we can excite multiple modes, we will get fields in different directions thus we can achieve pattern MIMO reconfigurability behavior [123]. Two different approaches can be used for feeding. Feeding Inductively and Feeding Capacitively. The main purpose of Inductive and capacitive should be in excitation of a particular mode, they should not affect the radiating properties of an antenna [124]. Inductive excitation (ICE) of a particular mode is applied at a position where we have maxima for the current. Capacitive coupling (CCE) is applied at a place where we have Voltage or Electric field maxima and current minima. Figure 3.7(a) shows the current distribution of rectangular chassis, We can observe in Figure 3.7(b) that the ICE's are installed at the current maxima of modes. Capacitive coupled elements are placed at current minima or voltage maxima, Figure 3.7 (c) shows the current distribution on the surface of chassis for the three modes.

ICE's and CCE's can be introduced in the geometry after some modifications in the chassis geometry as shown in Figure 3.8(a) and 3.8(b) respectively.

The excitation of such modes on the chassis is not an easy task. A systematic procedure was shown in [125]. Where a Feed Network (FN) was designed that consists of Matching Network (MN), Power dividers (PD) and Phase shifters (PS). The proposed method is shown in the Figure 3.9.



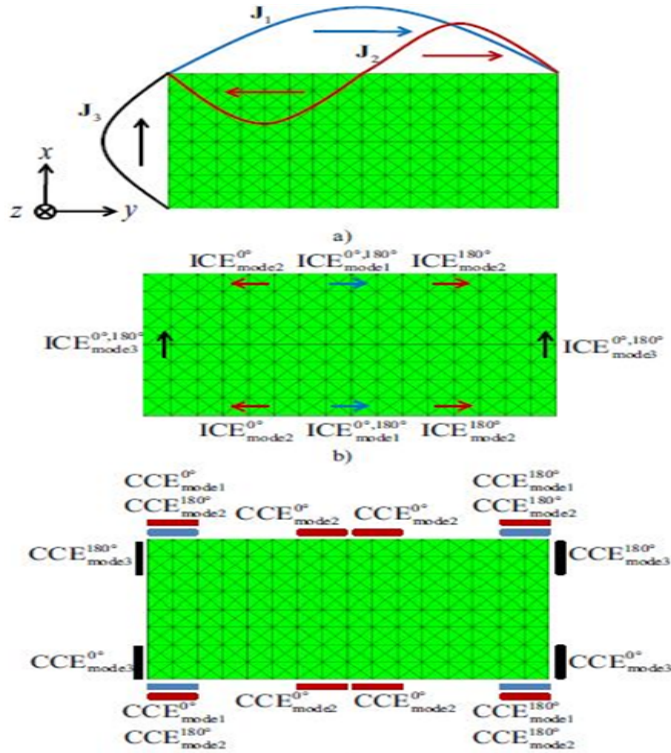


Figure 3.7: Characteristic modes excitation, (a) First 3 Modes characteristic modes current distribution patterns, (b) ICE's location for the excitation of 3 modes, and (c) CCE's location for the excitation of 3 modes [124].

### Frequency Reconfigurability from TCM

Frequency reconfigurability design from the perspective of TCM is very limited and almost no work was found in this research area. In [126, 127], frequency reconfigurability was achieved with the help of TCM. We know the general current pattern on the surface of antenna for few basic antenna designs like wire dipoles. To resonate the antenna at any frequency, we need to know how to excite the same current distribution on the surface of the antenna. Different combinations of the reactance were used for the antenna investigated to resonate it at different frequency. Two designs were analyzed using the proposed method, dipole and

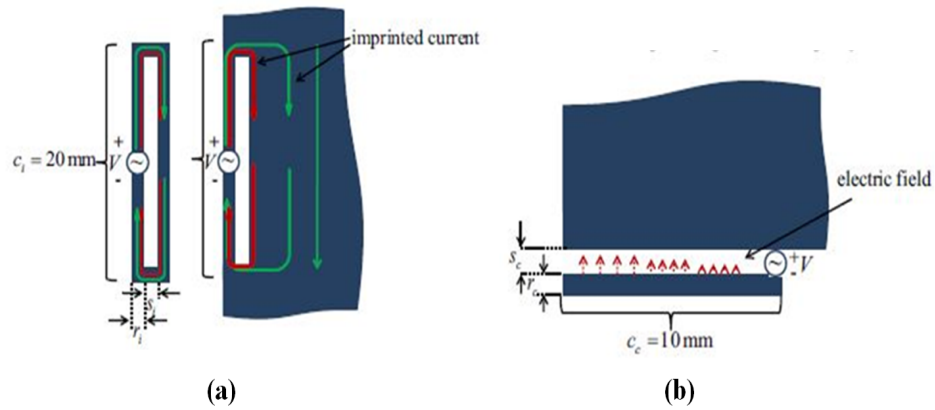


Figure 3.8: Geometry Modification of chassis to introduce (a) Inductive Coupled Elements (b) Capacitive Coupled Elements [124].

PIFA.

Limitations of the proposed method in [126] is that it cannot be generalized. The number of load ports as well as their location were taken empirically. Ports were tried to be placed at the point of maximum current density but in case of a dipole this assumption was not followed and the two ports were placed at the corners to create a current pattern similar to the dipole. In case of dipole 5 ports were used while in case of a PIFA, 7 ports were used. The main contribution from TCM perspective was to find the value of reactance needed that will be used to create the desired current pattern. The whole process depends on the prediction of the current distribution of the respective antenna, which is not possible in case of many complex designs. An extended version of this approach was used for obtaining enhanced BW [88].

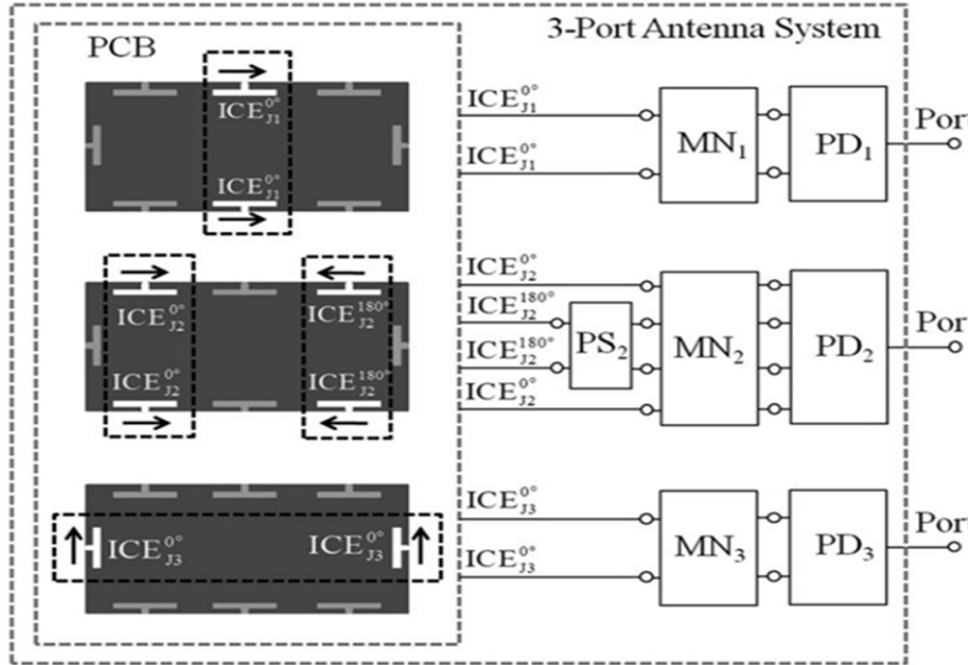


Figure 3.9: Feed Network for the selective excitation of modes [125].

### 3.2.4 Slot Antennas

We know that the inclusion of slots in antennas has demonstrated to be really helpful for creating extra resonances [128], band-notch effect [129], reducing size [130], or provide circular or dual polarization [131, 132]. Recently a wide variety of printed slot antennas have been proposed for wideband or ultra wideband operation [133–135]. A lot of slot antennas with different shapes such as rectangle, arc, triangle, circle and square have been reported in [135–139]. Empirical design guidelines for a slot antenna are presented in [140–142]. A summary of these guidelines has been also presented in [133].

## Slot Antennas in TCM

TCM was used for the analysis of a slot separating two media [143], a slot in a cylinder [144, 145] and multiple slots [146]. In [129], it was demonstrated that frequency notching is achieved by the generation of a new slot mode. The Selective excitation of circular slot modes by using multiple sources to achieve broadband behavior was discussed in [147]. It focused on the excitation of the modes while the effect of the circular slot modes on the chassis as well as whether the presence of the circular slot has generated some new modes or it has only modified the chassis modes was not shown.

In [148], the generation of a new slot mode was shown to depend on the size and location of the slot on the chassis. The response of various ground plane sizes on a slit line was discussed in [149]. No relationship between the slit and the chassis modes was provided. In [150], the effect of various ground plane sizes on a U-slot antenna was studied. It was observed that it is not only the parameters of the U-slot that determines its resonance frequency but the resonance frequency is also affected by the size of the ground plane. In [151–153], different slot shapes such as U, L, E, T and circle were investigated. It was observed that as the size of the slot increases the modes get affected. Analysis were performed for two modes only. No relationship was provided between the slot shape and the chassis modes as well as the slots were compared when they were present at different locations on the chassis.

In [154], unsymmetrical U and E slot antennas were analyzed in order to have

them radiate with circular polarization. In [155], three U slot antenna designs that were designed with Dimensional invariance (DI), Resonance frequency (ResF) and DIResF methods were analyzed with TCM. The effect of dielectric thickness, feed position variation, slot thickness and slot width variation on the performance of these methods were discussed. Orthogonal mode generation can improve the cross polarization while a slit introduction can reduce the mutual coupling [156]. A Diamond shaped meta material analyzed using TCM achieved better performance when fed using a slot [157]. A crossed slot antenna and a notched antenna were presented in [158, 159]. In [129, 148, 150, 158], it was concluded that the new mode that appeared was actually a new slot mode, while in [147, 149] it was claimed that the slot mode did not appear independently, but a new set of modes that are the combination of the slot and chassis modes appeared coherently.

### 3.2.5 Isolation Enhancement

The compactness of the terminals in MIMO antenna system may degrade the performance of the system due to high port and field coupling which affect the channel capacity, Bandwidth (BW) and efficiency of the system [57]. Many methods are proposed in literature to improve port isolation with minimal effect on the channel capacity, BW and efficiency of the system. The tree in 3.10 summarizes the literature review for the isolation enhancement using EMD and TCM approach.

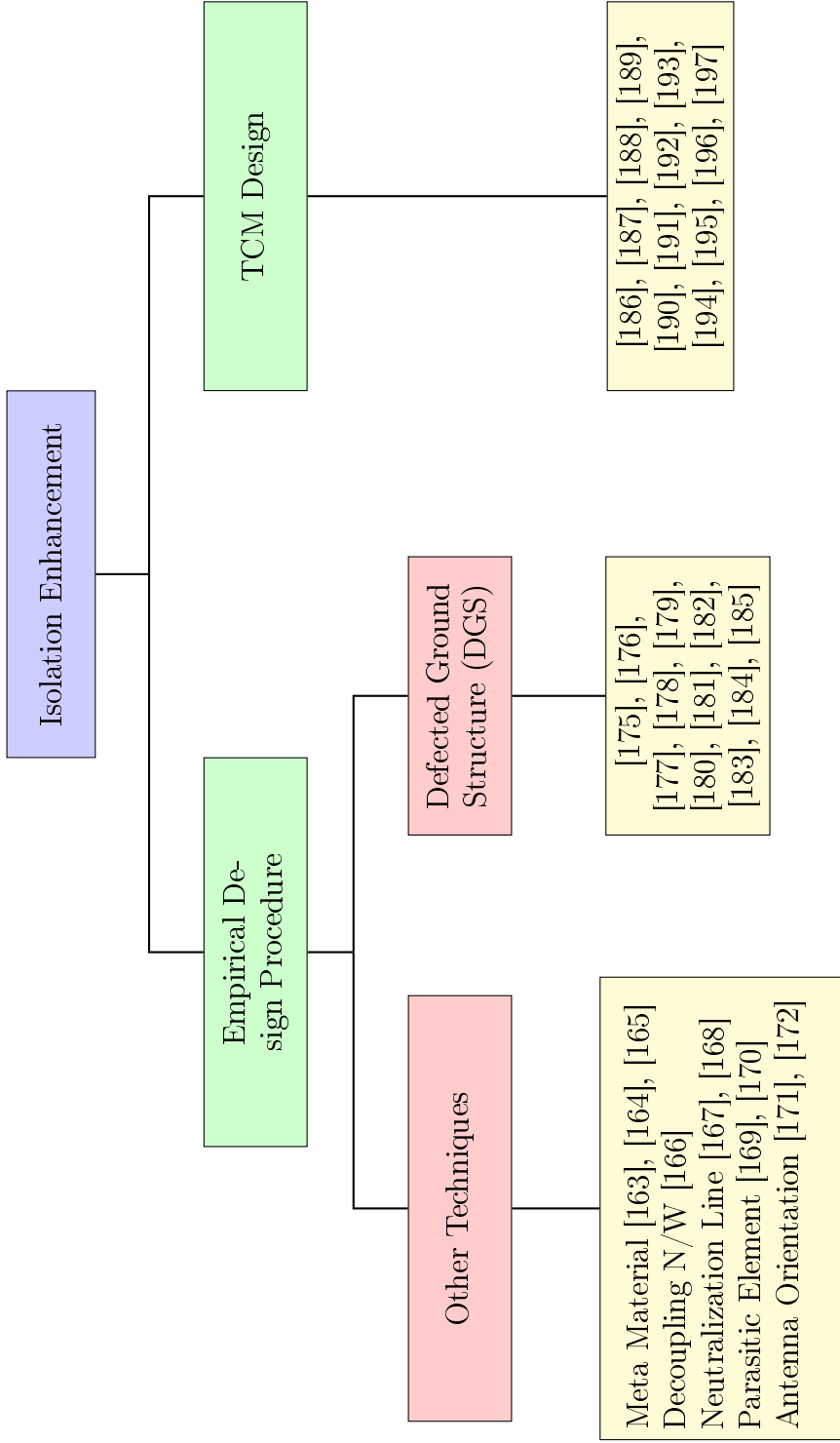


Figure 3.10: TCM used for Isolation Enhancement, Literature Review

## Isolation Enhancement Using EMD

Isolation can be improved by the use of electromagnetic bandgap structures and meta surfaces [163–165], decoupling networks [166], neutralization line technique [167, 168], parasitic elements [169, 170], optimization of the antenna system configuration [171, 172] and the use of Defected ground structures (DGS) [175–185]. Among all the aforementioned port isolation enhancement methods, DGS is the least complex and expensive.

In [175] a periodic S shaped DGS was used to improve the isolation between two patch antennas to 23 *dB*. An isolation was improved to 17 *dB* for a 2 element, 4 shaped dual band design, where the length of the rectangular slot and spirals in the DGS were used to tune the frequency band in [178]. Isolation enhancement for a MIMO antenna system for more than 2 elements is difficult. Isolation was enhanced to 12*dB* for a very closely packed 4-element MIMO design, where they used four wideband DGS with multi objective fractional factorial design [180]. A slitted pattern was etched between 2-element PIFA and wire monopole design that enhanced the isolation to reach 20 *dB* [181]. Moreover the study was extended to 4-element PIFA (aligned along a line) to get an isolation of 12 *dB*. Two DGS were used in [182] to improve isolation of a 4-element MIMO design. For an 8-element MIMO design a very complicated DGS that consist of closed loop frequency selective surfaces and quad strips connected with a circular arc were used to improve isolation to 15 *dB* respectively [185].

The main problem in the DGS method to enhance isolation is the shape, size,

number of DGS, position and the huge amount of optimization involved in the placement of DGS.

### **Isolation Enhancement using TCM**

TCM was used in [186–190] to enhance the isolation between the MIMO antenna designs. It was demonstrated in [186], that for frequencies below 1GHz, severe coupling is observed in MIMO configurations because all antennas are coupled via the chassis. From TCM, the first mode has electric field maximas at the edges of the chassis, while minimas at the center. Any electrical antenna located at the edge will excite the chassis effectively while those located at the center will not. For a Monopole located at the edge and a PIFA located at the center, an isolation enhancement of 5 dB was achieved without using any isolation scheme as compared to placing them at the edges of the chassis [186]. The placement of the antenna at the center of the chassis is impractical, that is why it was observed that instead of placing two electrical antennas at the edges of the chassis, an electric and magnetic ones will have better isolation. At the edge, the magnetic fields have minimas that is why electric and magnetic antennas placed at the edge will have better isolation [187]. Co-located antennas were introduced in [187], to have very compact MIMO antenna design.

The selective excitation of characteristic modes that have orthogonal behavior can enhance the isolation [191–195]. In [196], out-of-band interference was improved by the use of TCM. In [197], designs made with the application of TCM were compared with the empirically made designs. It was observed that designs



made with the help of TCM were performing better.

### 3.3 SIW

Waveguides are classified into two types (a) Standing wave type and (b) traveling wave type. The standing-wave arrays have elements spaced by  $\lambda_g/2$  and radiate a beam broadside to the waveguide. The fields repeat in a waveguide every  $\lambda_g/2$  but are of opposite phase. Therefore the slots are placed in a  $+/-$  configuration so that they are all fed in phase. Because of dispersion in a waveguide, the bandwidth around the center operating frequency cannot deviate by more than a few percent without causing rapid deterioration of the beam pattern and sidelobe levels, especially for the standing-wave array. Standing wave arrays can be fed either at one end of the waveguide with the other end terminated in a matched load or short circuit, or at the center of the waveguide with matched load or short circuit terminations at the waveguide ends. Short circuit terminations provide for a more efficient array since the reflected wave from the waveguide ends can be phased with the incident wave. This allows for a higher power handling capability. If a slightly larger bandwidth is desired, matched terminations minimize reflected waves that potentially could cause the array to radiate another beam in the opposite direction.

Traveling-wave arrays are used in applications where the direction of the main beam is pointed at angles that are not broadside to the waveguide wall or where frequency scanning is desired. Inter-element spacing does not have to be the same between the elements, and  $\lambda_g/2$  spacing is particularly avoided. In designing these

arrays it is important to have wideband terminations with a very low VSWR to prevent the formation of reflected or backward waves. Backward waves appear to originate from the opposite end of the waveguide and excite the slots to produce unwanted beams in the backward direction. Traveling-wave arrays can only be fed from the ends of the waveguide. To maximize the impedance bandwidth of the array, the slot elements are designed to be resonant at their center operating frequency, hence they are called resonant slots.

Waveguides are not planar in structure that's why they cannot be easily integrated with the planar structures. SIW's due to its small size, light weight, low cost, low profile and the ability to easily integrate with planar structures, SIW's are widely used in literature. Beside such features, SIW has the feature of high gain, high Front to Back (FBR) ratio and low cross polarization level like metallic waveguide antennas. SIW are normally used in array fashion. In [43], a  $4 \times 4$  slot array is presented at frequency of 10 GHz with BW of 600 MHz. The directivity offered was 17.4 dB with a gain of 15.7 dB. The concept of double resonant property was presented in [44]. A two layer substrate, where the lower substrate act as SIW and the upper substrate acts as a Substrate integrated cavity (SIC). A slot is introduced in SIC so that the energy can coupled to outside. The energy in SIW passes through Longitudinal slot coupled cavity slot (LSCS) to the upper substrate. From the coupled energy, some of energy goes directly through the slot while the rest excite  $TE_{210}$  mode of the cavity and ultimately also radiated from the slot. The geometry is shown in the Figure 3.11.

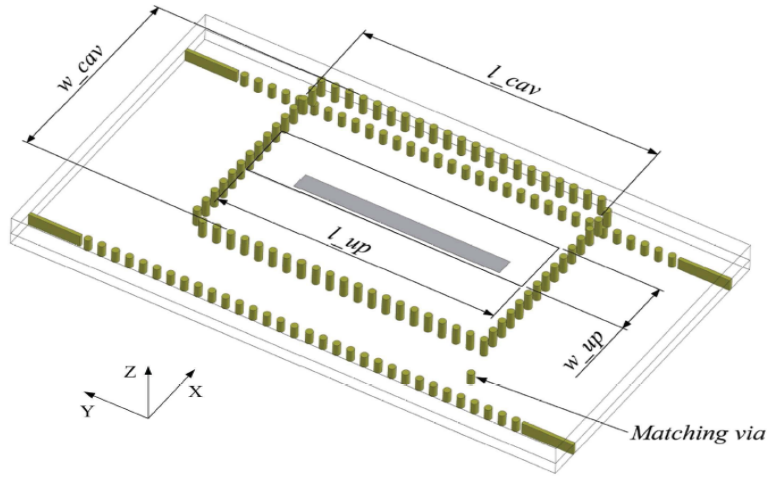


Figure 3.11: Double resonant SIW antenna [200].

The structure parameter of LSCS cause it to resonate it at 9.9 GHz, while the upper cavity resonate it at 10.8 GHz. The targeted center frequency was 10.4 GHz. Side lobe level (SLL) of -20dB is achieved with a impedance BW of 6.7%. Radiating Match Load (RML) was used at the end of the array to avoid wasting of the power at the end of the array. A nonlinear spaced sub array was introduced that consist of 13 elements, the array was made planar by implementing 4 sub arrays. A measured gain of 20.25 dB was obtained.

In [201], a compact circularly polarized mono pulse cavity backed dual mode SIW antenna is presented. The antenna consist of two planar ring slot cavity backed circularly polarized antenna, two transitions of microstrip to SIW and 180° hybrid coupler. A BW of 4.4%, with an axial ratio of 1.9% and a gain of 9.2  $dB_i$  was obtained. Two slots were engraved in SIW to create dual band resonance at 28 GHz and 38 GHz respectively [202]. At 28 GHz the impedance BW was 0.45 GHz with gain of 5.2  $dB_i$  while at 38 GHz an impedance BW and gain of 2.20

GHz and  $5.91 \text{ dB}_i$  was obtained respectively. To achieve high gain a linear array of 4 elements ( $1 \times 4$ ) was designed that increase the gain to  $11.5 \text{ dB}_i$  on average in both bands. Wilkinson power divider ( $1 \times 4$ ) was used to feed the array. To improve the radiation characteristic an EBG structure was used in the ground plane. The geometry of the design is shown in Figure 3.12.

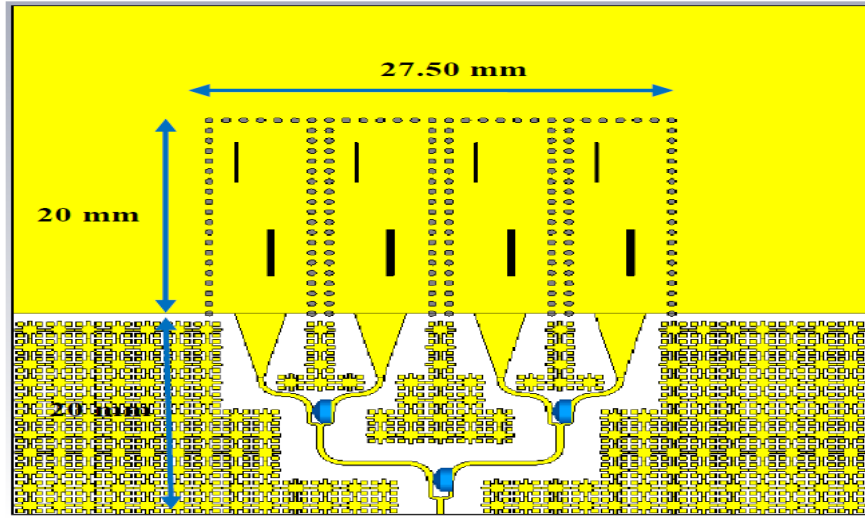


Figure 3.12: Double resonant SIW antenna [202].

HMSIW are also widely used because of its reduced size by 50% as compared to SIW [50, 51]. Open face of the HMSIW can be treated as a magnetic wall and thus can be used as a radiating slot. In [51], HMSIW was designed at frequency of 8.5 GHz on a rogers duroid 5880 board with relative dielectric constant of 2.2, and substrate thickness of  $0.78 \text{ mm}$ . The thickness of the cavity was  $\frac{\lambda_d}{45}$ , which is much less than the thickness of the metallic cavity  $\frac{\lambda_d}{4}$ . A BW of 420 MHz ranging from 8.37 to 8.79 GHz with a measured gain of 6.5 dB and measured FBR of 13.8 dB was achieved.

A HMSIW was designed on a cork material substrate so that it can be easily

integrated in walls or floors [203]. A non-resonant slot was introduced further to split the HMSIW cavity into two Hybrid cavity modes, this will enlarge the impedance BW. The cavity was fed through an SMA connector. An impedance BW of 1.30 GHz with radiation efficiency of 85 % and a gain of 4.3 dBi at 5.50 GHz was obtained.

### **3.3.1 Polarization**

Polarized antennas are normally designed by using multiple layers of substrate. Normally in one layer the antenna geometry is designed while the other layers are used to design the feeding mechanism. In [204], an 8x8 planar dual circularly polarized (CP) patch antenna array was designed at 60 GHz. In [205], a circularly polarized (LP) 4x4 helical antenna is designed at 60 GHz. Circular polarization was achieved by properly adjusting the arm lengths of the spiral antenna. In [206], a dual linearly polarized (LP) 16x16 planar slot antenna is designed at 60 GHz. For dual LP, it uses the same radiating element but rely on different feeding network. A 4x4 microstrip antenna planar array left hand circularly polarized resonating at 60 GHz is presented in [207]. A 4x4 helical antenna array right hand circularly polarized and an 8x8 magneto electric dipole antenna array left hand circularly polarized operating at 60 GHz is presented in [208,209]

### 3.3.2 Beam Scanning

A lot of SIW based designs were proposed to tune the beam. Majority of the literature focused on discrete tuning (shifting the beam to fixed angles) while some focused on the continuous tuning. The focus was either on the input matching network or on the geometry selection (Leaky wave antennas or placement of diodes). In [210], a ferrite substrate based 2x3 SIW antenna array resonating at 13 GHz is presented. A ferrite material when magnetically biased, produces a phase shift in the wave. In [211], a leaky wave antenna is designed by placing transverse stubs in the PCB. These stubs are made of different substrates and the stub is having different height.

Multi beam antennas can generate multiple beams pointing in different directions but they share the same antenna aperture. This switching between multiple beams takes place by playing with the input feeding. Normally wide beam width antenna is good for moving devices (not losing connectivity) but it suffers from gain issue. Narrow beam width antenna have high gain and they are good for satellite communication but perform poor for moving devices. Different type of feeding methods can be adopted, one of them is Rotman lens [212,213]. In [214], a slot is etched on the surface of the patch antenna. This etched slot acts as a radiating element as well as a capacitor (Left handed capacitor). Due to this presence of the Left-handed capacitor negative resonance occurs which means that all frequencies below the cutoff frequency will propagate. In [215], four pin diodes were used to switch the beam of the four slots, by properly adjusting the on and

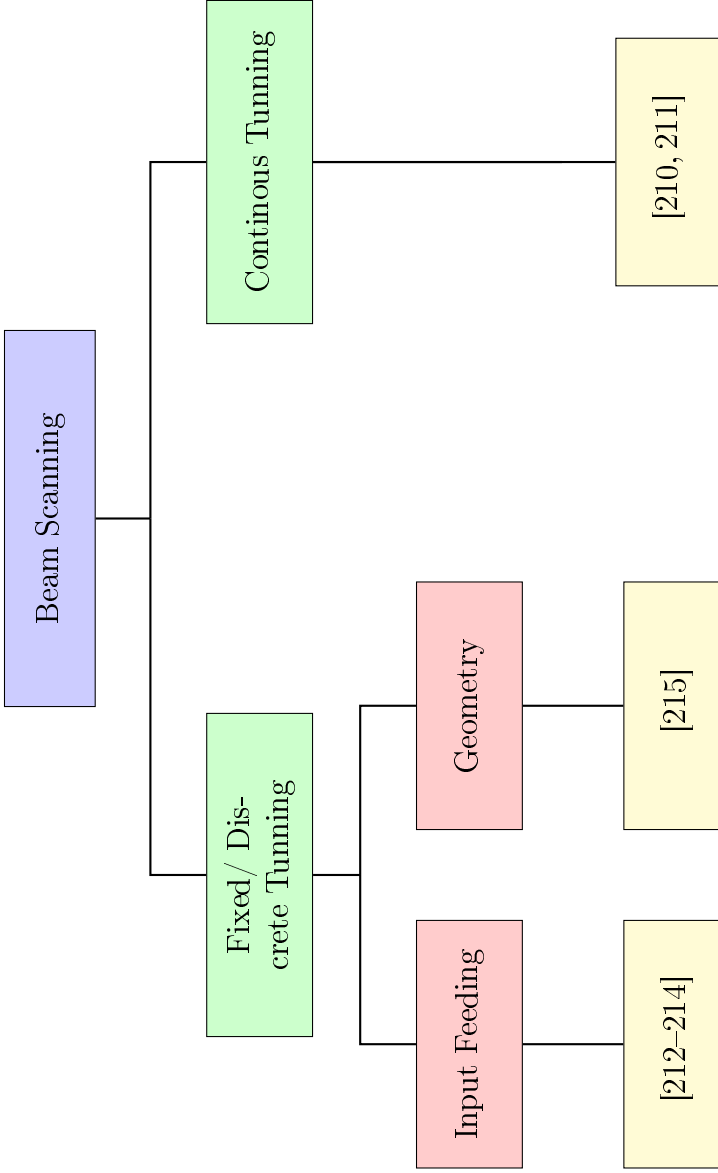


Figure 3.13: SIW based Beam-scanning based on scheme used

off state of the diodes.

### **3.3.3 Slot Antenna Arrays**

In [216], a 2x2 wide-band multilayer cavity backed antenna array with air vias having a wide BW from 18 GHz to 30 GHz is presented. A linear array of 8 patches on a multilayer substrate on unequal T-junction divider was designed in [217]. A total of 4 layers substrate were used. In [218], an 8x8 multilayer slot antenna array excited by a 4x4 substrate integrated cavity (SIC) operating at 82 GHz-104 GHz is proposed.

#### **Waveguide Slot Antenna Arrays**

A low cost multilayer antenna operating at 8.8 GHz with very low Average SLL is designed with the help of GA [219]. The AF equation was transformed into Schelkunoff polynomial and was optimized using GA to find the optimum roots that can give us an Average SLL less than -45 dB.

#### **SIW Slot Antenna Array**

In [225], a multilayer SIW antenna with cavity was proposed. This configuration greatly enhanced the bandwidth performance of the system. It is a 4x13 planar array i.e. having 4 uniform spaced array by 18 mm and then each array contains 13 non-uniformly spaced array elements. In [226], Elliot's design procedure was used first to design the slot antenna and then the linear array but the design was optimized using the simulation tool. The slots in the array depends on the follow-



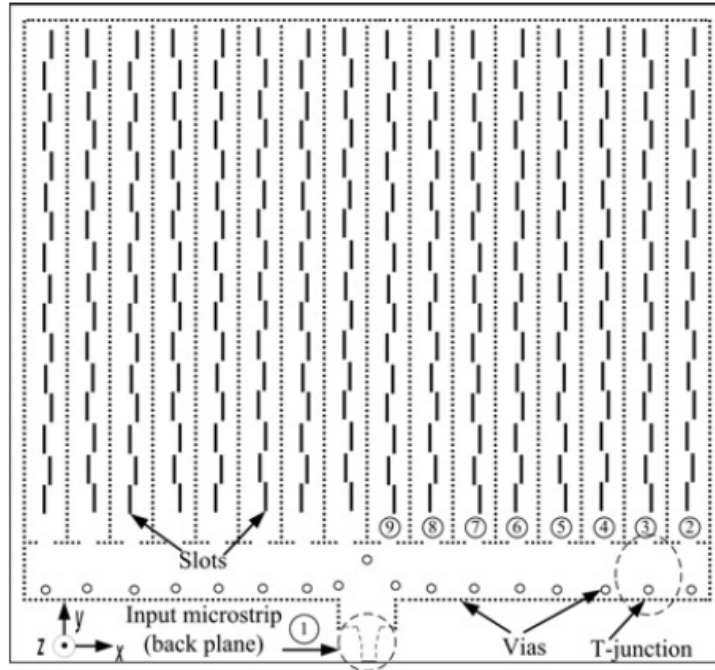


Figure 3.14: 16x16 planar slot array [226].

ing inputs; waveguide feeding, the coupling of the slot to the outer environment and the coupling of the slots to one another, this was the reason that they have to optimize the design further and the Elliot's design strategy was not good. The geometry of the 16x16 array is shown in the Figure 3.14. In [227], number of slots needed inside a single array are determined on the basis of required Gain and SLL. A Taylor distribution (25 dB) was used to measure or calculate the radiated power from a single slot.

### 3.4 Summary

In this chapter, we covered different aspects of the ACGF, TCM, CBF and SIW.

TCM has been widely used for the analysis of chassis based radiators (chassis

acting as the main radiating element) while the effect of the real antenna elements was totally ignored. So, the effect of the real antenna elements shall be investigated.

As we know that the modes obtained using TCM are orthogonal to one another. So, if different modes are excited we can achieve pattern reconfigurability very easily that's why many researchers focused on the use of TCM for pattern reconfigurability as shown in the Figure 3.5. The use of the TCM to achieve frequency reconfigurability is very limited that's why a complete study shall be made in this area.

From Figure 3.10, we can observe that TCM was used to enhance the isolation by observing the chassis modes. The techniques that are normally used for the enhancement of the isolation such as DGS e.t.c none were investigated.

In SIW a lot of focus was made on the designs of standing wave and multilayer SIW while very limited literature is available for the traveling wave SIW. The radiation pattern of the standing wave SIW is always broad side while the traveling wave SIW can produce a tilt in the main beam. Currently, researches tried to introduce tilt in the beam with the help of feeding network while very limited work is done in the area of traveling wave SIW.

## CHAPTER 4

# FREQUENCY RECONFIGURABILITY AND SLOT CURRENT MODES USING TCM

*“The most exciting phrase to hear in science, the one that heralds new discoveries, is not ‘Eureka!’ (I found it!) but ‘That’s funny...’”*

---

ISAAC ASIMOV

It was clear from the detailed literature review that, no one investigated whether the slot mode is actually a new or a modified chassis mode. How does the size, shape and location of a slot affect the chassis modes radiating bandwidth (BW). For a slot based MIMO antenna system, what is the effect of multiple slots on chassis modes? In addition to answering the aforementioned questions, we also

investigated whether reactive loading helps in the feed matching or it is some how altering the radiating BW of a mode thus investigating frequency reconfigurability for the first time using TCM.

The main contribution of this chapter are as follows:

- We have shown that the introduction of circular slots does not generate any new modes but the obtained modes are the original chassis modes that are affected (concentrated/ rerouted) by the presence of the slot. Different chassis modes are affected based on the location of the slot. For a fixed location, the radiating BW of the mode is affected based on the slot to chassis size ratio.
- The effect of different slot shapes (circle, triangle, rectangle and square) was investigated on a mobile phone chassis size. The size of the slot was varied and its size was increased such that it starts resonating at 2.0 GHz. The effect of the slot is observed on two locations, i.e. center and corner of the chassis.
- The effect of multiple (MIMO antenna) circular slots on chassis modes is investigated in detail for the first time. It was observed that a 2-element MIMO circular slot affects the modes significantly as compared to single and 4-element MIMO ones. With reference to ground modes, the 4-element MIMO antenna modes were the least affected as compared to single and 2-element cases. The main reason was the symmetry of the design that did not shift or alter the current distribution (current maxima or minima).

- A novel 4-port frequency reconfigurable MIMO antenna is designed and fabricated. The proposed design is annular slot-based MIMO frequency reconfigurable antenna structure. Moreover, the slot based MIMO antenna is a compact, low profile one that is realized on a  $60 \times 120$  mm<sup>2</sup> area of a typical smart phone. The proposed antenna covers a wide frequency band from 1.8 GHz to 2.45 GHz and thus supporting several well known wireless standards bands including GSM1800/LTE/UMTS/WLAN. The proposed antenna design was 50% miniaturized as compared to normal slot antennas
- All analysis and models were conducted in the presence of a dielectric substrate (unlike most of the literature that uses perfect metallic sheets with air).
- The physical mechanism behind frequency reconfigurability was investigated on a 4-element slot based MIMO antenna for the first time. It is shown that the varactors used to continuously tune the impedance BW do not affect the CM current distributions or Modal Significance (MS) curves, thus they only contribute to the input matching.

The rest of the chapter is organized as follows. Section 4.1 describes the generation and effects of the slot shape, location and size on the chassis modes. The antenna system design for MIMO antenna system as well as the simulation and measurement results are described in section 4.2. The analysis of multiple slots on a chassis and frequency reconfigurability is described in section 4.3 and 4.4, respectively. While the conclusions are provided in section 4.5.

## 4.1 Slot Effect on Chassis Modes

TCM analysis will be used to investigate the effect of a slot on the chassis modes. CM current distributions (eigen functions) and the eigen values are used for comparison. The Impedance BW is calculated in the presence of the excitation sources and is the range of frequencies for which the antenna has good impedance matching ( $VSWR < 2.0$ ). In this section, we will observe the behavior of different shaped slots so that we can design a better slot antenna.

### 4.1.1 Slot Mode Generation

Whenever a slot is introduced in the chassis, previous works in [129, 148, 150, 158] mentioned that new slot modes are created. Are these slot modes generated due to the slot or they are modified chassis modes? To investigate this issue we consider a ground plane size of  $80 \times 80 \text{ mm}^2$  following that in [147]. The antenna was simulated in CST to get its CM. The CM current distribution and the MS of the ground plane are shown in Figure 4.1 and 4.3(a) respectively. To compare it fairly with the modes in [147], a substrate was not used for this analysis. Due to the symmetry of the structure, some modes are degenerate. They resonate exactly at the same frequency, such pairs are M1-M2, M7-M8 and M9-M10. A circular slot having a radius of 15 mm is introduced at the center of the chassis. The circular slot will resonate at 3.182 GHz (circumference is equal to 94.25 mm, it corresponds to one wavelength at 3.182 GHz). The CM current distribution and the MS curves are shown in Figure 4.2 and 4.3(b) respectively. The introduction

of the slot did not affect the symmetry. So, the degenerate pairs are not affected. Modes 3 to 10 current maximas and even the current distribution (current maxima and current minimas or nulls) are totally undisturbed because of the introduction of such a slot. The only two modes that seems to be disturbed are modes 1 and 2.

We can observe a current maxima or concentration across the slot, such modes in the literature were denoted as new modes that are generated because of the slot. If these are new modes then what happened to the first two modes of the chassis and why the MS of these two modes is so much resembling the MS of modes 1 and 2? We investigated further and we observed the current distribution flow of the modes. The current flow of the first four modes on the chassis alone are shown in Figure 4.4(a1) to 4.4(a4) respectively (for brevity, only four modes are shown). We can observe that for modes 1 and 2 the current is flowing continuously across the center while for all other modes we are having a current null or current minima at the center. If any sort of discontinuity (slot) is introduced at the center of the chassis, it will effect the CM current distribution of modes 1 and 2 only while all the other modes will be unaffected. We can observe in Figure 4.4(b1) to 4.4(b4) that when the circular slot is introduced in the center of the chassis, for the current to flow continuously it will concentrate at the sides of the circular slot. Due to this current concentration we got a current maxima at the sides of the slot. The different current maxima for both the modes 1 and 2 is due to the different current flow in both modes.

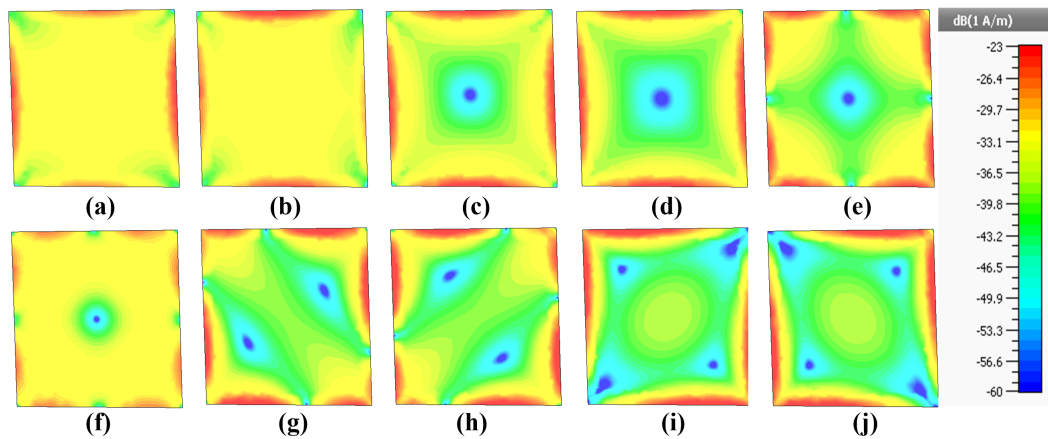


Figure 4.1: Current distribution of the first 10 modes of the chassis at 3.182 GHz, where (a) Mode 1 (b) Mode 2 (c) Mode 3 (d) Mode 4 (e) Mode 5 (f) Mode 6 (g) Mode 7 (h) Mode 8 (i) Mode 9 (j) Mode 10.

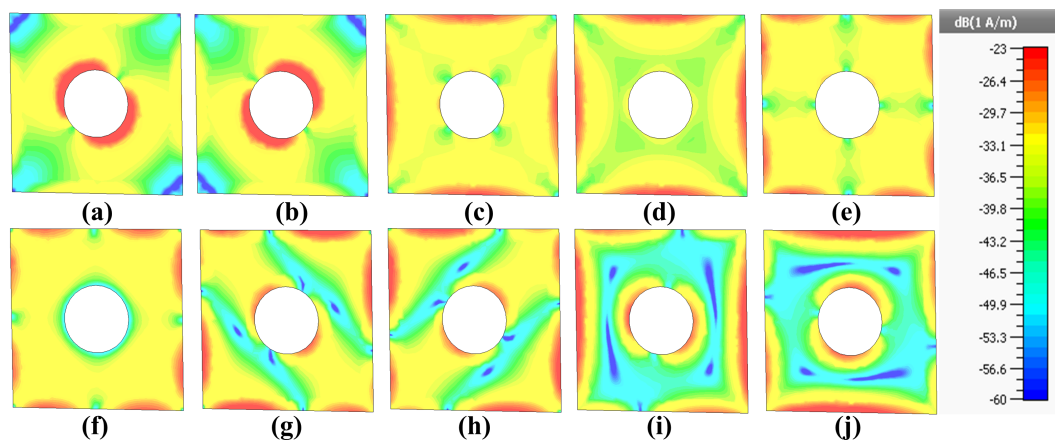


Figure 4.2: Current distribution of first 10 modes of a circular slot of radius 15 mm at the center of the chassis at 3.182 GHz, where (a)-(j) represents Mode 1 to 11 respectively.



To further validate our study, we introduced a slot of the same dimensions at the two corners of the chassis. The effective area of the slot is the same as the center one. From Figures 4.1 and 4.4(a) to 4.4(d), we can observe that the introduction of the slot at the edges will disturb the current flow in modes 1, 3 and 4, while all other modes will be unaffected. Modes 9 and 10 might be also affected but as they are not contributing to the radiating BW in our desired region of interest that is why we can ignore them (Figure 4.3(a)). Observe that in Figure 4.4(c1) to 4.4(c4) the current maxima are across the slot for modes 1, 3 and 4 while mode 2 current distribution is not affected that is why its current pattern is not affected significantly. When the slot was introduced at the center, modes 1 and 2 were modified while when the slot was introduced at the edge modes 1, 3 and 4 are affected. This means that the slot modes are not new modes but they are the modified chassis ones and the modes are affected based on the location of the slot.

We further investigated the effect of the size of the slot on the radiating BW of the chassis modes. For a fixed location of the circular slot we increased the size of the slot w.r.t a fixed chassis size. The effect was studied by observing the CM current distribution and the MS curves. Two locations were chosen, one at the center of the chassis and the other at the edge of the chassis. The size of the circular slot was varied between 15 mm and 30 mm. The summary of the analysis is shown in Table 4.1. The study was conducted for 15 modes between 1 GHz to 4 GHz. Only 10 modes are shown because all the higher order modes were

not contributing to the radiating BW in the desired region. We observed that the size and the location of the slot plays a significant role in its effect on the MS curve (radiating BW). We can observe that for a slot located at the center, the MS curves are not affected significantly until the size of the circular slot reaches up to 15 mm. The modes have similar behavior as chassis modes.

For a fixed location, the radiating BW of the modes is not affected for circular slots having small size as compared to the size of chassis, that is why we did not observe any significant difference between the modes of the chassis and a circular slot of radius 15 mm present at the center as shown in Figure 4.3(a) and 4.3(b) respectively. As the size of the slot increases, it will affect the current distribution more significantly because it will now start interacting (disturbing) the current maxima of other modes and thus the MS curves will be affected. Consider the circular slot of radius 20 mm and 30 mm placed at the center of the chassis, the MS curves are affected significantly as shown in Figures 4.3(c) and 4.3(d) respectively. The analysis was also performed for a 22.5 mm, 25 mm, 27.5 mm cases but for brevity purposes the results are not shown here.

So, if we take the size ratio of the circular slot w.r.t to chassis, we can conclude that for a circular slot located at the center, if the size ratio of the circular slot w.r.t the ground is less than  $\frac{1}{9}$  it will not affect the radiating BW. This ratio is taken in correspondence to a 15 mm circular slot. The interesting part is that this ratio is valid only for a circular slot introduced at the center of the chassis. For a circular slot at the corner this ratio is not valid and even with this ratio the

modes radiating BW is affected. For a 15 mm circular slot at the edge we can observe that modes 1,3 are slightly affected and mode 4 is significantly affected as shown in Table 4.1. All the values represent the starting frequency of the MS curve except frequencies with <sup>†</sup> represents that the mode is contributing to the radiating BW before 1 GHz and stops contributing to the radiating BW at the respective frequency. NC means, Not Contributing to the radiating BW. All frequencies are in GHz. Mode 4 is no longer contributing in the desired BW of interest. When the size of the slot placed at the corner increases, the modes radiating BW gets affected significantly that is why for a 30 mm circular slot 6 modes are not contributing (NC) in the desired BW of interest as shown in Figure 4.3(f). By comparing Figure 4.3(c) and 4.3(d) with 4.3(e) and 4.3(f) we can observe that the same size circular slot placed at different locations affected the radiating BW differently. The study was also extended for a circular slot having radii of 20 mm on a ground plane of  $60 \times 60$  mm<sup>2</sup> dimension and the same conclusions were found. For brevity purposes, the results are not shown here.

For all these cases we observed that the introduction of a slot in a chassis does not create any new modes. The slot modifies the chassis modes based on its location. The radiating BW of the mode for a fixed location slot is affected based on its size in comparison to the chassis size.

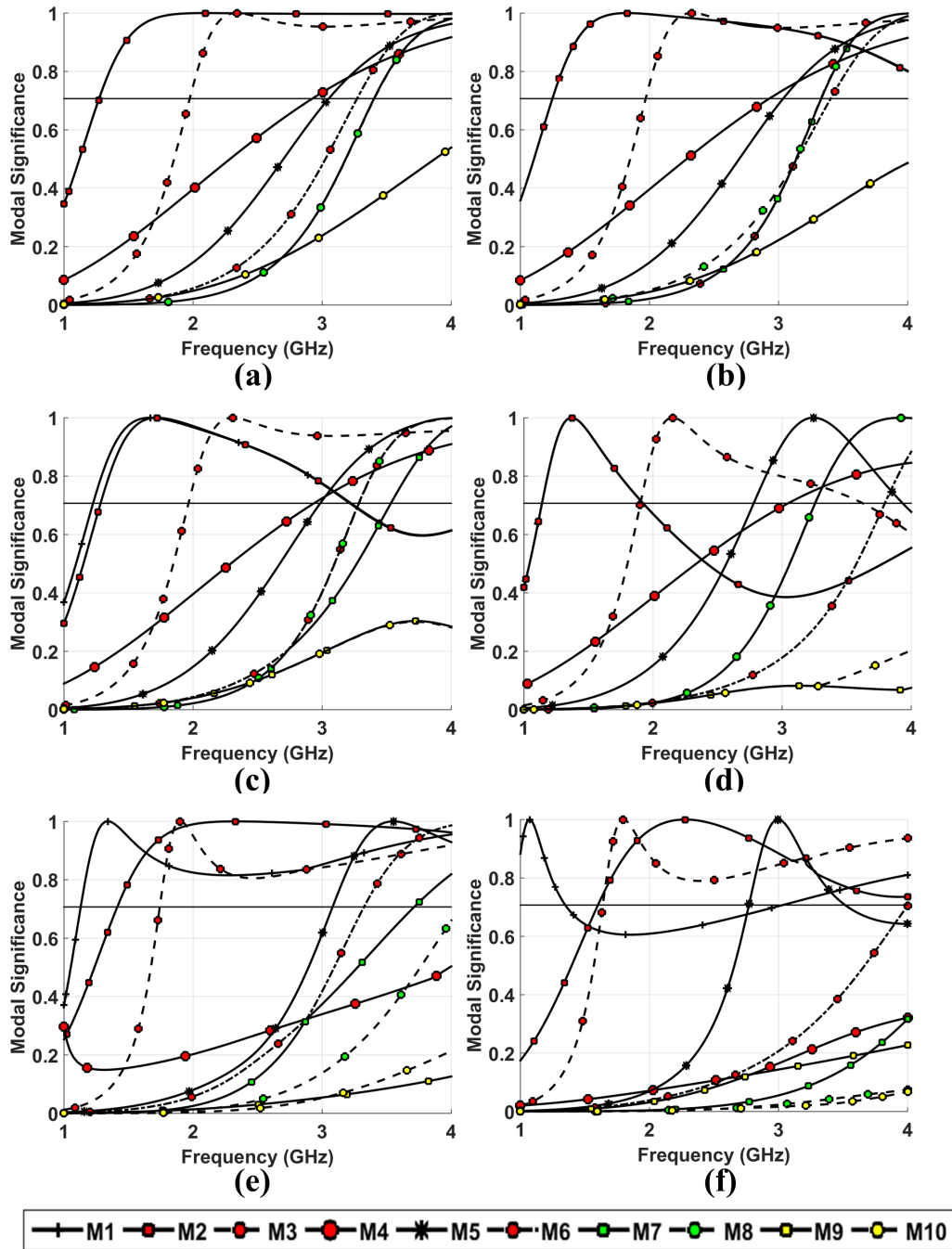


Figure 4.3: Modal Significance curves: (a) Ground plane or chassis, (b) Circular slot at center having radius of 15 mm, (c) Circular slot at center having radius of 20 mm, (d) Circular slot at center having radius of 30 mm, (e) Circular slot at corner having radius of 20 mm, (f) Circular slot at corner having radius of 30 mm

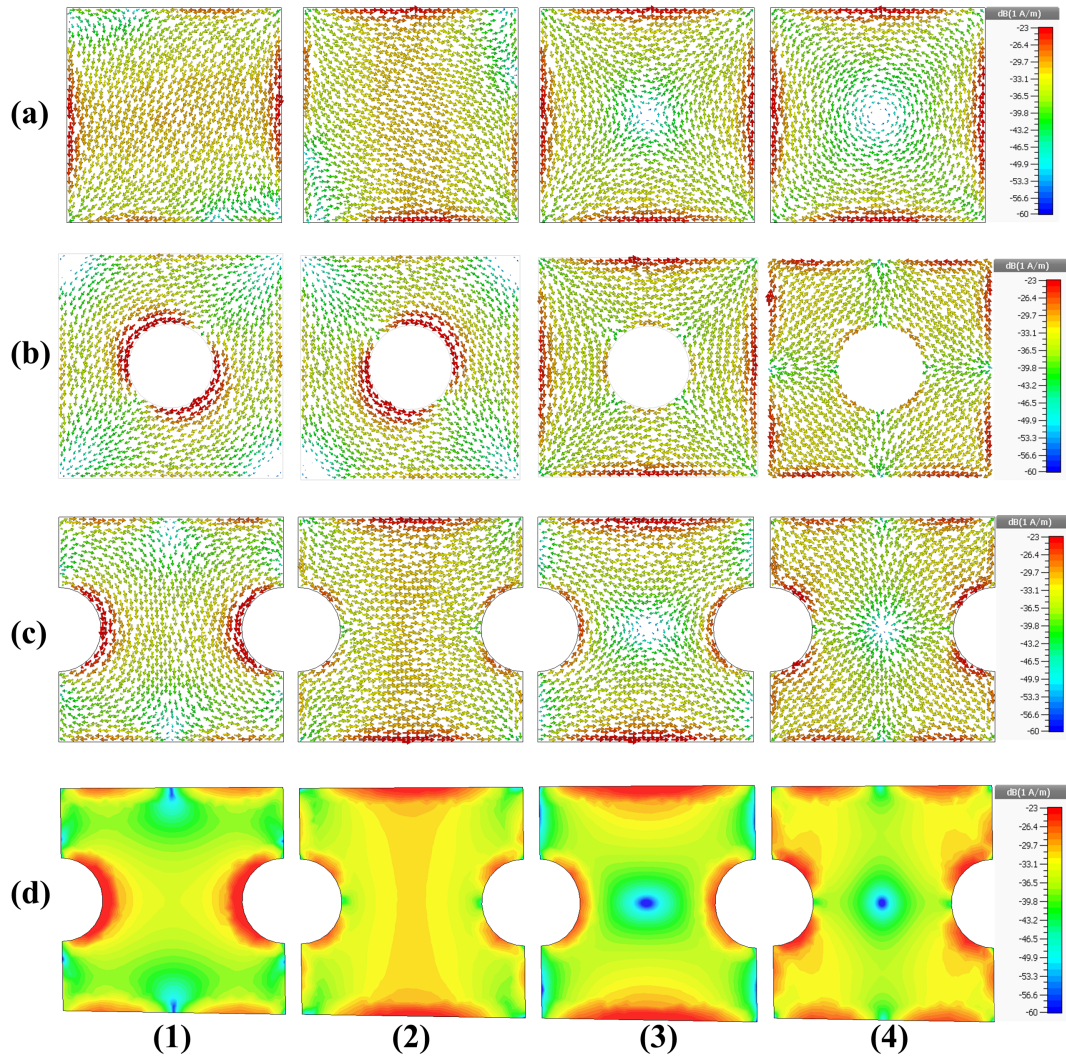


Figure 4.4: (1)-(4) represents the first four modes of (a) Chassis (b) Circular slot of radius 15 mm at center of chassis (c) Circular slot of radius 15 mm at both edges of chassis (d) Circular slot of radius 15 mm at both edges of chassis with continuous current flow.

Table 4.1: MS curve comparison of circular slot when introduced at the center and corner of the chassis.

Chassis		Circular slot at center			Circular slot at corner		
		15mm	20mm	30mm	15mm	20mm	30mm
M1	1.27	1.25	1.24-3.21	1.13-1.92	1.13	1.12	1.344 <sup>†</sup> ,3.03
M2	1.27	1.25	1.28-3.21	1.13-1.92	1.34	1.4	1.59
M3	1.97	1.97	1.97	1.92-3.62	1.8	1.74	1.63
M4	2.94	2.93	2.94	3.05	NC	NC	NC
M5	3.06	3.05	3	2.78-3.94	3.29	3.06	2.77-3.51
M6	3.26	3.4	3.27	3.79	3.18	3.32	NC
M7	3.39	3.32	3.53	3.25	3.49	3.72	NC
M8	3.39	3.32	3.27	3.25	3.84	NC	NC
M9	NC	NC	NC	NC	NC	NC	NC
M10	NC	NC	NC	NC	NC	NC	NC

#### 4.1.2 Slot Shape Effects on Chassis modes

The effect of different shaped slots such as circle, triangle, rectangle and square placed at two different locations; center and corner of the chassis are investigated. The size of the slot was varied (for all the cases) such that its size resonates around 2 GHz. The analysis was done in the presence of an RO4350 substrate having a dielectric constant of 3.48. Slot perimeters were chosen between 47 mm to 78.5 mm. Three cases were considered for all the slots from the prescribed range C1=47 mm, C2=63 mm and C3=78.5 mm. The cases are equivalent to a circular slot having radii of 7.5 mm, 10 mm and 12.5 mm respectively. The BW of interest was from 1 to 4 GHz. The total number of modes contributing to the radiating BW in this region were 10 but to be on the safe side we extended our study to 15 modes. For brevity, only 11 modes will be shown because all the higher order modes are not contributing to the radiating BW in the BW of interest.

We considered a standard chassis size of  $120 \times 60 \text{ mm}^2$  used for mobile phones.

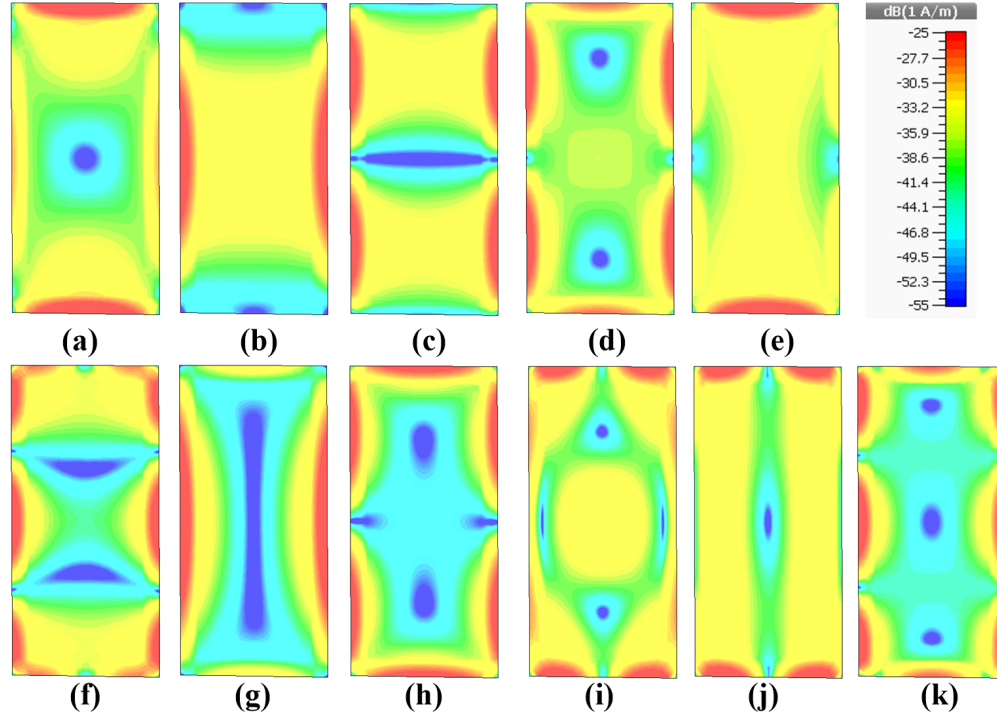


Figure 4.5: Current distribution of the first 11 modes of the chassis, where (a)-(k) represents Mode 1 to 11 respectively.

The CM and the MS curves are shown in Figure 4.5 and 4.15(a), respectively. When all slots were introduced at the center of the chassis, the current gets concentrated around the slot for modes 2, 5 and 9 irrespective of their shape while for all other modes, we did not get any current concentration across the slots. The amount of concentration varied for different shapes. The circular slot was the one having significant current concentration as compared to triangular, rectangular and square slots as shown in Figure 4.6. We can observe that we have good current concentration across the slot for the circular case. This means that the excitation of this mode (modified chassis modes) can be a bit easier as compared to other slot cases.

The analysis summary on the effect of slots having different shape and size

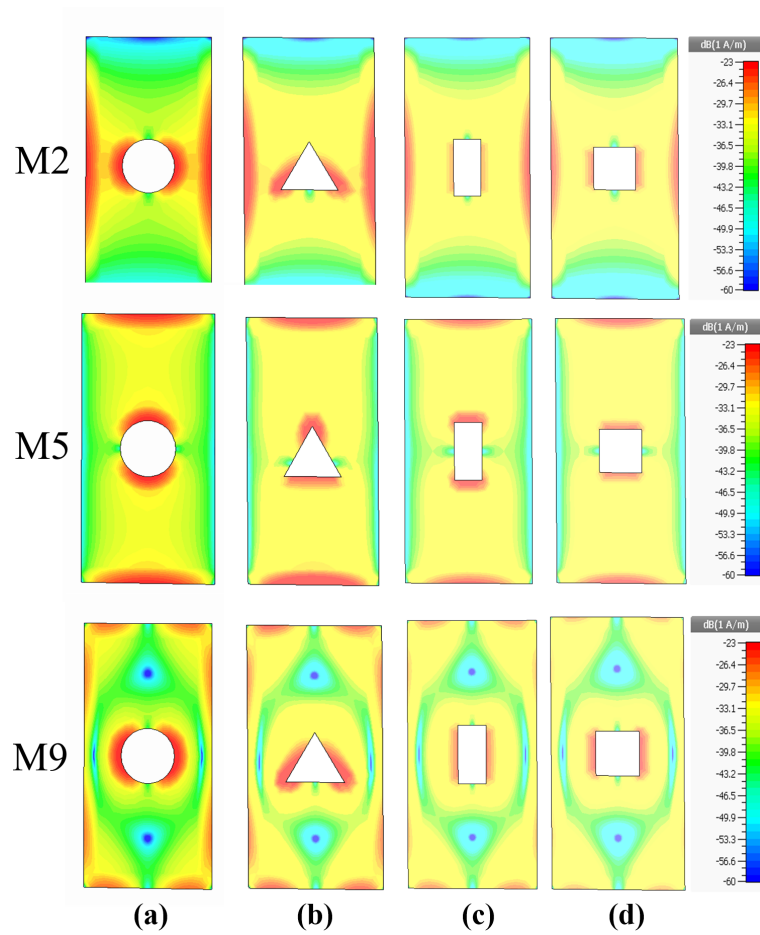


Figure 4.6: The rows represent mode 2, 5 and 9 respectively, where (a) Circular slot (b) Triangular slot (c) Rectangular slot (d) Square slot.



on the MS curves (radiating BW) is shown in Table 4.2. All the value represents the starting frequency of the MS curve i.e. when it starts contributing to the radiating BW. NC represent Not Contributing to the radiating BW. C2 and C3 refers to the cases when the parameter of the slot is equal to 63 mm and 78.5 mm respectively. All frequencies are in GHz. For brevity reasons the analysis of C1 are not shown. From our previous findings and as well as from Table 4.2 we can observe that the size of the slot is small as compared to the chassis size (less than  $\frac{1}{9}$ ), so the radiating BW will not be affected significantly that is why we can observe for all the cases of slot shapes circular, triangular, rectangular and square slot, the modes starting frequency are not affected and they follow the same pattern or remain in the radiating BW region till 4 GHz except for the square slot case C3 where its mode 1 starting frequency and for rectangular case C3 mode 5 stopping frequency are slightly affected.

For a slot introduced at the corner of the chassis, we got current concentration across it for all the modes because now the slot is placed near a current maxima (observe the current maxima of chassis in Figure 4.5). For brevity reasons, the CM distribution of a slot placed at the corner of chassis are not shown here. In the next section we will observe that whenever a slot is introduced at the corner of the chassis, for almost all modes we get a current concentration across the slot. The radiating BW is not affected because the size of slot is small as compared to the chassis size (because for mobile phones we cannot use large cuts in the chassis) and also the slot is not placed at the edge of the chassis. From all the

cases we observed that the current concentration of circular slots was uniform and more concentrated as compared to other slot shapes. So, designing a circular slot antenna will be a better option because it can be easily excited.

Table 4.2: MS curve comparison of different slot shapes when introduced at the center and corner of a chassis ( $120 \times 60mm^2$ ) in the presence of a RO4350 substrate.

Ground case	Center Placement						Corner Placement										
	Circle		Triangle		Rectangle		Square		Circle		Triangle		Rectangle		Square		
	C2	C3	C2	C3	C2	C3	C2	C3	C2	C3	C2	C3	C2	C3	C2	C3	
M1	1.86	1.87	1.87	1.87	1.87	1.86	1.86	1.71	1.86	1.85	1.86	1.83	1.86	1.85	1.86	1.85	1.85
M2	WB	WB	WB	WB	WB	WB	WB	WB	WB	WB	WB	WB	WB	WB	WB	WB	WB
M3	1.93	1.94	1.92	1.93	1.92	1.93	1.92	1.93	1.92	1.86	1.92	1.92	1.93	1.92	1.92	1.92	1.91
M4	2.63	2.6	2.62	2.6	2.6	2.57	2.61	2.64	2.62	2.6	2.62	2.6	2.62	2.63	2.61	2.62	2.62
M5	1.72	1.7	1.72	1.7	1.7	1.70-3.79	1.7	1.86	1.71	1.71	1.72	1.7	1.71	1.7	1.72	1.7	1.7
M6	3.09	3.09	3.07	3.09	3.07	3.09	3.09	3.09	3.05	3.05	3.07	3.07	3.08	3.08	3.06	3.06	3.06
M7	3.26	3.25	3.26	3.26	3.26	3.22	3.26	3.22	3.25	3.27	3.25	3.29	3.24	3.29	3.25	3.28	3.28
M8	3.77	3.76	3.77	3.76	3.7	3.79	3.75	3.78	3.85	NC	3.83	NC	3.8	NC	3.81	NC	NC
M9	NC	NC	NC	NC	NC	NC	NC	NC	NC	NC	NC	NC	NC	NC	NC	NC	NC
M10	3.93	3.96	3.96	3.96	3.95	3.97	3.96	3.97	3.85	3.8	3.87	3.82	3.8	3.66	3.8	3.8	3.8
M11	3.56	3.56	3.56	3.56	3.56	3.55	3.56	3.55	3.53	3.5	3.53	3.5	3.52	3.44	3.53	3.5	3.5

## 4.2 Antenna System Design

The geometry of the proposed 4-element miniaturized slot antenna system is shown in Figure 4.7. The antenna was designed on an RO4350 substrate with a relative permittivity ( $\epsilon_r$ ) of 3.48, loss tangent of 0.0036 and thickness of 0.76 mm. The total design area was  $60 \times 120 \text{ mm}^2$ . The radius and width of the annular slot were 10.1 mm and 0.5mm, respectively while the radius of the center circular slot was 8.5mm. The top layer of the antenna shown in Figure 4.7(a) contained the micorstrip feed-line and the biasing circuitry for the varactor diodes. The bottom layer is shown in Figure 4.7(b). It contained the four slot antennas that were etched out from the GND plane. The varactor diodes were placed on the outer annular slot and used to load the antenna by their reactive capacitance. The proposed MIMO antenna design is suitable to be used in wireless handheld devices. Most of these devices have their antennas systems on the top or bottom edges, to minimize the hand interference, avoid LCD blockage, improve port isolation and field correlation. That is why, the slots are placed on the top and bottom edges.

The proposed MIMO antenna was simulated using HFSS and fabricated using an LPKF S103 machine. Figure 4.7(c) shows the top view of the fabricated design having feeding lines and biasing circuitry while Figure 4.7(d) shows the bottom layer containing all the antenna elements.

A single antenna element consisted of annular and circular slots of radii 10.1mm and 8.5mm, respectively. The two slots were separated by an annular copper ring of radius 9.65mm. Varactor diodes ( $D_1$ ,  $D_2$ ,  $D_3$  and  $D_4$ ) connect the inner and

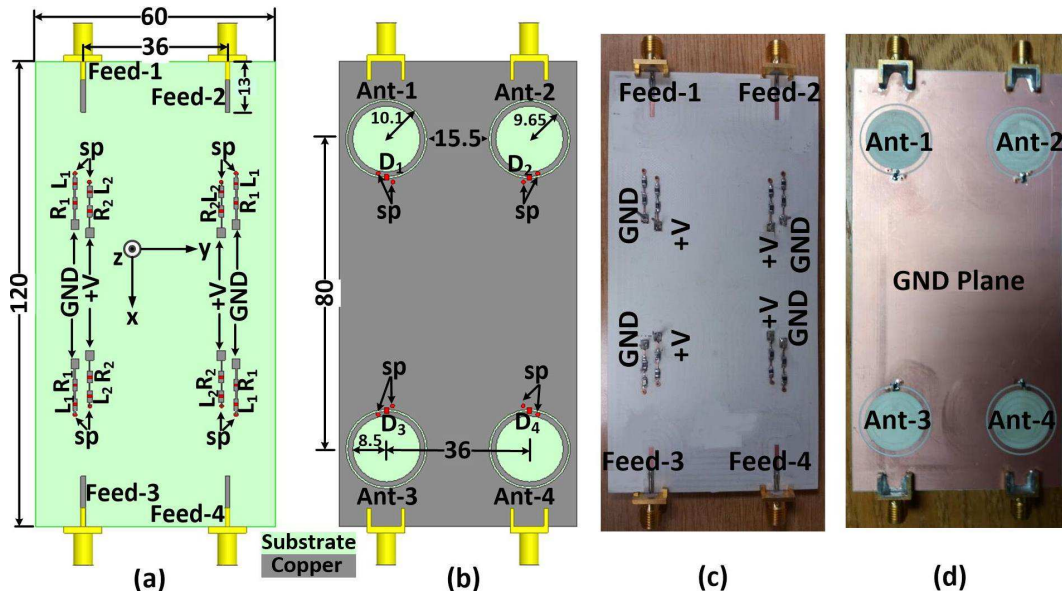


Figure 4.7: Proposed slot MIMO antenna system (a) Top layer (b) GND plane (c) Fabricated model top layer (d) Fabricated model GND plane- All dimensions are in millimeters (mm).

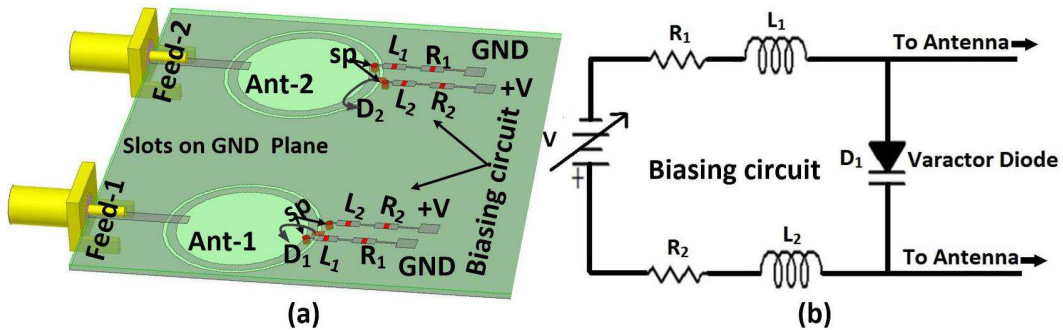


Figure 4.8: (a) Detailed view of proposed design (b) Biasing circuitry.

outer parts of the annular slot and thus bridging the slot with capacitive reactance. The varactor diode terminals, on the GND plane, were connected with the biasing circuit using two shorting pins (sp)/vias as shown on the bottom layer of Figure 4.7(b). The GND plane layer is also acting as a co-planar reflector for the MIMO antenna elements enabling beam tilting and thus lowering the field coupling for better MIMO performance.

To understand the antenna design better, an enlarged view of 2-elements of the proposed design is shown in Figure 4.8(a) while the biasing circuit is shown in Figure 4.8(b). The top and bottom layers, biasing circuit and feed lines are shown on the same figure to get more insight about the feeding mechanism and operation of the biasing circuit. The biasing circuitry consisted of  $1 \mu\text{H}$  RF chokes ( $L_1$  and  $L_2$ ) and  $2.1 \text{ k}\Omega$  resistors ( $R_1$  and  $R_2$ ) connected to the two terminals of the varactor diode. The varactor diodes used were SMV 1233 [117].

#### 4.2.1 Simulation and Measurement Results

The proposed slot reconfigurable MIMO antenna was modeled and simulated using HFSS<sup>TM</sup>. The antenna dimensions were optimized to maximize the number of covered bands for the given realizable capacitance values. Multiple parametric sweeps were performed to optimally place the antenna elements and select the positions of the varactor diodes to enhance MIMO performance metrics and improve isolation. The fabrication, development of the antenna prototype and port measurements were performed at the Antennas and Microwave Structure Design Lab (AMSDL) at King Fahd University of Petroleum and Minerals (KFUPM)

using an Agilent N9918A VNA. The gain patterns and efficiencies were measured using a SATIMO Starlab anechoic chamber at MVG-Italy.

### 4.2.2 MIMO Antenna Scattering Parameters

The simulated reflection coefficient curves for Ant-1 and Ant-2 are shown in Figure 4.9(a). The resonance frequency bands were smoothly varied over a wide range, as shown by the simulated reflection coefficient curves. The varactor diode was modeled as a variable capacitance with values ranging between 0.84pF to 5.08pF. The capacitance values used were  $C_1=0.84\text{pF}$ ,  $C_2=1.47\text{pF}$ ,  $C_3=1.33\text{pF}$ ,  $C_4=2.09\text{pF}$  and  $C_5=5.08\text{pF}$ . The corresponding sweep in frequency bands obtained were from 1.8~2.45 GHz. The particular position of the varactor diode had the maximum effect on the resonance while the other positions did not effect the resonance frequency sweep. The antenna was also simulated with and without the biasing circuitry and it was clear that the presence of the biasing circuit will have negligible effect on the resonance performance of the antennas.

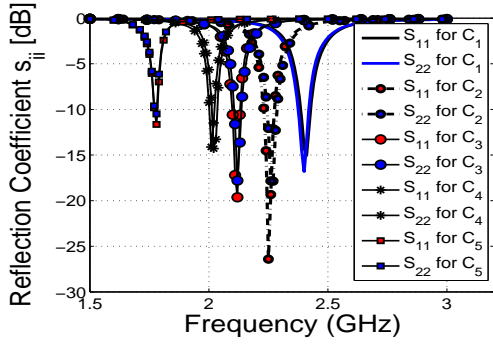
The measured reflection coefficient curves for Ant-1 and Ant-2 are given in Figure 4.9(b). The curves were obtained by applying variable reverse bias voltages (0~15 volts) across the varactor diodes. The measured frequency bands obtained were from 1.82~2.475 GHz. The average -10 dB bandwidth (BW) is 38 MHz and minimum -6dB BW is 46 MHz at 1.82 GHz. The simulated and measured  $s_{ii}$  results are in good agreement. As all the antenna elements are identical and placed symmetrically on the substrate, the same results were obtained from all

ports.

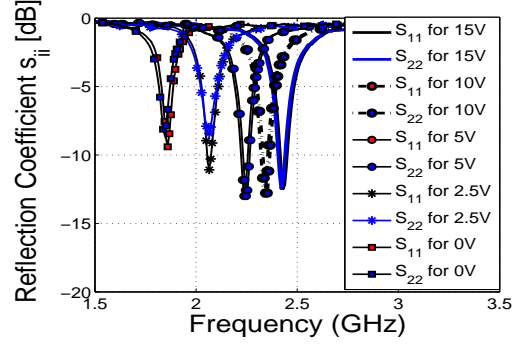
The simulated and measured reflection coefficient curves for Ant-1 and Ant-2 are given in Figures 4.9(c) and 4.9(d), respectively, to get a better understanding to compare the simulated and measured results. A slight shift about 30MHz was observed. The difference in the simulated and measured  $S_{xx}$  results were mainly due to the difference in the substrate properties of the fabricated antenna, fabrication tolerances and modeling of varactor diodes. The connectors were hand soldered and placed. In addition, the varactor diode was modeled as a variable capacitance. The modeling did not take into account the losses and packaging effects which might lead to some shift in the resonating bands. Moreover, any shift observed between simulated and measured values can be easily compensated for as we have a continuous sweep of antennas resonances from 1.8 GHz to 2.45 GHz.

The proposed slot antenna design was also evaluated for mutual coupling between all antenna elements. The simulated and measured isolation curves for Ant-1 and Ant-2 are shown in Figures 4.9(e) and 4.9(f), respectively. The closely spaced antenna elements, Ant-1 and Ant-2, showed relatively high coupling at 1.82 GHz of 9.5 dB while it improved to 13 dB at 2.4 GHz band. Similarly, the simulated and measured isolation curves for Ant-1 and Ant-3 are shown in Figures 4.9(g) and 4.9(h), respectively. The isolation between Ant-1 & Ant-3 and Ant-1 & Ant-4 was more than 10 dB in all operating bands. These values shows good isolation with minimal coupling between various antenna elements. Also,

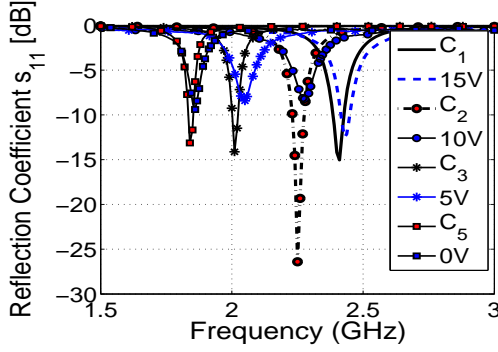




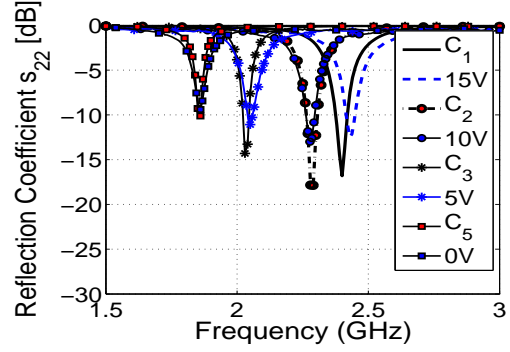
(a)



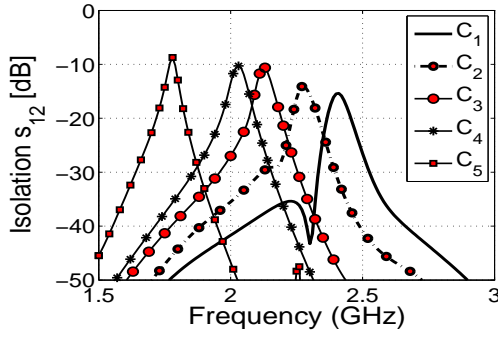
(b)



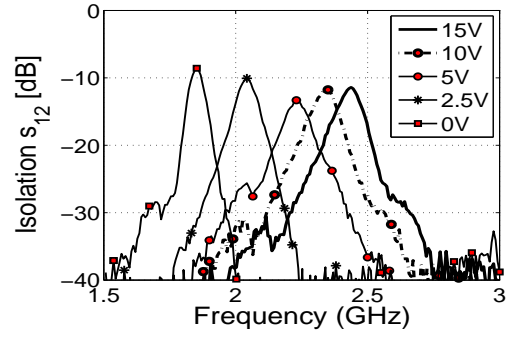
(c)



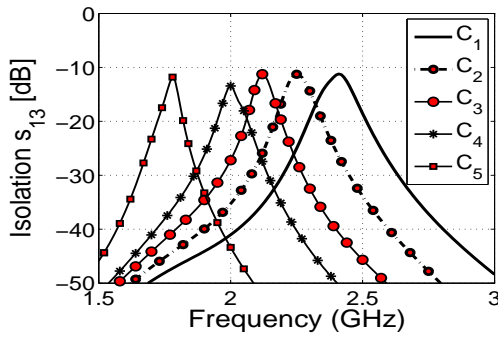
(d)



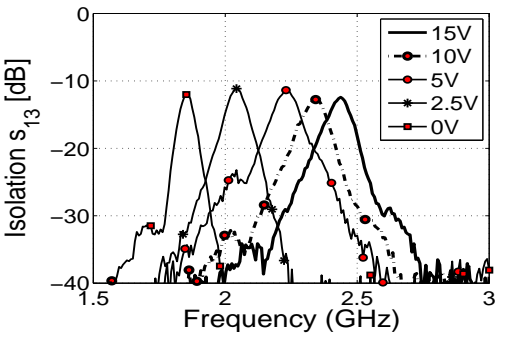
(e)



(f)



(g)



(h)

Figure 4.9: (a)  $|s_{11}|$  and  $|s_{22}|$ -simulated (b)  $|s_{11}|$  and  $|s_{22}|$ -measured (c)  $|s_{11}|$  simulated and measured (d)  $|s_{22}|$ -simulated and measured (e)  $|s_{12}|$ -simulated (f)  $|s_{12}|$ -measured (g)  $|s_{13}|$ -simulated (h)  $|s_{13}|$ -measured.

the measurements and simulations results are in good agreement.

In order to understand the coupling between various antenna elements, the surface current distribution is shown in Figure 4.10. Ant-2 was active while all other ports were terminated with  $50\Omega$  impedance. It is clear from the given figure that most of the current distribution was around Ant-2 and the coupling with other ports was insignificant.

### 4.2.3 MIMO Antenna Gain Patterns

The gain pattern of an individual antenna element was obtained while the other ports were terminated with  $50\Omega$  loads. The simulated and measured normalized 2D radiation patterns in terms of the total E-field ( $E_{total}$ ), for antennas 1-4 at 1.86 GHz are given in Figure 4.11. The patterns show the x-y and y-z planes for all the antenna elements. The simulated and measured  $\theta$ -cut curves for all four antenna elements for  $\phi = 0$ , at 1.86 GHz are shown in Figures 4.11(a), 4.11(c), while the  $\phi$ -cut curves for all four antenna elements for  $\theta = 90$ , at 1.86 GHz are shown in Figures 4.11(b), 4.11(d). The gain pattern measurement setup is shown in Figure 4.11(e).

The presence of a metallic object (i.e. wire, lumped components) near to an antenna might tilt the pattern a little bit. The wires were bent to the level of the antennas to minimize their effect. Good agreement between simulated and measured results is obtained.

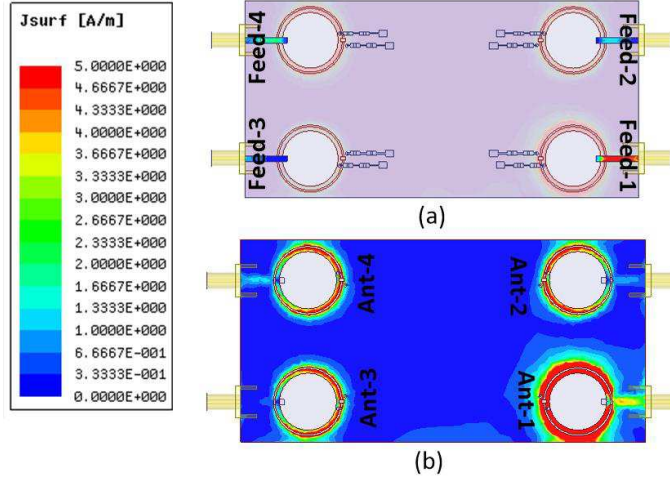


Figure 4.10: Surface current distribution at 1.820 GHz (a) Top view (b) Bottom view.

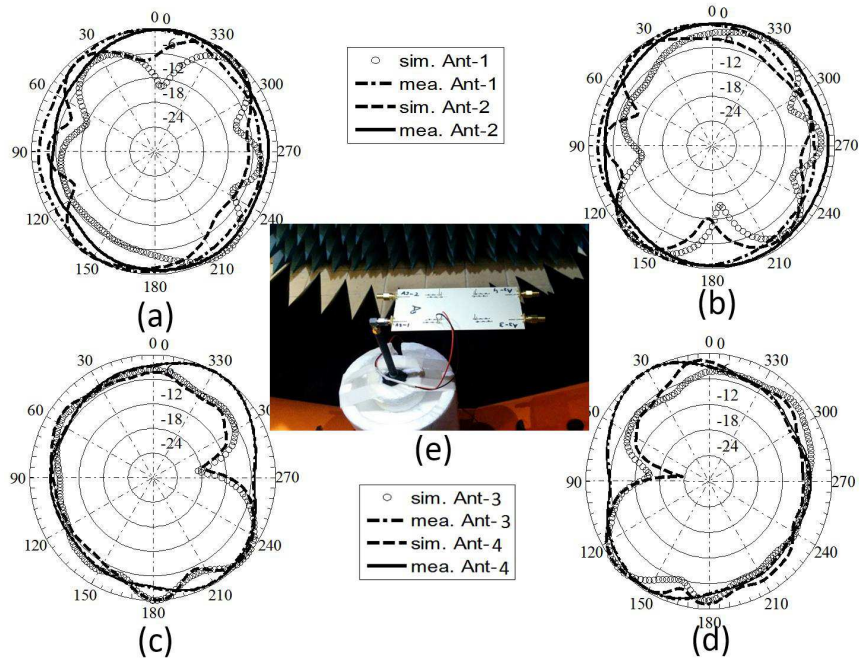


Figure 4.11: Measured and simulated normalized radiation patterns at 1.86 GHz ( $E_{total}$ ) (a) ( $\theta$ -cuts) Ant-1 and Ant-2 at  $\phi = 0^\circ$  (b) ( $\phi$ -cuts) Ant-1 and Ant-2 at  $\theta = 90^\circ$  (c) ( $\theta$ -cuts) Ant-3 and Ant-4 at  $\phi = 0^\circ$  (d) ( $\phi$ -cuts) Ant-3 and Ant-4 at  $\theta = 90^\circ$  (e) Radiation pattern measurement setup.

#### 4.2.4 MIMO Antenna Characterization

The envelope correlation coefficient (ECC) is a measure to show how MIMO channels are correlated. ECC values were computed using the radiation patterns in an isotropic multi-path environment. For good MIMO performance, ECC value should be less than 0.5 [57]. For the given MIMO antenna system, ECC values were calculated at five distinct frequencies. The details of simulated and measured values are given in Table 4.4. It is clear that the given MIMO antenna system satisfies the requirement for good MIMO operation.

The measured peak gain values at resonance frequencies of 1.86 GHz, 2.1 GHz, 2.317 GHz, 2.405 GHz and 2.430 GHz were -2.6 dBi, 0.5 dBi, 2.1 dBi, 2.36 dBi and 2.43 dBi, respectively. The maxima of the radiation pattern of each element is tilted by the GND plane reflector. This helps in reducing the field coupling between various antenna elements. The radiation efficiencies ( $\eta$ ) were also measured for the given MIMO antenna system. The  $\eta$  were measured at resonance frequencies of 1.86 GHz, 2.1 GHz, 2.317 GHz, 2.405 GHz and 2.430 GHz with corresponding values, 51%, 67%, 71.5%, 72% and 73%.

Table-4.3 compares the features of the proposed antenna with other works. It is clear that the proposed design has the minimum number of diodes with a continuous turning range, good gain and efficiency, smallest radius, and maximum number of elements in a small GND size.

Table 4.3: Comparison between the proposed antenna and other works.

Ref.	Ant. Type	Ant. Elem.	Single Elem. Dimensions	GND size (mm <sup>2</sup> )	Freq. bands (GHz) covered	Diodes/Ant.	Peak Gain(dBi)	Max % $\eta$
[106]	annu. slot	1	R = 12.5 mm	50 × 50	2.43, 2.85, 3.33, 4.4	3	2.5, 2.7, 3.6, 5.3	-
[107]	rect. slot	1	30 × 70 mm <sup>2</sup>	70 × 30	1.227, 1.381, 1.575, 2.45	3	2.1, 2.2, 2.1, 2.7	-
[108]	annu. slot	1	R = 11 mm	40 × 40	2.4, 5.2	2	2.1, 2.8	93, 96
[109]	patch-slot	1	18.3 × 50 mm <sup>2</sup>	50 × 40	3.49, 3.36, 3.25, 3.10, 2.49, 2.37, 2.26, 2.18, 2.12 to 3.49	5	0.2 to 4.8	-
[110]	rect. slot	1	29 × 31.3 mm <sup>2</sup>	50 × 50	2.19, 2.35, 2.55, 3.1, 3.25, 3.5	3	3.1, 3.67, 3.76, 5.28, 6.18, 7.35	-
[111]	rect. slot	1	87 × 3.2 mm <sup>2</sup>	130 × 304	1.82, 1.93, 2.10	2	5.7, 5.6, 6	85, 86, 87
[112]	rect. slot	1	26 × 40 mm <sup>2</sup>	52.8 × 62	1.5, 1.6, 1.8, 1.9, 2.24	2	1.7, 2.2, 2.5, 1.75, 1.2	68, 72, 78, 76, 60
[113]	rect. slot	1	25 × 27 mm <sup>2</sup>	25 × 27	2.3, 5.8, 2.3/4.5, 4.51/5.8	3	0.3, 2.5, 0.7/2.3, 1.8/2.8	55, 75, 65/66, 76/64
[116]	rect. slot	2	20 × 23 mm <sup>2</sup>	20 × 46	2.4, 5, 5.5,	2	0.05, 2.9, 2.44	41, 83, 65
<b>Prop.</b>	<b>annu. slot</b>	<b>4</b>	<b>R = 10.1 mm</b>	<b>60 × 120</b>	<b>cont. tun. 1.8 to 2.5</b>	<b>1</b>	<b>-2.6, 0.5, 2.1, 2.36, 2.43</b>	<b>51, 67, 71.5, 72, 73</b>

Table 4.4: Simulated and measured ECC

Simulated ECC				Measured ECC			
f(GHz)	ECC <sub>12</sub>	ECC <sub>13</sub>	ECC <sub>14</sub>	f(GHz)	ECC <sub>12</sub>	ECC <sub>13</sub>	ECC <sub>14</sub>
1.84	0.009	0.093	0.025	1.86	0.079	0.053	0.045
2.0	0.035	0.248	0.035	2.10	0.061	0.131	0.014
2.12	0.062	0.186	0.075	2.317	0.013	0.123	0.022
2.25	0.11	0.16	0.036	2.405	0.045	0.114	0.098
2.41	0.095	0.171	0.091	2.430	0.082	0.081	0.038

### 4.3 Circular Slot (Single/MIMO) Antenna TCM

#### Analysis

The effect of single, 2-element and 4-element MIMO circular slots was investigated on the chassis modes. For this purpose circular slot antenna in Figure 4.10 is considered. The study was done from 1 GHz to 4 GHz. 10 modes were contributing to the radiating BW in this region. To be on the safe side the study was done for 15 modes. All the analysis were done in the presence of RO4350 substrate and the feeding lines. Single slot case is similar to the circular slot case placed at the corner but the design here is complex and consists of two concentric circles. The CM and the MS plots are shown in Figure 4.12 and 4.15(b), respectively. For all the modes we can observe that their is no significant shift in the current maxima distribution of the mode even the current nulls are located at their original places but the current patterns across the whole chassis is little disturbed, observe mode 2 current null. Due to this slight disturbance in the current distribution we observed a little shift in the starting frequencies of the MS curve. We can observe a current concentration across the circular slot for all the modes. Observe the difference in

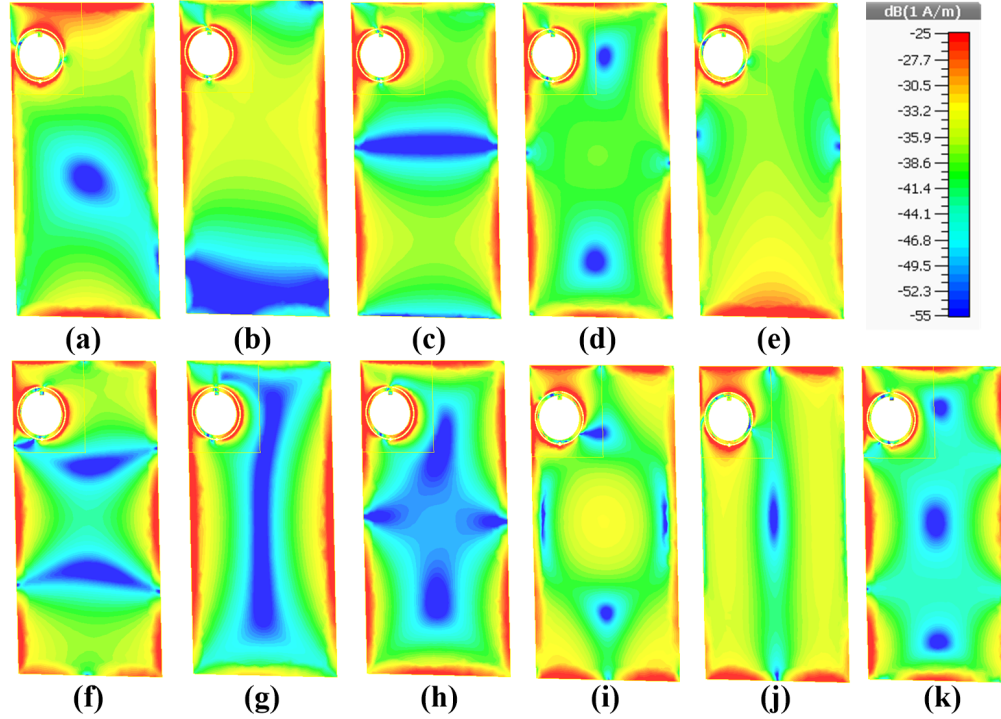


Figure 4.12: Current distribution of the first 11 modes of single circular slot antenna when introduced on chassis, where (a) Mode 1 (b) Mode 2 (c) Mode 3 (d) Mode 4 (e) Mode 5 (f) Mode 6 (g) Mode 7 (h) Mode 8 (i) Mode 9 (j) Mode 10 (k) Mode 11.

the starting frequency of the radiating BW in Figure 4.15 and Table 4.5.

For the two element case, as both slots are located at one edge of the chassis, this will disturb the modal current distribution a lot. The CM current distribution and MS curves are shown in the Figure 4.13 and 4.15(c) respectively. Comparing the CM current distribution with the chassis modes, we can observe that the modes maxima are concentrated across the slot for modes 1 and 2. The nulls in modes 1 and 2 has greatly enhanced and they have affected the current distribution in the lower half of the chassis. For mode 3 the current is concentrated across the slot and the null is shifted towards the slot. Modes 4 to 11 are not affected that much except that their current maximas are little reduced. As expected, the MS curves

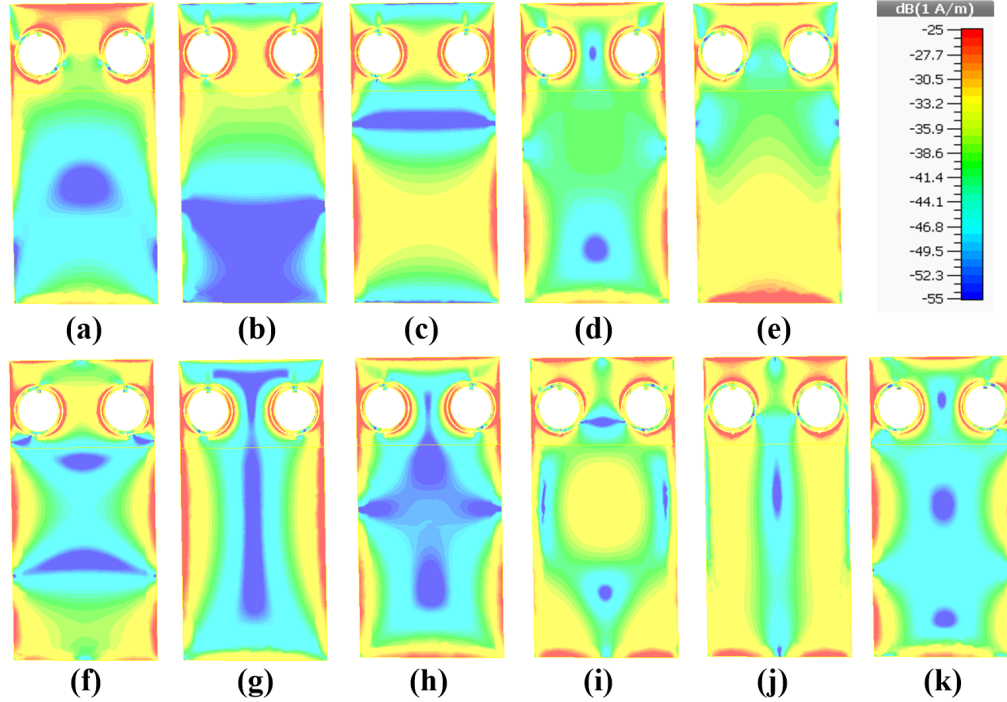


Figure 4.13: Current distribution of the first 11 modes of 2-element circular slot antenna when introduced on chassis, where (a) Mode 1 (b) Mode 2 (c) Mode 3 (d) Mode 4 (e) Mode 5 (f) Mode 6 (g) Mode 7 (h) Mode 8 (i) Mode 9 (j) Mode 10 (k) Mode 11.

were shifted noticeably as compared to chassis only modes as shown in Figure 4.15(c) and Table 4.5.

For the 4-element design case it was expected that as more slots were introduced, the MS curves and the current distribution will be affected significantly. But surprisingly the, 4-element slot case was the least affected. If we observe the CM current distribution in Figure 4.14, we can observe that due to the symmetry of the slots, the current pattern (current maxima and minima location) in general remains the same as compared to chassis only ones. Although the current is concentrated across the slot, but the location of the current maxima and null are not shifted except for M2 (Here the maxima is distributed uniformly across the



edge). Mode 2 is a wideband mode and this shift did not affect its radiating BW. The current maxima concentration seems little reduced but the current pattern is the same as the chassis and by increasing the scale, exactly the same current pattern with similar maxima size can be obtained. The antenna is resonating at 2.45 GHz, so the modes present at 2.45 GHz in the radiating BW are modes 1, 2, 3 and 5. The radiating BW of these modes is totally unaffected as observed in Figure 4.15(d) and Table 4.5. From Table 4.5, we can observe that for a symmetrical design (4-element) case the chassis modes are not affected significantly as compared to the single and 2-element MIMO slot case. For higher order modes we can observe that they are little affected and this can be due to the generation of some higher order resonances.

From all the modes, mode 2 seems to be more preferable because of its wide radiating BW and its coverage of lower band frequencies. If we observe the CM current distribution across the slot (not chassis) of mode 2 in Figure 4.14(b), we have a current null on the top and bottom sides of the circular slot and current maxima across its right and left edges. Remember that in real designs, chassis excitation is not possible and we need to excite the antenna element itself. The excitation of the CM can be done either through capacitive coupling elements (CCE) or inductive coupling elements (ICE). ICE's are placed at the current maxima while the CCE are placed at the electric field maxima (current null or minima). We used CCE excitation via a microstrip beneath the slots that will not alter the geometry as well. Modes 3 and 4 current minima (across the slot)

are exactly at the same location as mode 2. So such CCE excitation of mode 2 will also excite modes 3 and 4. The excitation of multiple modes will deteriorate the performance of the system. Its better to excite single mode of the antenna. Instead of CCE, let us consider ICE excitation of mode 2 but the problem still persists because modes 2, 3 and 4 current maxima also lies at the same location. Now we need to search for another preferable mode. Mode 1, can be a viable option because of its presence of its radiating BW at lower frequencies but mode 5 and 9 have current maxima and null are present at the same location as mode 1. So we stick to the CCE excitation of mode 2. This method of excitation generates a combination of modes on the surface of the antenna and the GND thus it degrades the system performance in terms of good matching and cause narrow BW antennas. That is why slot antennas are narrow band.

From the CM current distribution of the single element and 4-element MIMO cases shown in Figures 4.12 and 4.14, respectively, we can observe that the current concentration lies across the slot and we have to deal with more modes in our desired BW. ECC evaluation from TCM perspective will be more involved due to the excitation of multiple modes that will contribute to the radiated fields (all previous works used single chassis modes and thus were easily able to map the mode currents to a single radiated field pattern). Here we have used the normal MIMO antenna designing concept that is to place the antenna as far as possible from one another on the chassis so that we can get acceptable isolation and envelope correlation coefficient (ECC). So, the best possible locations are the

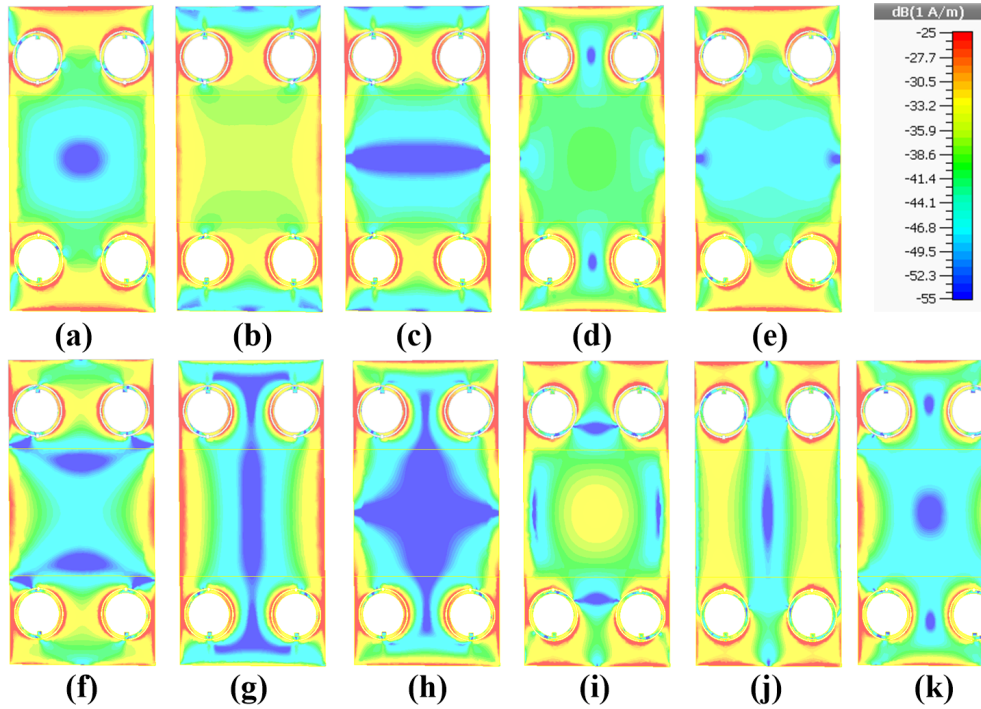


Figure 4.14: Current distribution of the first 11 modes of 4-element circular slot antenna when introduced on chassis, where (a) Mode 1 (b) Mode 2 (c) Mode 3 (d) Mode 4 (e) Mode 5 (f) Mode 6 (g) Mode 7 (h) Mode 8 (i) Mode 9 (j) Mode 10 (k) Mode 11.

corners of the chassis.

## 4.4 Reconfigurability using TCM

An annular ring was introduced to install the capacitor that can make the antenna frequency reconfigurable. To analyze the mechanism behind the frequency reconfigurability with the help of TCM, we analyzed the circular slot antenna in Figure 4.7 with different capacitor values. Initially we started with single slot antenna with a varactor installed. TCM analysis were performed for different values of capacitance and conclusions were drawn. There is no difference in frequency

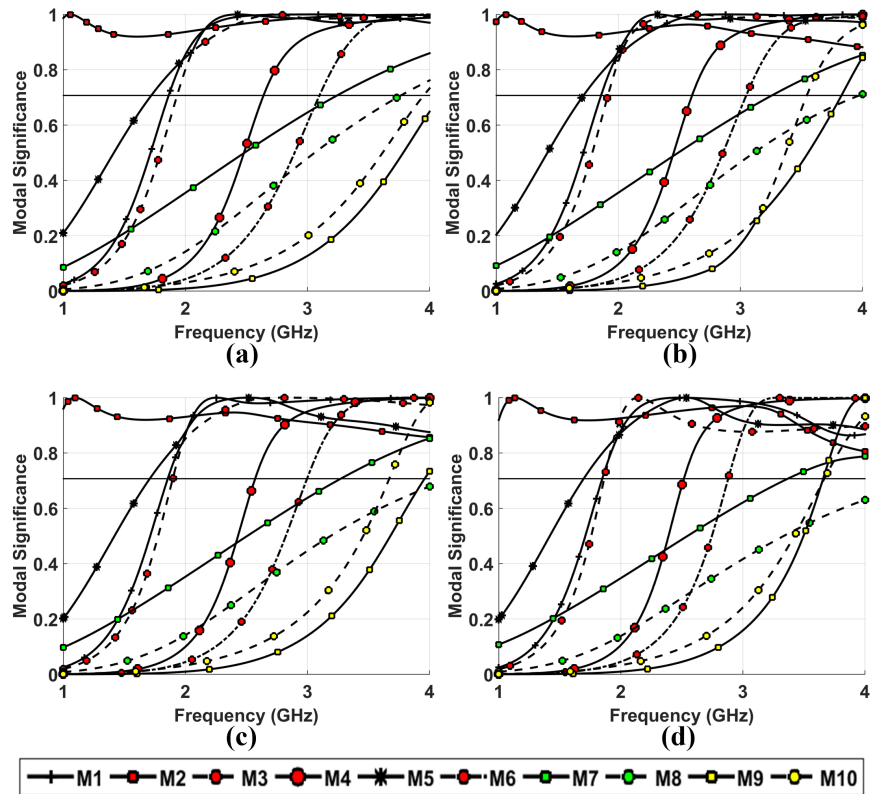


Figure 4.15: Modal Significance curves: (a) Ground plane or chassis, (b) Single circular slot antenna, (c) 2-element circular slot antenna, (d) 4-element circular slot antenna.

Table 4.5: Comparison of MS curves to observe the effect of multiple slots on chassis modes. WB refers to whole BW, which is from 1 to 4 GHz.

Chassis modes		Circular slot Antenna		
		Single element	2 element	4 element
Mode	F_start	F_start	F_start	F_start
	GHz	GHz	GHz	GHz
M1	1.86	1.86	1.86	1.86
M2	WB	WB	WB	WB
M3	1.9	1.921	1.89	1.89
M4	2.63	2.6	2.55	2.56
M5	1.72	1.71	1.71	1.71
M6	3.09	3.04	3	2.91
M7	3.26	3.24	3.28	3.36
M8	3.77	3.95	>4	>4
M9	>4	3.82	3.96	3.65
M10	3.93	3.54	3.67	3.67
M11	3.57	3.95	3.48	3.36

reconfigurability for a single or MIMO antenna cases, but to validate our results for a single slot antenna regarding frequency reconfigurability and to explain the frequency reconfigurability in a MIMO configuration, we used the same procedure for the MIMO case as well by taking different values of capacitors and performing TCM analysis step by step.

The modal characteristic currents and the MS plots of the chassis shown in Figures 4.5 and 4.15(a) are taken as a reference. All the cases for single or MIMO configurations with different values of capacitance are compared against them. The MS curves of single/ 4-element MIMO circular slot antenna with 2.0 pF and 5.0 pF capacitor installed are shown in Figure 4.16.

We can observe from Figure 4.16, that modes 4,6 and 7 start contributing to the radiating BW after 2.45 GHz, which is out of our desired BW of interest that is why modes 4,6 and 7 if not studied will not affect our analysis but we included them in order to observe the effect of this changing capacitance on the higher order modes. We can observe from Figure 4.16 that Mode 2 is contributing in the whole band of interest; all other modes contribute in specific other bands. After 1.96 GHz, 4 modes are contributing to the radiating BW. Between 1.73 and 1.86 GHz only 2 modes are contributing while below 1.73 GHz only one mode (mode 2) is contributing to the radiating BW. From the MS plots we observe that the first four modes have wide ( $> 100\%$ ) radiating BW as shown in Figure 4.16. Wide BW antennas can be obtained if we are able to excite a single mode purely.

The summary of analysis with different capacitor values for single and 4-

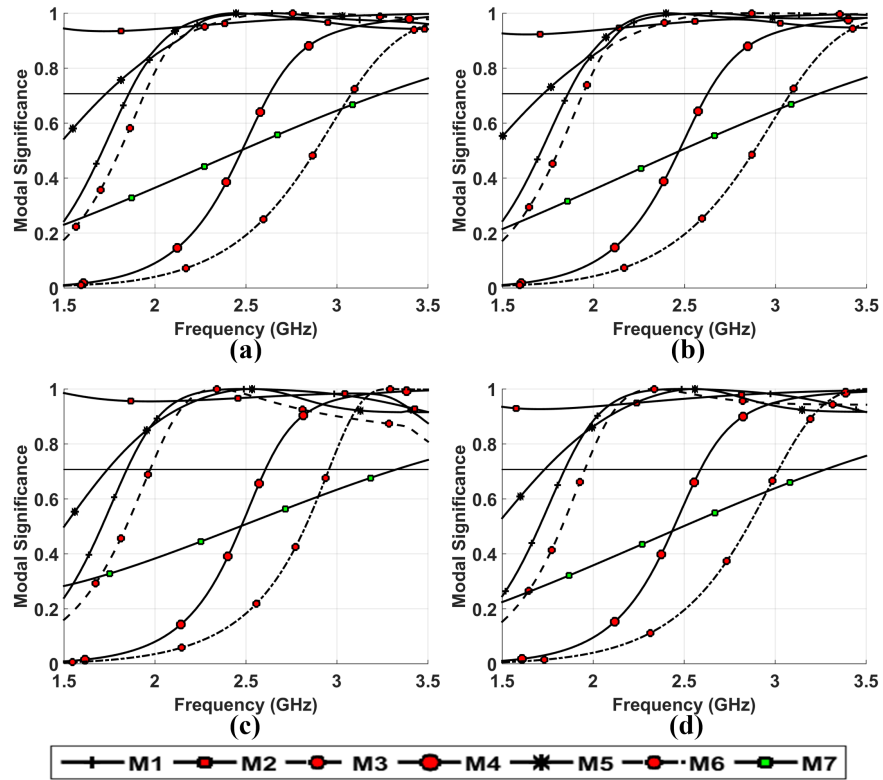


Figure 4.16: Modal Significance curves: (a) Single Circular slot antenna with 2.0 pF capacitor, (b) Single Circular slot antenna with 5.0 pF capacitor, (c) 4-element MIMO Circular slot antenna with 2.0 pF capacitor, (d) 4-element MIMO Circular slot antenna with 5.0 pF capacitor.

element MIMO designs is shown in Table 4.6. In the Table 4.6, Table 4.6, Cap and  $M_x$  : refers to capacitance of capacitor and mode- $x$  respectively. Starting Frequency refers to the frequency at which mode  $x$  starts contributing to the radiating BW,  $WB$  refers to whole bandwidth that is assumed to be from 1  $GHz$  to 4  $GHz$ . To be brief, the results of the 2-element MIMO design are not shown. If we look at the modes (M1,...,M7) in Table 4.6, we can observe that the installation of different values of capacitance have not affected the modes significantly. As the CM have wide BW, these little variations do not affect the radiating BW.



Table 4.6: Comparison of MS plots for reconfigurability analysis of first 7 modes analyzed at their respective resonance frequencies.

Single/ MIMO	Cap (pF)	M1	M2	M3	Starting Frequency						
					M4	M5	M6	M7			
Single	1.33	1.86	WB	1.96	2.6	1.73	3.05	3.25			
Single	1.5	1.86	WB	1.96	2.63	1.73	3.07	3.25			
Single	2	1.86	WB	1.96	2.63	1.73	3.07	3.25			
Single	3	1.86	WB	1.94	2.63	1.73	3.07	3.25			
Single	5	1.86	WB	1.94	2.63	1.73	3.07	3.23			
Single	10	1.86	WB	1.94	2.63	1.73	3.07	3.23			
Single	15	1.86	WB	1.94	2.63	1.73	3.07	3.23			
MIMO	1.33	1.86	WB	1.96	2.58	1.73	2.98	3.33			
MIMO	1.5	1.86	WB	1.96	2.58	1.73	2.98	3.33			
MIMO	2	1.86	WB	1.96	2.58	1.73	2.99	3.33			
MIMO	3	1.86	WB	1.95	2.58	1.73	3.01	3.23			
MIMO	5	1.86	WB	1.95	2.58	1.73	3.01	3.26			
MIMO	10	1.86	WB	1.95	2.58	1.73	3.01	3.26			
MIMO	15	1.86	WB	1.95	2.58	1.73	3.01	3.26			

We already observed that with changing the capacitance, there is no change in the MS plots as shown in Table 4.6 and Figure 4.16, but in a real designs, with changing capacitance we are able to sweep the frequency. CM are calculated using the Method of moments (MoM). We can observe that the modes depend on the impedance operator, the addition of a single lumped component (discrete reactive loading) basically changes the impedance at a single point (very few entries in the impedance matrix) on the antenna and does not affect the impedance matrix in general, that is why we didn't observe any significant change in the MS plots. Frequency reconfigurability from our extensive observations is nothing new, but the operation of the antenna in the same mode with the varactor specific value is only affecting the input matching at the different frequency portions of the same mode. The conclusions in [87] are only applicable to wire antennas and the mode changes were mainly due to the change (cut) in the wire structure and not only the reactive loading.

The main reason behind having narrow band slots is the high mismatch at the feeding. The changing value of the capacitance only improves in matching at different frequency bands of the same mode and that is why frequency reconfigurability is achieved. So, we are basically looking at the same mode but with different feeding/matching values. We can also conclude that if a mode is excited purely and the input matching circuit is defined properly then the same antenna will be able to provide very large BW.

## 4.5 Conclusions

In this chapter, it was found that the introduction of circular slots do not generate any new modes but the obtained ones are the chassis modes that are slightly modified due to the presence of the slot. Different chassis modes are affected based on the location of slot on the chassis. The size of a slot plays an important role in affecting the radiating BW of the chassis modes. Different slot shapes were also investigated. It was found out that a circular slot (at the center of the chassis) size to ground ratio below  $\frac{1}{9}$  will not cause any significant changes in the radiating BW.

Based on the analysis, a 4-element MIMO annular slot antenna is proposed. The proposed design is a low profile compact antenna design with very wide frequency tuning. Frequency reconfigurability is achieved by optimally placing varactor diodes on one side of each annular slot. The proposed design is tuned over a wide-band from 1.8 GHz to 2.45 GHz, covering several well-known wireless standards. Only single varactor diode is utilized in achieving this wide band operation. Moreover, the proposed design is suitable to be used for wireless handheld devices and mobile terminals in cognitive radio applications. The effect of multiple circular slot radiators was investigated and it was observed that as long as there is symmetry in the antenna design (4-element MIMO slot) the MS plots are not affected significantly when compared to a pure chassis case, single element and 2-element cases.

The physical principle behind frequency reconfigurability was also investigated.

It is found that varactor diodes used did not alter the MS plots but helped in improving the impedance matching at different frequency bands of the same mode.

## CHAPTER 5

# ISOLATION ENHANCEMENT BETWEEN MIMO ANTENNAS USING TCM

*“The world which you create (through your efforts and ideas) is yours  
Not these stones and bricks (the existing world) which you are aiming at.”*

---

— ALLAMA IQBAL

High data rates in current and future generations of wireless terminals (without increasing the frequency or power levels) can be achieved by installing multiple antennas at the base station and terminal sides. The compactness of the terminals may degrade the performance of MIMO systems due to high port and field coupling which affect the channel capacity, BW and efficiency of the system [57]. Many methods are proposed in literature to improve port isolation with minimal effect on the channel capacity, BW and efficiency of the system. Isolation can be improved

by the use of electromagnetic band-gap structures and meta-surfaces [163–165], decoupling networks [166], neutralization line technique [167, 168], parasitic elements [169, 170], optimization of the antenna system configuration [171, 172], introducing planar modified mushroom structures [173, 174] and the use of defected ground structures (DGS) [175–185]. Among all the aforementioned port isolation enhancement methods, DGS is the least complex and expensive.

Several DGS shapes were used between 2 and sometimes 4-element MIMO antenna systems to improve isolation such as using periodic S-shapes [175], T-shapes and slot lines [176], rectangular rings and slots [177, 178], ground (GND) slits [179–183] and arcs [184, 185]. The main problem in the DGS method for enhancing isolation is determining its shape, size and position along with the large amount of optimization time involved, and until now, no systematic design method is available.

For frequencies below 1 GHz, the chassis (GND plane) acts as the main radiator. That is why severe coupling is observed in MIMO configurations because all antennas are coupled via the chassis. Isolation enhancement was also addressed from the perspective of TCM. From TCM analysis, the first mode has electric field maximas at the edges of the chassis, while minimas are at the center. Any electrical antenna located at the edge will excite the chassis effectively while those located at the center will not. For a monopole located at the edge and a planar inverted-F antenna (PIFA) located at the center an isolation enhancement of 5 dB was achieved without using any isolation scheme as compared to placing them

at the edges of the chassis [186]. The placement of the antenna at the center of the chassis is impractical, that is why it was observed that instead of placing two electrical antennas at the edges of the chassis, an electric and magnetic ones will have better isolation. At the edge, the magnetic fields have minimas that is why electric and magnetic antennas placed at the edge will have better isolation [187]. In [186, 187], only the behavior of the first mode using TCM was examined (low frequencies i.e. less than 1GHz) and the analysis were based on it and no DGS behavior was investigated.

In this chapter, We have used TCM to analyze the behavior of a DGS (never done before in the literature) in order to give an insight into the physical phenomena of isolation enhancement in MIMO antennas and to develop a systematic approach that can predict whether a DGS for a particular design can enhance the isolation or not. Our major contributions in this chapter are:

- Using TCM, an explanation to the physical behavior of DGS is provided. CM current distribution and MS curves are used for the comparison of modes. All modes present in the impedance BW region are considered for comparison while previously in [186, 187] the comparison was performed only for one mode. In addition the DGS behavior or its placement were not investigated before.
- To develop a systematic approach that can predict whether a DGS can enhance the isolation between MIMO antenna elements or not. We consider three real antenna designs from the literature with different element types

and characteristic (i.e. PIFA and monopole like) while previous works focused on chassis modes and their excitation.

- An average of 11 dB of isolation enhancement is achieved in three different designs considered.
- The effect of small antenna elements on the chassis modes is also investigated. It is observed that different antenna types affect the CM and MS differently which is usually overlooked in literature.
- For the first time, we compare the real/total currents on the surface of antennas with the CM currents and it is verified that real currents are approximately the weighted sum of the modal currents, which means that it is difficult to have isolated modes excited with real antenna elements. In the presence of real antenna elements, the chassis modes are significantly affected and we cannot rely only on the CM of the chassis.
- The two printed designs investigated include the effect of the dielectric substrate when TCM was performed.

The rest of the chapter is organized as follows. Section 5.1 describes the antenna designs and their analysis using TCM. Section 5.2 describes the behavior of DGS as well as discusses the method developed for isolation enhancement. MIMO antenna parameters are analyzed in section 5.3, while in section 5.4 the chapter is concluded.



## 5.1 Antenna Design And Analysis Cases

For the analysis purposes of the DGS using TCM, we have considered one wire [181] and two printed [183, 184] based MIMO antenna designs of different types: PIFA and monopole. Performing the analysis on different designs will help us in generalizing our findings. For a fair comparison, the chassis size is the same for the printed antenna designs, that is  $100 \times 60 \text{ mm}^2$ , also the targeted BW is 150 MHz (2.15 – 2.33 GHz).

TCM analysis was performed with a series of cases, starting from a rectangular chassis representing the GND plane of a standard smart phone, chassis with a single cut (the cut below the antenna), chassis with double cuts and four cuts in the ground plane (for 2 and 4-element MIMO designs), chassis with a single antenna, 2-element MIMO connected along the width and then along the length of the chassis and finally the 4-element MIMO design. The isolation between the antennas was enhanced by properly studying the modal behavior. First, modes were identified in the desired band of interest and then a DGS was placed to block the modes that were causing high coupling. After the placement of the DGS, the antennas were again analyzed using TCM and we observed that the modes (causing high coupling) were not contributing in the desired BW of interest.

To be brief, we will present the main cases from our TCM analysis which are: the rectangular chassis, 4-element PIFA and Monopole based MIMO designs as well as the cases when the DGS was introduced. All the analysis was conducted using CST electromagnetics package.

Since the chassis is the same in both designs, the CM current distributions at 2.2 GHz on its surface as well as the MS curves for the first 6-modes on the rectangular chassis are plotted in Figures 5.1 and 5.2, respectively. Figure 5.1 shows the modes on the chassis, where high current locations are marked with big red arrows. The black circular dots show the current null or current minima location while the thin violet arrows represent the current distribution on the surface of the chassis. The MS is an important figure of merit that represents the normalized amplitude of current modes and determines the radiation performance of modes. It depends on the size and shape of the object. The range of frequencies for which the power radiated is not less than one half the power radiated by the mode at resonance is known as the radiating BW and it is marked by the 0.707 point on the MS curves [23]. The impedance BW is calculated in the presence of the excitation sources and is the range of frequencies for which the antenna has good impedance matching ( $VSWR < 2.0$ ). Only 4 modes (1-4) are contributing in the desired impedance BW. These modes are the ones that we will compare against in the analysis to come.

### 5.1.1 PIFA based 4-element MIMO Antenna Design

The geometry of the 4-element MIMO PIFA like design is shown in Figures 5.3(a) and 5.3(b). The antenna was designed on an FR4 substrate with a relative permittivity ( $\epsilon_r$ ) of 4.0, loss tangent of 0.02 and thickness of 0.8 mm. The total design area was  $100 \times 60$  mm<sup>2</sup>. Figure 5.3(c) shows the top view of the fabricated

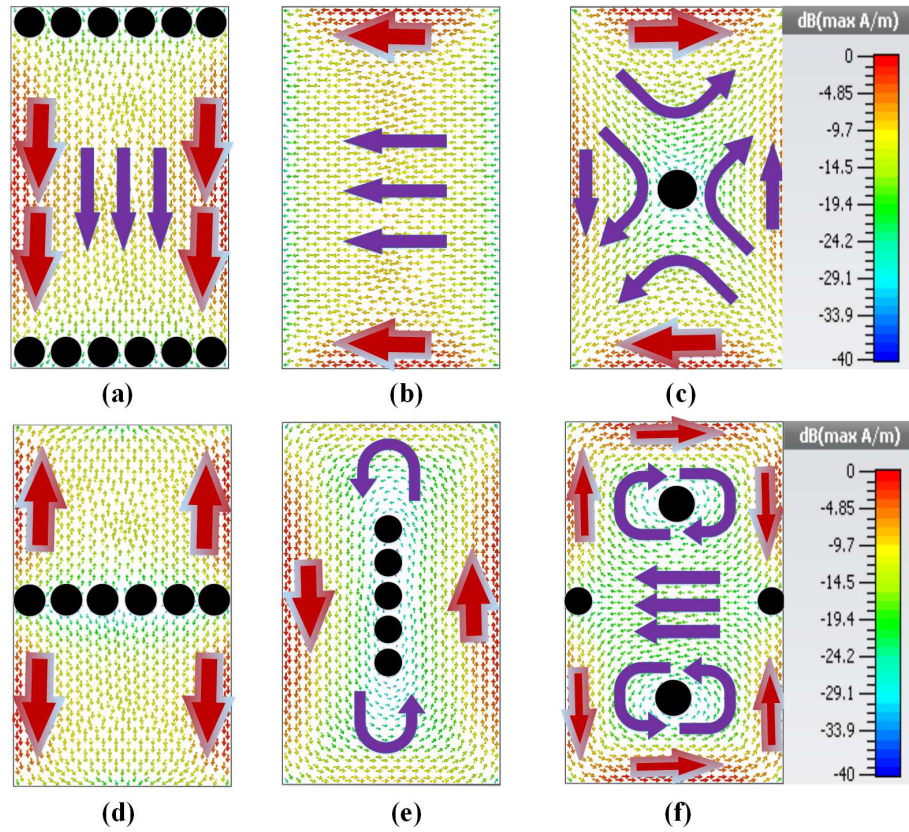


Figure 5.1: Current distribution of the first six modes of the chassis in the presence of an FR-4 substrate at 2.20 GHz, where (a)-(f) represents mode 1 to 6 respectively.

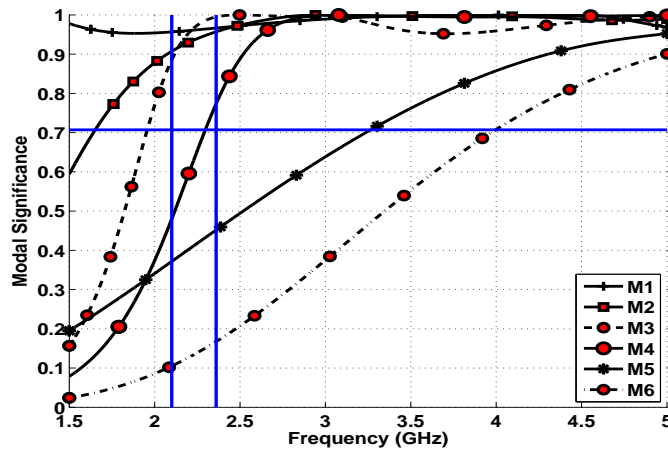


Figure 5.2: Modal Significance curves of the ground plane or chassis.

design containing the 4-elements PIFA like MIMO antenna system while Figure 5.3(d) shows the bottom layer containing the ground for all the antenna elements. The 3D view of the PIFA is shown in the Figure 5.4(a), where SP represents the shorting post. Three prototypes were made, without DGS, with one DGS and with 2 DGS structures. Only the final prototype is shown for brevity.

The fabrication, development of the antenna prototype and port measurements were performed at the Antennas and Microwave Structure Design Lab (AMSDL) at King Fahd University of Petroleum and Minerals (KFUPM) using an LPKF S103 machine and an Agilent N9918A Vector Network Analyzer (VNA). The gain patterns and efficiencies were measured using a SATIMO Starlab anechoic chamber at Microwave Vision Group (MVG), Italy.

The measured impedance BW ( $VSWR < 2$ , -10 dB) of the design without DGS slots was 180 MHz ranging from 2.153 to 2.333 GHz (Figure 5.3(e)) while a measured isolation of 16.25 dB was achieved between Ant-1 and Ant-3 as shown in Figure 5.3(f). To improve the performance of the system we need to enhance the isolation.

TCM was applied to the 4-element PIFA like MIMO design including its substrate as shown in Figure 5.3. The modal current distribution on the surface of the chassis at 2.2 GHz and the MS curves are shown in Figures 5.5 and 5.6, respectively. One can clearly observe from Figures 5.5 and 5.6 that it is not only the chassis that decides the CM behavior. If we observe the current distribution we can see that the current maximas are now shifted towards the antenna

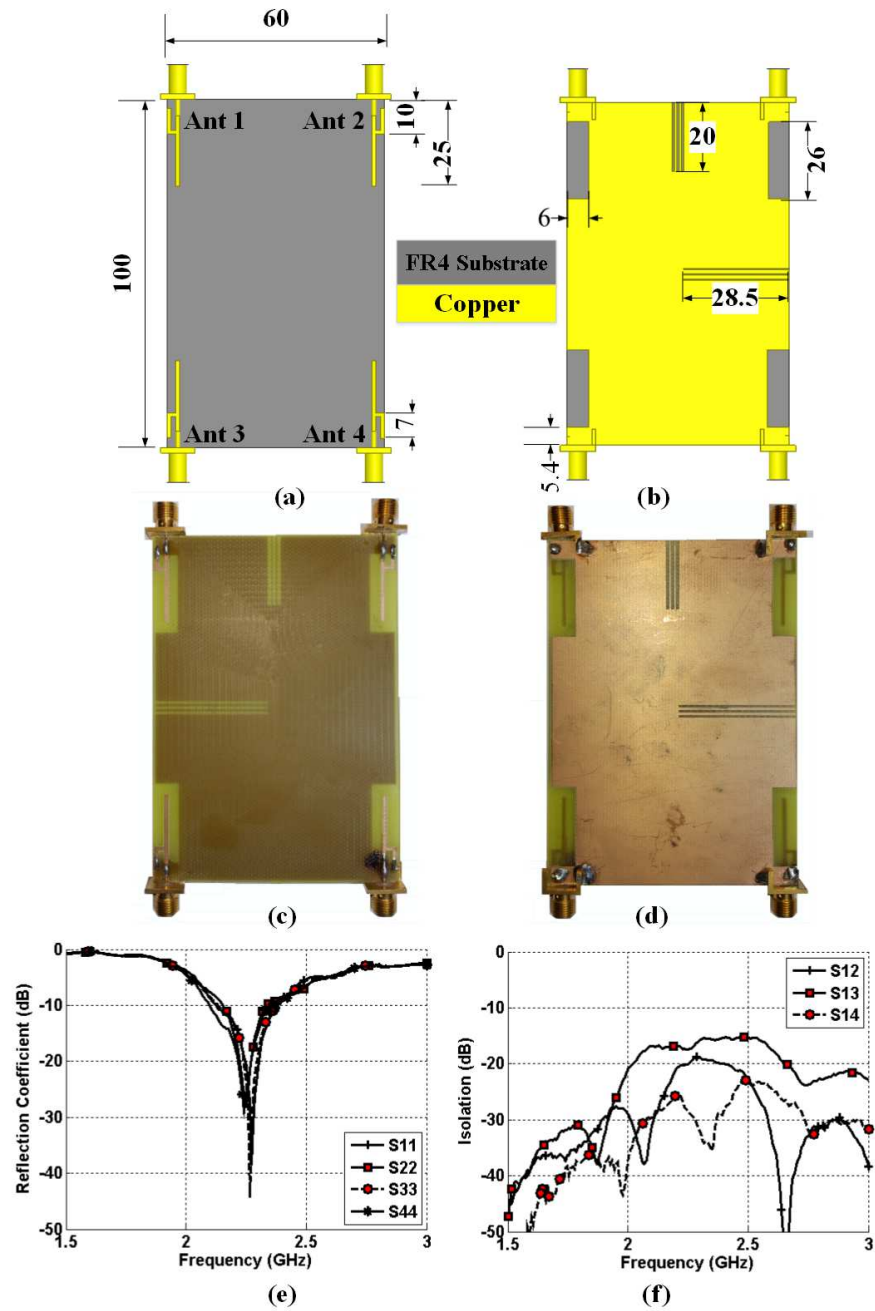


Figure 5.3: Geometry of the 4-element MIMO PIFA design (a) top view, (b) bottom view with DGS, all dimensions are in mm (c) fabricated prototype top view, (d) fabricated prototype bottom view with DGS, (e) measured reflection coefficient without DGS, (f) measured isolation without DGS.

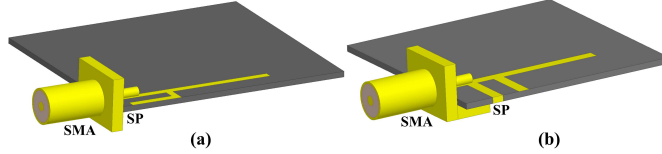


Figure 5.4: 3D view of single element (a) PIFA, (b) monopole.

elements, but the general pattern of chassis modes are not affected significantly except modes 1 and 4 where the null position has shifted. The CM current distribution was significantly reduced on the chassis that is why we showed it on a 50 dB scale. The current reduction on the chassis and the shifting of the current maxima to the antenna elements shows that the antennas are playing a major role in the radiation mechanism. If we look at the MS curves, we observe that the addition of these antennas has significantly affected the modes in terms of the radiating BW as observed in Figure 5.6. The antennas have limited radiating BW of modes 1 and 3 to 3.2 GHz. Modes 2 and 4 start contributing to the radiating BW at around 2.18 GHz which is exactly the same point where our measured BW starts, this is an indication that one or both can be excited on the surface of the antenna by the real excitation/source.

### 5.1.2 Monopole Based 4-element MIMO Design

The geometry of the 4-element MIMO Monopole like design is shown in Figures 5.7(a) and 5.7(b). The 3D view of the Monopole is shown in the Figure 5.4(b), where SP represents the shorting post. The antenna was designed with the same substrate properties as the PIFA one. The fabricated prototype with the DGS is

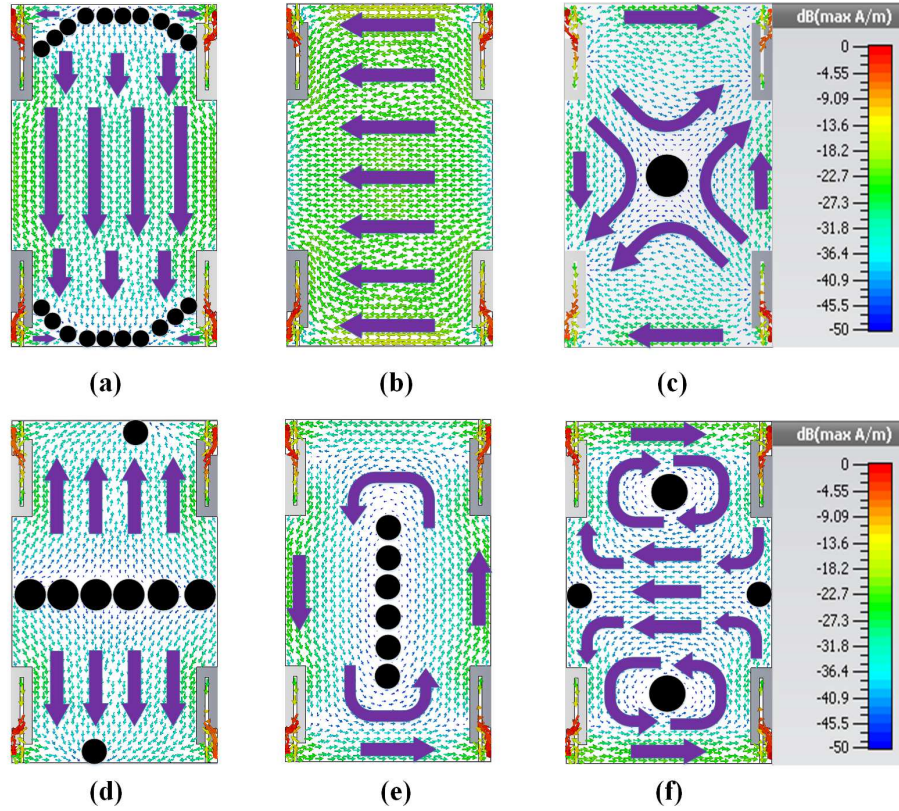


Figure 5.5: Current distribution of the first six modes of the 4-element MIMO PIFA in the presence of an FR-4 substrate at 2.20 GHz, where (a)-(f) represents mode 1 to 6 respectively.

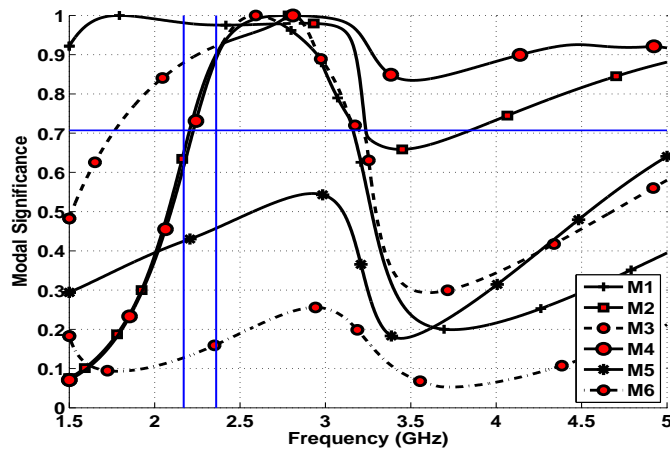


Figure 5.6: Modal significance curves of the 4-element PIFA based MIMO in the presence of the FR-4 substrate.

shown in Figures 5.7(c) and 5.7(d) for the top and bottom views respectively.

The measured impedance BW without the DGS was 165 MHz ranging from 2.085 to 2.25 GHz as shown in Figure 5.7(e), while the minimum measured isolation was 15.5 dB as shown in Figure 5.7(f) between Ant-1 and Ant-3. To improve the isolation we will use a DGS.

Like the PIFA design, TCM was also applied to the 4-element MIMO Monopole like design including the substrate. The modal current distribution at 2.2 GHz and MS curves are shown in Figure 5.8 and 5.9, respectively. We can clearly observe that the antennas in both designs affected the CM and MS curves differently. This verifies that small antenna elements have a noticeable effect on the CM. For the 4-element MIMO Monopole like antenna system, the CM are affected except for mode 2 current distribution which seems to be totally unaffected. Mode 3 is severely affected and is no longer contributing to the radiating BW in the desired impedance BW of interest while mode 6 is contributing at lower frequencies. Mode 1 has now a limited radiating BW. Only modes 1 and 2 are contributing to the radiating BW in the desired impedance BW of interest.

## 5.2 Defected Ground Structure Analysis

### 5.2.1 PIFA based MIMO Design

We can observe from Figure 5.6 that modes 1, 2, 3 and 4 are contributing to the radiating BW in the desired impedance BW of interest while modes 5 and 6 are



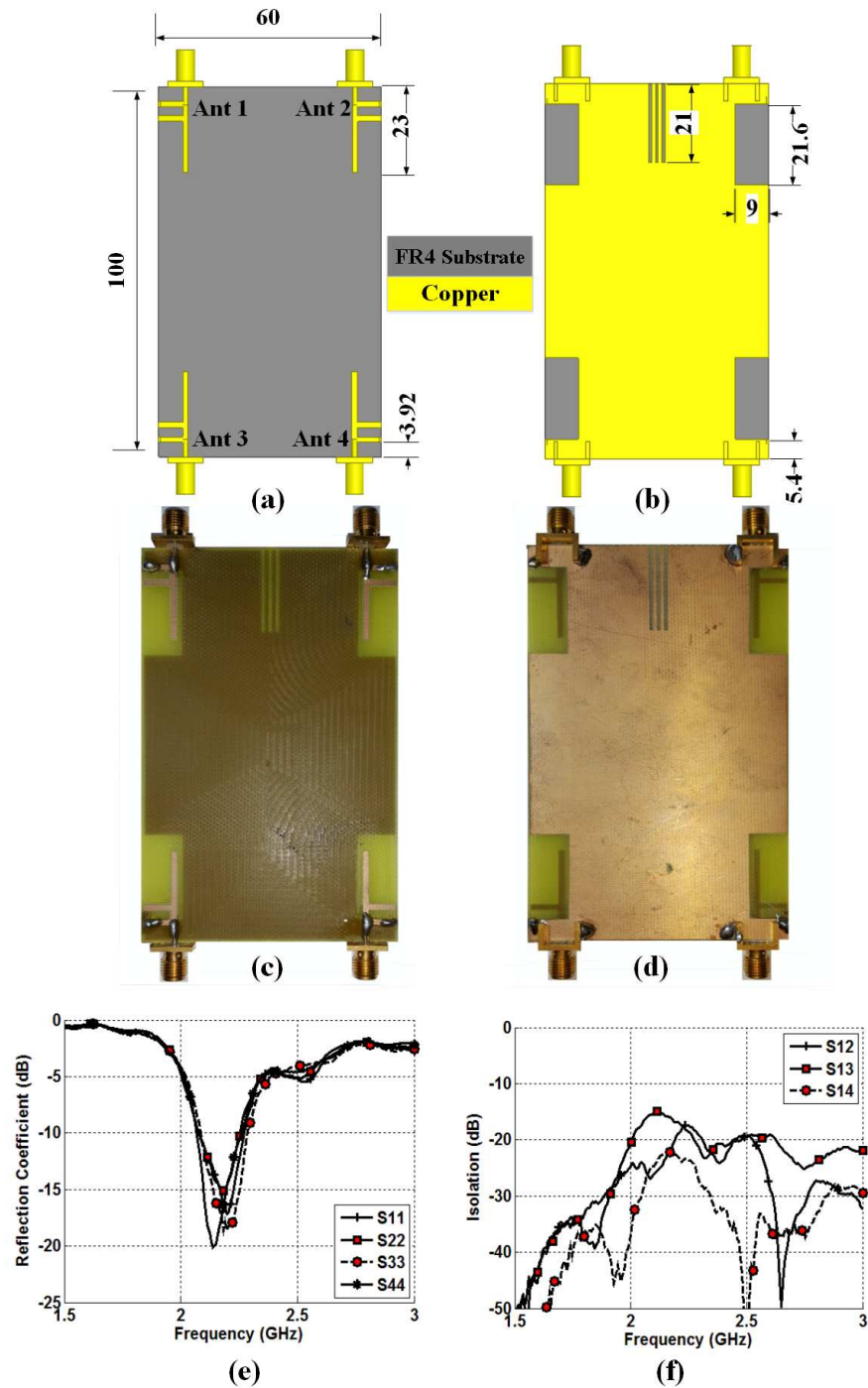


Figure 5.7: Geometry of the 4-element MIMO PIFA design (a) top view, (b) bottom view with DGS, all dimensions are in mm (c) fabricated prototype top view, (d) fabricated prototype bottom view with DGS, (e) measured reflection coefficient without DGS, (f) measured isolation without DGS.

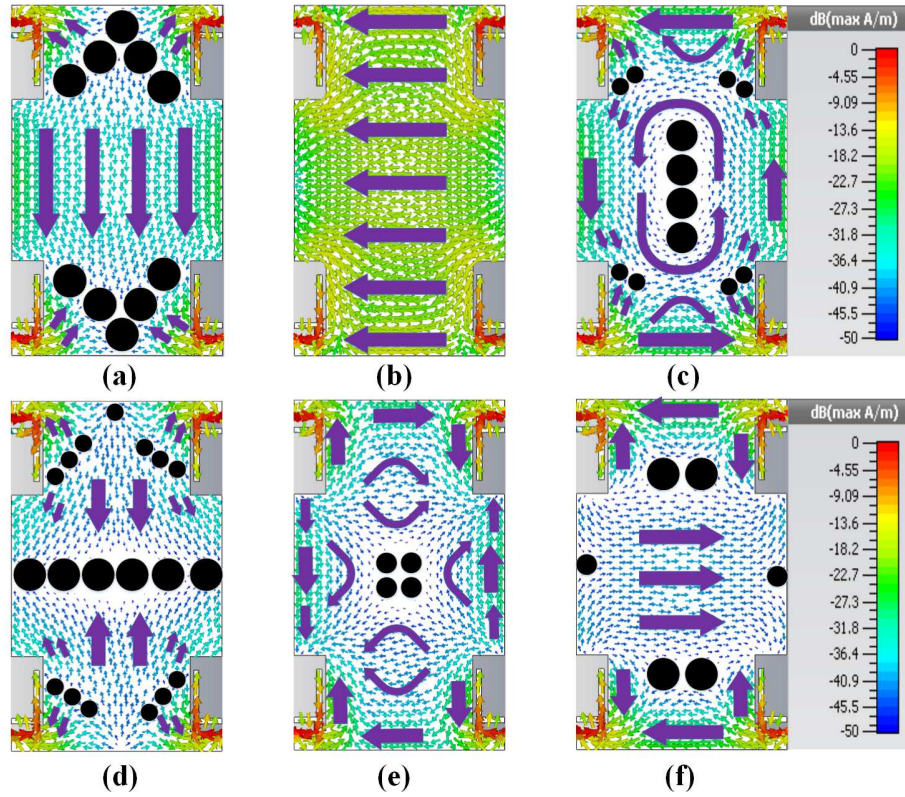


Figure 5.8: Current distribution of the first six modes of the 4-element MIMO monopole in the presence of an FR-4 substrate at 2.20 GHz, where (a)-(f) represents mode 1 to 6 respectively.

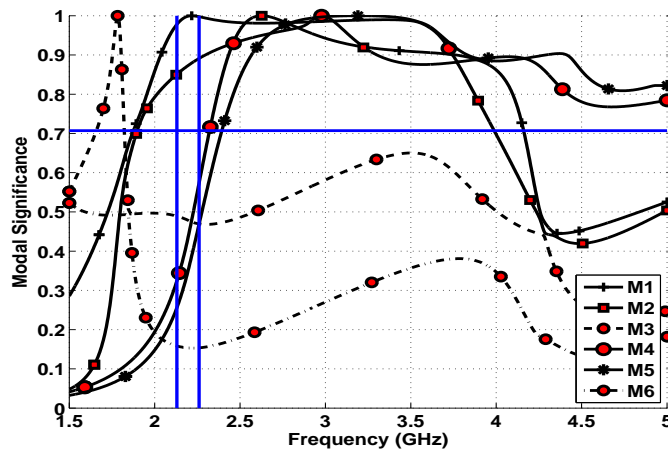


Figure 5.9: Modal significance curves of the 4-element MIMO monopole in the presence of FR-4 substrate.

not contributing at all. Moreover based on the current directions, we can observe that mode 1 is neither contributing to the coupling between the horizontal or vertical antennas (due to the presence of current nulls) while mode 3 is causing the coupling between the antennas connected on the longitudinal side (Ant1-Ant3) as well as the horizontal side (Ant1-Ant2) and modes 2 and 4 are causing the coupling between Ant-1 and Ant-2. Modes 2 and 4 are not contributing to the coupling between the Ant1 and Ant3.

The total current on the surface of the antenna and chassis is shown in Figure 5.10(a). It can be clearly observed that the total current on the surface of the antenna seems to be the combination of modes 1 and 4 in particular, that is why we observe a current null (blue spot) near the antennas (representing mode 1 because other modes do not have such a null at this location) and in the middle of the chassis (representing mode 4 because other modes do not have such a null at this location) while modes 2 and 3 seem to be excited less effectively because mode 2 current is uniform (Figure 5.5(b)) and there is no uniformity in Figure 5.10(a).

From the isolation plot shown in Figure 5.3(f) the isolation is worst between the antennas 1 and 3, so we need to improve it. The concept of placing the slots is simple and straight forward. The slot should be placed at a location such that it blocks the coupling modes, but at the same time it should not affect or block the non-coupling modes. The idea is simple if we have two modes in the desired impedance BW where one is a coupling mode and the other is a non-coupling one

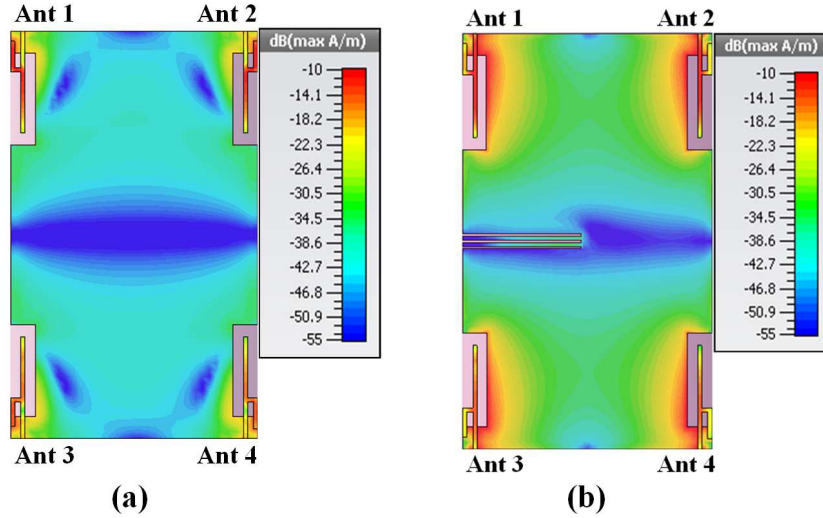


Figure 5.10: Current distribution on the surface of the 4 element MIMO PIFA antenna at 2.2 GHz when all antenna's are excited (a) without any DGS, (b) DGS between Ant-1 and 3.

and they can be separated where one can be blocked without affecting the other.

But it gets complicated whenever we have to deal with more modes.

The only mode that is contributing to the coupling between Ant1 and Ant3 is mode 3. Mode 3 is behaving as a coupling mode so we need to block it in order to improve the isolation but at the same time we should be careful that the DGS to be introduced does not affect the non-coupling modes (mode 1 and 4) significantly. Both modes 1 and 4 have got different current distributions, so we need to place the DGS at a location with minimum non-coupling mode disturbance. There can be three possibilities, current null location of mode 4 (will not affect mode 4 but will affect mode 1), or mode 1 (will not affect mode 1 but will affect mode 4), or any other location (will affect modes 1 and 4) on the chassis. The current null location of mode 1 is very close to the edge of the chassis so placing any slot at this location will completely isolate the antennas and it will seem that the antennas

are operating with different ground planes which is not acceptable. If we place the slot at any other location, it will affect both the non-coupling modes of mode 1 and 4 and it will severely affect the impedance BW. So, the optimum position to block mode 3 seems to be the current null location of mode 4 (which is at the middle of chassis), placing a DGS at this location will block mode 3 but will not affect modes 4 and 2, while mode 1 will be slightly affected. For mode 1, its radiating BW covers up to 3.2 GHz, so introducing a discontinuity in the current path will affect its radiating BW.

A DGS structure consisting of single slit line could not meet the criteria that is why a simple DGS structure consisting of three slit lines was chosen so that the concept can be proved and can be generalized to any design irrespective of its antenna type. In general, the width, length and inter-slot separation are optimized for a certain center frequency of interest. This will also help the designer to spend minimum time on optimization. The DGS was introduced in the center of the chassis between Ant 1 and 3 (Figure 5.3(b)). The total size of the DGS was  $28.5 \times 3.5 \text{ mm}^2$  with an arm length of 28.5 mm, slit width of 0.5 mm and slit separation of 1 mm.

Before showing the improvement in S-parameters, let us discuss how the DGS affects the CM. The CM current distribution at 2.2 GHz and the MS plots are shown in Figures 5.11 and 5.12, respectively. The green thin arrows show the current distribution created due to the introduction of DGS. The black dots show the current null or current minima location while the violet thin arrows repre-

sent the current distribution on the surface of chassis. Modes 2 and 4 current distributions are totally unaffected because the DGS structure is parallel to the current direction (mode 2) or its lying at the current null (mode 4). Modes 1 and 3 current patterns are affected. The DGS generates a current distribution that is opposite to the original current flow as shown in modes 1, 3 and 5, thus reducing the coupling between the antenna elements. The interesting part is that mode 3 is no longer contributing in the desired radiating BW of interest and is shifted to lower frequencies with very narrow radiating BW as shown in Figure 5.12. Mode 1 has greater than 100 % radiating BW starting at 1.87 GHz. In the desired BW of interest, it is not affected. Mode 1 radiating BW was affected (compared to Figure 5.6) but in our BW of interest its not affected significantly. Modes 5 and 6 are also affected. Mode 6 radiating BW is shifted to lower frequencies while mode 5 is contributing to the radiating BW after 2.42 GHz. The isolation between the antenna elements was improved by 12.75 dB.

The second objective is to improve the isolation between the Ant1 and Ant2. Modes 1,2 and 4 are contributing to the radiating BW in the desired band as shown in Figure 5.12. Modes 2 and 4 seem to be contributing to the coupling between antennas 1 and 2. The total current on the surface of the antenna and chassis in the presence of the first DGS was shown in Figure 5.10(b). It can be clearly observed that the addition of the DGS has confined the current distribution more towards the antenna elements. The total current on the surface of the antenna and chassis seems to be the combination of modes 1 and 4. Mode 2 has uniform

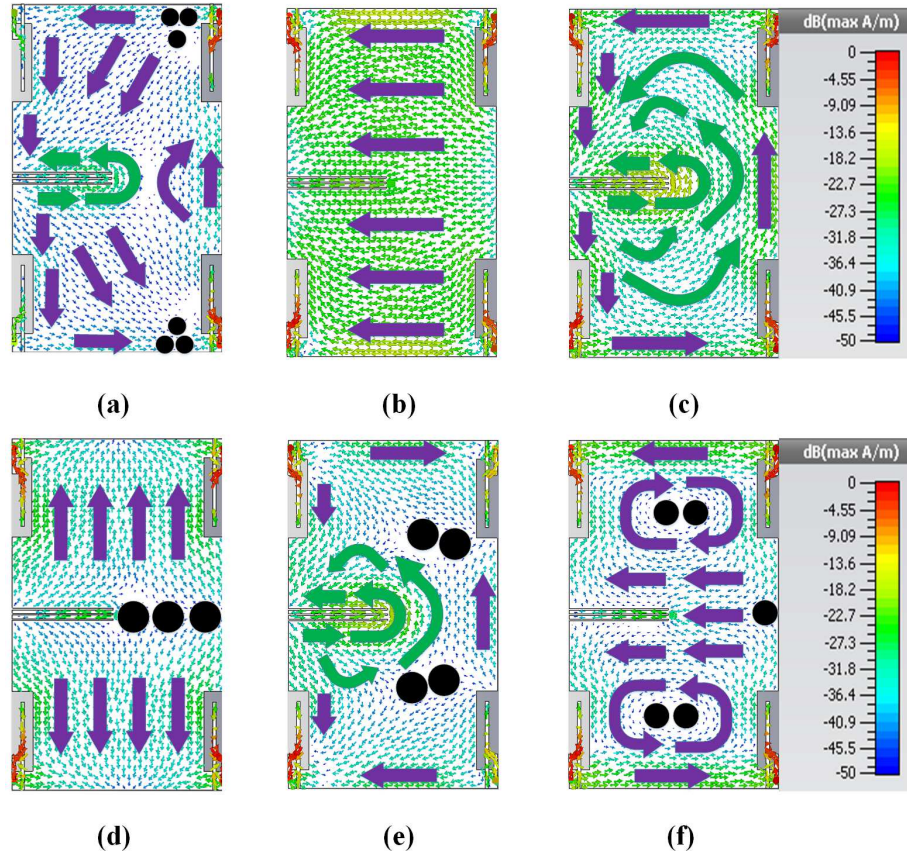


Figure 5.11: Current distribution of the first six modes of the 4-element PIFA like MIMO in the presence of the DGS at 2.20 GHz, where (a)-(f) represents the mode 1 to 6 respectively.

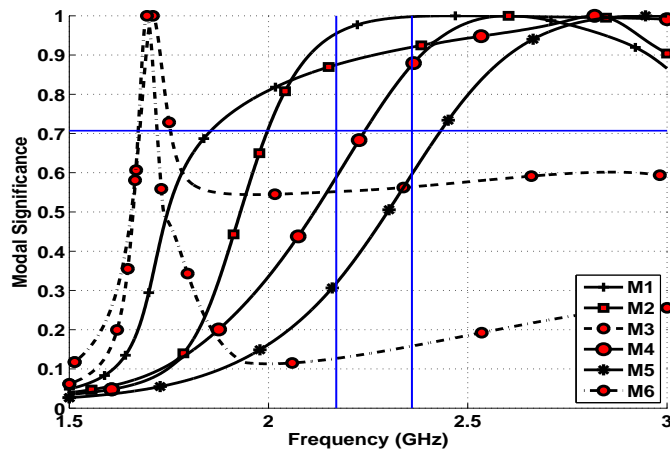


Figure 5.12: Modal significance curves of the 4-element PIFA like MIMO in the presence of DGS.

current distribution so it seems that either mode 2 is not excited or it is excited with minimum contribution. The only mode left that can cause the coupling seems to be the mode 4 as mode 1 has a current null between the antennas connected on the horizontal side.

If we place a DGS between Ant1 and Ant2 this will help us in separating the current direction of mode 4 as well as it will not affect the current distribution of mode 1 significantly. Again the simplest DGS structure consisting of three slit lines was chosen. After few parametric sweeps the DGS was tuned with a the total size of  $20 \times 3.1 \text{ mm}^2$  with an arm length of 20 mm, width of the slit is 0.7 mm and slit separation of 0.5 mm. The geometry of the proposed two DGS structures on the 4-element PIFA like MIMO design are shown in Figure 5.3(b), while Figure 5.3(d) shows the fabricated bottom layer containing the DGS on the ground.

The CM current distribution at 2.2 GHz and the MS plots are shown in Figure 5.13 and 5.14, respectively, for the design in Figure 5.3 with the two DGS structures. From the MS curves we can observe that only modes 1 and 2 are present in the radiating BW region while mode 4 is blocked in the desired band. We can conclude that either mode 1 or mode 2 or a combination of them are responsible for the radiation. The radiating BW of mode 1 and the impedance BW of the real design stops exactly at the same point, as shown in Figure 5.15, this means that mode 1 is playing a significant role. Modes 3, 5 and 6 are not contributing in the desired impedance BW of interest.

The reflection coefficient and the isolation curves of the PIFA MIMO antenna



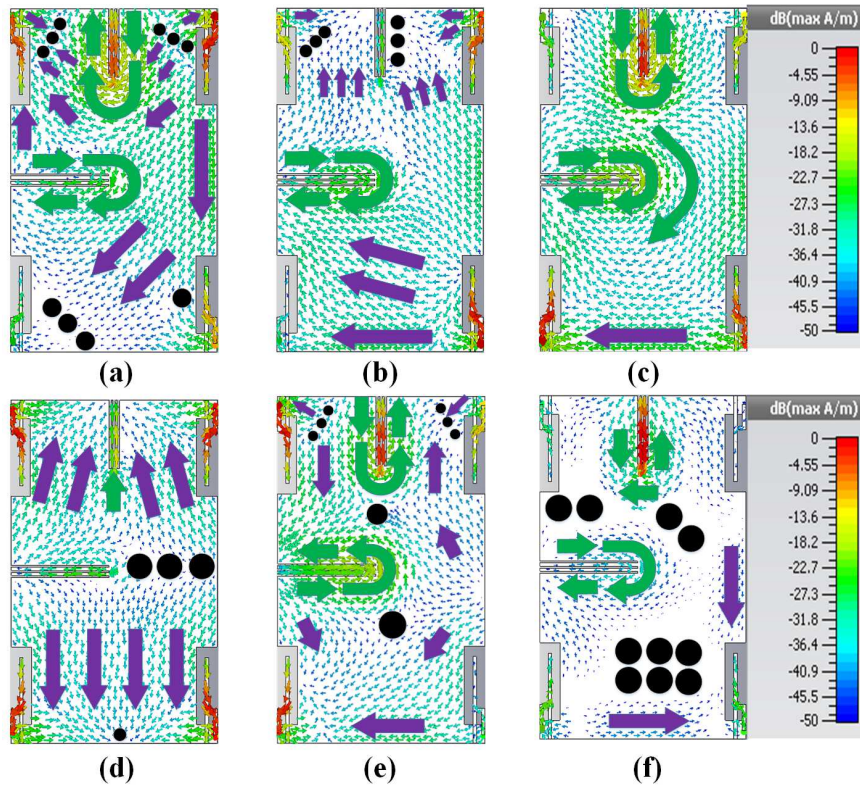


Figure 5.13: Current distribution of the first six modes of the 4-element MIMO PIFA in the presence of two DGS at 2.20 GHz, where (a)-(f) represents mode 1 to 6 respectively.

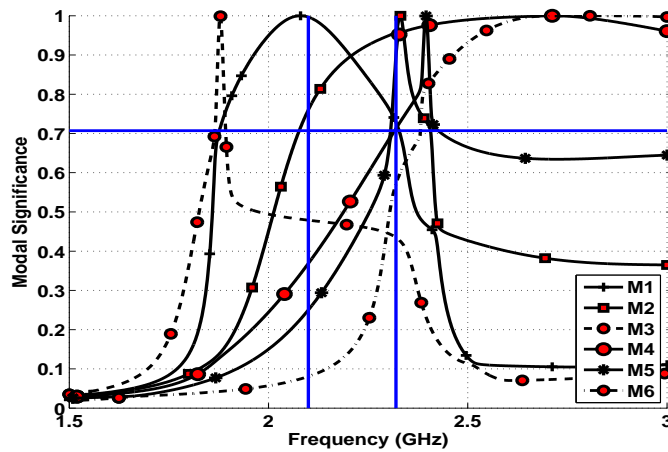


Figure 5.14: Modal significance curves of the 4-element MIMO in the presence of two DGS. The vertical blue lines represent the impedance BW.

with DGS is shown in Figure 5.15(a) and 5.15(b). We can observe that a measured isolation of 30 dB is achieved between Antenna 1 and 2 while 29 dB was achieved between Antenna 1 and 3. An isolation improvement of 12 dB was obtained on average. There was a slight reduction of 30 MHz in the frequency BW and the main reason in our opinion seems to be the blockage of mode 4. Figure 5.15(c) and 5.15(d) show the current distribution on the surface of the antenna in the presence and absence of the DGS when only Ant-1 is excited. A significant improvement is obtained in isolation.

## 5.2.2 Monopole Based MIMO Design

We will extend our study now to the 4-element MIMO monopole design. We can observe from Figure 5.9 that only modes 1 and 2 are contributing in the desired impedance BW while modes 3, 4, 5 and 6 are not contributing at all. From Figure 5.8 we can observe that mode 1 is not causing significant coupling between the antennas connected on the longitudinal or horizontal sides. Mode 2 is causing the coupling between the antennas connected on the horizontal side.

The total current on the surface of the antenna and chassis is shown in Figure 5.16. The total current seems to be a combination of modes 1 and 2 but mode 1 seems to be more dominant because if mode 2 was dominant then the current distribution will be uniform and secondly the position where we have applied sources are more likely to enforce the excitation of longitudinal modes (i.e mode 1).

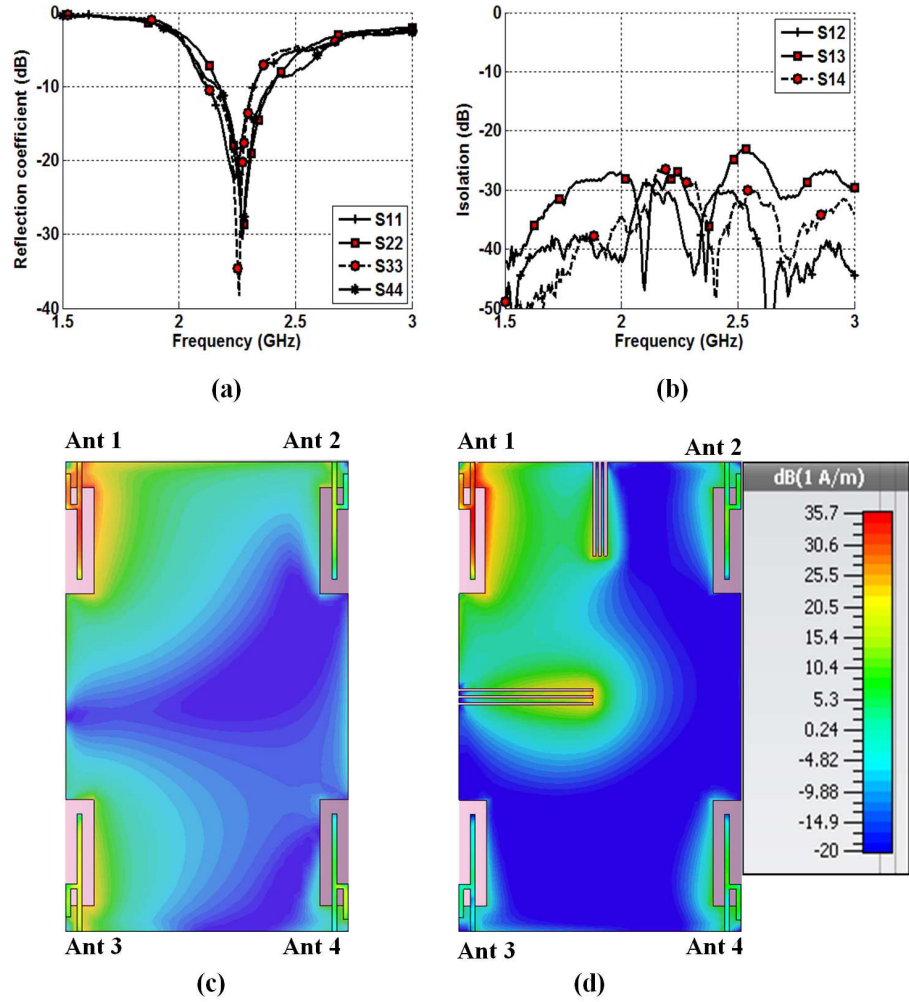


Figure 5.15: 4-element PIFA design, (a) measured reflection coefficient with DGS, (b) measured isolation curve with DGS, (c) current distribution without DGS when Ant-1 is excited, (d) current distribution with DGS when Ant-1 is excited.

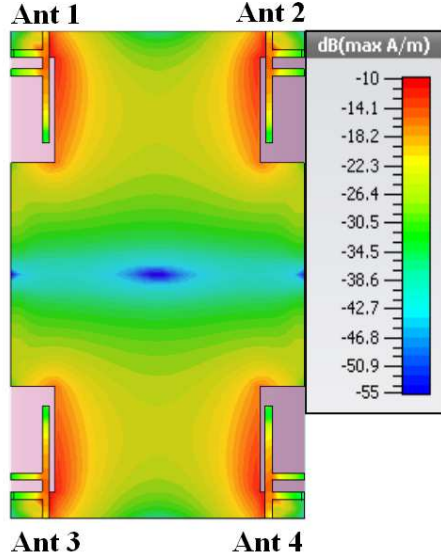


Figure 5.16: Current distribution on the surface of the 4-element MIMO monopole antenna and chassis at 2.2 GHz when all antennas are excited.

To enhance the isolation between Ant1 and Ant2, mode 2 seems to be the coupling mode, so it should be blocked but the position/location of the DGS should not affect mode 1 significantly. So we place the DGS at the horizontal center between Ant-1 and 2 as shown in Figure 5.7(b). It is the point where mode 1 has the current minima. The size of the DGS was optimized by having a length of 21 mm, width of the slit was 0.7 mm while separation was 1 mm. The total size of the DGS was  $21 \times 4.1 \text{ mm}^2$ .

The CM current distribution at 2.2 GHz and the MS plots after introducing the DGS are shown in Figure 5.17 and 5.18, respectively. The CM current distribution of mode 2 is significantly affected and the DGS is producing currents in the direction opposite to the direction of mode 2 flow. Although mode 2 is blocked, it still appears in the middle of the impedance BW. But due to the current oppo-

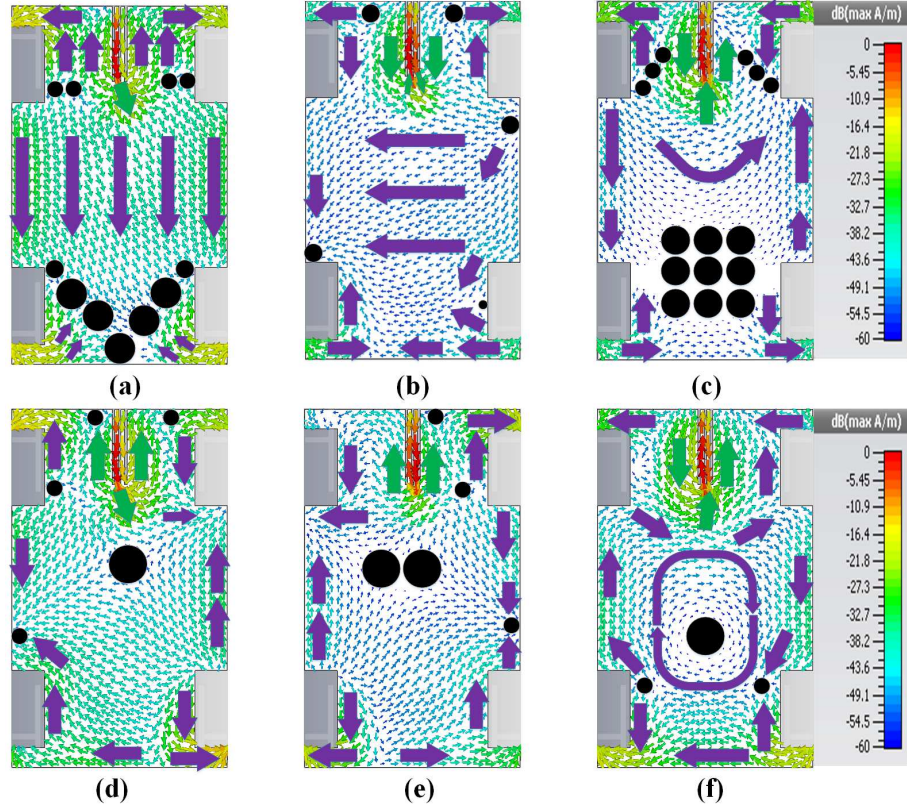


Figure 5.17: Current distribution of the first six modes of the 4-element Monopole based MIMO in the presence of DGS at 2.20 GHz, where (a)-(f) represents mode 1 to 6 respectively.

sition by the DGS, even if it is present in the radiating BW region it will not be excited effectively. Since the addition of a DGS affects the geometry, now another mode is contributing in the band of interest i.e mode 3.

The reflection and isolation curves of the 4-element monopole design with DGS are shown in Figure 5.19(a) and 5.19(b) respectively. We can observe an improvement of 14.5 dB in the measured isolation between Ant-1 and 2 ( $S_{12}$ ). Figure 5.19(c) and 5.19(d) show the current distribution on the surface of the antenna with and without DGS when Ant-1 is excited. A significant isolation improvement is obtained.

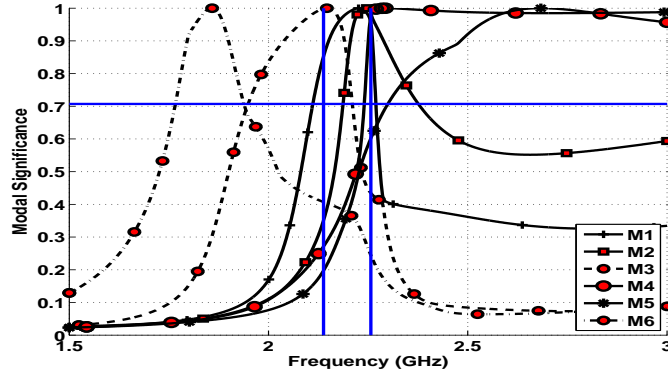


Figure 5.18: Modal significance curves of the 4-element MIMO Monopole in the presence of FR-4 substrate in the presence of DGS. The vertical blue lines represent the impedance BW.

The second objective is to improve the isolation between the antennas connected on the longitudinal side. From the MS plot and the impedance BW in Figures 5.18 and 5.19(a), Mode 1 and the impedance BW nearly have the same radiating and impedance BW. That is mode 1 radiation BW is from 2.112 to 2.265 GHz while the impedance BW is from 2.138 to 2.257 GHz. Mode 3 is contributing from 1.952 to 2.209 GHz. Mode 3 decays in the middle of the impedance BW. From these two observations we can conclude that mode 1 is the non-coupling mode and mode 3 is the coupling mode.

To enhance the isolation, we need to block mode 3. But the current patterns on the edge and side of the chassis are nearly the same for both modes. Mode 1 has a current null nearly at the same location as mode 3 so placing a slot at this location will create two problems. First, it will not meet the purpose because the slot will not affect the coupling mode significantly and second, placing a slot at such a location is not a realistic because it can completely isolate the antennas. The other strategy to improve the isolation will be to place the slot at such a



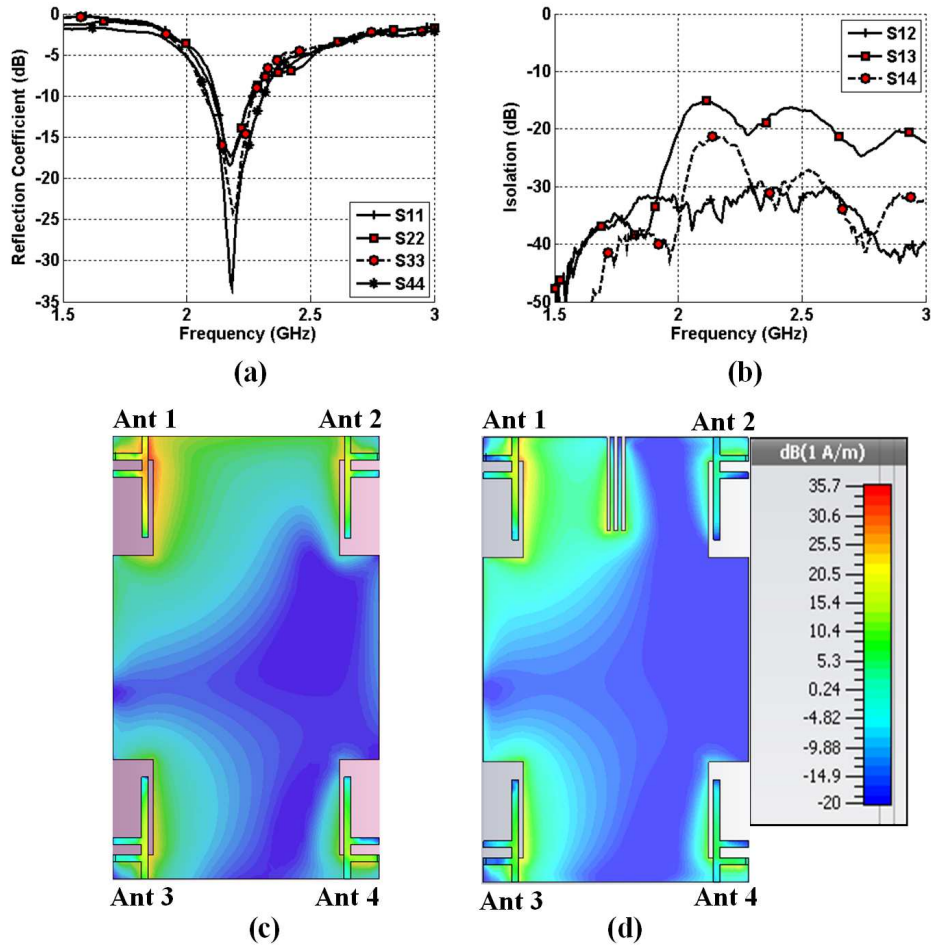


Figure 5.19: 4-element Monopole design, (a) measured reflection coefficient with DGS, (b) measured isolation curve with DGS, (c) current distribution without DGS when Ant-1 is excited, (d) current distribution with DGS when Ant-1 is excited.

location that it affects the coupling mode significantly while non-coupling mode is affected less severely. The optimum position seems to be the center of the chassis, but we cannot place the slot at the center of the chassis again due to two reasons. First, mode 1 current distribution seems stronger as compared to mode 3 (Figure 5.17) at the center so it will greatly affect mode 1 and will thus affect the impedance BW. Second, mode 1 radiating BW is very limited and introducing any discontinuity in the path will severely affect it. In such scenarios, using a DGS for isolation enhancement cannot be used and will not provide the improvement anticipated. We tried several parametric studies but we were not able to improve the isolation, thus it verified our conclusion.

### 5.2.3 Wire Monopole 2-element MIMO Design

A Wire Monopole antenna of length 32.5 mm and wire diameter of 1 mm was placed on a ground plane of  $40 \times 25$  mm<sup>2</sup> size [181]. The center to center separation between the two antennas is  $0.093\lambda_0$ . The antennas are resonating with an impedance BW covering 2.2 – 2.45 GHz while the isolation between the two antenna elements was 5.5 dB at 2.2 GHz as shown in Figure 5.20(a) and 5.20(b) respectively. To enhance the isolation, our proposed method was used, and for brevity purposes only the MS curves are shown in Figure 5.20(c). In our desired impedance BW region only two modes are contributing to the radiating BW they are mode 1 and 4. Mode 1 is having a current null between the antennas while mode 4 current was coupling the antennas. So, mode 1 is a non-coupling mode



while mode 4 is a coupling mode. To block mode 4, we introduce a slitted DGS at the current null location of mode 1. The addition of the DGS significantly improved the isolation as shown in Figure 5.20(b) and mode 4 is no longer contributing in the desired BW as shown in Figure 5.20(d). We can observe a 20 dB improvement in the isolation at 2.45 GHz while in the BW of interest (the BW which we have initially from Figure 5.20(a) is 2.2 GHz to 2.45 GHz) the minimum isolation was 12.5 dB, which represents a 7-dB improvement. Comparing the isolation improvement using our method to the isolation improvement in [18], we observe that at 2.2 GHz the improvement in isolation is only 2.5 dB in [181], and it is not meeting the impedance matching criteria ( $VSWR < 2.0$ ) at 2.2 GHz (frequency shift) while in our case it is 12.5 dB and thus it is meeting the criteria.

#### **5.2.4 Systematic Approach to isolation enhancement in MIMO antennas**

In the above sections we have provided a physical explanation to the operation of a DGS with the help of TCM, as well we have proposed a method that can directly help the designer use such structures in a systematic way and in identifying whether isolation can be improved or not.

The Block diagram of the proposed method is shown in Figure 5.21. After analyzing three different designs we developed steps for improving the isolation between antenna elements of monopole or PIFA like structures. For the system under consideration, first we need to perform TCM analysis to identify the modes

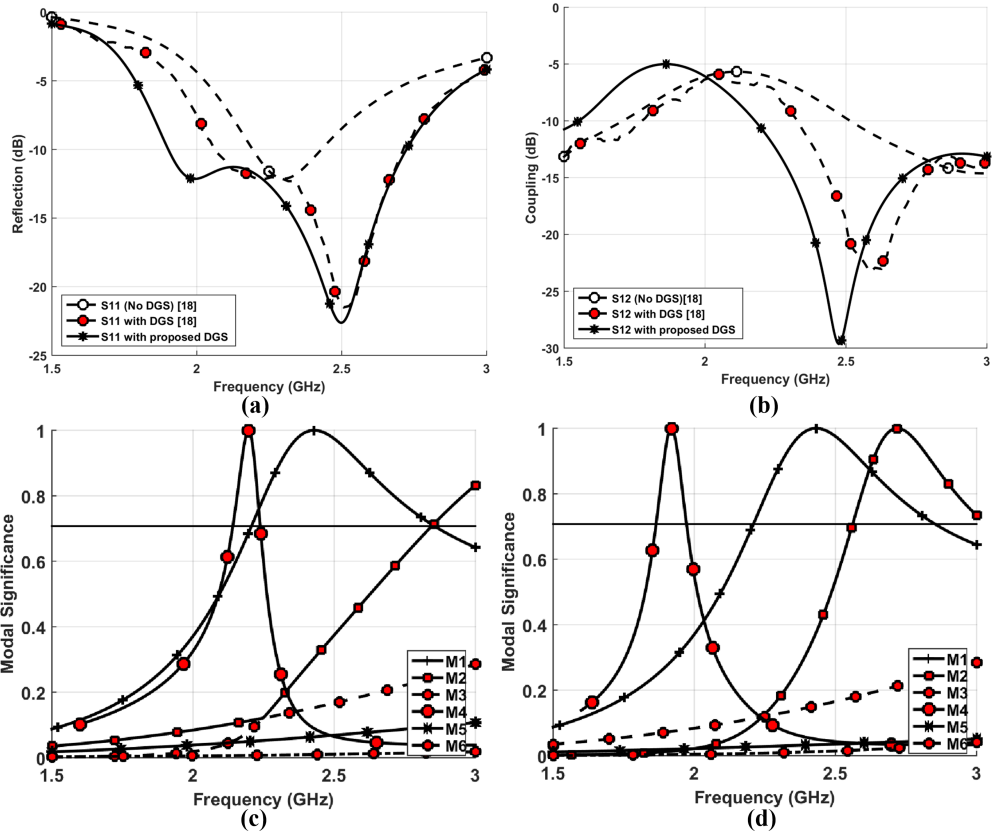


Figure 5.20: 2-element wire monopole design, (a) reflection coefficient, (b) coupling coefficient, (c) modal significance curves of the 2-element MIMO wire monopole (no DGS), and (d) modal significance curves of the 2-element MIMO wire monopole in the presence of DGS.

present in the band of interest. Then we need to check the current patterns on the surface of the antenna and identify coupling and non-coupling modes visually. Based on the current patterns, the DGS shall be placed at certain locations so that the non-coupling modes are unaffected while the coupling modes are blocked. After observing the CM current distribution, if there is no such point on the chassis or the current pattern of the coupling and non-coupling modes is almost same on the chassis, then isolation cannot be enhanced further.

Isolation enhancement that was achieved by our proposed TCM based method was compared against the isolation achieved by other specific DGS based structures that appeared in literature. Table 5.1 shows that our proposed scheme is providing the highest isolation improvement and at the same time is the lowest in complexity and more generalized as compared to other methods. In other techniques, we need to apply several methods and parametric studies but still we are not sure whether the system can provide the desired isolation. In the proposed TCM based systematic method just by studying the first few modes we can deduce for a particular system, whether isolation can be achieved or not.

For isolation enhancement most of the works have focused on 2-element designs and listed the isolation at the best point. In case of [181] the 3 and 4 elements are placed on one axis (not in rectangular or square fashion), so its the same as a 2 element design extended in one axis. We have achieved the highest improvement in the isolation for the whole impedance BW with a relatively small DGS size. The improvement in isolation between Ant1 and Ant3 does not guarantee isolation

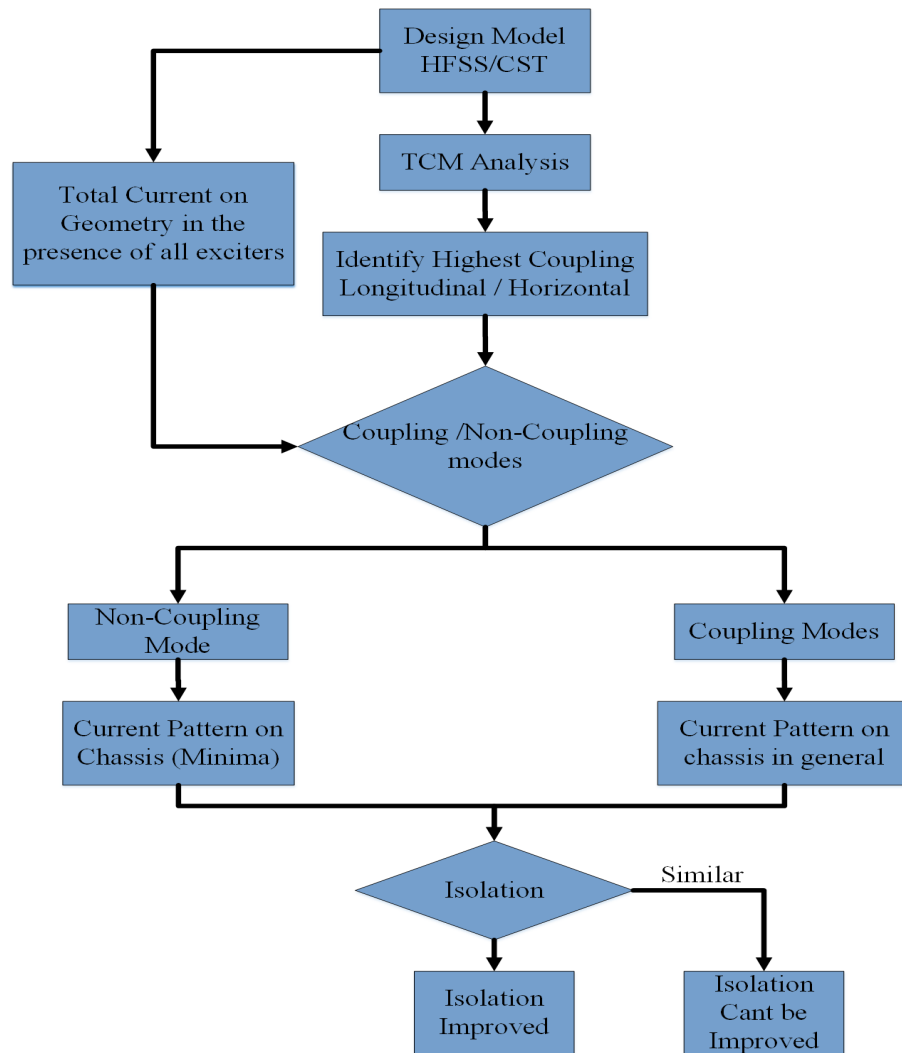


Figure 5.21: Block diagram of the proposed isolation enhanced TCM based method using DGS

improvement between Ant2 and Ant4. But to improve the isolation between Ant2 and Ant4, the same DGS (with little modification) shall be also placed between Ant 2 and 4. This is the shortcoming of DGS approach in general. Here our focus was to develop a systematic approach with the help of TCM and verify its effectiveness.

Table 5.1: Isolation enhancement comparison with previous works

References	No. Of Ant.	Antenna Type	No. of Isol.	Isolation method	Antenna Size (mm <sup>2</sup> )	DGS size (mm <sup>2</sup> )	Operating bands (GHz)	Without DGS Isol.(dB)	Worst DGS isol. (dB)	Improv. across band (dB)
[175]	2	Patch	1	DGS	-	16×20.76	2.57	15	23	5
[176]	2	Slot	2	DGS	22×26	-	3.1-10.6	8	18	10
[177]	2	Patch	1	DGS	60.2×60.2	38×38	2.45 0.803-	18	25	7
[178]	2	4 shaped	1	DGS	100×50	52×11	0.823 & 2.44-2.9	-	17 & 9	-
[179]	2	L-slot	2	DGS + Orth.Placement	32×32	13×1	3-4.5	11.5	15	3.5
[180]	4	Cylindrical Monopole	3	DGS + MO-FFD	$\pi \times 80^2 \times 50$	-	0.698-0.960	10	12 & 18	2 & 6
[181]	2	PIFA	1	DGS	43×43	21×9	2.27-2.35	12.5	20	7.5
	2	Wire Monopole	1	DGS	40×25	5×25	2.2-2.45	5.5	8.0	2.5
	3	PIFA	1	DGS	103×43	21×9	-	-	12	-
[182]	4	F-shaped	2	DGS	120×60	120×47	Reconfig.	9	12.5	3
	4	PIFA	1	DGS	100×60	28.5×2.5	2.07-2.21	15 & 10	15 & 15	0 & 5
[184]	4	Monopole	1	DGS	100×60	35×10.5 & $\pi(9)^2$	2.02-2.205	15 & 15	15 & 20	0 & 5
[185]	8	Ring slot	3	DGS+CL-FSS+Arcs	93×60	93×60	4.0-10	-	15 & 20	-
Proposed Method	4	PIFA [183]	1	DGS	100×60	28.5×3.5,20×4.5	2.17-2.33	16.25 & 18.5	29 & 30	12.75 & 11.5
	4	Monopole [184]	1	DGS	100×60	21×4.1	2.13-2.26	15.5 & 17.3	17.5 & 32.8	14.5
	2	Monopole [181]	1	DGS	40×25	3.7×25	2.2-2.45	5.5	12.5	7

## 5.3 MIMO Antenna Parameter Evaluation

MIMO antenna systems shall be evaluated for parameters such as Envelope correlation coefficient (ECC), Gain, efficiency and 2D/3D radiation patterns. ECC ( $\rho_e$ ) values are computed using the 3D measured radiation patterns in an isotropic multi-path environment [57]:

$$\rho_e = \frac{|\int \int_{4\pi} [\vec{F}_1(\theta, \varphi) * \vec{F}_2(\theta, \varphi) d\Omega]|^2}{\int \int_{4\pi} |\vec{F}_1(\theta, \varphi)|^2 d\Omega \int \int_{4\pi} |\vec{F}_2(\theta, \varphi)|^2 d\Omega} \quad (5.1)$$

where  $\vec{F}_i(\theta, \varphi)$  is the field radiation pattern of the antenna when port  $i$  is excited and  $*$  denotes the Hermitian product. For the given MIMO antenna systems, ECC was calculated at four distinct frequencies for the printed designs. The gain pattern and efficiency measurement setup is shown in Figure 5.22. The gain pattern of an individual antenna element was obtained while the other ports were terminated with  $50 \Omega$  loads.

### 5.3.1 PIFA Based MIMO Design

The simulated and measured normalized 2D radiation patterns in terms of the total E-field ( $E_{total}$ ) at 2.20 GHz are shown in Figure 5.23. The patterns show the x-y and y-z planes for all the antenna elements. Good agreement is obtained between the simulated and measured results. The measured gain and efficiency curves for Ant1 are shown in the Figure 5.24(a) (other elements have similar values). The measured highest gain of 6.45 dB was obtained with an efficiency

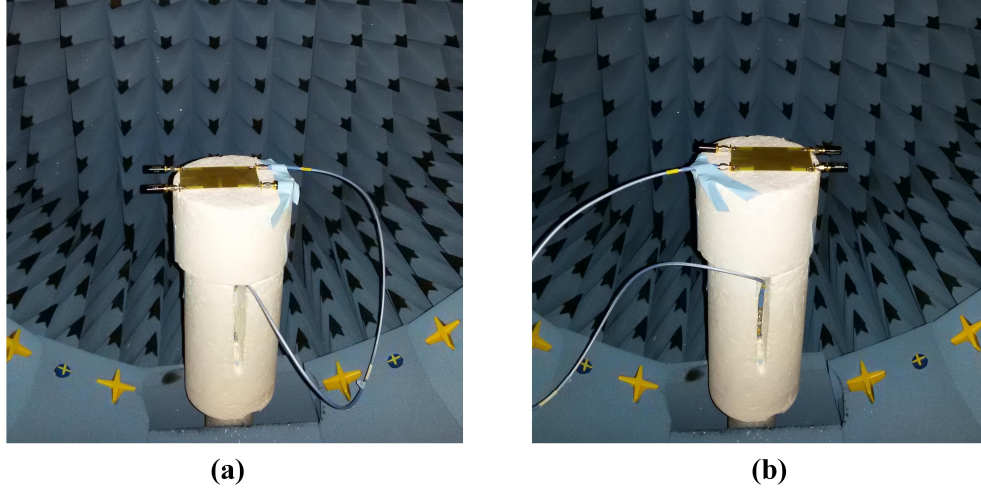


Figure 5.22: Radiation pattern measurement setup (a) 4-element MIMO PIFA (b) 4-element MIMO Monopole.

Table 5.2: Measured  $ECC(\rho_e)$  . All frequencies are in GHz

Freq (GHz)	$\rho_{e12}$	$\rho_{e13}$	$\rho_{e14}$	$\rho_{e23}$	$\rho_{e24}$	$\rho_{e34}$
2.20	0.175	0.040	0.041	0.012	0.123	0.132
2.22	0.165	0.037	0.040	0.013	0.134	0.122
2.24	0.160	0.033	0.039	0.014	0.146	0.116
2.26	0.160	0.028	0.038	0.015	0.159	0.113

of around 97 % at 2.257 GHz. ECC values are shown in the Table 5.2. We can observe that the worst ECC value is 0.175 which is far below the threshold value of 0.5.

### 5.3.2 Monopole Based MIMO Design

The simulated and measured normalized 2D radiation patterns in terms of the total E-field ( $E_{total}$ ), at 2.20 GHz are shown in Figure 5.25. The patterns show the x-y and x-z planes for all the antenna elements. Good agreement is obtained



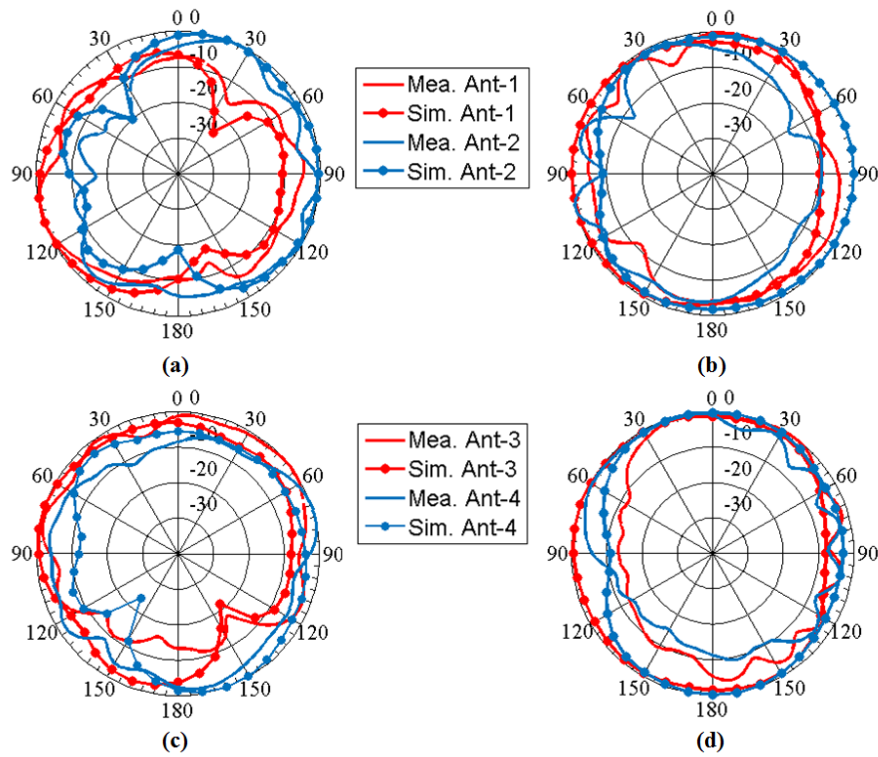


Figure 5.23: PIFA-based MIMO antenna measured and simulated normalized radiation patterns at 2.20 GHz ( $E_{total}$ ) (a) ( $\phi$  cut) Ant 1 and 2 at  $\theta = 90$ , (b) ( $\theta$  cut) Ant 1 and 2 at  $\phi = 90$ , (c) ( $\phi$  cut) Ant 3 and 4 at  $\theta = 90$ , (d) ( $\theta$  cut) Ant 3 and 4 at  $\phi = 90$ .

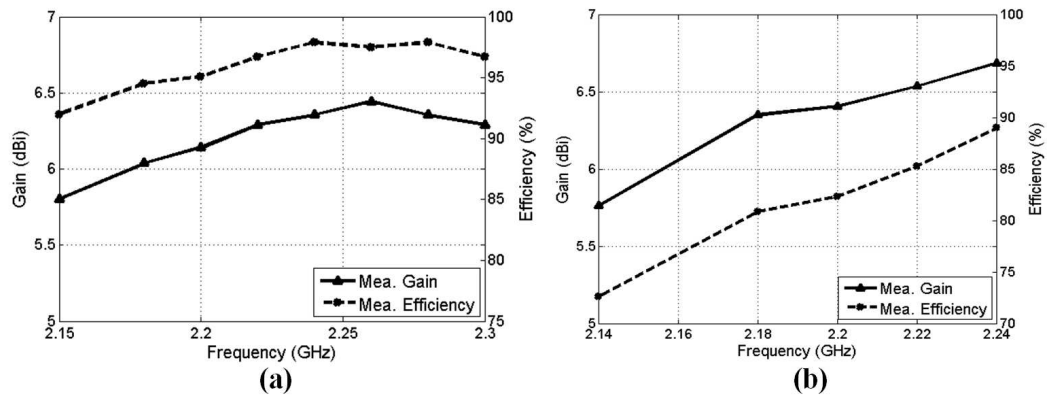


Figure 5.24: Measured Gain and efficiency curves for (a) 4-element MIMO PIFA, (b) 4-element MIMO Monopole.

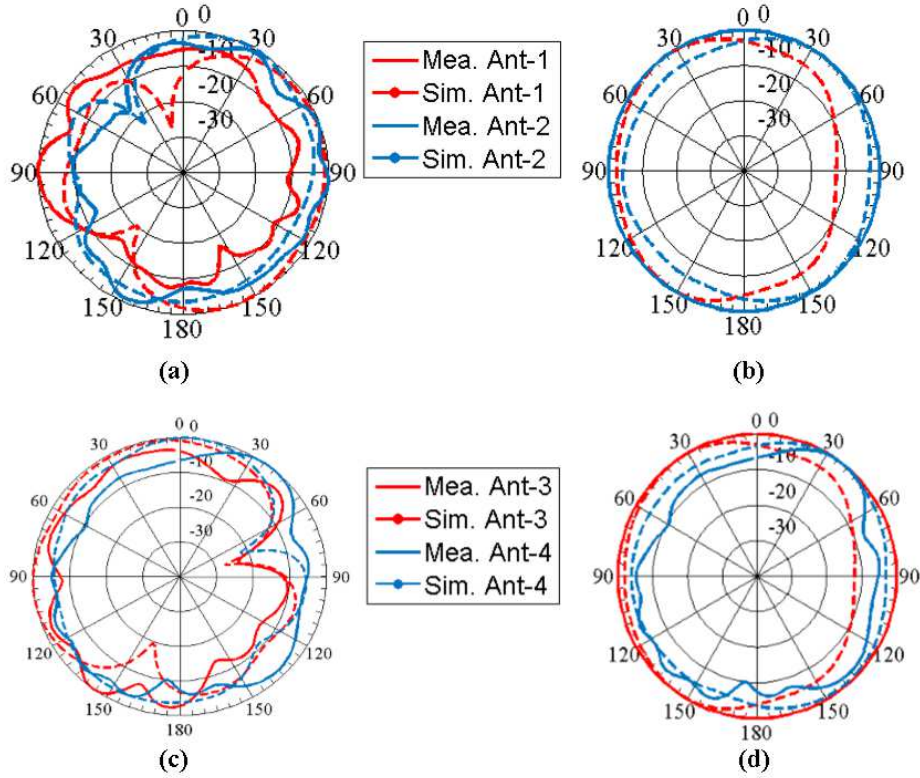


Figure 5.25: Monopole-based MIMO antenna measured and simulated normalized radiation patterns at 2.20 GHz ( $E_{total}$ ) (a) ( $\phi$  cut) Ant 1 and 2 at  $\theta = 90$ , (b) ( $\theta$  cut) Ant 1 and 2 at  $\phi = 0$ , (c) ( $\phi$  cut) Ant 3 and 4 at  $\theta = 90$ , (d) ( $\theta$  cut) Ant 3 and 4 at  $\phi = 0$ .

between the simulated and measured results. Measured gain and efficiency curves for Ant1 are shown in the Figure 5.24(b). The measured highest gain of 6.55 dB was obtained with an efficiency of around 89 % at 2.24 GHz. ECC values are shown in the Table 5.3. We can observe that the worst ECC value is 0.256.

## 5.4 Conclusions

In this work, TCM was used to analyze the behavior as well as development of a systematic approach for the placement of DGS in MIMO antenna configurations.

Table 5.3: Measured ECC( $\rho_e$ ) . All frequencies are in GHz

Freq (GHz)	$\rho_{e12}$	$\rho_{e13}$	$\rho_{e14}$	$\rho_{e23}$	$\rho_{e24}$	$\rho_{e34}$
2.20	0.193	0.098	0.068	0.029	0.126	0.256
2.22	0.203	0.109	0.075	0.033	0.135	0.250
2.24	0.211	0.118	0.083	0.036	0.143	0.246
2.26	0.216	0.124	0.091	0.036	0.149	0.244

We considered one 2-element wire and two 4-element printed MIMO antenna designs in the analysis. The presence of PIFA and Monopole antennas significantly affect the CM and MS curves. The developed approach was applied to all designs and an average isolation enhancement of almost 11 dB was achieved. The method is compared to the already published approaches in which isolation was achieved by DGS and any other schemes. Our proposed method is simple, achieved more isolation and can be generalized to different antenna designs. The two MIMO antennas, PIFA and Monopole were fully characterized and showed efficiency values higher than 85 % and 75 % and ECC lower than 0.175 and 0.256 respectively. All the analysis included the effect of the dielectric substrate. Very good agreement between simulated and measured results is obtained.

## CHAPTER 6

# EFFECT OF PRACTICAL ANTENNA ON CHASSIS CURRENT MODES

*“You can see some more dimensions of life*

*If your enthusiasm is coupled with your vision”*

---

— ALLAMA IQBAL

TCM has proven to be useful because it provides an insight about the behavior of antennas. From the perspective of TCM, Chassis based radiators gained popularity because of their ease of analysis. Due to the large size of the chassis, dealing (analysis and excitation) with the modes is easy. TCM was used to analyze the chassis modes of Unmanned Air Vehicle (UAV) [221], Shipboards [222] and military applications [223]. The chassis in all cases is large and the excitation of modes was done either through probe feeding or coupling elements. In most

cases, the targeted frequency band was less than 1 GHz. The idea of the use of chassis as a radiating element was also extended to the excitation of mobile chassis modes. Chassis plays an important role in the antenna isolation at lower frequencies (i.e. below 1 GHz) but for high frequencies it acts as a ground plane.

For frequencies greater than 1 GHz, the contribution of chassis is very negligible and the antenna is the main radiating element. So, the idea of using the mobile chassis as the main radiating element for frequencies greater than 1 GHz is highly unrealistic and unacceptable. In [224], antenna designs of some real phones are shown and none of them are using the complete chassis as the main radiating element. The use of the chassis as the main radiating element were emphasized in many recent works because of the ease of characteristic mode analysis of chassis and also the ease of excitation of the chassis modes.

The main contribution of this chapter is to investigate the effect of using practical antennas on chassis current modes and to show that the use of the chassis as a main radiating element for frequencies greater than 1 GHz is unrealistic and unjustifiable from a design perspective. To emphasize this point we consider 2 antenna designs (PIFA and Monopole) operating at two different frequencies, i.e. 2 GHz and 0.9 GHz. So, a total of 4 cases are considered. In order to observe the effect of chassis w.r.t frequency in the presence of the antenna the size of the chassis was eventually reduced and its effect on the resonance was observed. For frequencies resonating at 2 GHz a chassis reduction of 90 % did not affect its resonance but for antennas resonating less than 1 GHz the effect of the chassis was

significant. This proves that further relying on the chassis for frequencies greater than 2 GHz is not practical. It was observed that irrespective of frequency and chassis size, CM current maxima shifts towards the antenna (radiating element) whenever an antenna is introduced on the chassis and under such scenarios pure excitation of single CM is nearly impossible.

## 6.1 Analysis Process

We consider 2 different practical antenna designs, i.e PIFA and Monopole, operating at two different frequencies each, i.e. 2 GHz and 0.93 GHz. A total of 4 cases (antennas) will be considered. The antennas are designed on an RO4350 substrate having a dielectric constant of 3.48 and thickness of 0.8 mm unlike most of other works that were in air. The geometry of the antennas are shown in Fig. 6.1. TCM is used to investigate the effect of the antenna on chassis modes. CM currents and MS curves are used in the comparison. The CM currents and the MS curves of the chassis alone are shown in Figs. 6.2(1)(a)-(f) and 6.4(a), respectively, for the first 6 modes using CST. Note that the small slots below the antenna will not affect the chassis modes much.

### 6.1.1 Design 1

The Geometry of the PIFA antenna is shown in Fig. 6.1(b). The CM currents and the MS curves are shown in the Figs 6.2(2)(a)-(f) and 6.4(b) respectively. We can observe from Fig. 6.2(2)(a) that the introduction of the antenna has

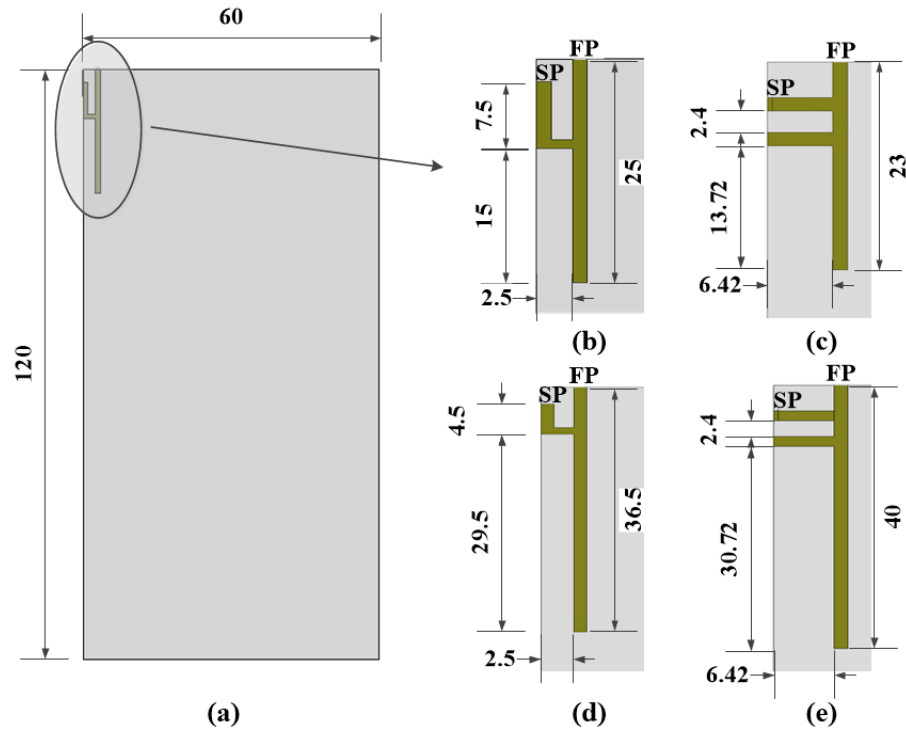


Figure 6.1: Design Geometries, (a) Antenna element on mobile chassis (b) Design 1, PIFA antenna resonating at 2.2 GHz, (c) Design 2, Monopole antenna resonating at 2.2 GHz, (d) Design 3, PIFA antenna resonating at 0.93 GHz and (e) Design 4, Monopole antenna resonating at 0.95 GHz. SP and FP represents the shorting point and the feeding point respectively. All dimensions are in mm.

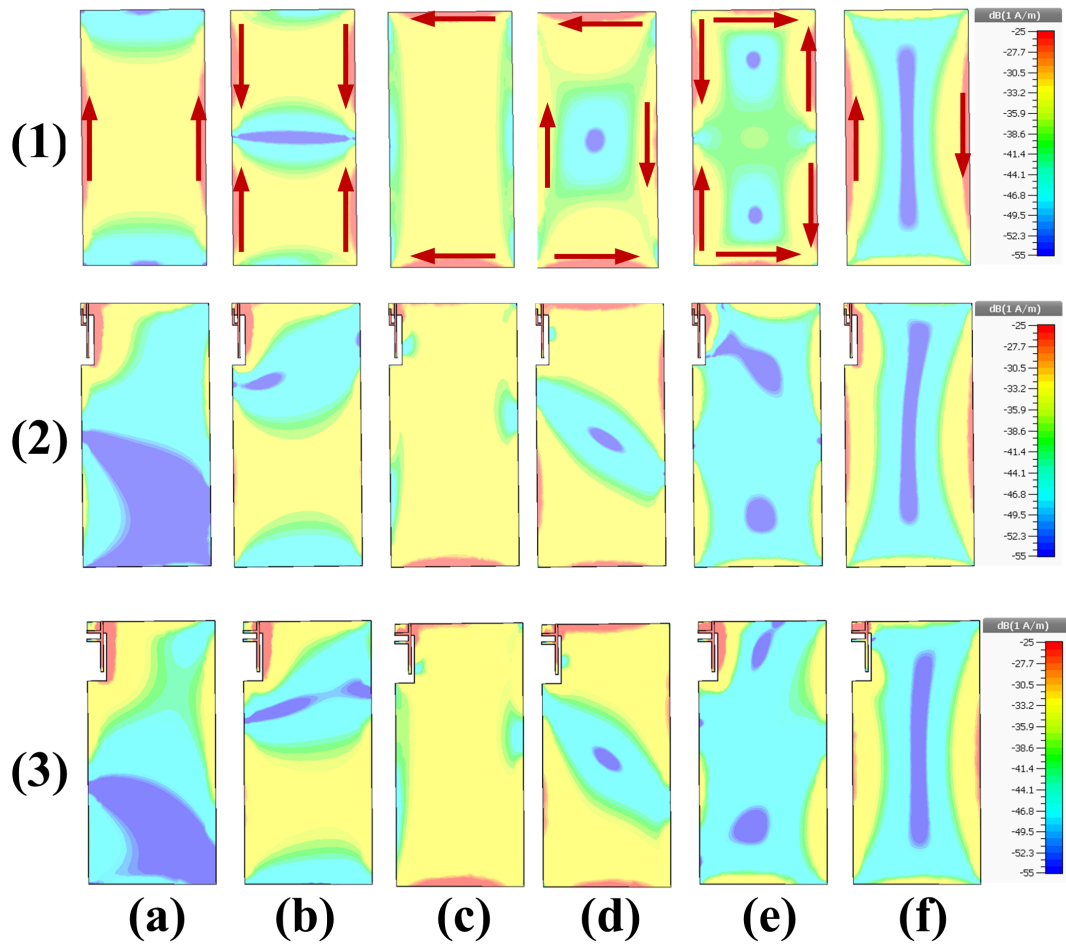


Figure 6.2: CM Current distribution, where (a)-(f) represents mode 1 to 6 of (1) Ground plane/chassis, (2) Design 1, PIFA, (3) Design 2, Monopole. Red arrows show the location as well as the direction of the maximum current of a mode.



strongly affected the CM current distribution of mode 1. The radiating BW of mode 1 is also severely affected as shown in Fig. 6.4(b). For almost all the modes, the current is concentrated around the antenna element. Other modes radiating BW (Observe the starting frequency of the radiating BW) are slightly affected. From mode 1, we can observe that the current is more concentrated around the antenna so cutting the chassis from the lower edge should not affect the impedance BW of the antenna. For an antenna placed at the center of the long/short edges, the MS curves are affected differently, which shows the location dependence as well. For a standard smart phone size of  $120 \times 60mm^2$  the chassis size was reduced systematically by steps of 10mm and 5mm along the long and short edges, respectively. This reduction translates to 0% (no reduction), 16%, 30%, 44%, 56%, 66%, 75%, 83%, 90% and 94% of the original chassis size. These percentage reduction are referred to C1 to C10 in Fig. 6.3. The effect of this reduction on the impedance BW was analyzed. For Design 1, whose operating frequency is around 2 GHz, the impedance BW was not affected even when the size of the chassis was reduced up to 90% as shown in Fig. 6.3(a). We can observe a slight shift in the impedance BW as the ground size is changed (a maximum shift of 180 MHz) as shown in Table 6.1. From this analysis we can observe that the chassis is not the major contributor and all the relevant currents are localized.

The CM and the MS curves of the 90% reduced chassis ( $40 \times 20mm^2$ ) are shown in Fig. 6.5(1)(a)-(f) and 6.4(d), respectively. The CM remains the same but due to the reduced size, the radiating BW of the modes is shifted to higher

Table 6.1: Effect of chassis reduction on the resonance and BW

	Design 1			Design 2		
	f_start	f_stop	BW	f_start	f_stop	BW
	GHz	GHz	MHz	GHz	GHz	MHz
C1	2.128	2.356	228	2.133	2.391	258
C2	2.128	2.364	236	2.109	2.376	267
C3	2.141	2.341	200	2.122	2.329	207
C4	2.168	2.337	169	2.16	2.31	150
C5	2.207	2.364	157	2.202	2.325	123
C6	2.238	2.425	187	2.233	2.385	152
C7	2.255	2.475	220	2.244	2.441	197
C8	2.255	2.475	220	2.159	2.441	282
C9	2.108	2.295	187	2.042	2.22	178

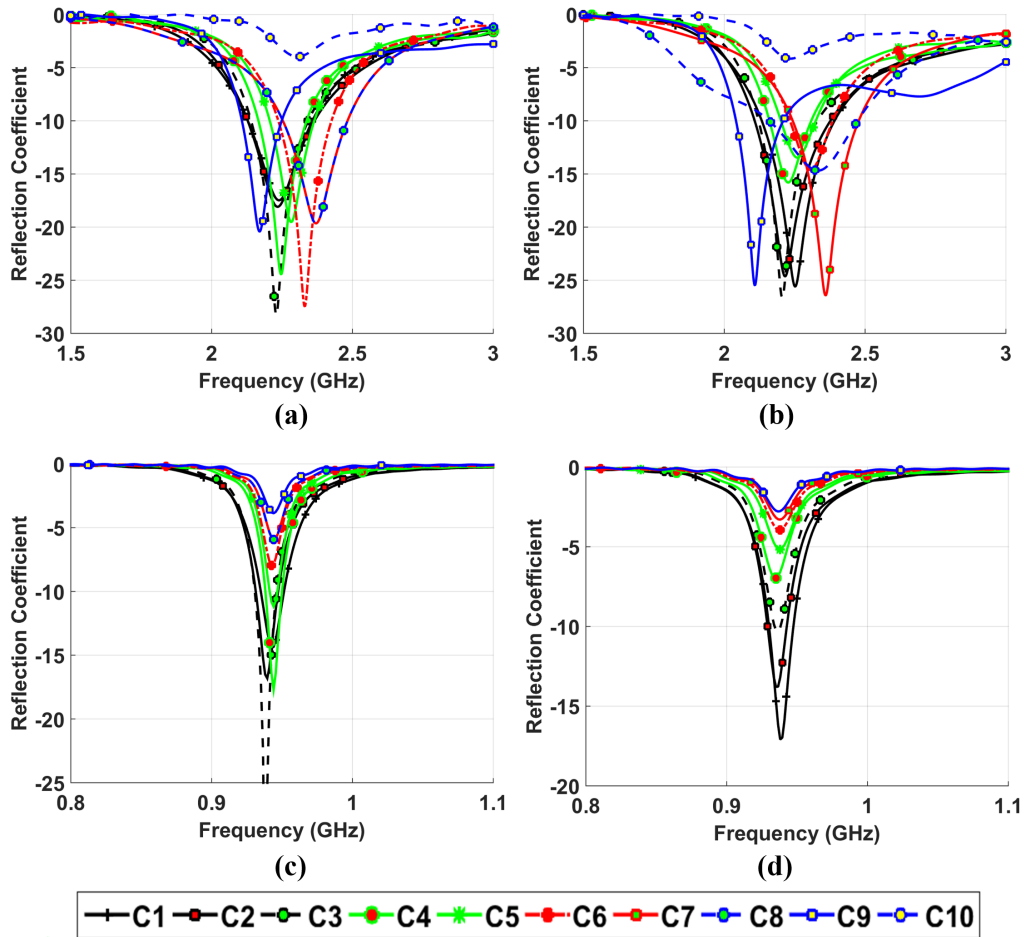


Figure 6.3: Reflection Coefficient Curves for (a) Design 1, (b) Design 2, (c) Design 3 and Design 4. C1 to C10 refers to chassis size reduction by 0%, 16%, 30%, 44%, 56%, 64%, 75%, 83%, 90% and 94%, respectively.

frequencies. Only one mode is present in the radiating BW region that starts contributing at 2.32 GHz. If the chassis was the main radiating element, it could not radiate between 2.1 to 2.3 GHz.

Since in Design 1, the antenna is resonating with a 90% reduced chassis, we also analyzed this case. From Fig. 6.4(e) we can observe that the introduction of the antenna had significantly affected mode 1 and its radiating BW is shifted to lower frequencies i.e. 1.85 to 2.32 GHz and this is the region where the antenna is resonating. This gives a clear indication that the antenna is the main radiating element. Also observe that mode 1 radiating BW (90% reduced chassis) and the impedance BW of Design 1 with 90% reduced chassis finishes at the same point. This means that mode 1 was the major contributor and mode 1 has a current maxima across the antenna. If we observe modes 2 to 6 shown in Fig. 6.5 (2)(b)-(f), we can clearly see the current concentration or maxima is across the antenna itself. To get optimum performance in terms of BW we need to purely excite these CM separately which seems a nearly impossible task because all of them have current maximas across the antenna. This is the reason that many researchers do not investigate the effect of real antenna elements and relied on the excitation of chassis modes. But from our study we have already shown that in practical scenarios, antenna elements are used. To further validate our study we will apply the same procedure on three more designs.

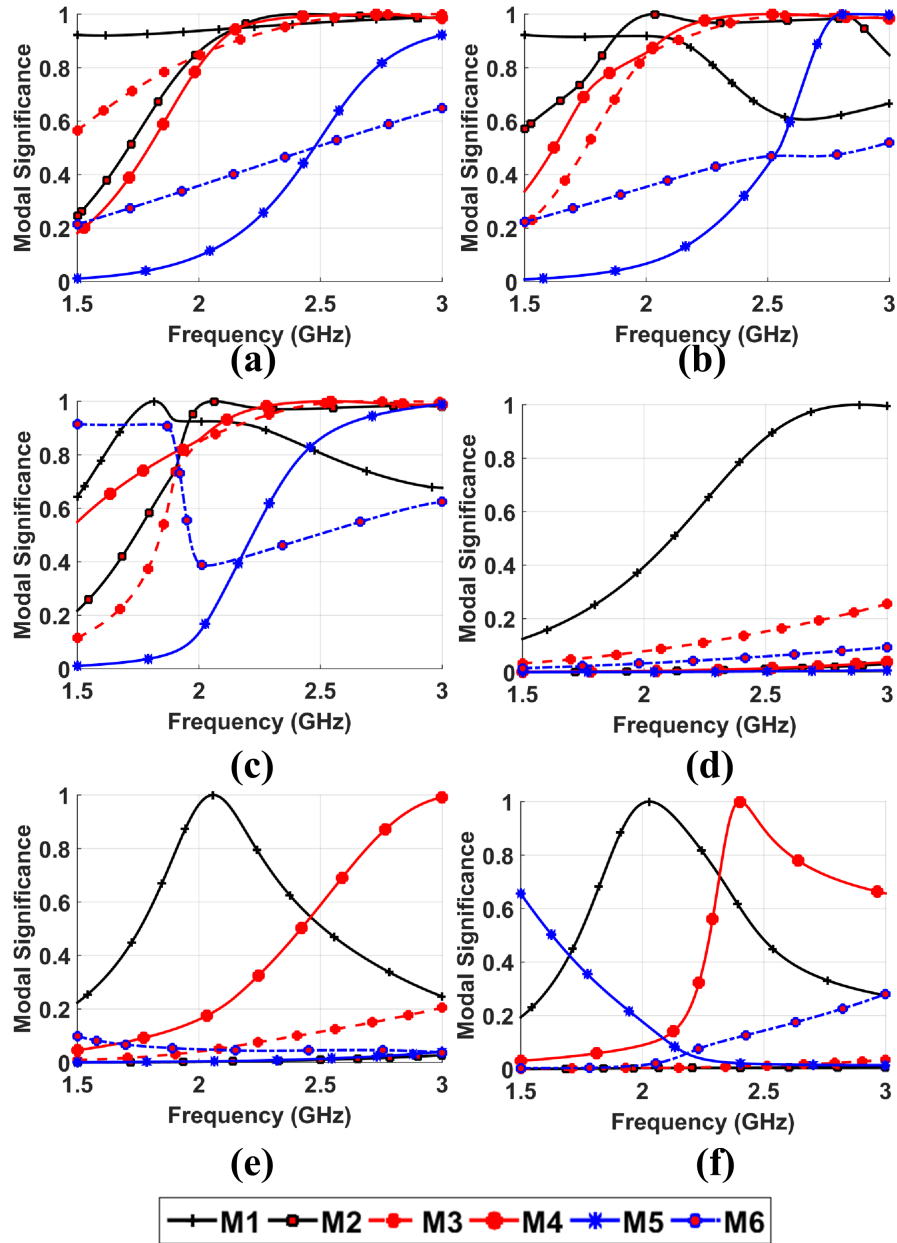


Figure 6.4: Modal Significance curves (a) Chassis ( $120 \times 60mm^2$ ), (b) Design 1, (c) Design 2, (d) 90% reduced chassis ( $40 \times 20mm^2$ ), (e) Design 1 on 90% reduced chassis, (f) Design 2 on 90% reduced chassis.

### 6.1.2 Design 2

The geometry is shown in Fig. 6.1(c), and is for a shorted monopole radiating around 2.2 GHz. The effect of the radiating element on the chassis modes in terms of CM current distribution and MS is shown in Figs. 6.2 (2)(a)-(f) and 6.4(c), respectively. Comparing Figs. 6.4(a), 6.4(b) to Fig. 6.4(c) we can observe that these small radiating elements affect the CM of the chassis differently. The CM current distributions are concentrated across the antenna (similar to Design-1). The chassis size was reduced systematically similar to Design 1 and similar behavior was observed. For a 90% reduction in the chassis, the antenna impedance BW was not affected significantly although a shift in the resonance frequency (of 220 MHz) was observed as shown in the Fig. 6.3(b) and Table 6.1. The CM and the MS curves of the antenna on a 90% reduced chassis are shown in Figs. 6.5(3)(a)-(f) and 6.4(f), respectively. We can observe that the CM current distribution of mode 2 in 6.5(3)(b) is not uniform. For Design 1 the current is uniformly spread across the antenna element it self. This means that these small radiating elements have different effects on the chassis modes. It is also observed that for two designs operating at 2.2 GHz, a 90 % chassis reduction did not affect their resonance behavior other then a slight shift and slightly narrower BW.

### 6.1.3 Design 3

Fig. 6.1(d) shows the geometry of this case. It is an extended version of design 1 operating at a lower frequency (0.94 GHz). The same methodology is applied. As

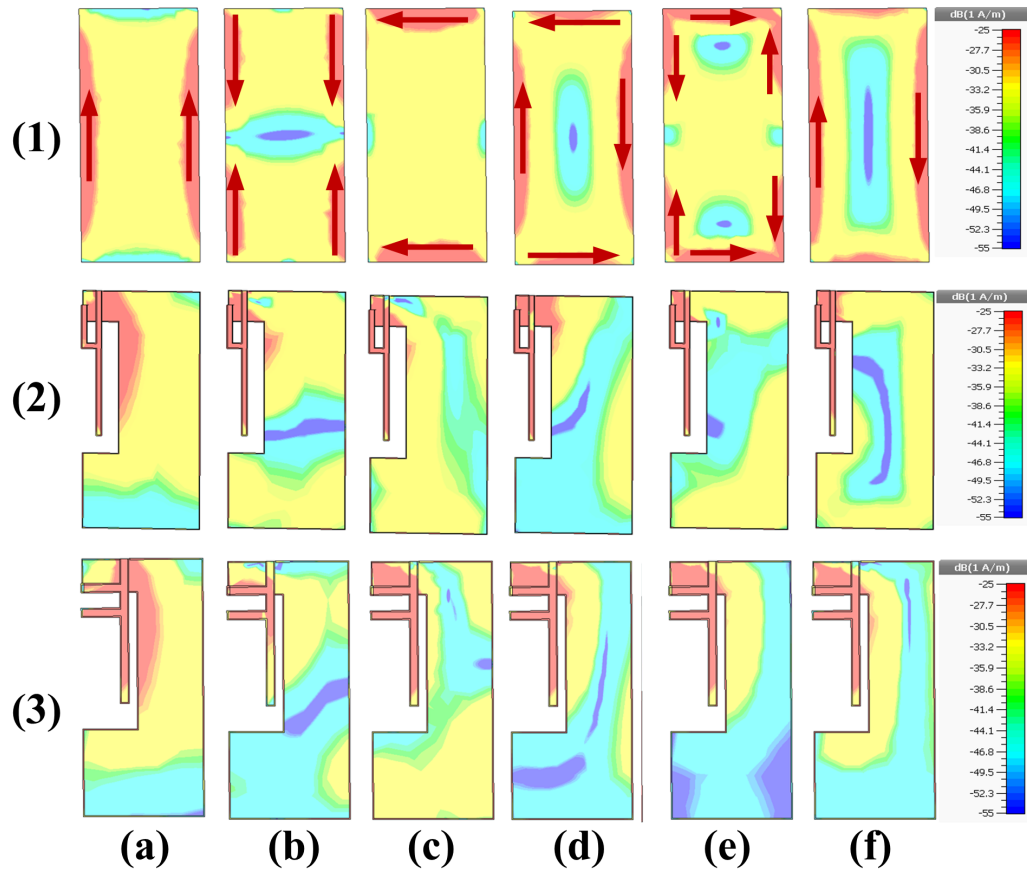


Figure 6.5: CM Current distribution, where (a)-(f) represents mode 1 to 6 of (1) 90% reduced Chassis, (2) Design 1 on 90% reduced Chassis, (3) Design 2 on 90% reduced Chassis.

the antenna is resonating at lower frequencies, the analysis was performed from 0.5 GHz to 2.0 GHz. We can observe that the introduction of the antenna element affect the chassis modes differently as shown in Fig. 6.6(a) and 6.6(b). The inclusion of the antenna has introduced mode 5 at 560 MHz which was initially not present. This means that at lower frequencies the antenna is still the main radiator but as mentioned earlier the excitation of such modes is not easy. To observe the effect of the chassis size at lower frequencies the same procedure was applied. The reflection coefficient of the antenna with different chassis sizes is shown in Fig. 6.3(c). We can observe that the antenna is resonating until the chassis was reduced by 44%. For any reduction in chassis size greater than 44% the antenna does not resonate according to the  $VSWR < 2$  criteria. This is the reason that at lower frequencies the chassis contributes to isolation and coupling significantly. If we place 4 antennas on a mobile chassis ( $120 \times 60mm^2$ ) then every antenna needs chassis dimensions of 56% that is why the chassis starts contributing to the isolation significantly. As observed from Designs 1 and 2, at higher frequencies an antenna can operate with a 90 % reduced chassis that is why the chassis does not contribute to coupling significantly.

#### **6.1.4 Design 4**

The geometry of this design is shown in Fig. 6.1(e). It is an extended version of design 2 operating at 0.94 GHz. It was observed that the antenna affects the chassis modes differently as shown in Fig. 6.6(c). The chassis size was reduced and

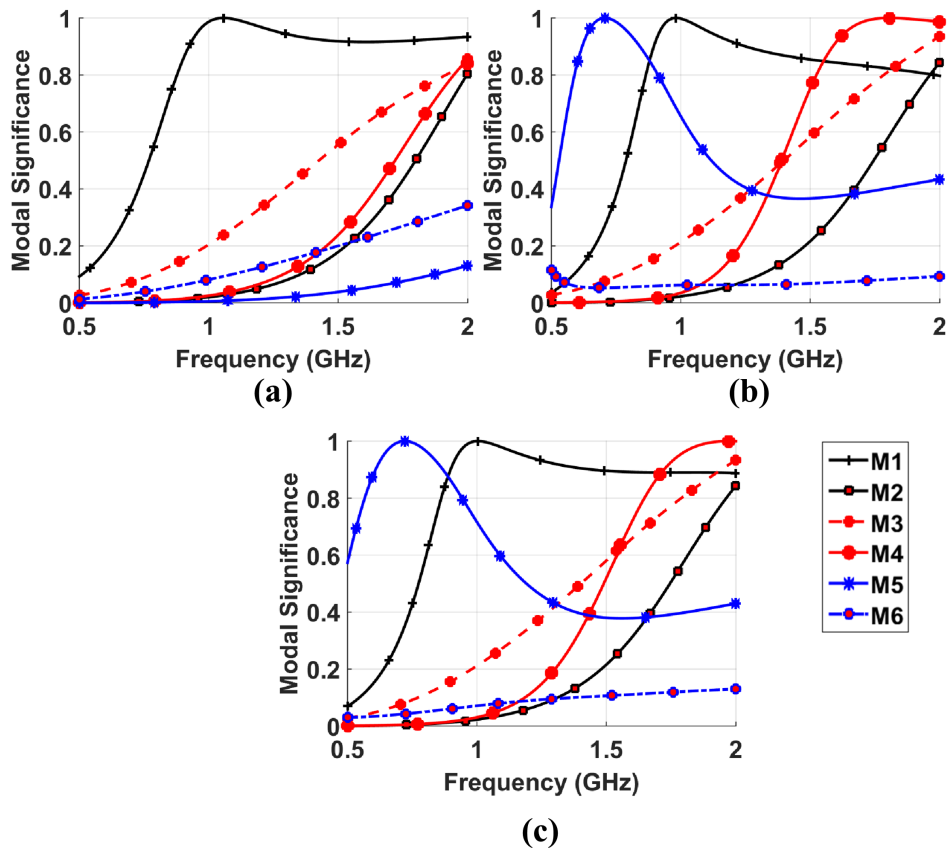


Figure 6.6: Modal Significance curves (a) Chassis ( $120 \times 60mm^2$ ), (b) Design 3, (c) Design 4.



similar to design 3 it was observed that beyond 30 % reduction in the chassis the impedance BW is significantly affected. Here one thing shall be noted is that the chassis is decreasing the matching of the antenna but the current concentration for all the modes lie across the antenna so it means that the antenna is the main radiating element while the ground is playing a key role in the matching.

## 6.2 Conclusions

In this chapter, it was shown that for an antenna and chassis combination at frequencies  $> 1$  GHz the antenna is the main radiating element and chassis only plays role in the impedance matching, that is why a 90 % reduction in the chassis size for two different designs i.e. PIFA and Monopole did not affect its resonance (impedance BW). At lower frequencies the effect of chassis was more significant and the antenna was not significantly dependent on the chassis size until 30 % reduction in the chassis size. This is the reason that at lower frequencies the chassis contributes to coupling/isolation. Remember by the reduction in the ground plane we are not claiming that the form-factor shall be reduced but we wanted to emphasize that the use of mobile chassis as a main radiating element for frequencies greater than 2 GHz is unrealistic and unpractical. Moreover, the effect of practical antenna elements on chassis modes in smart phone backplanes is investigated. It is observed that different antenna types affect the chassis modes significantly and differently and CM current maxima shifts towards the antenna element, that is why pure excitation of single CM is not possible.

## CHAPTER 7

# A NEW CURRENT MODE FOR PRACTICAL ANTENNAS

*“You are not a drop in the ocean*

*You are the entire ocean, in a drop”*

---

— JALĀL AD-DĪN MUHAMMAD RŪMĪ

In many existing works [63, 94, 118–120, 123–125, 194] mobile chassis was considered as the main radiating element for frequencies greater than 1 GHz and the chassis modes were excited. Remember that all these antennas have different applications such as MIMO, pattern reconfigurability and wide-band but the common thing is that all of them rely on the chassis as the main radiator. The main reason of using the chassis modes was the ease in the excitation of the chassis modes through an ICE or CCE. In reality (practical scenarios), we do not rely on the chassis as the main radiating element but instead we rely on the antenna elements as shown in [224]. In [186], only the placement of the antennas on the

chassis was investigated to get enhanced isolation. As the antennas were present at the lower frequency, only one chassis mode was discussed. The method is not applicable for higher frequency ( $> 1$  GHz) because at higher frequencies more than one mode is present. Secondly, the effect of the antenna behavior on the chassis mode was not investigated. Does the presence of these antenna elements effect the chassis mode and whether its presence creates any new modes? This chapter answers all these questions that were not addressed in previous works.

## 7.1 Analysis Process

To investigate the effect of real antenna elements, we consider 3 different practical printed antenna designs, i.e. PIFA [183], monopole [184] and a loop antenna all operating at 2.2 GHz. Three different antenna types were used to observe the behavior of different antenna elements on the chassis. PIFA and monopole antennas are designed on an RO4350 substrate having a dielectric constant of 3.48 while the loop antenna is designed on an FR4 substrate having a dielectric constant of 3.8. The thickness of the substrate is 0.8 mm. The chassis size for all the designs is taken  $120 \times 60$  mm<sup>2</sup>. The geometries of all the three designs are shown in Figure 7.1. The impedance BW of the antennas are shown in the Figure 7.2, where we can observe that the antennas are resonating around 2.2 GHz. The modes of the chassis in a desired BW are identified based on the eigenvalue zero crossing of the mode. The modal significance (MS) is an alternative representation of the eigenvalue. The half power radiating BW is represented by an MS value

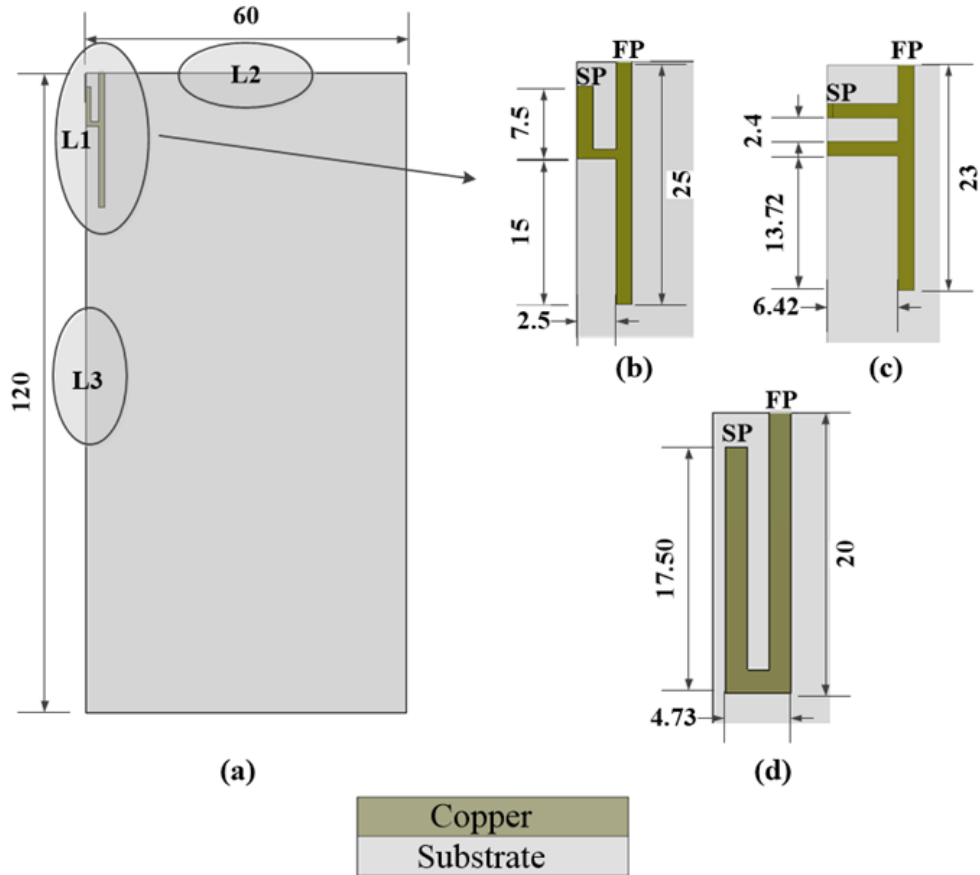


Figure 7.1: Design geometries, where (a) Antenna element on chassis showing different locations for the placement of the antenna. L1, L2 and L3 refers to the placement of the antenna at the corner, middle of the short edge and middle of long edge respectively, (b) Design 1, PIFA, (c) Design 2, Monopole and (d) Design 3, Loop antenna. SP and FP represents the shorting point and the feeding point respectively. All the dimensions are in mm.

of 0.707 ( $\lambda_n = \pm 1$ ). The impedance BW is calculated in the presence of the excitation sources and is the range of frequencies for which the antenna has good impedance matching ( $VSWR < 2.0$ ).

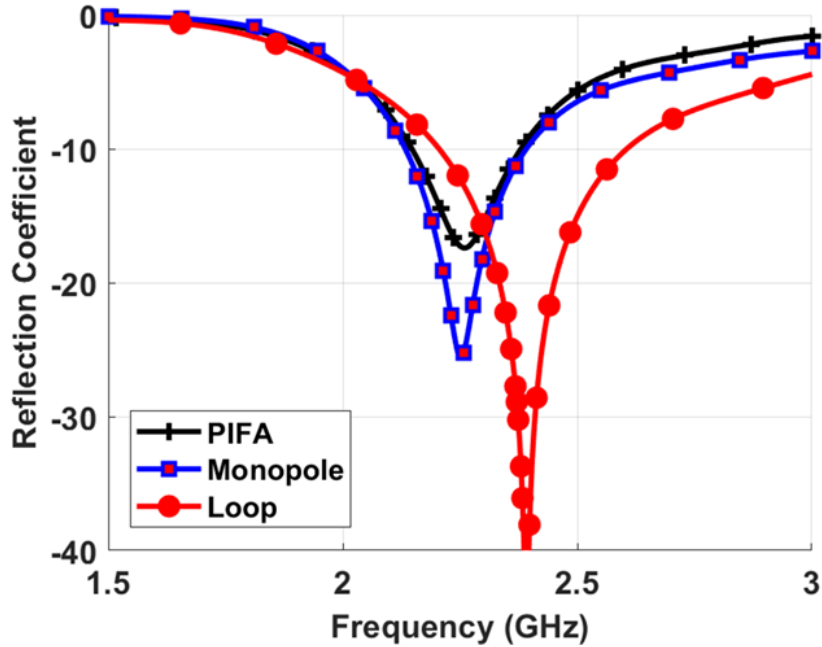


Figure 7.2: Reflection Coefficient curves for the three antennas.

## 7.2 Effect on Chassis Modes

We systematically analyzed the design in order to investigate the effect of real antenna elements on chassis modes and also to observe or investigate the effect on the chassis modes when the antenna is placed at different locations on the chassis. The chassis modes are identified as shown in Figure 7.3. While the CM current distribution and the MS plot are shown in the Figure B.4(1a-1f) and B.5(a) respectively.

A total of 9 cases were investigated. Three designs and each design placed at three distinct locations on the chassis, i.e. corner of the chassis, middle of the short arm (width arm) and middle of the long arm (longitudinal arm) as shown in Figure 7.1. From Figure B.4 and B.5, we can observe that different antennas are effecting the chassis modes differently. Table 1 shows the effect of different

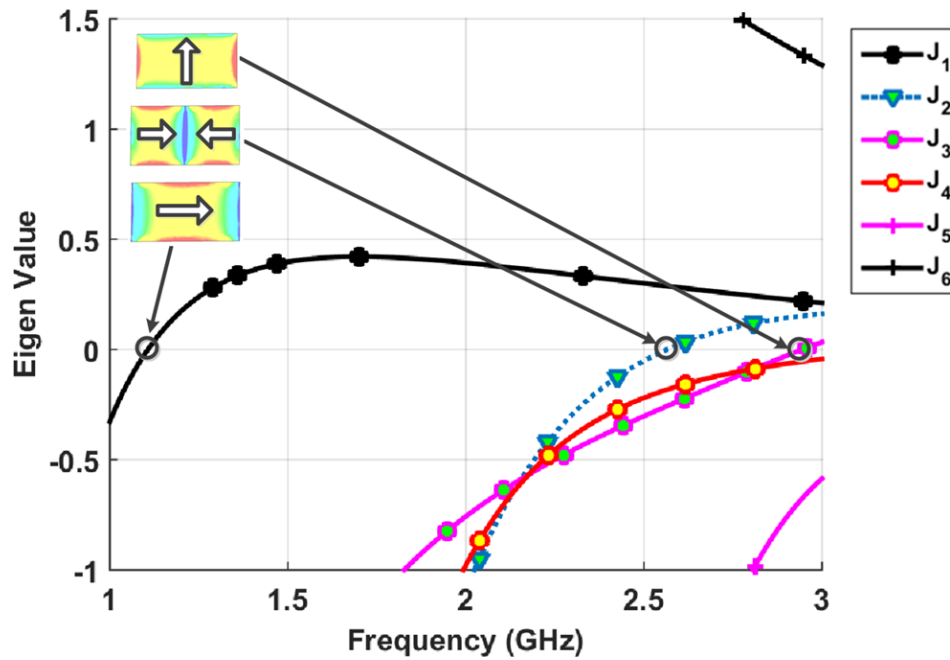


Figure 7.3: Eigenvalues of the first six characteristic modes (J1-J6) of chassis  $120 \times 60 \text{ mm}^2$

antennas on the radiating BW of the chassis modes. We can observe that for all the three antenna designs the CM current of mode 1 is severely affected and this is the reason that its radiating BW is also severely affected while mode 3 current distribution is not affected for all the three designs, that is why we do not observe any shift in the radiating BW of mode 3 as shown in Figure B.5 and Table 7.1. Mx refers to mode-x while NC represents that the modes is not contributing in the desired BW of interest i.e. from 0.5GHz to 3.0 GHz. Starting Frequency refers to the frequency at which mode x starts contributing to the radiating BW. WC refers to width center and LC refers to the Longitudinal center. Modes 2, 4, 5 and 6 are affected differently for different antenna types. Mode 5 is severely affected in case of Design 1, i.e. PIFA, and is no more contributing in the desired BW of

Table 7.1: Comparison of MS curves to observe the effect of the antenna on the chassis modes.

	Gnd	PIFA	Monopole	Loop	PIFA_WC	PIFA_LC
	Starting Frequency (GHz)					
M1	0.84	0.84-2.4	0.84-2.8	0.83-2.52	1.0-2.44	0.97-2.57
M2	1.93	1.89	1.88	1.87	2.22	2.2
M3	1.72	1.72	1.71	1.68	1.56	1.64
M4	1.86	1.78	1.79	1.71	1.9	1.91
M5	2.64	NC	2.35	2.63	2.93	NC
M6	NC	NC	NC	NC	NC	NC

interest while it is not affected in case of Design 3, i.e. loop antenna, as shown in Figure B.5 and Table 1. We can observe that chassis modes are affected in the presence of the antenna that is why further relying on the chassis modes and then placing the antenna according to it is not accurate because we already observed that such placement totally affects the CM. The interesting part is that all current maxima are shifted to the antenna element itself. There are high currents on the chassis but the current on the antenna is also maximum.

To observe the behavior of the placement of these antennas at different locations on the chassis we placed the antennas at the prescribed locations as shown in Figure 7.1 and analyzed them using TCM. We observed that for the same antenna placed at different locations on the chassis, the chassis modes are effected differently. Observe Figure B.4 (5a-5f) and B.4(6a-6f) for design 1. Mode 1 CM current distributions are significantly affected that is why we observe a significant effect on the radiating BW of mode 1. Unlike the previous case (corner case

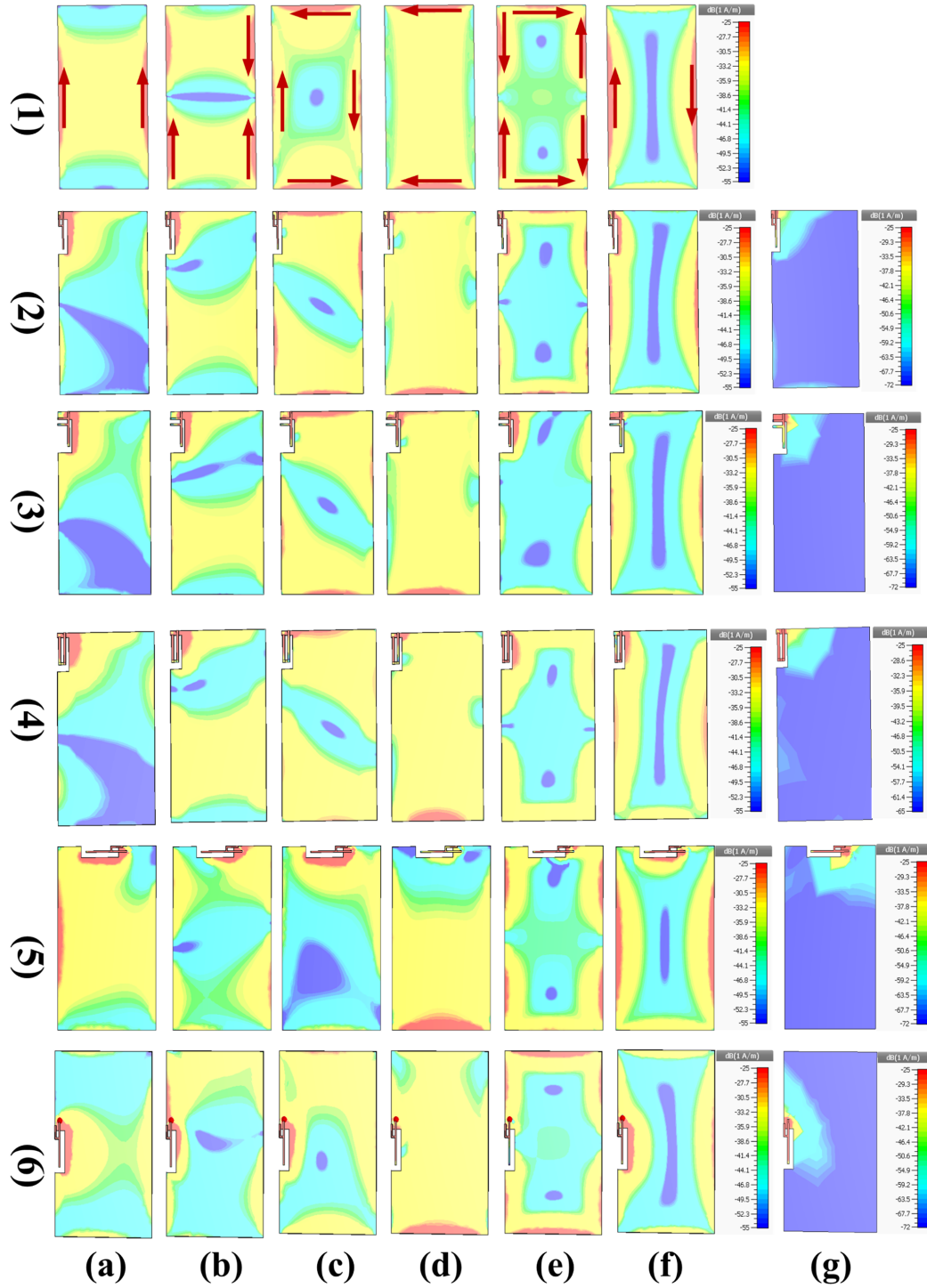


Figure 7.4: CM current distribution, where (a)-(f) represents the mode 1 to 6 and (g) represents the newly generated mode of (1) Ground plane, (2) Design 1, PIFA located at the corner of the chassis, (3) Design 2, Monopole located at the corner of the chassis, (4) Design 3, Loop antenna located at the corner of the chassis, (5) Design 1, PIFA located at the middle of the shorter edge and (6) Design 1, PIFA located at the middle of the longer edge.



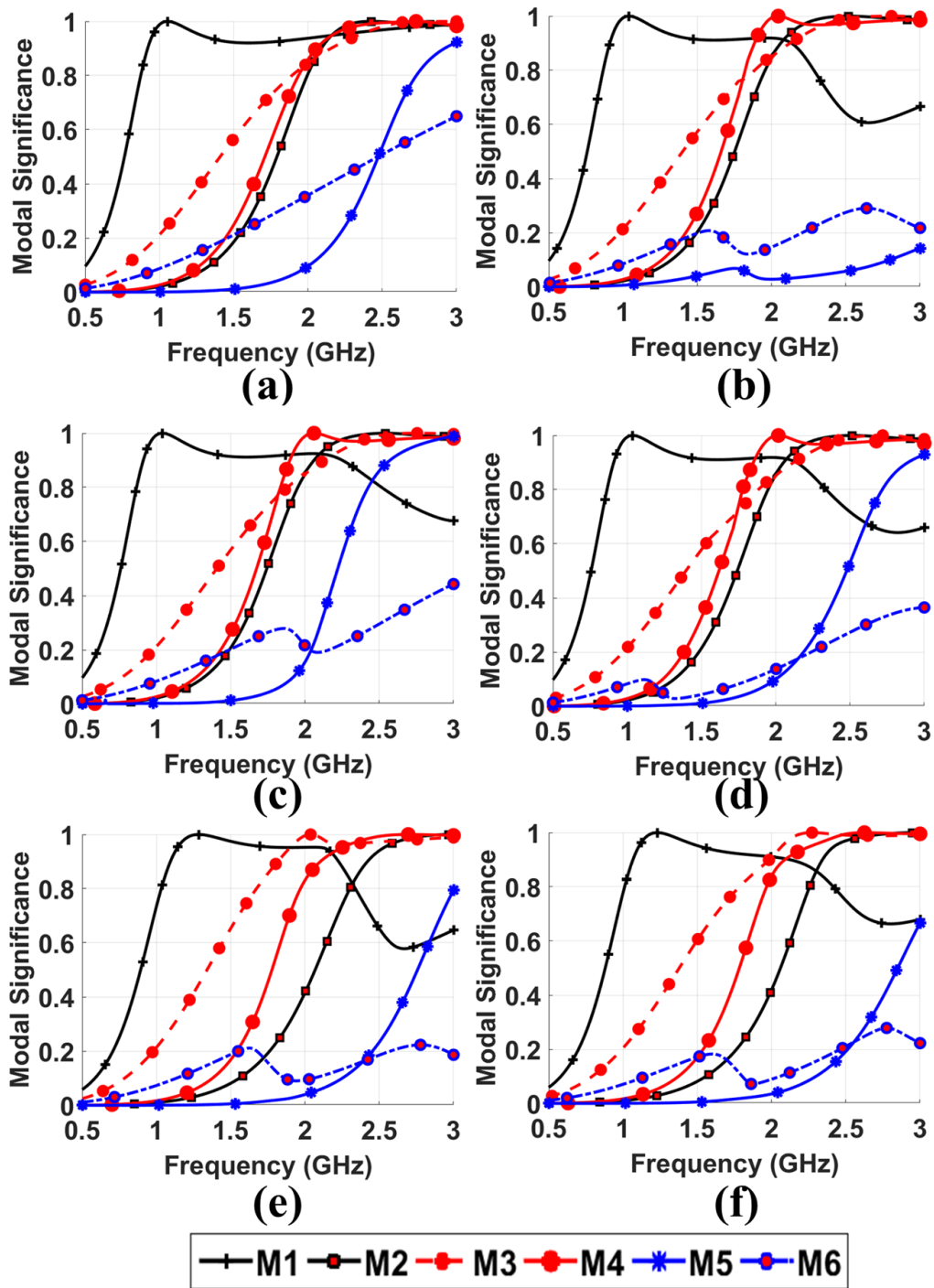


Figure 7.5: Modal Significance curves (a) Chassis ( $120 \times 60 \text{ mm}^2$ ), (b) Design 1, PIFA, (c) Design 2, Monopole, (d) Loop antenna, (e) Design 1, PIFA located at width (shorter edge) center, (f) PIFA located at longitudinal (longer edge) center.

i.e. L1), mode 3 CM current distribution and MS curves are affected when the antenna is placed at the shorter edge of the chassis as shown in the Figure B.4 (5c) and B.5(e), respectively. More detailed analysis on the effect on the radiating BW of the antenna is shown in the Table 1. Similar behavior was observed for designs 2 and 3 where the chassis modes were affected differently as compared to the antenna placed at the corner of the chassis (L1) but because of limited page count the results are not shown here. This study confirms that different placement locations of the antenna on the chassis affect the modes differently. One thing should be noted that irrespective of the location, for all the cases there is a significant current concentration for all the modes on the surface of the antenna. This confirms that further relying on the chassis modes and not investigating the modes in the presence of the antenna is neither realistic nor a practical approach.

### 7.3 Antenna Mode Generation

In the previous section, we discussed that the placement of the antenna affects the chassis modes noticeably. Another interesting observation is that the presence of the antenna generates a new mode that was not present initially as a chassis mode. It appeared because of the presence of the antenna as shown in Figure B.4 (2g-6g). The current is concentrated on the antenna only and there is no current present on the chassis, this has never been identified before. The current distribution for the new antenna mode is plotted on a different scale because if the current was plotted on the same scale as was used for modes 1 to 6 in Figure B.4, we would

have observed current concentration across the antenna element only and there will be no current present on the chassis which would have been very difficult for the reader to observe. Kindly note that the current lower scale is reduced but the upper scale remains fixed. For the new mode, the current is concentrated across the antenna element so we can call this mode as an antenna mode. We shall remind the reader that if we carefully observe the current concentration on all the modes, we observe that for almost all the modes the currents are maximum across the antenna element itself.

We already know that the antenna location affects the chassis mode differently. So, to observe the effect of the antenna location on this new antenna mode, let us consider all the 9 cases again. We observe that the antenna mode is not location dependent on the chassis but it is dependent on the antenna geometry only that is why for a specific design the antenna mode always has the same radiating BW as shown in the Figure B.6. It confirms that the antenna mode depends on the antenna element and not on the chassis.

## **7.4 Antenna Mode Excitation**

The new antenna mode is present at very low frequency. If we can purely excite the newly generated antenna mode, it will help in getting large miniaturization factors. The excitation of a specific mode can be possible either through use of CCE or ICE excitation. To excite a mode, an ICE is placed at the current maxima while the CCE is placed at the current minima of the mode. The problem is

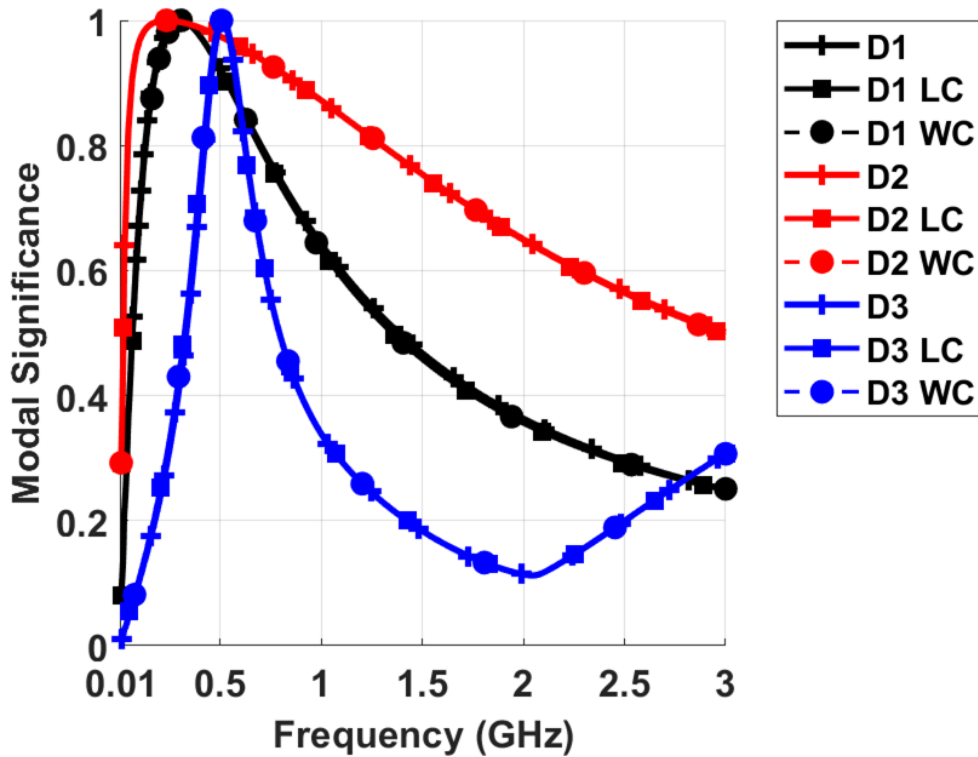


Figure 7.6: MS curve of the new antenna mode. D1 to D3 refers to the PIFA, Monopole and Loop antenna respectively. LC and WC refers to the cases when the antenna is placed at the center of the long arm, and short arm respectively.

that if an ICE is placed at the current maxima it will excite the antenna mode and several other modified chassis modes, as all the modes have current maxima at same location. This will deteriorate the performance of the system instead of getting the desired response [23]. If we carefully observe the current concentration of modes 1 to 6 for any design in Figure B.4, we can observe in all the modes, the antenna mode has a current maxima across the antenna element itself and the pure excitation is not possible for a single mode. This is the main reason that the antenna cannot resonate at lower frequencies. The excitation of such mode can be made possible by using or designing a new excitation technique. The study of

such a mode is very important and if we can find a method to excite the antenna mode only, we can achieve enhanced performance.

## 7.5 Conclusion

In this chapter, it is shown that relying on the chassis modes without considering the effect of the antenna element is not a realistic approach. We observed that different placement of the antennas at the chassis affect the chassis modes differently. In the presence of the antenna, all the antenna current maxima shift towards the antenna element itself. It is also shown that the presence of the antenna generates a new antenna mode for the first time. Remember that this mode is a new mode and it was not identified before. Also, the chassis modes are modified based on the location of the antenna on the chassis but the antenna mode depends only on the antenna element itself and not on the location of the antenna on the chassis. As the new antenna mode and all the modified chassis modes have current maxima at the same location that explains that the pure excitation of the antenna mode by using the existing methods of excitation like CCE or ICE is not possible. The analysis was conducted on three antennas at 2.2 GHz.

## CHAPTER 8

# SIW BASED MIMO ANTENNA

*“Raise your words not voice*

*It is rain that grows flowers not thunder”*

---

— JALĀL AD-DĪN MUHAMMAD RŪMĪ

Slotted Rectangular waveguide (SRWG) are widely used in radio communications due to their high gain, directivity, low side lobe level (SLL) and the ability to operate in harsh environments. The main disadvantage of these antennas is their large size. But for stationary applications such as base stations or access points the size is not an issue at all. The design of SRWG is well known in literature and several systematic methods are present to design such antennas [228, 229].

SRWG operates based on the concept that a slot provides a way for radiation of the internal fields and coming up with the proper size and combination of these slots give us a desired radiation pattern. SRWG can be of two types, Standing wave and traveling wave. Standing wave SRWG have broad side spectrum, the inter element spacing between the two slots is fixed at  $\lambda/2$ , it can be terminated

in a short circuit or matched load. Standing wave SRWG can be fed at the center or at the edge of the waveguide. Traveling wave SRWG can have tilts in the main beam, the inter-element spacing between the slots is not fixed. These varying distance between the slots helps in producing tilts in the beam. Desired low SLL can be achieved through the use of Dolph Tschebyscheff distribution or any other amplitude distribution and based on these amplitude values, offsets around the center of the waveguide can be calculated. Approximations are done in the calculation of these offsets.

Waveguides cannot be easily integrated with planar structures. Substrate integrated waveguides (SIW) have small size, light weight, low cost, low profile and the ability to easily integrate with planar structures are becoming widely used in literature. Beside such features, an SIW has the feature of high gain, high Front to Back (FBR) ratio and low cross polarization level like metallic waveguide antennas. SIWs are normally used in antenna arrays. An SIW utilizes a dielectric substrate that is plated on its top and bottom. Vias are used to short the top and bottom metal coated layers, thus creating the guided waveguide. To feed an SIW antenna, a connector and a microstrip to SIW transition is used.

## 8.1 Analysis Process

Genetic Algorithm (GA) optimizers are widely used due to their robustness. So, a GA [230] was modeled to effectively find the locations of the slots on the top wall of the SIW.

### 8.1.1 Genetic Algorithm

The stochastic search method of GA works on the concept of natural selection and evolution. In this work, a GA is applied to the SIW model to find the optimized position of the slots, i.e. offset and the position along x-axis as well as z-axis on the waveguide respectively, to achieve a specific beam tilt and SLL. The assumption is that the current on the surface of the slot is of a cosine nature. The inputs to the GA are the number of slots, the beam shift or tilt and the desired SLL. The current distribution on the surface of the slot is assumed to be found by the combination of infinitesimal dipoles. We started with an initial population of 40 chromosomes. The cost function was defined by the mean Square error (MSE) between the desired pattern to the calculated pattern. The main advantage of the GA is that it tell us about the feasibility of our design, whether with a particular number of slots, we can achieve our desired response or not without spending time with length full wave simulations.

Remember that the GA is not taking into account the effect of the mutual coupling between the slots that's happening because the slots are present in close proximity to one another. Also, to feed the antenna through a connector, we need to have a microstrip to SIW transition. Such transition severely affects the antenna performance. So, the GA algorithm gives us a rough estimate about the location and offset of the slot via a matlab script and we need to re-optimize the slots location and offset whenever we consider a real design, in a full wave model. The flow chart of the GA is shown in the Figure 8.1. The desired radiation pattern



is given as an input to the GA. An initial population of 40 chromosomes is selected. The 2 parameters that need to be optimized are the offset ( $x$ ) and the location ( $z$ ) of the slot on the top surface of SIW. The far-field Electric and Magnetic field components are calculated and the cost function that is the MSE between the desired pattern and the calculated pattern. If the MSE is minimized, we can get our optimized output else the chromosomes are ranked according to the least fit to the best fit criteria. 50% of the chromosomes are discarded. Cross over is done to create child and then a mutation rate of 0.5 was used. The process is repeated until and unless the MSE is minimized or the iterations limit is achieved.

### **8.1.2 Antenna 1 (tilt of $10^0$ )**

The GA algorithm was optimized for 10 slots at a desired SLL of 15 dB at 28 GHz. The desired and optimized normalized radiation patterns are shown in Figure 8.2. We can observe that it was not possible to exactly obtain a -15 dB of SLL. A traveling wave SIW slot array was designed based on the offset and location of the slot from the GA.

A microstrip to SIW transition was introduced to properly feed the antenna. The presence of the transition greatly affected the antenna response. The location and the offset of the slots were optimized again to have a better performance and the desired pattern tilt was achieved. The geometry of the proposed design is shown in Figure 8.3. The offset and the location of the slots is shown in Table 8.1. The simulation was very well matching the desired results. The reflection

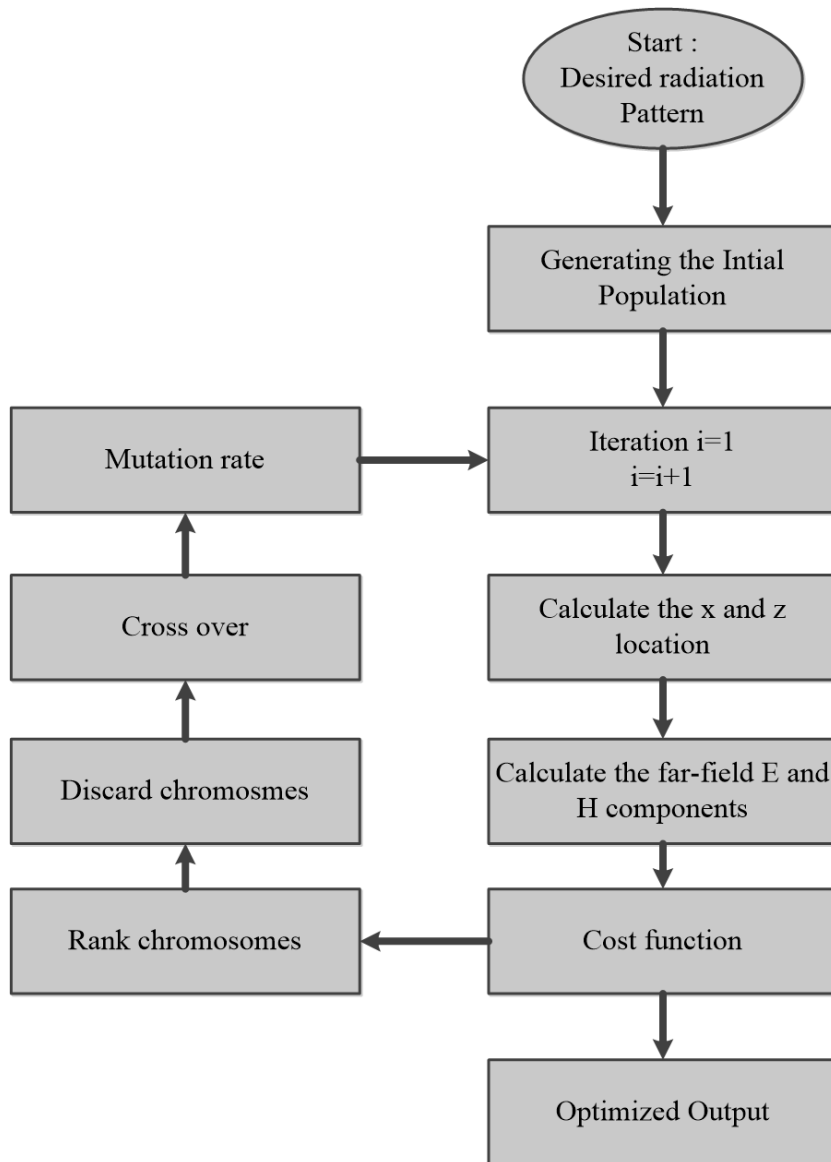


Figure 8.1: Genetic Algorithm (GA) flow chart.

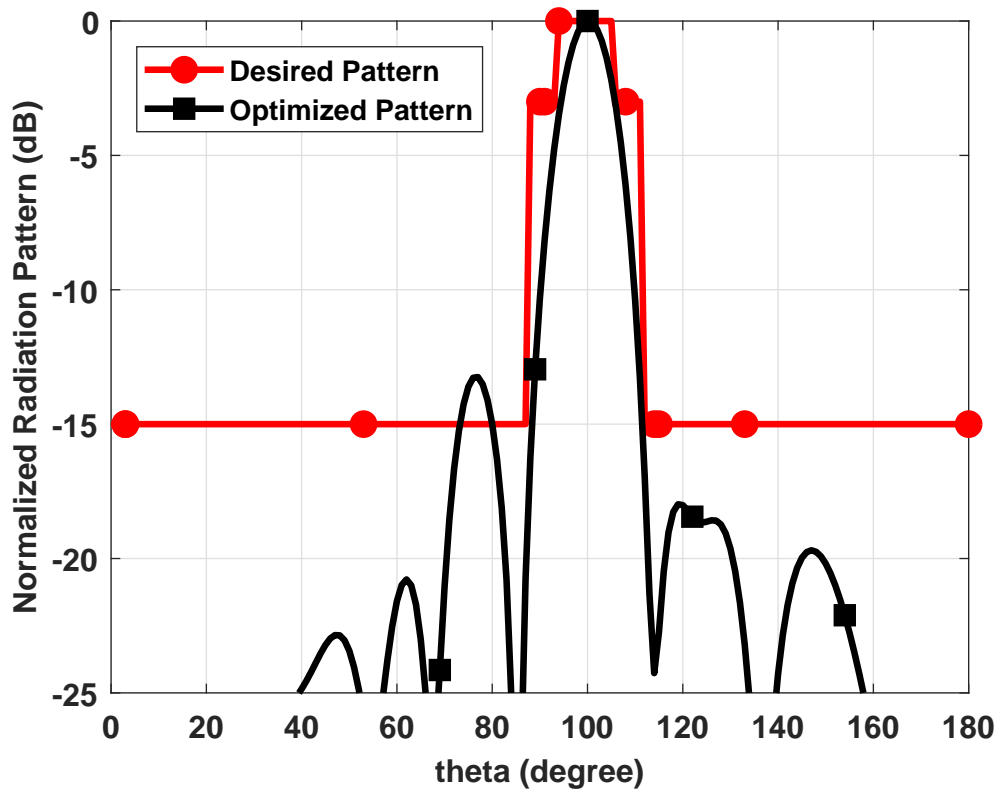


Figure 8.2: The desired normalized radiation pattern and the GA algorithm based optimized radiation pattern for a  $\theta$  cut at  $\phi = 270^0$ .

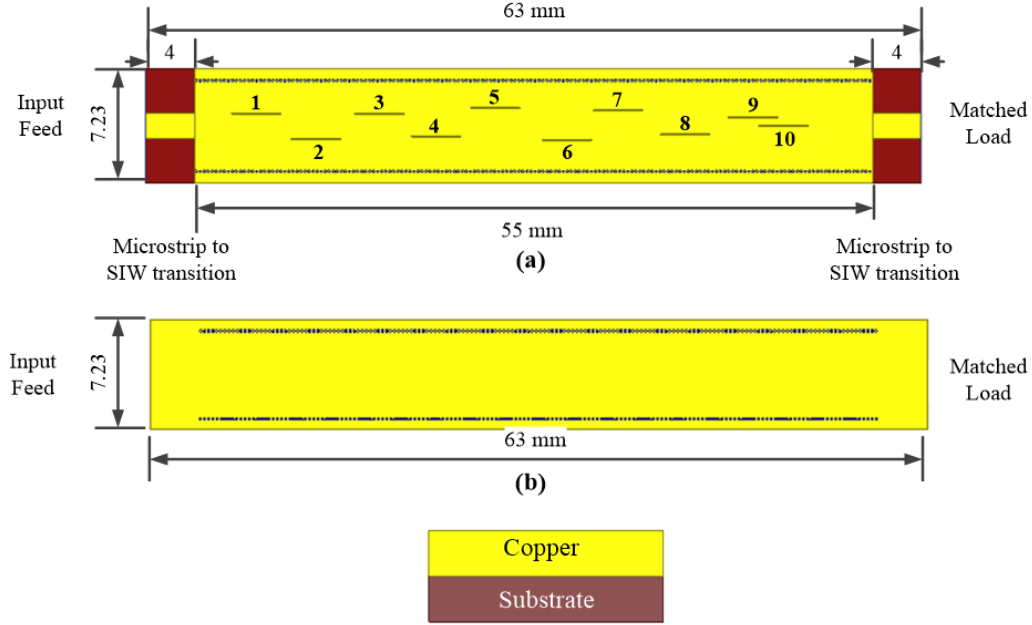


Figure 8.3: Design geometries, where (a) Top view showing the locations of different slots on the top conductors and (b) bottom view. All the dimensions are in mm.

coefficient of the proposed design is shown in the Figure 8.4. We can observe a very wide -10 dB impedance BW.

The 3D radiation pattern of the proposed design at different frequencies is shown in the Figure 8.5. We can observe that for all the desired frequencies we are having a tilt of  $10^0$  or is within the HPBW at least. The tilt of  $10^0$  over here is referring to the beam at  $100^0$ , because the antenna is lying in the xz plane, with its width along x-axis and length along z-axis. To be more quantitative, the 2D normalized rectangular radiation pattern plots at different frequencies for a  $\theta$  cut at  $\phi = 270^0$  is shown in Figure 8.6. To more accurately trace the tilt in the pattern, the scale of the  $\theta$  is limited between  $0^0$  to  $180^0$  as shown in Figure 8.7. We can observe from Figures 8.5 and 8.6 that a SLL of at least 8.5 dB was

Table 8.1: The offset and location of the slots on the top conductor of the SIW in Figure 8.3, for a tilt of 10 degrees in the beam. All numbers are in mm.

Slot Number	Offset (x axis)	Slot location (z axis)
1	0.98520	0.00000
2	-1.07025	4.82912
3	0.94976	10.03008
4	-0.81509	14.62258
5	1.39629	19.43480
6	-1.11278	25.26113
7	1.20492	29.41418
8	-0.69460	34.86867
9	0.66625	40.35697
10	0.00000	42.88743

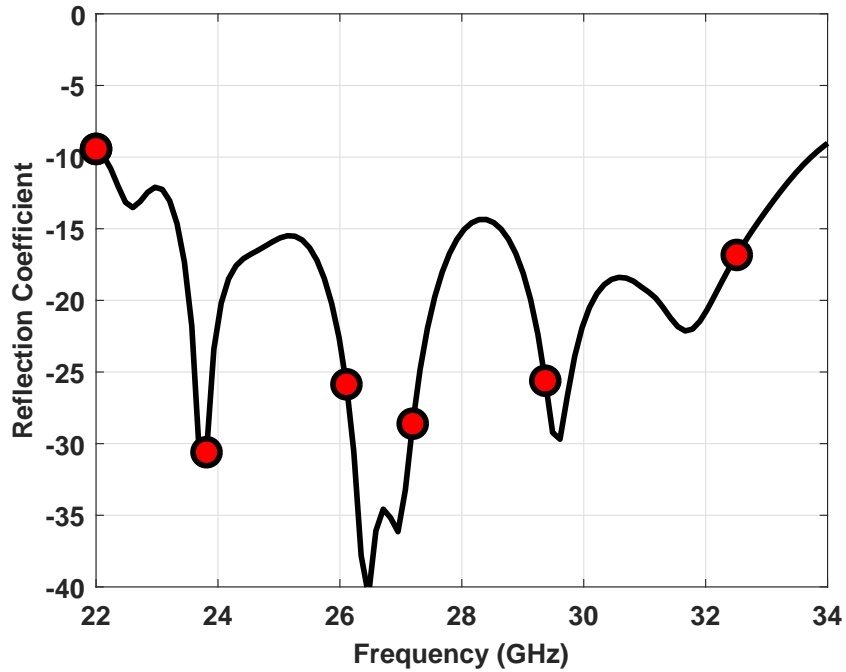


Figure 8.4: Reflection coefficient of the SIW antenna in Figure 8.3.

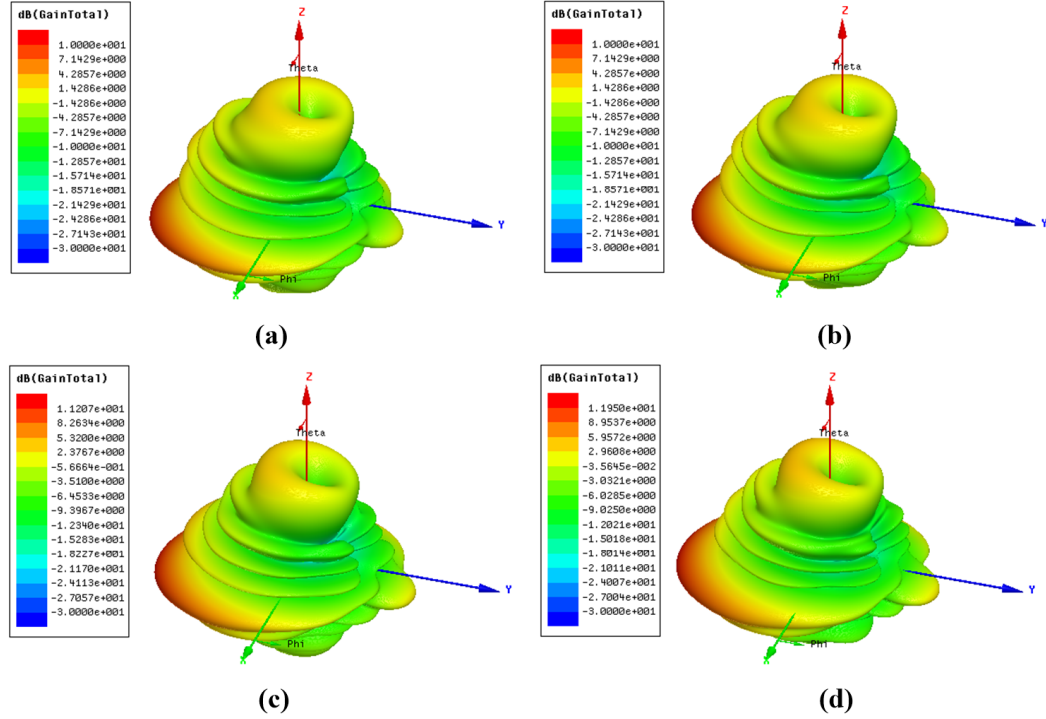


Figure 8.5: The 3D radiation pattern showing a tilt of 10 degrees at different frequency band where, (a) 28.75 GHz, (b) 29 GHz, (c) 30 GHz and (d) 31.5 GHz

obtained. At 30 GHz the antenna is pointing at  $100^\circ$  ( $10^\circ$  tilt) but with changing frequency the tilt is varying. At 28.7 GHz and 32 GHz the radiation main beam is pointing at  $105^\circ$  and  $94^\circ$  respectively.

### 8.1.3 Antenna 1 (tilt of $-10^\circ$ )

To get a tilt of  $-10^\circ$  (referring to the beam at  $80^\circ$ ), we just need to change the direction of the feeding. Our antenna has two ports as shown in the Figure 8.3, feeding port and matched load. If we inter-change their positions, we can get a tilt in the negative direction. The 3D radiation patterns are shown in Figure 8.8.

We can observe that now the main beam is having a tilt of  $-10^\circ$ .

To be more quantitative, the 2D normalized rectangular radiation pattern plots

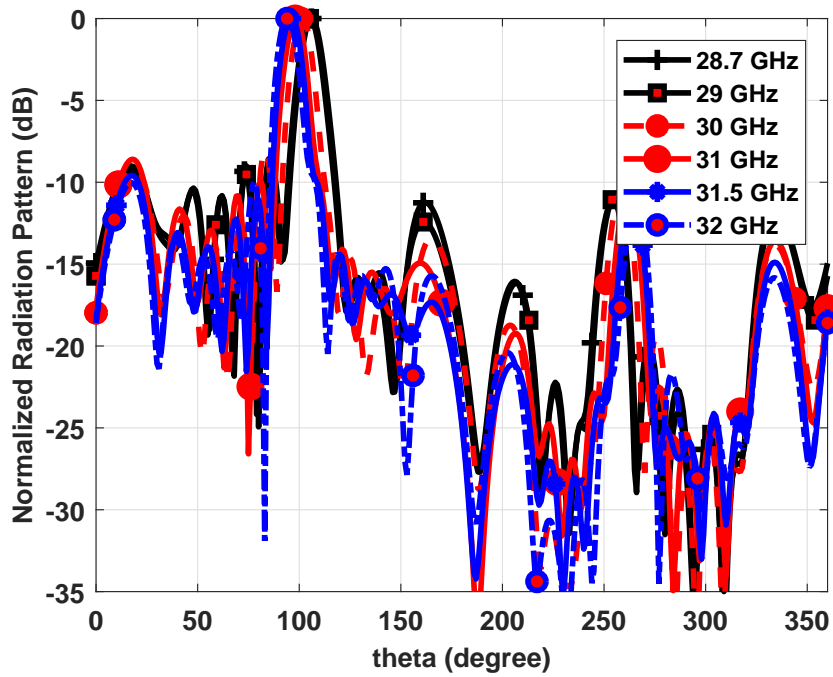


Figure 8.6: Normalized radiation pattern showing a tilt of 10 degrees at different frequency bands for a  $\theta$  cut at  $\phi = 270^\circ$ .

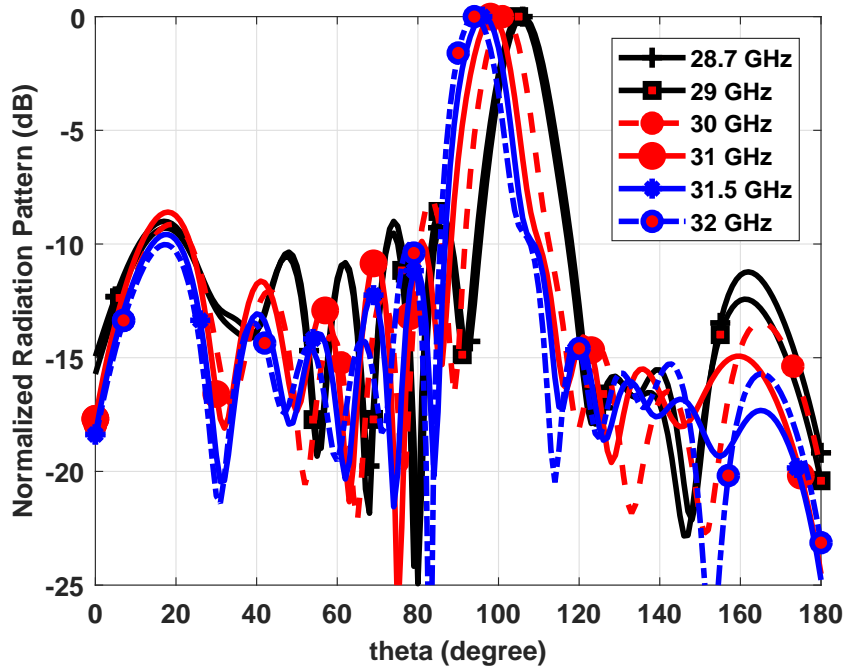


Figure 8.7: Normalized radiation pattern showing a tilt of 10 degrees at different frequency bands for a  $\theta$  cut at  $\phi = 270^\circ$ , limited between  $0^\circ \leq \theta \leq 180^\circ$ .

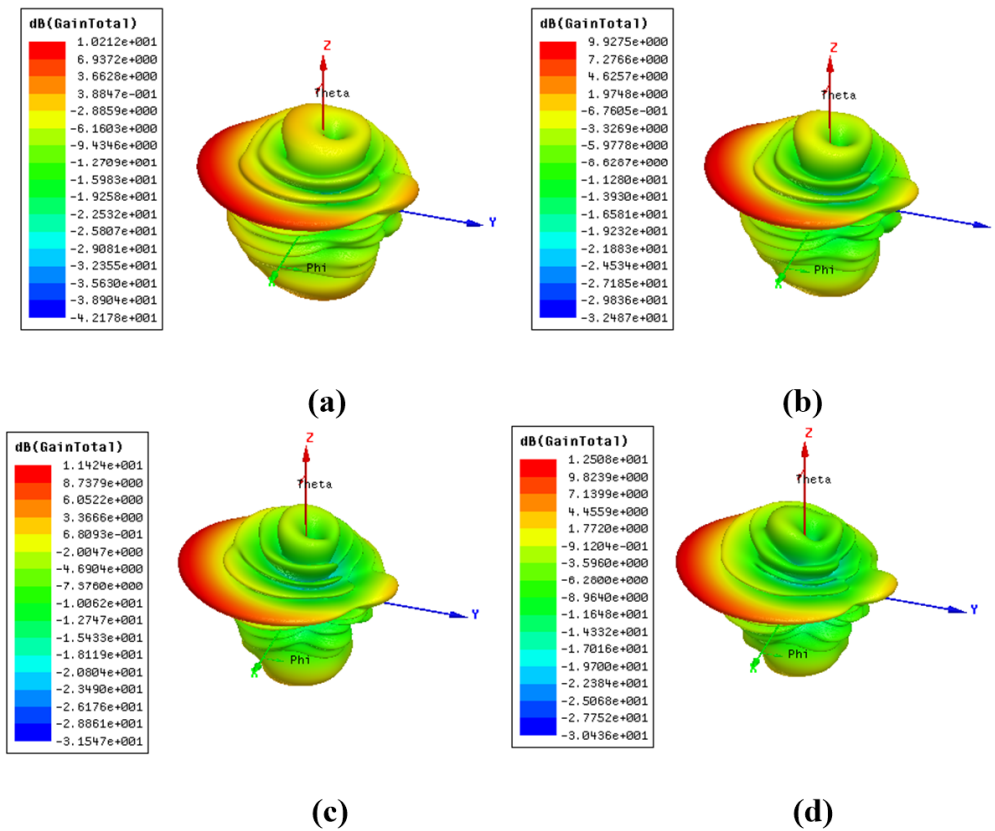


Figure 8.8: The 3D radiation pattern showing a tilt of  $-10^\circ$  at different frequency band where, (a) 28.75 GHz, (b) 29 GHz, (c) 30 GHz and (d) 31.5 GHz



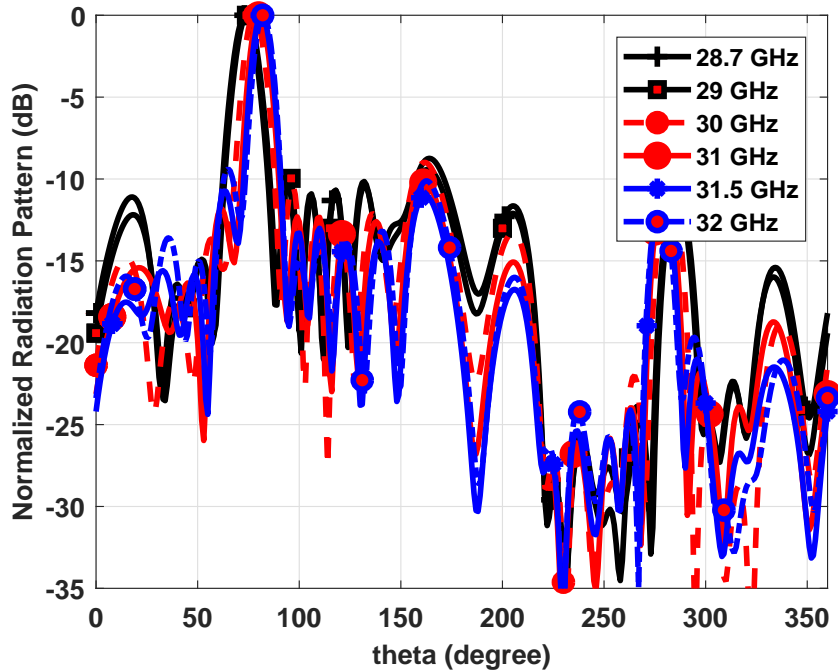


Figure 8.9: Normalized radiation pattern showing a tilt of  $-10$  degrees at different frequency bands for a  $\theta$  cut at  $\phi = 270^0$ .

at different frequencies for a  $\theta$  cut at  $\phi = 270^0$  is shown in Figure 8.9. To more accurately trace the tilt in the pattern, the scale of the  $\theta$  is limited between  $0^0$  to  $180^0$  as shown in Figure 8.10. We can observe from Figures 8.8 and 8.9 that a SLL of at least 8.5 dB was obtained.

#### 8.1.4 Antenna 2 (tilt of $35^0$ )

The GA algorithm was optimized for 14 slots at a desired SLL of 15 dB at 28 GHz. The desired and optimized normalized radiation pattern are shown in Figure 8.11. We can observe that it was not possible to exactly obtain a -15 dB of SLL. A traveling wave SIW slot array was designed based on the offset and location of the slot from the GA. The simulation was very well matching to the results.

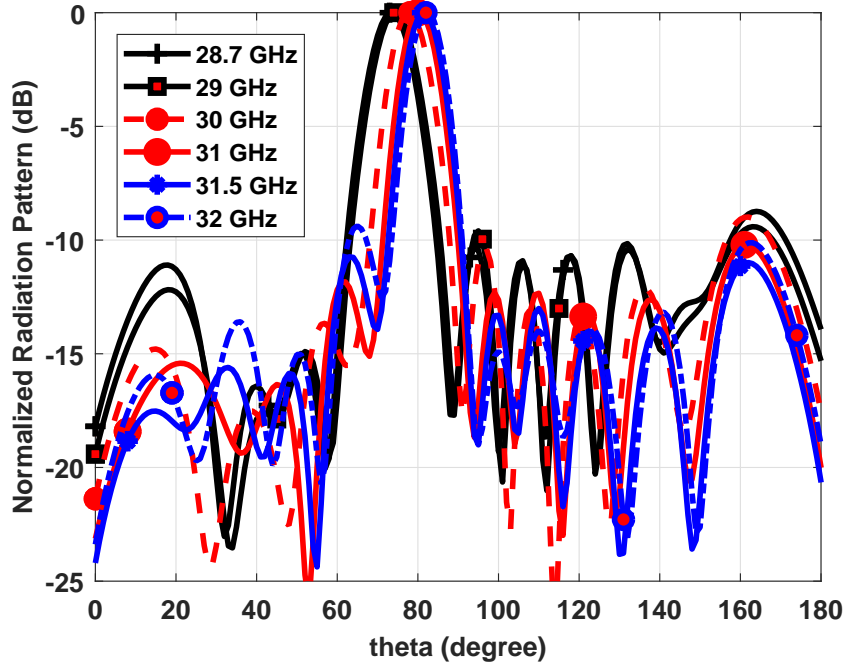


Figure 8.10: Normalized radiation pattern showing a tilt of  $-10$  degrees at different frequency bands for a  $\theta$  cut at  $\phi = 270^0$ .

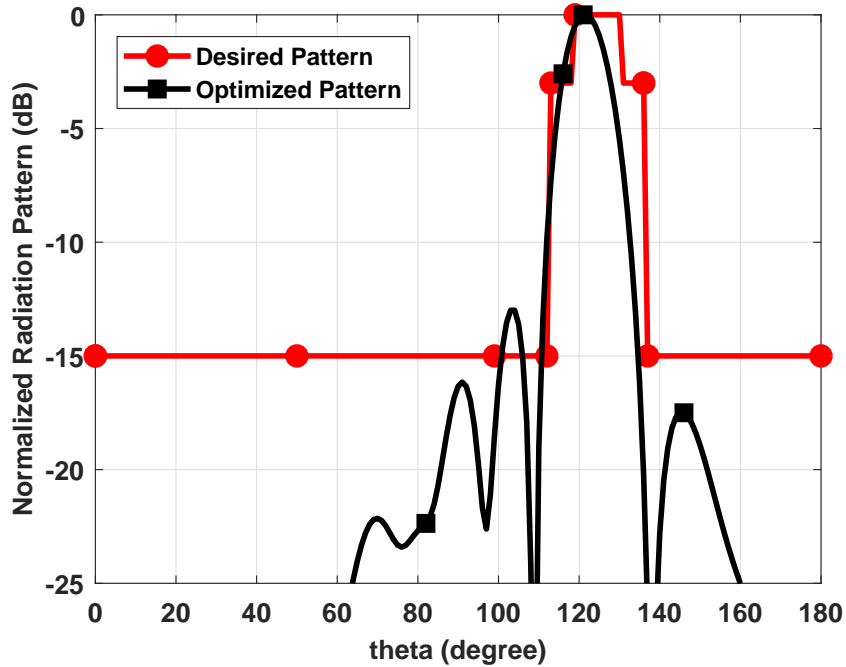


Figure 8.11: The desired normalized radiation pattern and the GA algorithm based optimized radiation pattern for a 14 element slot SIW with a  $\theta$  cut at  $\phi = 270^0$ .

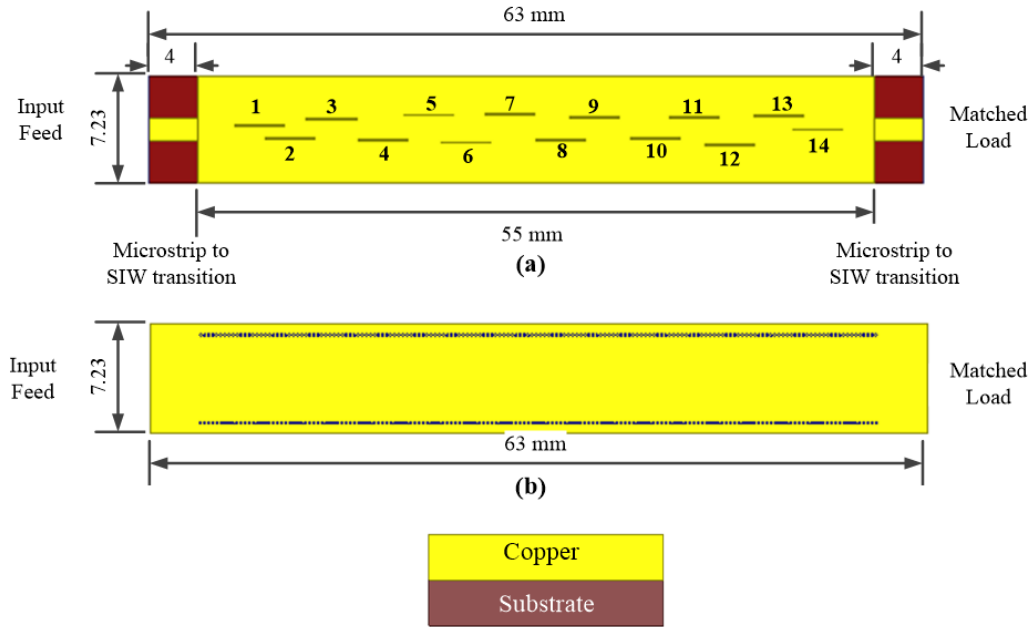


Figure 8.12: Design geometries, where (a) Top view showing the locations of different slots on the top conductors and (b) bottom view. All the dimensions are in mm.

An microstrip to SIW transition was introduced to properly feed the antenna. The presence of the transition greatly affected the antenna response. The location and the offset of the slots were optimized again to have a better performance and the desired pattern tilt was achieved. The geometry of the proposed design is shown in Figure 8.12. The offset and the location of the slots are shown in Table 8.2. The reflection coefficient of the proposed design is shown in Figure 8.13. We can observe a very wide impedance BW.

The 2D normalized rectangular radiation pattern plots at different frequencies for a  $\theta$  cut at  $\phi = 270^\circ$  is shown in Figure 8.14. To more accurately trace the tilt in the pattern, the scale of the  $\theta$  is limited between  $0^\circ$  to  $180^\circ$  as shown in Figure 8.15. We can observe from Figures 8.14 and 8.15 that a SLL of at least 7 dB was

Table 8.2: The offset and location of the slots on the top conductor of the SIW for a tilt of 35 degrees in the beam. All numbers are in mm.

Slot Number	Offset (x axis)	Slot location (z axis)
1	0.390	0.000
2	-0.737	2.497
3	0.858	5.889
4	-0.886	10.076
5	1.255	13.773
6	-1.106	16.776
7	1.262	20.372
8	-0.886	24.491
9	1.035	27.359
10	-0.787	32.222
11	1.063	35.446
12	-1.283	38.264
13	1.120	42.383
14	-0.007	45.454

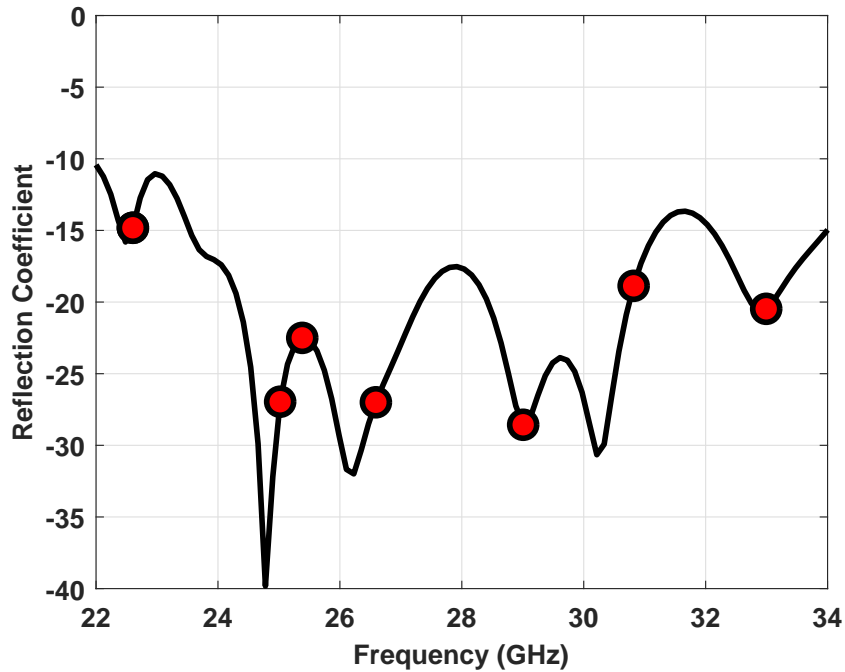


Figure 8.13: Reflection coefficient of antenna.

obtained. At 30 GHz the antenna is pointing at  $120^{\circ}$  ( $30^{\circ}$  tilt) but with changing frequency the tilt is varying. At 28.7 GHz and 32 GHz the radiation main beam is pointing at  $130^{\circ}$  and  $117^{\circ}$  respectively.

To get a tilt of  $-35^{\circ}$  (referring to the beam at  $55^{\circ}$ ), we just need to change the direction of feeding. The 2D normalized rectangular radiation pattern plots at different frequencies for a  $\theta$  cut at  $\phi = 270^{\circ}$  is shown in Figure 8.16. To more accurately trace the tilt in the pattern, the scale of the  $\theta$  is limited between  $0^{\circ}$  to  $180^{\circ}$  as shown in the Figure 8.17. We can observe from Figures 8.16 and 8.17 that a SLL of at least 7 dB was obtained.

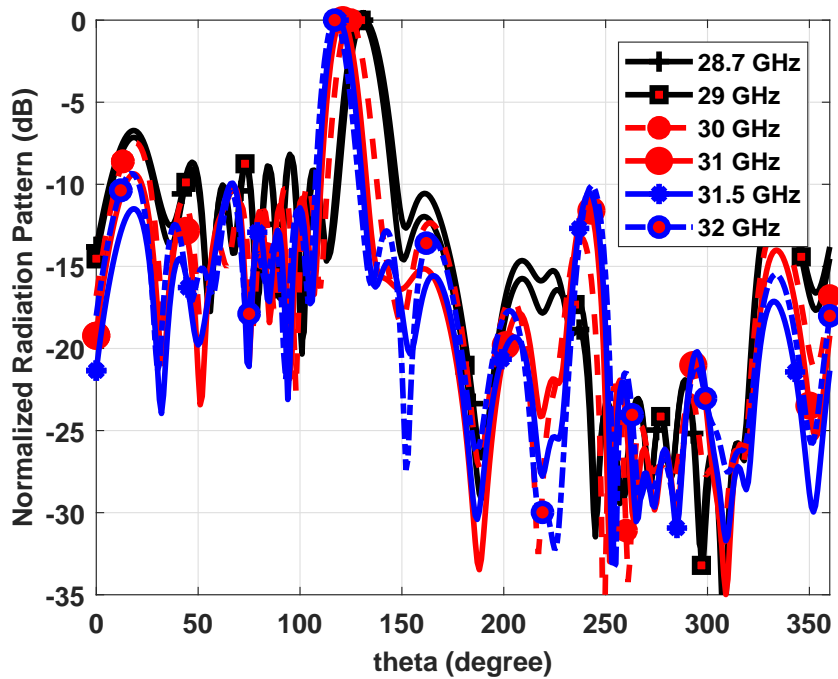


Figure 8.14: Normalized radiation pattern showing a tilt of 35 degrees at different frequency bands for a  $\theta$  cut at  $\phi = 270^0$ .

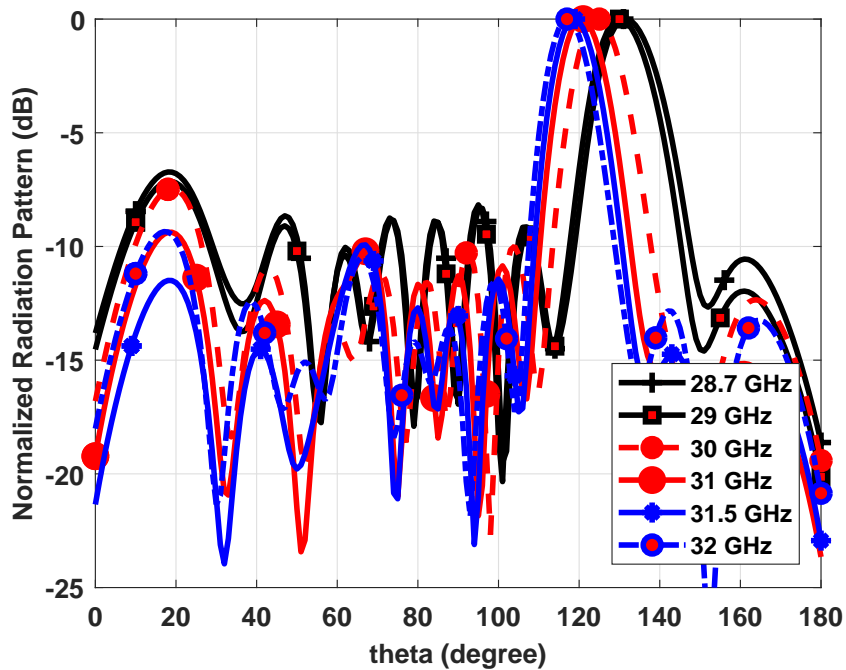


Figure 8.15: Normalized radiation pattern showing a tilt of 35 degrees at different frequency bands for a  $\theta$  cut at  $\phi = 270^0$ .

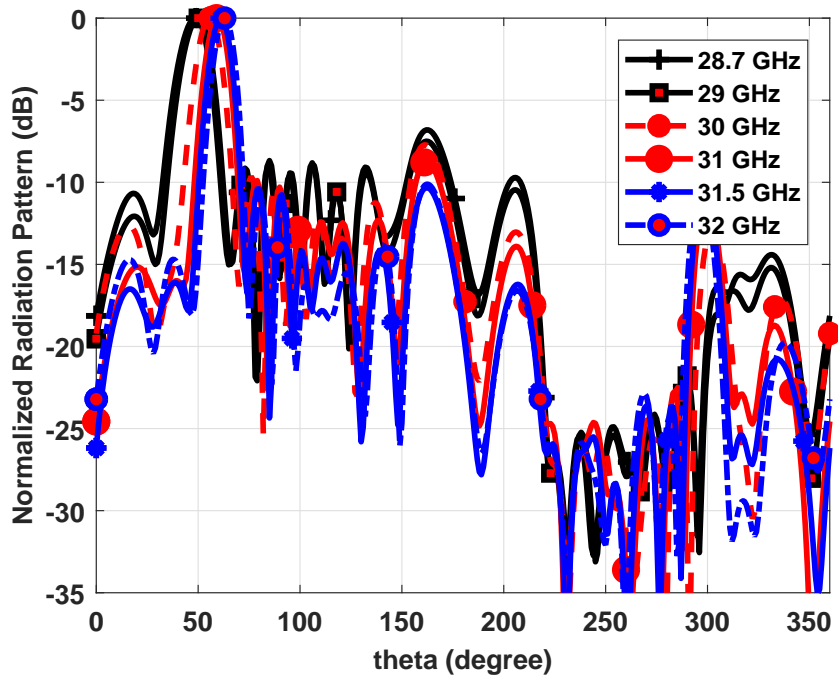


Figure 8.16: Normalized radiation pattern showing a tilt of  $-35$  degrees at different frequency bands for a  $\theta$  cut at  $\phi = 270^0$ .

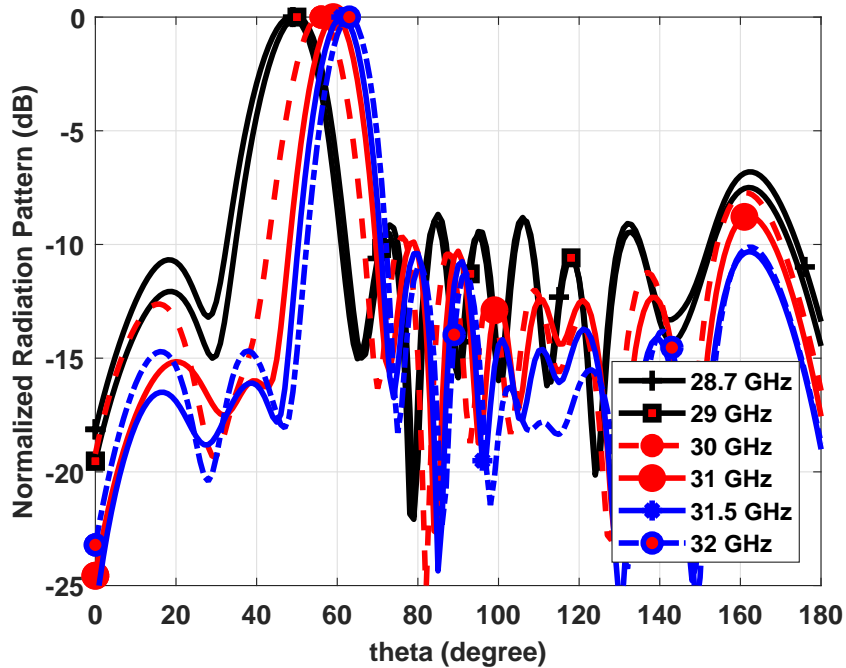


Figure 8.17: Normalized radiation pattern showing a tilt of  $-35$  degrees at different frequency bands for a  $\theta$  cut at  $\phi = 270^0$ .

### 8.1.5 4 element MIMO

The antenna elements were co-located to get a MIMO performance. The geometry of the proposed design is shown in the Figure 8.18. We can observe that we have 4 slotted SIW arrays. The reflection and the isolation curves of the array are shown in Figure 8.19 and 8.20 respectively. We can observe that the antenna is having very wide impedance BW and although the antennas are co-located but still we have significant isolation between the antenna elements.

The input feed 1 will produce a tilt of  $-10^{\circ}$  as shown in the Figure 8.21 and 8.22. We can observe that the SLL is affected due to the presence of the other antenna elements. The SLL is now 6 dB. The antennas are placed such that the adjacent antenna will have maximum spatial separation in terms of radiation pattern that is why the input feed 2 will produce a tilt of  $+30^{\circ}$  as shown in Figure 8.23 and 8.24. The input feed 3 will produce a tilt of  $-30^{\circ}$  as shown in the Figure 8.25 and 8.26. A tilt of  $10^{\circ}$  is produce by input feed 4 as shown in the Figure 8.27 and 8.28. The worst SLL is in the case of  $30^{\circ}$  tilt.



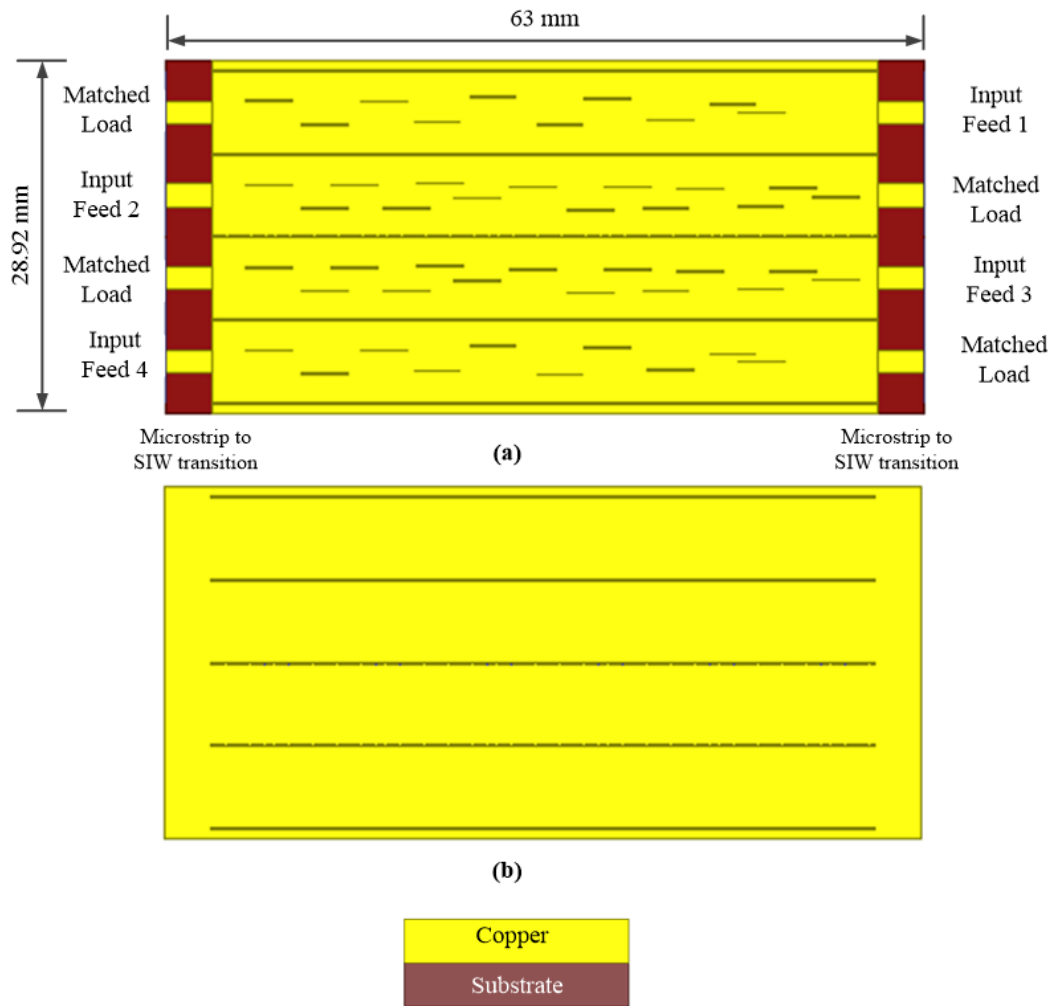


Figure 8.18: Design geometry of 4 element MIMO case, where (a) Top view showing the 4 antenna array and (b) bottom view. All the dimensions are in mm.

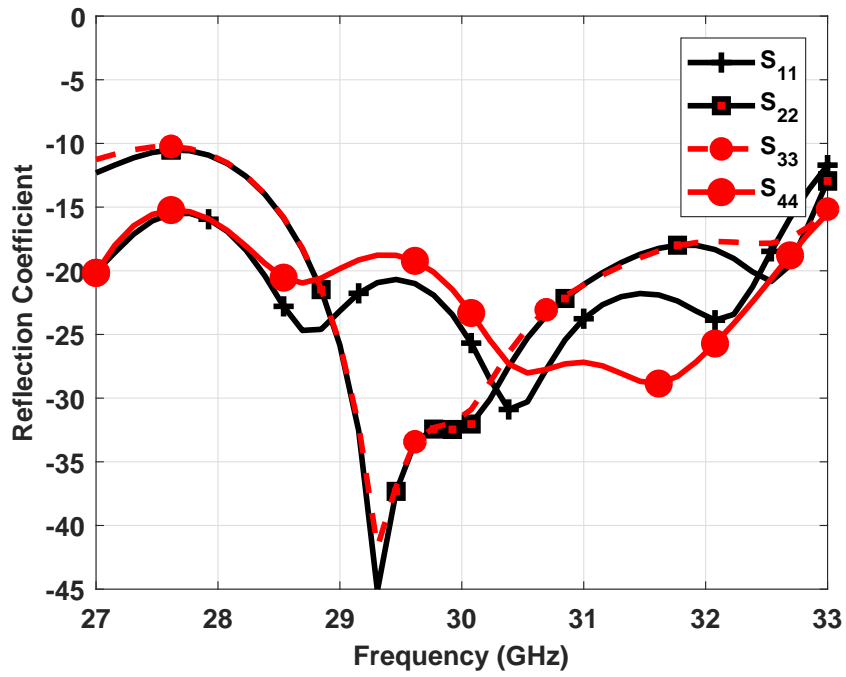


Figure 8.19: Reflection coefficient of 4 element MIMO.

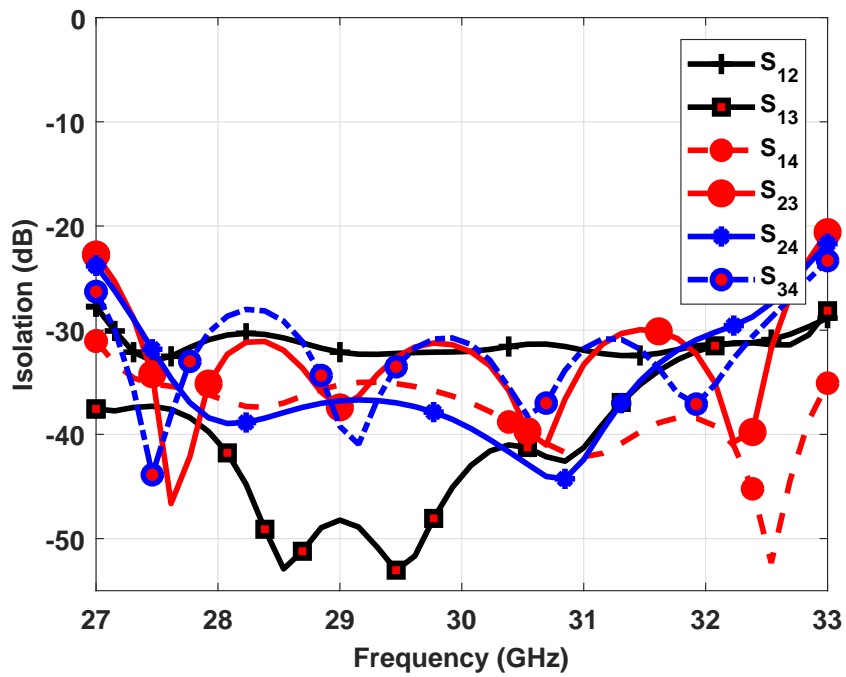


Figure 8.20: Isolation enhancement of 4 element MIMO.

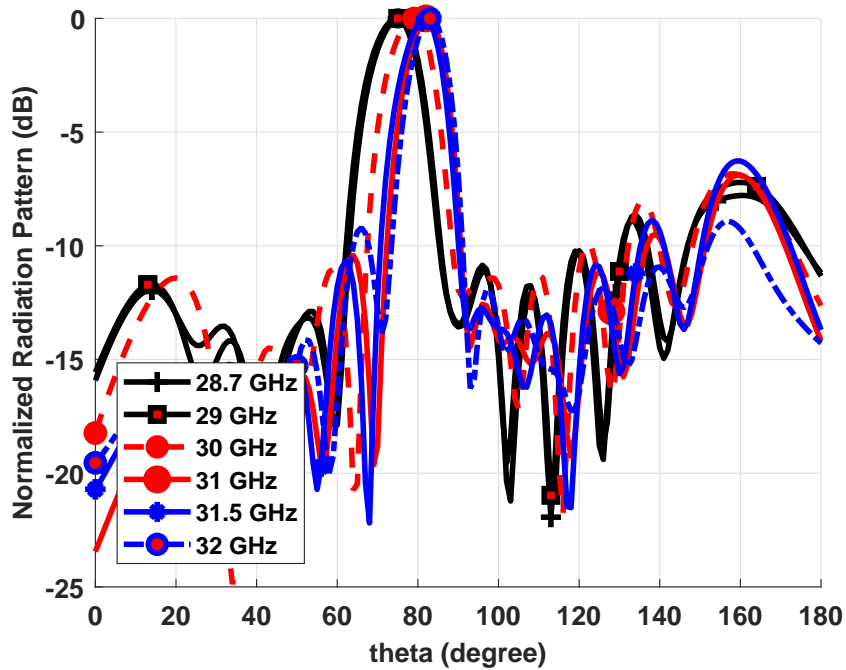


Figure 8.21: Normalized radiation pattern showing a tilt of -10 degrees at different frequency bands for a  $\theta$  cut at  $\phi = 270^0$  by antenna element 1.

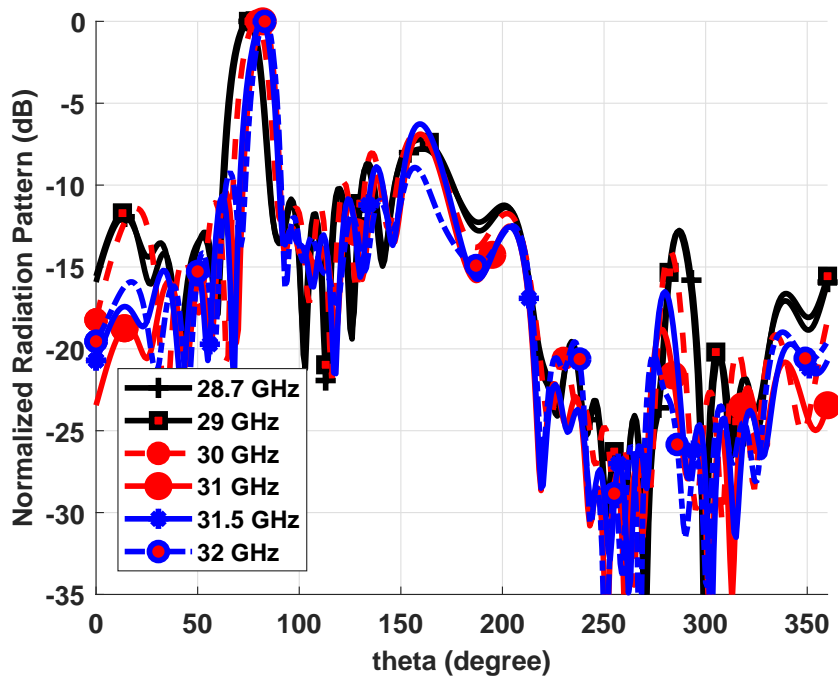


Figure 8.22: Normalized radiation pattern showing a tilt of -10 degrees at different frequency bands for a  $\theta$  cut at  $\phi = 270^0$  by antenna element 1.

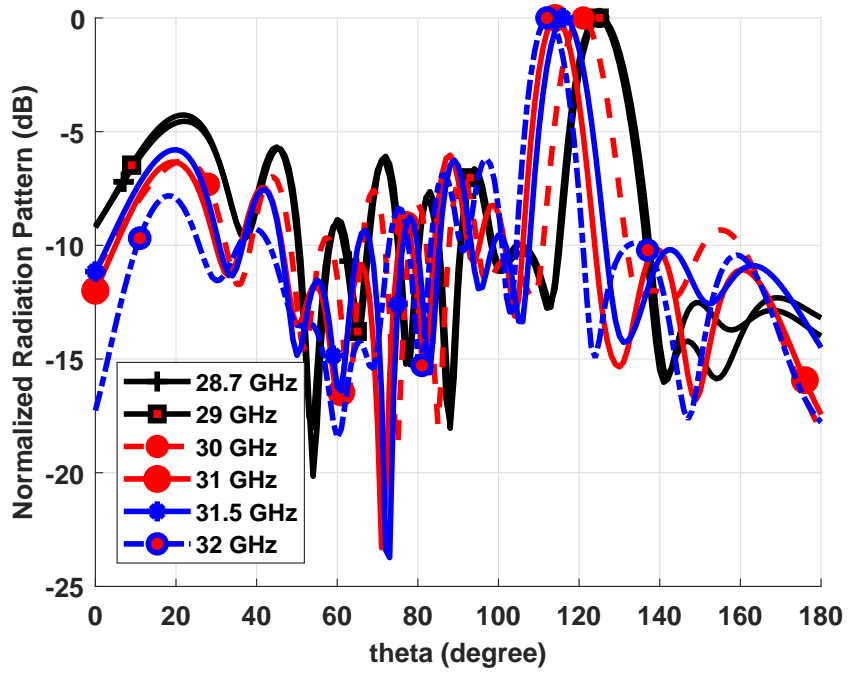


Figure 8.23: Normalized radiation pattern showing a tilt of 30 degrees at different frequency bands for a  $\theta$  cut at  $\phi = 270^0$  by antenna element 2.

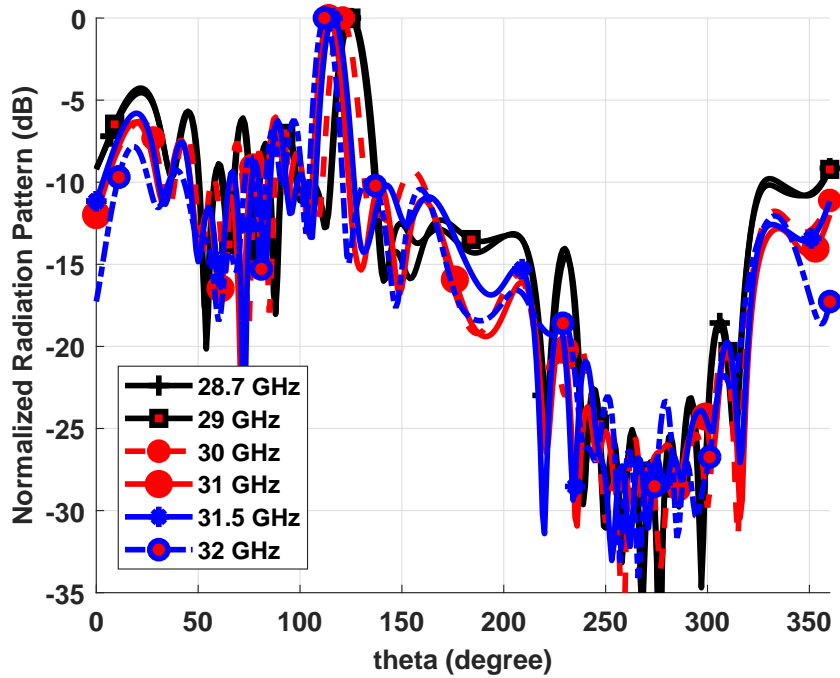


Figure 8.24: Normalized radiation pattern showing a tilt of 30 degrees at different frequency bands for a  $\theta$  cut at  $\phi = 270^0$  by antenna element 2.

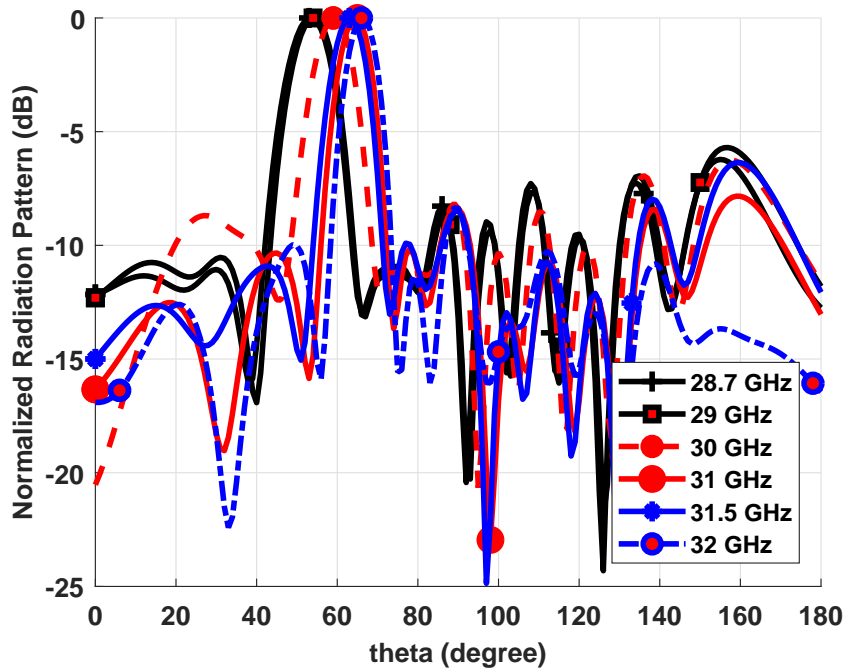


Figure 8.25: Normalized radiation pattern showing a tilt of -30 degrees at different frequency bands for a  $\theta$  cut at  $\phi = 270^\circ$  by antenna element 2.

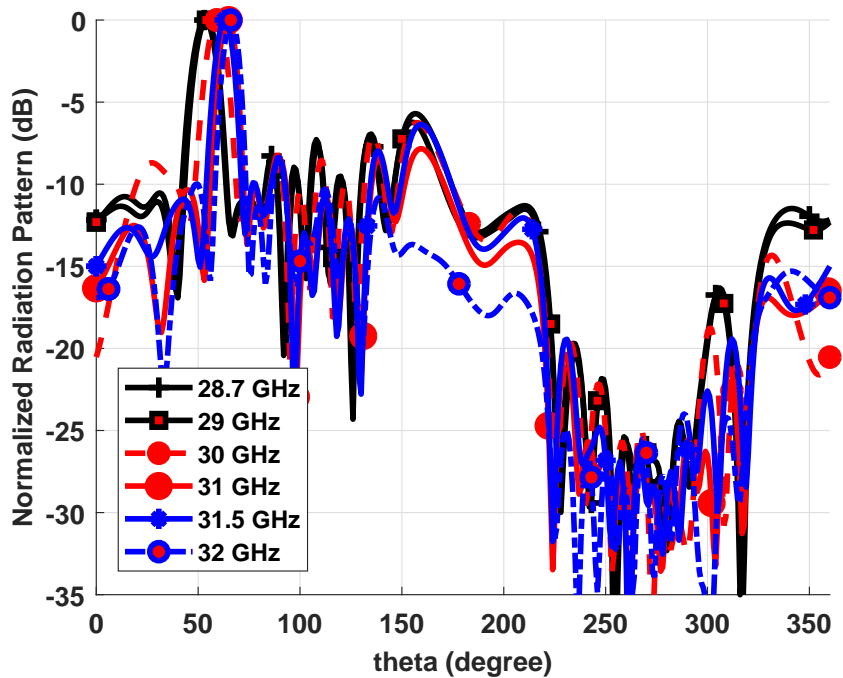


Figure 8.26: Normalized radiation pattern showing a tilt of -30 degrees at different frequency bands for a  $\theta$  cut at  $\phi = 270^\circ$  by antenna element 2.

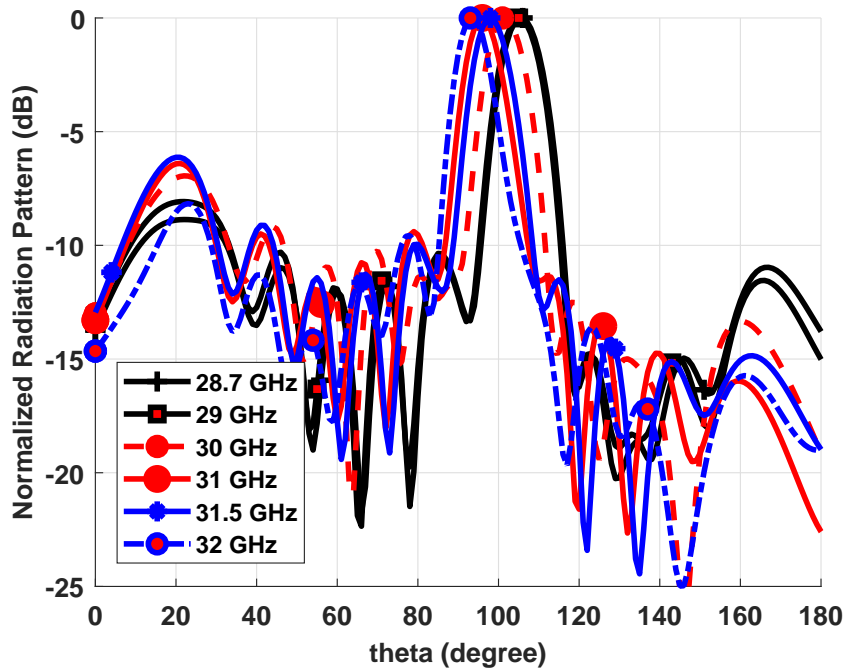


Figure 8.27: Normalized radiation pattern showing a tilt of 10 degrees at different frequency bands for a  $\theta$  cut at  $\phi = 270^\circ$  by antenna element 4.

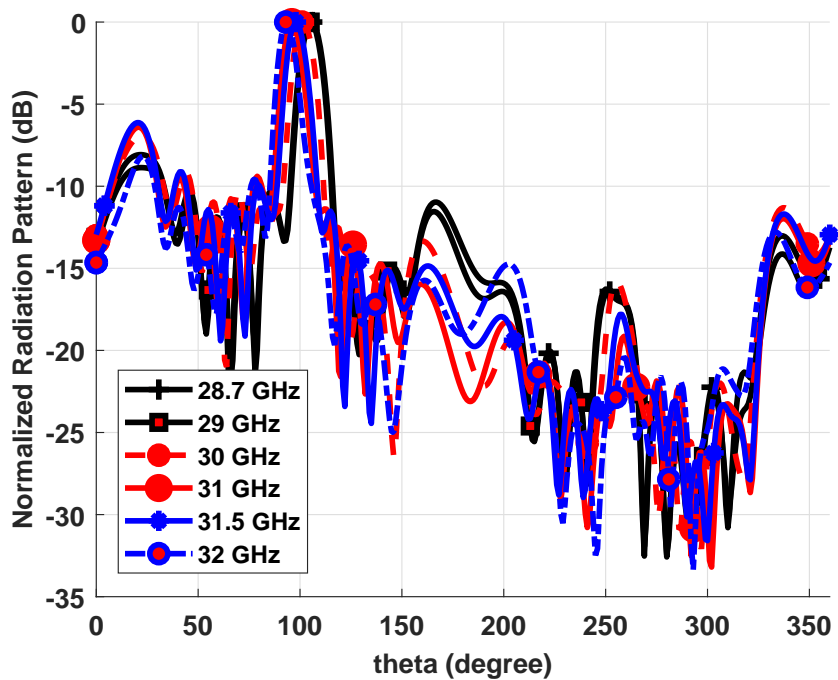


Figure 8.28: Normalized radiation pattern showing a tilt of 10 degrees at different frequency bands for a  $\theta$  cut at  $\phi = 270^\circ$  by antenna element 4.

## CHAPTER 9

# CONCLUSIONS & FUTURE WORK

*“A sunset here is a sunrise on the other end of the world. What appears to be the end  
may really be a new beginning”*

---

ANONYMOUS

### 9.1 Conclusions

Printed MIMO antenna design is a challenging task in any communication system because till now it lacks a lot of explanation to many physical phenomena. There are no general guidelines developed for printed antenna design up to now, and all works depend on past experiences. This work investigated the three methods ACGF, TCM and CBF and discussed the feasibility and the applicability of these methods to any printed antenna design. Although some have answered some issues but they are not feasible to be used for the design of printed antennas

with this current methods. ACGF, which is an extension to the Electric field integral equation (EFIE), answered many physical process like the transformation from near-field to far field radiation, provided optimum response for correlation coefficient but it cannot be used for the design of real antennas because it still relies on a closed form expression for the current ( $J(r)$ ), thus is intractable.

TCM relies on the MoM, to find the real antenna modes of any geometry under consideration and they are found in the absence of any excitation. The main problem lies in the proper excitation of the mode. A mode can provide very good radiating BW and radiation pattern but if not excited properly results in degraded performance because multiple modes are excited at the same time. For real printed antenna designs, the current maximas of all modes lie on the antenna itself, thus pure excitation of a single mode is nearly impossible. This is the reason that a vast majority of literature have applied TCM analysis to chassis based radiators because of the ease of excitation of its modes. TCM from any antenna design approach, lacks significance. But, it can be used to efficiently enhance the antenna parameters, like isolation enhancement, pattern reconfigurability e.t.c.

TCM was used for the analysis of the slot antennas and it was found that the presence of the slot does not generate any new mode (slot mode) but the obtained ones are the chassis modes that are slightly modified due to the presence of the slot. The location and the size of the slot on the chassis plays an important role in affecting its modes. Based on the analysis, a 4-element MIMO annular slot antenna was proposed designed and fabricated, covering 1.8 GHz to 2.45 GHz.



The effect of multiple circular slot radiators was investigated and it was observed that as long as there is symmetry in the antenna design (4-element MIMO slot) the MS plots are not affected significantly when compared to a pure chassis case, single element and 2-element cases. The physical principle behind frequency reconfigurability was also investigated. It is found that varactor diodes used did not alter the MS plots but helped in improving the impedance matching at different frequency bands of the same mode.

TCM was also used to analyze the behavior as well as develop a systematic approach for the placement of DGS in MIMO antenna configurations for port isolation enhancement. For this purpose, 2-element wire and two 4-element printed MIMO antennas were used. An average isolation enhancement of 11 dB was achieved using the proposed approach.

Using TCM, it was shown that the use of the chassis alone for radiation for frequencies greater than 1 GHz is an unrealistic approach. For frequencies greater than 1 GHz the antenna is the main radiating element and chassis only plays role in the impedance matching, that is why a 90 % reduction in the chassis size for two different designs and antenna types. At lower frequencies the effect of chassis was more significant and the antenna was not significantly dependent on the chassis size until 30 % reduction in the chassis size. This is the reason that at lower frequencies the chassis contributes to coupling/isolation.

Using TCM, it was also shown that the presence of a practical antenna generates a new antenna mode. In the presence of the antenna, all the antenna current

maxima shift towards the antenna element. The chassis modes are modified based on the location of the antenna on the chassis but the antenna mode depends only on the antenna element itself and not on the location of the antenna on the chassis. As the new antenna mode and all the modified chassis modes have current maximas at the same location that explains that the pure excitation of the antenna mode by using the existing methods of excitation like CCE or ICE is not possible.

A GA algorithm was developed based on the current distribution across the slot on the surface of SIW to design an antenna at 28 GHz. The GA optimizes the offset (from the center) and location of the slots on the SIW. A microstrip to SIW transition was used to excite the antenna. Two SIW traveling wave slot arrays having a tilt of  $10^0$  and  $30^0$  across the broad side are designed. The antenna are having an overall dimensions of 63 mm designed on a Rohacell substrate having a dielectric constant and loss tangent of 1.1 and 0.0045, respectively. The antennas are having a gain of 10 dB. The antenna is having an impedance BW from 28.75 GHz to 31.2 GHz. A 4-element MIMO configuration was designed for future 5G mobile terminals.

## 9.2 Future Work

One of the most appealing aspect of TCM is the reactive (continuous) loading that significantly affects the radiating BW of the mode. As we already know that wire antennas are significantly affected by the presence of the discrete reactive load

but this was not the case for such printed antennas. So, new loading techniques shall be developed for such printed antennas that can affect the mode attributes. Remember that the reactive loading can tune the antenna resonance at any desired frequencies.

Moreover, the main challenge in controlling the behaviour of antennas is the excitation of a single mode because all modes have current maxima and current minima almost at the same location. A new feeding technique can be designed that does not rely on the current maxima or minima location but on other parameters that can efficiently excite the mode. This will achieve a huge miniaturization and we will be also able to fine tune the antenna at any desired frequencies. Coming up with general guidelines can be investigated to obtain optimum performance for different MIMO antenna parameters like envelope correlation coefficient (ECC).

A new algorithm or technique can be developed that addresses the shortcomings of the existing TCM method. It should include the effect of the feeding location and the feeding type and then solve for the optimum mode. This will solve the problem of the possible excitation of the mode. Optimization algorithms can be integrated with TCM to enable the test of the different feeding methods and the possible placement of the feed on the chassis or the antenna will achieve enhanced performance.

We observed that whenever SIW based longitudinal slot arrays are collocated the SLL degrades due to the presence of the antenna elements. An optimization technique can be developed for a co-located MIMO case or the same existing

optimizing code can be used taking into the effect of the mutual coupling or isolation from the neighboring antenna.

## APPENDIX A

# DERIVATION OF THE ACGF

*“The laws of Nature are written in the language of Mathematics, and its characters are triangles, circles and other geometrical figures, without which it is humanly impossible to understand a single word of it”*

---

—GALILEO GALILEI.

In normal scenario for every input we had to use the Maxwells equation and then a complete numerical techniques to find the output of the system. Now if the input is changed, we had to repeat the whole process by first using maxwell and then Numerical Techniques. This is tedious process.

Green Function provided us with a better solution. Green Function is response of a Electromagnetic system for an impulse input. Once we know the response of the system then by using convolution we can very easily find out the response for other type of inputs. There are different ways to find out the Green Function of an Electromagnetic system.

### 1. Direct construction Approach

## 2. Eigen Function Expansion

## 3. Fourier Transform Approach

For Finding the Green Function of 1D problem these methods are used separately but for higher dimensions these are used together in order to find the green function easily.

We already know that the region around an antenna can be divided into three main regions [6],

1. Reactive near field
2. Radiating near field (Fresnel region)
3. Far field (Fraunhofer Region)

Figure A.1 shows the regions around the antenna surface. The Reactive near field region is located at

$$R < 0.62\sqrt{\frac{D^3}{\lambda}}$$

while the Radiating near field region is present between

$$0.62\sqrt{\frac{D^3}{\lambda}} < R < 2\frac{D^2}{\lambda}$$

while the far field starts from

$$R > 2\frac{D^2}{\lambda}$$

These definitions don't give physical insight on near field regions that's why we

will start addressing these regions and look at them from another perspective. A perspective which will properly define everything.

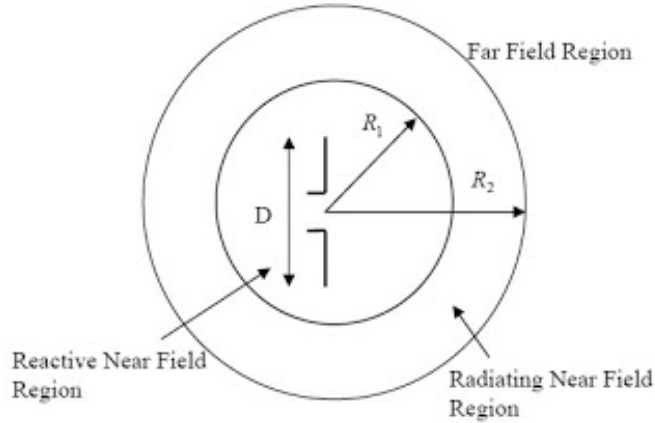


Figure A.1: Regions around antenna.

So we are in need of a proper definition or expression that can express the field clearly in terms of the near and far field components. Also we need such definition that can clearly explain how the energy transfer takes place between the near and far-field layers. To give this clear picture an idea of representing the fields by the wilcox expansion was presented in [21,22]. These expressions were representing both Near and Far Field.

## A.1 Wilcox Expansion

To find the Electric and magnetic fields, the spatial structure around antenna is divided into many regions as shown in Figure A.2 [21]. The antenna is excited by current density  $J$ . According to the Wilcox expansion the Electric and Magnetic

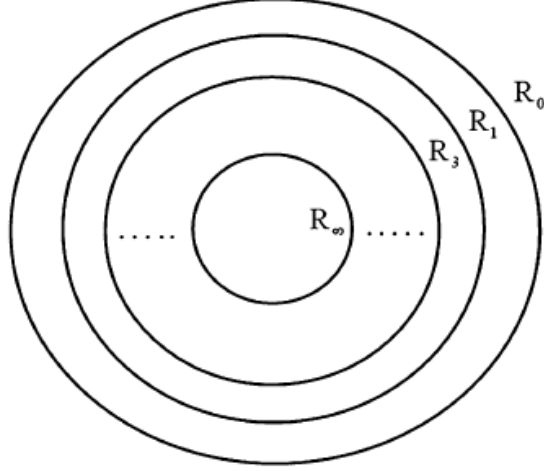


Figure A.2: Regions surrounding antenna.  $R_o$  is referring to far field.  $R_1, R_2, \dots, R_\infty$  refers to near field [21].

fields can be represented by the series [40]

$$E(r) = \frac{e^{jkr}}{r} \sum_{n=0}^{\infty} \frac{A_n(\theta, \varphi)}{r^n} \quad (\text{A.1})$$

$$H(r) = \frac{e^{jkr}}{r} \sum_{n=0}^{\infty} \frac{B_n(\theta, \varphi)}{r^n} \quad (\text{A.2})$$

$A_n$  and  $B_n$  are angular functions that are dependent on the far field component.

The layers in Figure A.2 are defined with respect to the Wilcox series. Each layer corresponds to  $\frac{1}{r^{n+1}}$  term. The far field can be represented by  $A_o$  and  $B_o$ .

$$E(r) = \frac{e^{jkr}}{r} A_o(\theta, \varphi) \quad (\text{A.3})$$

$$H(r) = \frac{e^{jkr}}{r} B_o(\theta, \varphi) \quad (\text{A.4})$$



The E and H field components in the  $R_1$  region are

$$E(r) = \frac{e^{jkr}}{r^2} A_1(\theta, \varphi) + \frac{e^{jkr}}{r} A_o(\theta, \varphi) \quad (\text{A.5})$$

$$H(r) = \frac{e^{jkr}}{r^2} B_1(\theta, \varphi) + \frac{e^{jkr}}{r} B_o(\theta, \varphi) \quad (\text{A.6})$$

The difference between the two layers is

$$E(r) = \frac{e^{jkr}}{r^2} A_1(\theta, \varphi) \quad (\text{A.7})$$

$$H(r) = \frac{e^{jkr}}{r^2} B_1(\theta, \varphi) \quad (\text{A.8})$$

Thus we finally got an expression for Electric and Magnetic field associated with  $R_1$  layer are given in expression (A.7) and (A.8). These are the fields that are only associated with the  $R_1$  layer. In the same way we can clearly and easily define fields for a near field layer. One important point is that Maxwell's equations are not applicable to just the Electric and magnetic fields for a single layer but are applicable to Electric and magnetic fields when they are taken for all the layers collectively. Localized and non-localized energies exist in each layer, that is each layer contains propagating and non-propagating energies. Based on the expressions of the electric and magnetic fields we will calculate the energy associated with a near field layer and also the energy associated with the far field layer.

$$\omega_e = \frac{\epsilon}{4} E \cdot E^* = \frac{\epsilon}{4} \sum_{n=0}^{\infty} \sum_{n'=0}^{\infty} \frac{A_n \cdot A_n^*}{r^{n+n'+2}} \quad (\text{A.9})$$

$$\omega_h = \frac{\mu}{4} H.H^* = \frac{\epsilon}{4} \sum_{n=0}^{\infty} \sum_{n'=0}^{\infty} \frac{B_n.B_n^*}{r^{n+n'+2}} \quad (\text{A.10})$$

Let us rearrange the terms in order to present it in a more suitable manner,

$$\omega_e(r) = \frac{\epsilon}{4} \sum_{n=0}^{\infty} \frac{A_n.A_n^*}{r^{2n+2}} + \frac{\epsilon}{4} \sum_{n=0}^{\infty} \frac{Re(A_n.A_n^*)}{r^{n+n'+2}} \quad (\text{A.11})$$

$$\omega_h(r) = \frac{\mu}{4} \sum_{n=0}^{\infty} \frac{B_n.B_n^*}{r^{2n+2}} + \frac{\mu}{4} \sum_{n=0}^{\infty} \frac{Re(B_n.B_n^*)}{r^{n+n'+2}} \quad (\text{A.12})$$

The first term on Right hand side represents the interaction of field with itself (non-propagating energy) while the second term represents the interaction of a layer with other layers (propagating energy).

## A.2 Multipole Expansion

Multipole expansion was used to verify the expressions of Electric and magnetic fields representing the energies that were obtained by using wilcox expansion A.2 [21]. Multipole expansion is basically a representation of fields in terms of eigen vectors. We will start from the far field equations and will try to reconstruct the near field equations and it shall match the Wilcox expansion. Electric and Magnetic fields in terms of Multipole expansion can be represented as a sum of vector spherical Harmonics [41],

$$E(r) = \eta \frac{e^{jkr}}{kr} \sum_{l=0}^{\infty} \sum_{m=-l}^l (-1)^{l+1} [a_E(l, m) X_{lm} - a_M(l, m) \hat{r} \times X_{lm}] \quad (\text{A.13})$$

$$H(r) = \frac{e^{jkr}}{kr} \sum_{l=0}^{\infty} \sum_{m=-l}^l (-1)^{l+1} [a_M(l, m)X_{lm} + a_E(l, m)\hat{r} \times X_{lm}] \quad (\text{A.14})$$

Here  $\eta$  represents the free space wave intrinsic impedance. The coefficients of  $TE_{lm}$  and  $TM_{lm}$  modes are represented by  $a_E(l, m)$  and  $a_M(l, m)$  respectively.  $X_{lm}$  represents the vector spherical harmonic and is represented by

$$X_{lm} = \frac{1}{\sqrt{l(l+1)}} LY_{lm}(\theta, \varphi)$$

where  $L$  is the angular momentum operator and is given by

$$L = -ir \times \nabla \quad (\text{A.15})$$

and  $Y_{lm}(\theta, \phi)$  is the spherical harmonics of degree  $l$  and order  $m$

$$Y_{lm}(\theta, \phi) = \sqrt{\frac{(2l+1)(l-m)!}{4\pi(l+m)!}} P_l^m(\cos\theta) e^{jm\varphi} \quad (\text{A.16})$$

After performing mathematical calculation it was proved in [21, 22] that Electromagnetic field can be represented by Wilcox series.

By using few mathematical derivations the coefficients were derived as

$$B_0(\theta, \phi) = \sum_{l=0}^{\infty} \sum_{m=-l}^l \frac{(-i)^{l+1}}{k} [a_M(l, m)X_{lm} + a_E(l, m)\hat{r} \times X_{lm}] \quad (\text{A.17})$$

$$\begin{aligned}
B_n(\theta, \phi) = & \sum_{l=n}^{\infty} \sum_{m=-l}^l [a_M(l, m)b_n^l X_{lm}] - \\
& \sum_{l=n-1}^{\infty} \sum_{m=-l}^l \frac{ia_E(l, m)}{k} (c_n^l \hat{r} Y_{lm} + d_n^l \hat{r} x X_{lm}), \quad n \geq 1
\end{aligned} \tag{A.18}$$

Similarly, we can also derive

$$A_0(\theta, \phi) = \eta \sum_{l=0}^{\infty} \sum_{m=-l}^l \frac{(-i)^{l+1}}{k} [a_E(l, m)X_{lm} - a_M(l, m)\hat{r} \times X_{lm}] \tag{A.19}$$

$$\begin{aligned}
A_n(\theta, \phi) = & \eta \sum_{l=n}^{\infty} \sum_{m=-l}^l [a_E(l, m)b_n^l X_{lm}] + \\
& \eta \sum_{l=n-1}^{\infty} \sum_{m=-l}^l \frac{ia_M(l, m)}{k} (c_n^l \hat{r} Y_{lm} + d_n^l \hat{r} x X_{lm}), \quad n \geq 1
\end{aligned} \tag{A.20}$$

### A.3 Weyl Expansion

Weyl Expansion is basically a spectral representation of the Electric field. The main goal was to decompose the field into a sum (spectrum) of propagating and evanescent modes. This will help in providing a clear understanding of the interaction (energy transfer) between the propagating energy and non-propagating energy. Let us suppose that the antenna is surrounded by a homogeneous and isotropic medium having magnetic permeability  $\mu$  and electric permittivity  $\epsilon$ . If the current density on the antenna is  $J$  then the Electric field produced by this antenna can be given by the dyadic Greens function theorem [22,37].

$$E(r) = j\omega\mu \int_V \bar{G}(r, r') \cdot J(r') d^3r \quad (\text{A.21})$$

Where the Free Space Green Function (FSGF) is given by

$$\bar{G}(r, r') = [1 + \frac{\nabla\nabla}{k^2}]g(r, r') \quad (\text{A.22})$$

The scalar green function is given by

$$g(r, r') = \frac{e^{jk|r-r'|}}{4\pi|r-r'|} \quad (\text{A.23})$$

Using the Weyl expansion identity, the scalar green function can be divided into propagating and non-propagating parts. After mathematical calculations we get an expression for the electric field as

$$E(r) = \frac{-wk\mu}{8\pi^2} \int_{-\infty}^{+\infty} \frac{\bar{I}k^2 - KK}{k^2m} \cdot \bar{J}(k) e^{jk \cdot r} \quad (\text{A.24})$$

here

$$k = \hat{x}kp + \hat{y}kq + \hat{z}sgn(z - z')km$$

and  $J(K)$  is representing the spatial Fourier transform of the current density on the source (antenna).

$$\bar{J}(K) = \int_V J(r') e^{-jk \cdot r'} d^3r$$

By using the Wilcox and Weyl expansion the near field theory was studied from a perspective that has got much resemblance to the reality. They give very better explanation to the near field phenomena. Now the study was extended to find an expression for how the currents are excited on antenna surface by a source, how radiated fields are related to antenna currents and how currents are excited on antenna surface by the fields. As we have seen that Electric field can be represented in terms of green function, so a new transfer function known as Antenna Current green Function (ACGF) was introduced [19, 20].

Due to the complexity involved in the calculation of the current density function, few researchers have addressed the issue. Recently a few publications appeared in this area and now researchers are trying to dig into the problem more from a practical point of view.

## A.4 ACGF

Wave equation for source free region is given by

$$(\nabla^2 + k^2)E(r) = 0 \tag{A.25}$$

where  $\nabla^2$  represents the laplacian operator,  $k$  represents the propagation constant and  $E$  represents the Electric field, In the presence of any source, it is given by

$$(\nabla^2 + k^2)E(r) = S(r) \tag{A.26}$$

Green function is the solution of differential equation for an impulse input, so for any input  $S(r)$  the solution will be

$$E(r) = \int_v g(r, r') S(r) \quad (\text{A.27})$$

Now to find  $g(r, r')$ ,

$$(\nabla^2 + k^2)g(r) = -\delta(r - r') \quad (\text{A.28})$$

for an impulse input at  $r' = 0$ , the solution to

$$g(r) = C \frac{e^{jkr}}{r} + D \frac{e^{-jkr}}{r} \quad (\text{A.29})$$

after few mathematical derivations, the solution of the  $g(r)$  is

$$g(r) = \frac{e^{jkr}}{4\pi r} \quad (\text{A.30})$$

and for any generalized point, where the impulse was not applied at  $r' = 0$ . The expression for the  $g(r, r')$  is given by

$$g(r, r') = \frac{e^{jk|r-r'|}}{4\pi|r-r'|} \quad (\text{A.31})$$

This is free space green function. Now from the basic of electromagnetics we know that  $\nabla \times E = -j\omega\mu H$  and  $\nabla \times H = J + j\omega\epsilon E$ , we can get

$$\nabla \times \nabla \times E(r) - k^2 E(r) = -j\omega\mu J(r) \quad (\text{A.32})$$

Now  $\nabla \times \nabla \times E = \nabla(\nabla \cdot E) - \nabla^2 E$ , and from equation of continuity  $\rho = -\frac{\nabla \cdot J}{j\omega}$  and from Maxwell's equation  $\nabla \cdot E = \frac{\rho}{\epsilon}$ , we can derive

$$\nabla^2 E(r) + k^2 E(r) = j\omega\mu J(r) - \frac{\nabla \nabla \cdot J}{j\omega\epsilon} \quad (\text{A.33})$$

$$\nabla^2 E(r) + k^2 E(r) = j\omega\mu \left(1 + \frac{\nabla \nabla}{k^2}\right) J(r) \quad (\text{A.34})$$

Equation (A.34) is similar to (A.26), if

$$S(r) = j\omega\mu \left(1 + \frac{\nabla \nabla}{k^2}\right) J(r) \quad (\text{A.35})$$

We already know that the solution of (A.26) is given by (A.31). So, using green function for any input  $S(r)$ , the solution will be (A.27)

$$E(r) = \int_v dv' \frac{e^{jk|r-r'|}}{4\pi|r-r'|} \cdot j\omega\mu \left(I + \frac{\nabla \nabla}{k^2}\right) \cdot J(r) \quad (\text{A.36})$$

re-arranging the terms

$$E(r) = j\omega\mu \int_v dv' \left[ I + \frac{\nabla \nabla}{k^2} \right] \cdot \frac{e^{jk|r-r'|}}{4\pi|r-r'|} J(r) \quad (\text{A.37})$$

So, the above equation is the Electric field integral equation (EFIE) and it was assumed as an antenna current green function. So ACGF is

$$E(r) = \int_v ds' G(r, r') \cdot J(r') \quad (\text{A.38})$$



## APPENDIX B

# COMPUTER SIMULATION TECHNOLOGY (CST)

*“The expert in anything was once a beginner.”*

---

—HELEN HAYES.

Computer simulation technology (CST) is a simulation software that can solve an EM problem by using many numerical approaches like finite element method (FEM), multilevel fast multipole method (MLFMM), method of moments (MoM) and shooting boundary ray (SBR) method depending on the problem nature. The list of different solvers provided by CST are.

- Transient solver
- Frequency domain solver
- Eigen mode solver
- Resonant solver

- Integral equation solver
- Asymptotic solver
- Multilayer solver

TCM analysis is offered by the Integral equation (IE) solver as well as the Multilayer solver. For the case of the TCM analysis of metallic structures i.e. in the absence of any dielectric material, the IE is used. When ever we have multiple layers of metal and dielectric then the Multilayer solver is used for TCM analysis.

To perform TCM analysis we need to follow some basic steps to get some fundamental responses, then further analysis can be conducted as needed.

1. Start CST and choose IE solver.
2. Draw the geometry (metallic object) you are interested in finding the characteristic modes (CM) as shown in the Figure B.1.
3. To assign a frequency sweep go to  $\rightarrow$  simulation  $\rightarrow$  Frequency. Insert the start and the stop frequencies as shown in the Figure B.2.
4. To plot the current distribution as well as the radiation pattern for modes at different frequencies. Go to  $\rightarrow$  Simulation  $\rightarrow$  Field Monitor. Enter the different frequencies for which you want to find the current, Electric field e.t.c as shown in the Figure B.3.
5. To specify the number of modes. Go to  $\rightarrow$  Simulation  $\rightarrow$  Setup Solver as shown in the Figure B.4. You can start the simulation after this step.

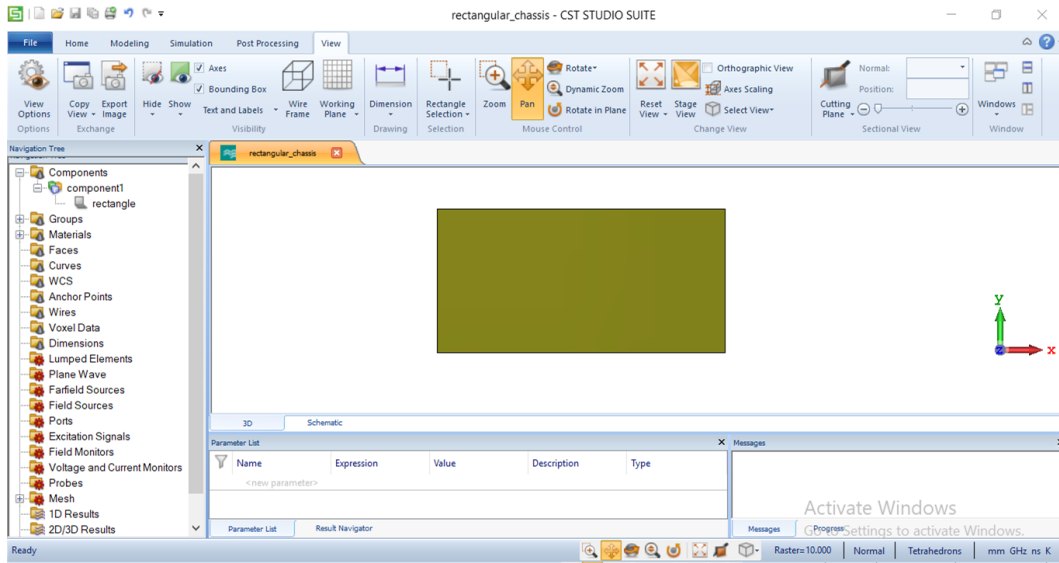


Figure B.1: CST design environment. A metallic chassis of  $120 \times 60 \text{ mm}^2$  is shown.

6. To check the eigenvalues, characteristic angles or modal significance curves.  
Go to  $\rightarrow$  to 1D Results as shown in the Figure B.5.
7. To observe the modal current distribution on the surface of the geometry.  
Go to  $\rightarrow$  2D/3D Results section as shown in the Figure B.6.
8. To observe the radiation pattern of a mode. Go to  $\rightarrow$  Far fields section as shown in the Figure B.7

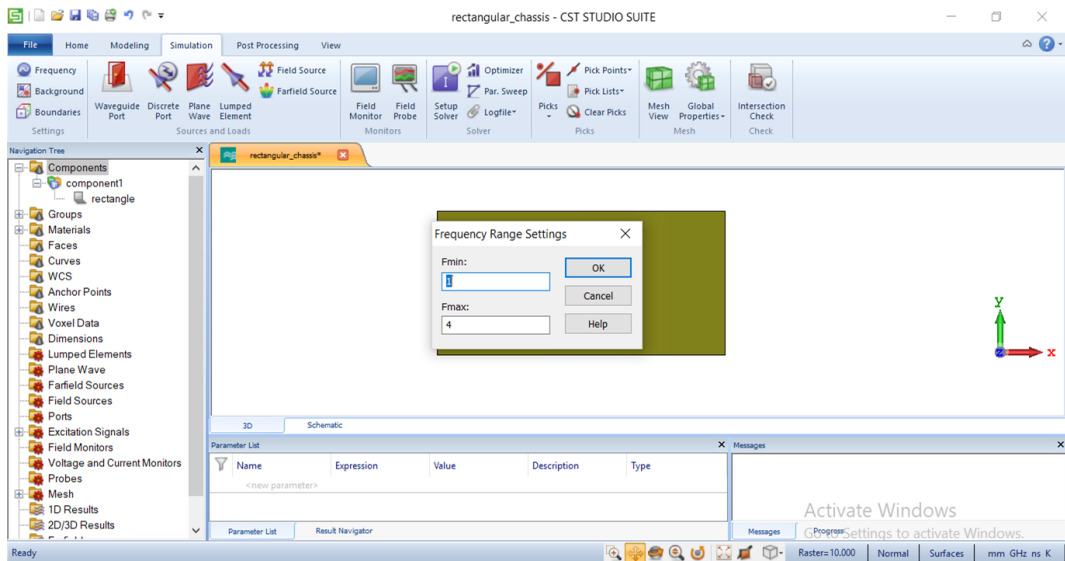


Figure B.2: CST design environment. Frequency BW on which the CM are need calculated.

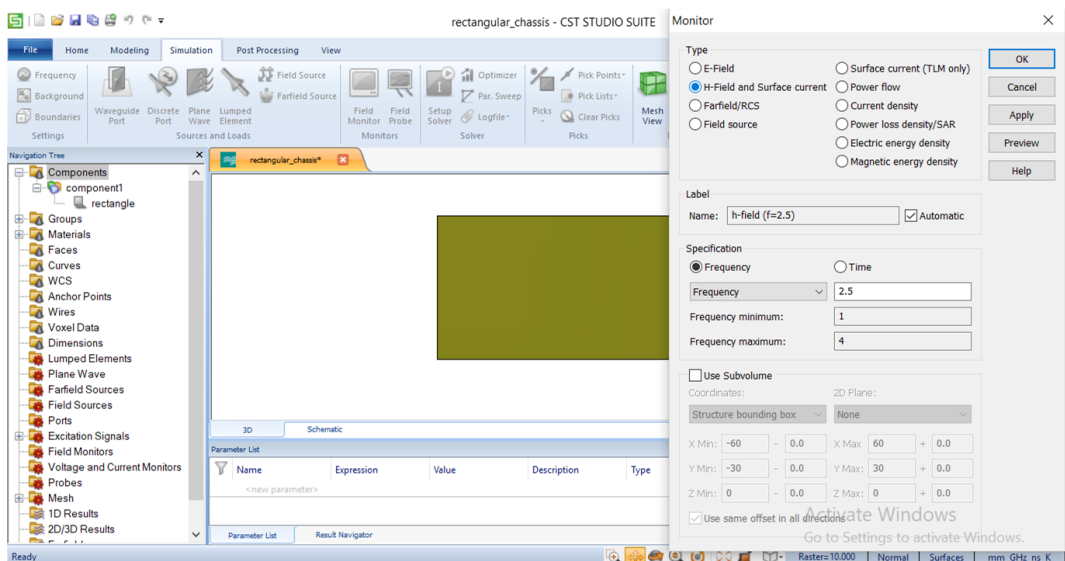


Figure B.3: CST design environment. Frequencies on which the user want to plot the currents or the far-field radiation pattern shall be entered.

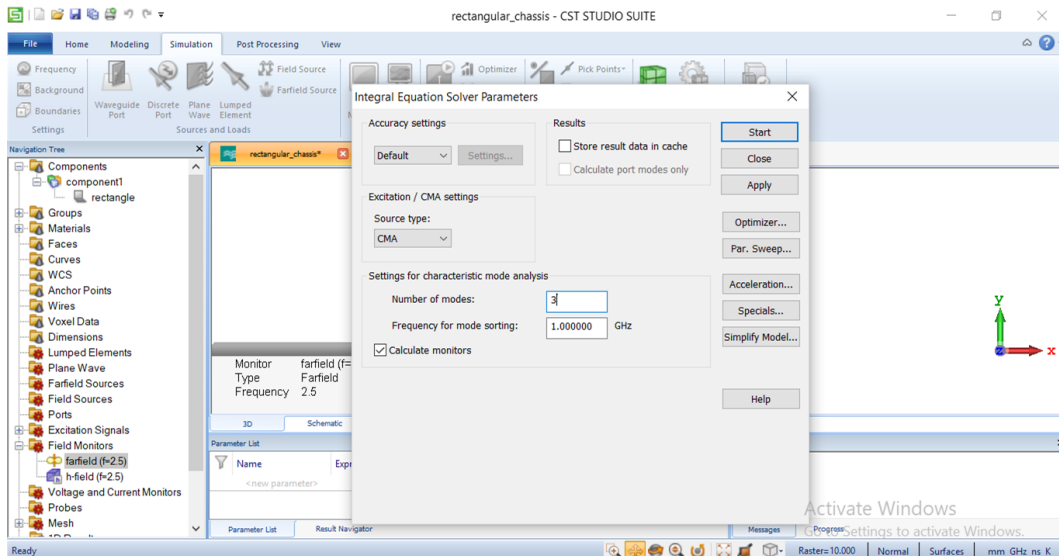


Figure B.4: CST design environment. Enter the number of modes.

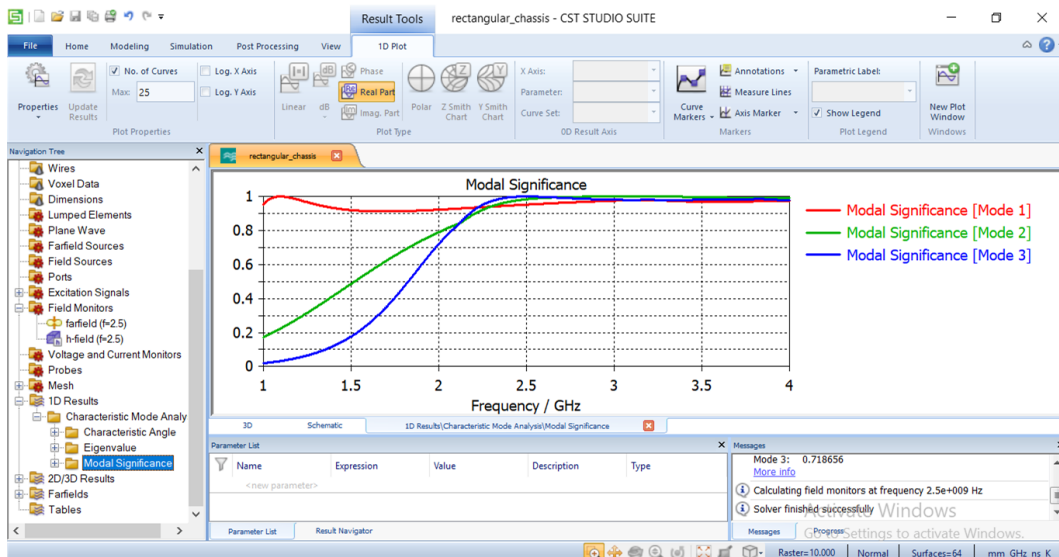


Figure B.5: CST design environment. Modal Significance curves.

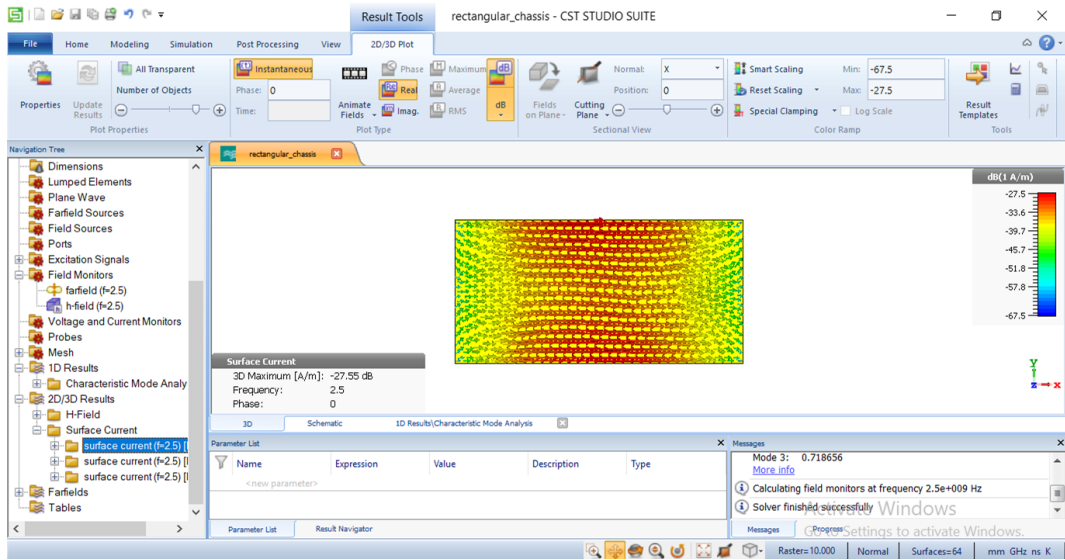


Figure B.6: CST design environment. Current distribution on the surface of the antenna for particular mode.

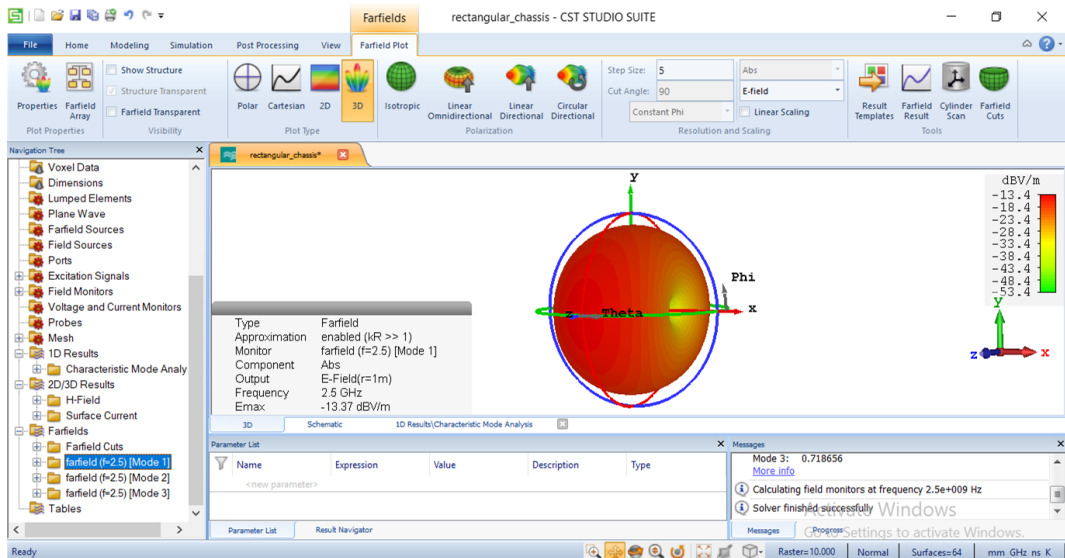


Figure B.7: CST design environment. Far-field radiation pattern of the modes.

# REFERENCES

- [1] D. Evans, “The Internet of Things, How the Next Evolution of the Internet Is Changing Everything,” Cisco Internet Business Solutions Group (IBSG), Tech. Rep., April 2011.
- [2] “Forecast: PCs, Ultramobiles and Mobile Phones, Worldwide, 2013-2020, 1Q16 Update.” [Online], Available: <http://www.gartner.com/>, March 2016, accessed: 2016-12-17.
- [3] H. Morishita, Y. Kim, and K. Fujimoto, “Design concept of antennas for small mobile terminals and the future perspective,” *IEEE Antennas and Propagation Magazine*, vol. 44, no. 5, pp. 30–43, Oct 2002.
- [4] K. L. Wong, “Planar antennas for wireless communications,” *Wiley-Interscience, John Wiley & Sons*, 2000.
- [5] R. Hussain, “Reconfigurable mimo antenna system with direction finding capability for cognitive radio platforms,” Ph.D. dissertation, king fahd university of petroleum and minerals, Saudi Arabia, 2015.

- [6] C.A.Balanis, *Antenna Theory, Analysis and Design*, 2 ed. John Wiley & Sons, 2005.
- [7] K. L. Wong, *Compact and Broadband Microstrip Antennas*. John Wiley & Sons, 2002.
- [8] “FEKO user’s manual,” *Suite 5.1, EM Software & Systems*, Dec. 2005.
- [9] “User manual for HFSS,” *Ansoft Corporation, Pittsburg, PA, USA*.
- [10] “CST Studio suite; getting started,” *CST Studio suite, USA.*, Jan. 2016.
- [11] A.Taflove and S.C.Hagnes, *Computational Electrodynamics: The Finite-difference Time-domain method*. Artech House, 2005.
- [12] R.F.Harrington, *Field Computation by Moment Methods*. John Wiley & Sons, 1968.
- [13] A.Elsherbeni and V.Demir, *The Finite-difference Time-domain method for Electromagnetics with MATLAB Simulations*. SciTech Publishing, Inc, 2008.
- [14] Y.R.Samii and E.Michielsen, *Electromagnetic Optimization by Genetic Algorithms*. John Wiley & Sons, July 1999.
- [15] J. Robinson and Y. Rahmat-Samii, “Particle swarm optimization in electromagnetics,” *IEEE Transactions on Antennas and Propagation*, vol. 52, no. 2, pp. 397–407, Feb 2004.
- [16] C.Christodoulou, M.Georgiopoulos, and C.Christopoulos, *Applications of Neural Networks in Electromagnetics*. Artech House, 2001.



- [17] R. J. Garbacz, "A generalized expansion for radiated and scattered fields," Ph.D. dissertation, Ohio State University, Columbus, 1968.
- [18] R. Harrington and J. Mautz, "Theory of characteristic modes for conducting bodies," *IEEE Transactions on Antennas and Propagation*, vol. 19, no. 5, pp. 622–628, Sep 1971.
- [19] S. M. Mikki and Y. M. M. Antar, "The Antenna Current Green's Function Formalism—Part I," *IEEE Transactions on Antennas and Propagation*, vol. 61, no. 9, pp. 4493-4504, Sept. 2013.
- [20] S. M. Mikki and Y. M. M. Antar, "The Antenna Current Green's Function Formalism—Part II," *IEEE Transactions on Antennas and Propagation*, vol. 61, no. 9, pp. 4505-4519, Sept. 2013.
- [21] S. M. Mikki and Y. M. M. Antar, "A Theory of Antenna Electromagnetic Near Field—Part I," *IEEE Transactions on Antennas and Propagation*, vol. 59, pp. 4691-4705, Dec. 2011.
- [22] S. M. Mikki and Y. M. M. Antar, "A Theory of Antenna Electromagnetic Near Field—Part II," *IEEE Transactions on Antennas and Propagation*, vol. 59, pp. 4706-4724, Dec. 2011.
- [23] M. C. Fabres, "Systematic design of antennas using the theory of characteristic modes," Ph.D. dissertation, Universidad Politecnica de Valencia, Feb. 2007.

- [24] E. Antonino, "Analysis and design of antennas for wireless communications using modal methods," Ph.D. dissertation, Universidad Politecnica de Valencia, Feb. 2008.
- [25] M. Cabedo-Fabres, E. Antonino-Daviu, A. Valero-Nogueira, and M. F. Bataller, "The theory of characteristic modes revisited: A contribution to the design of antennas for modern applications," *IEEE Antennas and Propagation Magazine*, vol. 49, no. 5, pp. 52–68, Oct 2007.
- [26] E. Lucente, A. Monorchio and R. Mittra, "An iteration-free MoM Approach based on excitation independent characteristic basis functions for solving large multiscale electromagnetic scattering problems" *IEEE Transactions on Antennas and Propagation*, vol. 56, no.4, April, 2008.
- [27] V.V.S.Parkash and R.Mittra, "Characteristic Basis function method: A new technoque for efficient solution of method of moment matrix equations", *Microwave and optical technology letters*, vol.36,no 2, Jan. 2003.
- [28] R.Mitra and K.Du, "Characteristic Basis function method for iteration-free solution of large method of moments problems," *Progress in Electromagnetics Research*, Vol.6, pp 307-388, 2008.
- [29] H.Li, "Decoupling and evaluation of multiple antenna systems in compact mimo terminals," Ph.D. dissertation, KTH Electrical Engineering, Sweden, 2012.

- [30] S.Wang, “Characteristic modes analysis for antenna parameteres optimization,” Ph.D. dissertation, Yokohama National University, Japan, March 2015.
- [31] R.Ma and I.Chountalas, “Pattern reconfigurable MIMO antennas for Multi-band LTE Operation,” Master’s thesis, Lund University, Sweden, 2015.
- [32] F.C.Zadeh, “Feeding of Characteristic Modes in Multi-Antenna Handsets,” Master’s thesis, Lund University, Sweden, 2014.
- [33] J. Mautz and R. Harrington, “Modal analysis of loaded n-port scatterers,” *IEEE Transactions on Antennas and Propagation*, vol. 21, no. 2, pp. 188–199, Mar 1973.
- [34] R.Garg, *Analytical and Computational Methods in Electromagnetics*. Artech House, 2008.
- [35] C.T.Tai, *Dyadic Green Functions in Electromagnetic Theory*. IEEE Press,1993.
- [36] H.J.Eom,*Electromagnetic Theory for Boundary-Value Problems*. Springer,2004.
- [37] W.C.Chew, *Waves and fields in Inhomogenous Media*. Nan Nostrand Reinhold, New york, 1990.
- [38] I.Stakgold, *Green’s function and Boundary value Problems*. John Wiley & Sons, New York,1979.

- [39] C.A.Balanis, *Advanced Engineering Electromagnetics*. John Wiley & Sons, New York,2012.
- [40] C. H. Wilcox,“An expansion theorem for the electromagnetic fields,” *Commun. Pure Appl. Math.*, vol. 9, pp. 115–134, 1956.
- [41] D. J. Jackson, *Classical Electrodynamics*. New York: Wiley, 1999.
- [42] E. Lucente, A.Monorchio and R.Mittra,“An iteration-free MoM Approach based on excitation independent characteristic basis functions for solving large multiscale electromagnetic scattering problems” *IEEE Transactions on Antennas and Propagation*, vol. 56, no.4, April, 2008.
- [43] V.V.S.Parkash and R.Mittra,“Characteristic Basis function method: A new technoque for efficient solution of method of moment matrix equations”, *Microwave and optical technology letters*, vol.36,no 2, Jan. 2003.
- [44] R.Mitra and K.Du,“Characteristic Basis function method for iteration-free solution of large method of moments problems,” *Progress in Electromagnetics Research*, Vol.6, pp 307-388, 2008.
- [45] C.Li and R.Mittra,“Controlling radiation patterns of antennas mounted on complex platforms using the characteristic basis functions (CBFs),” *Journal of Electromagnetic waves and Applications*“, 2016.
- [46] C.Li and R.Mittra,“Control of radiation patterns of antennas mounted on complex platforms by using the Characteristic basis functions (CBFs),” *IEEE*

- International Symposium on Antennas and Propagation (APSURSI)*, Fajardo, pp. 427-428, 2016.
- [47] M. Bozzi, A. Georgiadis and K. Wu, "Review of substrate-integrated waveguide circuits and antennas," *IET Microwaves, Antennas & Propagation*, vol. 5, no. 8, pp. 909-920, June 2011.
- [48] Li Yan, Wei Hong, Guang Hua, Jixin Chen, Ke Wu and Tie Jun Cui, "Simulation and experiment on SIW slot array antennas," *IEEE Microwave and Wireless Components Letters*, vol. 14, no. 9, pp. 446-448, Sept. 2004.
- [49] G.Q.Luo, T.Y.Wang and X.H.Zhang, "Review of Low profile substrate integrated waveguide cavity backed antennas," *International Journal of Antennas and Propagation*, 2013.
- [50] W. Hong, B.Liu, Y.Wang, Q.Lai. and K.Wu "Half Mode Substrate Integrated Waveguide: A New Guided Wave Structure for Microwave and Millimeter Wave Application," *31<sup>st</sup> International Conference on Infrared Millimeter Waves and 14<sup>th</sup> International Conference on Terahertz Electronics*, Shanghai, pp. 219-219, 2006.
- [51] S. A. Razavi and M. H. Neshati, "Development of a Linearly Polarized Cavity-Backed Antenna Using HMSIW Technique," *IEEE Antennas and Wireless Propagation Letters*, vol. 11 , pp. 1307-1310, 2012.

- [52] S. M. Mikki and A. A. Kishk, "Theory and Applications of Infinitesimal Dipole Models for Computational Electromagnetics," *IEEE Transactions on Antennas and Propagation*, vol. 55, no. 5, pp. 1325-1337, May 2007.
- [53] S. Clauzier, S. M. Mikki and Y. M. M. Antar, "Design of Near-Field Synthesis Arrays Through Global Optimization," *IEEE Transactions on Antennas and Propagation*, vol. 63, no. 1, pp. 151-165, Jan. 2015.
- [54] S. R. Best and B. C. Kaanta, "A Tutorial on the Receiving and Scattering Properties of Antennas," *IEEE Antennas and Propagation Magazine*, vol. 51, pp. 26-37, Oct. 2009.
- [55] S. M. Mikki and Y. M. M. Antar, "On the Fundamental Relationship Between the Transmitting and Receiving Modes of General Antenna Systems: A New Approach," *IEEE Antennas and Wireless Propagation Letters*, vol. 11, pp. 232-235, 2012.
- [56] A. Ghalib and M. S. Sharawi, "A comparison between the antenna current green function and theory of characteristic modes," *IEEE Middle East Conference on Antennas and Propagation (MECAP)*, Beirut, pp. 1-4, 2016.
- [57] M. S. Sharawi, *Printed mimo antenna engineering*. Artech House, 2014.
- [58] S. M. Mikki and Y. M. M. Antar, "On Cross Correlation in Antenna Arrays With Applications to Spatial Diversity and MIMO Systems," *IEEE Transactions on Antennas and Propagation*, vol. 63, pp. 1798-1810, April 2015.

- [59] S. Clauzier, S. M. Mikki and Y. M. M. Antar, "A Generalized Methodology for Obtaining Antenna Array Surface Current Distributions With Optimum Cross-Correlation Performance for MIMO and Spatial Diversity Applications," *IEEE, Antennas and Wireless Propagation Letters*, vol. 14, no. , pp. 1451-1454, 2015.
- [60] S. M. Mikki and Y. M. M. Antar, "A Rigorous Approach to Mutual Coupling in General Antenna Systems Through Perturbation Theory," *IEEE Antennas and Wireless Propagation Letters*, vol. 14, pp. 115-118, 2015.
- [61] S. M. Mikki and Y. M. M. Antar, "Near field analysis of electromagnetic interactions in antenna arrays through equivalent dipole models," *IEEE Transactions on Antennas and Propagation*, vol. 60, no. 3, pp. 1381–1389, Mar. 2012.
- [62] S. Henault, S. K. Podilchak, S. M. Mikki, and Y. M. M. Antar, "A methodology for mutual coupling estimation and compensation in antennas" *IEEE Transactions on Antennas and Propagation*, vol. 61, no. 3, pp. 1119–1131, Mar. 2013.
- [63] E.A.Daviu, C.A.S.Fajardo, M.C.Fabres and M.F.Bataller, "Wideband antenna for mobile terminals based on the Handset PCB resonance," *Microwave and Optical Technology letter, Wiley InterScience*, Vol.48, July 2006.
- [64] E. Antonino-Daviu, M. Cabedo-Fabres, M. Ferrando-Bataller, A. Valero-Nogueira and M. Martinez-Vazquez, "Novel antenna for mobile terminals

- based on the chassis-antenna coupling,” *IEEE Antennas and Propagation Society International Symposium*, Vol. 1A, pp. 503-506, 2005.
- [65] Kin-Lu Wong, Chih-Hsien Wu and Saou-Wen Su, “Ultrawide-band square planar metal-plate monopole antenna with a trident-shaped feeding strip,” *IEEE Transactions on Antennas and Propagation*, vol. 53, pp. 1262-1269, April 2005.
- [66] Z.N.Chen and M.Y.W.Chia, “A feeding scheme for enhancing the impedance Bandwidth of a suspended plate antenna” *Microwave and Optical Technology letter, Wiley InterScience*, Vol.38, July 2003.
- [67] R. Serrano, “Active balanced feeding for compact wideband antennas,” *IEEE Antennas and Propagation Society International Symposium*, pp. 2829-2832, 2007.
- [68] E. Antonino-Daviu, M. Cabedo-Fabres, M. Ferrando-Bataller and A. Valero-Nogueira, “Wideband double-fed planar monopole antennas,” *IEE, Electronics Letters*, vol. 39, pp. 1635-6-, Nov. 2003.
- [69] A. Krewski, W. L. Schroeder and K. Solbach, “Multi-band 2-port MIMO LTE antenna design for laptops using characteristic modes,” *Loughborough Antennas & Propagation Conference (LAPC)*, pp. 1-4, 2012.
- [70] S.W.Su, K.L.Wong and C.L.Tang, “Ultra-wideband square planar monopole antenna for IEEE 802.16a operation in the 2-11 GHz Band” *Microwave and Optical Technology letter, Wiley InterScience*, Vol.42, Sept 2004.



- [71] M. Cabedo-Fabres, E. Antonino-Daviu, A. Valero-Nogueira and M. Ferrando-Bataller, "Wideband radiating ground plane with notches," *IEEE, Antennas and Propagation Society International Symposium*, vol. 2B, pp. 560-563, 2005.
- [72] C. Deng, Z. Feng and S. V. Hum, "MIMO Mobile Handset Antenna Merging Characteristic Modes for Increased Bandwidth," *IEEE Transactions on Antennas and Propagation*, vol. 64, pp. 2660-2667, July 2016.
- [73] P. Miškovský and A. von Arbin, "Evaluation of MIMO handset antennas with decorative metal elements, using characteristic modes," *IEEE Antennas and Propagation Society International Symposium (APSURSI)*, pp. 1423-1424, 2014.
- [74] Z. Miers, H. Li and B. K. Lau, "Design of Bandwidth-Enhanced and Multi-band MIMO Antennas Using Characteristic Modes," *IEEE Antennas and Wireless Propagation Letters*, vol. 12, pp. 1696-1699, 2013.
- [75] Z. Miers, H. Li and B. K. Lau, "Design of bezel antennas for multiband MIMO terminals using Characteristic Modes," *8th European Conference on Antennas and Propagation (EuCAP 2014)*, pp. 2556-2560, 2014.
- [76] H. Li, Z. Miers and B. K. Lau, "Generating multiple characteristic modes below 1GHz in small terminals for MIMO antenna design," *IEEE Antennas and Propagation Society International Symposium (APSURSI)*, Orlando, pp. 180-181, 2013.

- [77] Z. Miers, H. Li and B. K. Lau, "Design of multi-antenna feeding for MIMO terminals based on characteristic modes," *IEEE Antennas and Propagation Society International Symposium (APSURSI)*, Orlando, pp. 182-183, 2013.
- [78] H. Li, Z. T. Miers and B. K. Lau, "Design of Orthogonal MIMO Handset Antennas Based on Characteristic Mode Manipulation at Frequency Bands Below 1 GHz," *IEEE Transactions on Antennas and Propagation*, vol. 62, no. 5, pp. 2756-2766, May 2014.
- [79] E. Antonino-Daviu, M. Cabedo-Fabres, M. Ferrando-Bataller and A. Valero-Nogueira, "A discussion on the feed configuration of planar monopole antennas to obtain ultra wide band performance," *IEEE Antennas and Propagation Society Symposium*, Vol.2, pp. 1867-1870, 2004.
- [80] M. Cabedo-Fabres, A.V.Nogueira, and M.F.Bataller, "A wideband arrowhead planar monopole antenna for multi-service mobile system," *Microwave and Optical Technology letter, Wiley InterScience*, Vol.37, May 2003.
- [81] M. Cabedo-Fabres, E. Antonino-Daviu, A. Valero-Nogueira and M. Ferrando-Bataller, "Analysis of wide band planar monopole antennas using characteristic modes," *IEEE Antennas and Propagation Society International Symposium*, USA, vol.3, pp. 733-736, 2003.
- [82] M.F.Bataller, M. Cabedo-Fabrés, E. Antonino-Daviu and A. Valero-Nogueira, "Overview of planar monopole antennas for UWB applications," *EuCAP*, France, Oct. 2006.

- [83] I. Makris, D. Manteuffel, R. D. Seager and J. C. Vardaxoglou, "Modified Designs for UWB Planar Monopole Antennas," *IEEE, Loughborough Antennas and Propagation Conference*, pp. 249-252, 2007.
- [84] N. L. Bohannon and J. T. Bernhard, "Design Guidelines Using Characteristic Mode Theory for Improving the Bandwidth of PIFAs," *IEEE Transactions on Antennas and Propagation*, vol. 63, pp. 459-465, Feb. 2015.
- [85] D. Manteuffel and R. Martens, "Multiple antenna integration in small terminals," *IEEE International Symposium on Antennas and Propagation (ISAP)*, pp. 211-214, 2012.
- [86] R. Martens and D. Manteuffel, "Mobile LTE-A handset antenna using a hybrid coupling element," *IEEE Antennas and Propagation Society International Symposium (APSURSI)*, pp. 1419-1420, 2014.
- [87] E. Safin and D. Manteuffel, "Manipulation of Characteristic Wave Modes by Impedance Loading," *IEEE Transactions on Antennas and Propagation*, vol. 63, pp. 1756-1764, April 2015.
- [88] E. A. Elghannai, B. D. Raines and R. G. Rojas, "Multiport Reactive Loading Matching Technique for Wide Band Antenna Applications Using the Theory of Characteristic Modes," *IEEE Transactions on Antennas and Propagation*, vol. 63, no. 1, pp. 261-268, Jan. 2015.
- [89] K. A. Obeidat, B. D. Raines and R. G. Rojas, "Application of Characteristic Modes and Non-Foster Multiport Loading to the Design of Broadband

- Antennas,” *IEEE Transactions on Antennas and Propagation*, vol. 58, pp. 203-207, Jan. 2010.
- [90] R. Martens and D. Manteuffel, “Element correlation of MIMO antennas on small terminals,” *European Conference on Antennas and Propagation (EuCAP)*, Barcelona, Spain, pp. 1-5, 2010. .
- [91] R. Martens, E. Safin and D. Manteuffel, “On the relation between the element correlation of antennas on small terminals and the characteristic modes of the chassis,” *Loughborough Antennas & Propagation Conference*, Loughborough, pp. 457-460, 2010.
- [92] J. Rahola and J. Ollikainen, “Optimal antenna placement for mobile terminals using characteristic mode analysis,” *European Conference on Antennas and Propagation (EuCAP)*, pp. 1-6, 2006.
- [93] J. Villanen. Compact antenna structure for mobile handsets. Master’s thesis, Helsinki University of Technology, 2003.
- [94] R. Martens and D. Manteuffel, “2-port antenna based on the selective excitation of Characteristic Modes,” *IEEE International Symposium on Antennas and Propagation*, Chicago, pp. 1-2, 2012.
- [95] R. Martens and D. Manteuffel, “A feed network for the selective excitation of specific characteristic modes on small terminals,” *6th European Conference on Antennas and Propagation (EUCAP)*, Prague, pp. 1842-1846, 2012.

- [96] E. Safin and D. Manteuffel, "Reconstruction of the Characteristic Modes on an Antenna Based on the Radiated Far Field," *IEEE Transactions on Antennas and Propagation*, vol. 61, no. 6, pp. 2964-2971, June 2013.
- [97] G.Hu, J.Feng, S.Zhang, and J.Bernhard, "A novel radiation pattern and frequency reconfigurable single turn square spiral microstrip antenna," *Microwave and Wireless Components Letters, IEEE*, vol. 13, pp. 57-59, 2003.
- [98] E. Palantei, D. Thiel, and S. O'Keefe, "Rectangular patch with parasitic folded dipoles: A reconfigurable antenna," *Antenna Technology: Small Antennas and Novel Metamaterials*, pp. 251-254, 2008.
- [99] S. Nikolaou, G.E.Ponchak, J. Papapolymerou, and M. M. Tentzeris, "Design and development of an annular slot antenna (asa) with a reconfigurable radiation pattern," *IEEE, Microwave Conference Proceedings (APMC)*, vol.5, 2005.
- [100] W. Kang, J. Park, and Y. Yoon, "Simple reconfigurable antenna with radiation pattern," *Electronics Letters*, vol. 44, no. 3, pp. 182-183, 2008.
- [101] D.Jiawei, W.Anguo, and L.Hang, "A simple radiation pattern reconfigurable printed dipole antenna," *IEEE Microwave Antenna Propagation and EMC Technologies for Wireless Communications*, pp. 619-622, 2009.
- [102] M. Donelli, R. Azaro, L. Fimognari, and A. Massa, "A planar electronically reconfigurable wi-fi band antenna based on a parasitic microstrip structure,"

- Antennas and Wireless Propagation Letters (AWPL)*, vol. 6, pp. 623-626, 2007.
- [103] A. Ghasemi, N. Ghahvehchian, A. Mallahzadeh, and S. Sheikholvaezin, "A reconfigurable printed monopole antenna for mimo application," *IEEE European Conference on Antennas and Propagation (EUCAP)*, pp. 1-4, 2012.
- [104] A. Lackpour, P. Mookiah, M. Olivieri, and K. Dandekar, "Evaluation of the reconfigurable printed fractal tree antenna for enhanced pattern diversity in mimo systems," *IEEE, Radio and Wireless Symposium (RWS)*, 2010.
- [105] J. Mitola, "Cognitive radio architecture evolution," *Proceedings of the IEEE*, vol. 97, no. 4, pp. 626-641, 2009.
- [106] T.-Y. Han, Y.-J. Liao et al., "A frequency reconfigurable half annular ring slot antenna design," *IEEE Transactions on Antennas and Propagation*, vol. 62, no. 6, pp. 3428-3431, 2014.
- [107] C. Hung and T. Chiu, "Dual-band reconfigurable antenna design using slot-line with branch edge," *IEEE Transactions on Antennas and Propagation*, vol. 63, no. 2, pp. 508-516, 2015.
- [108] B. A. Cetiner, G. R. Crusats, L. Jofre, and N. Biyikli, "Rf mems integrated frequency reconfigurable annular slot antenna," *IEEE Transactions on Antennas and Propagation*, vol. 58, no. 3, pp. 626-632, 2010.

- [109] H. A. Majid, M. K. A. Rahim, M. R. Hamid, N. A. Murad, and M. F. Ismail, "Frequency-reconfigurable microstrip patch-slot antenna," *IEEE antennas and wireless propagation letters*, vol. 12, pp. 218–220, 2013.
- [110] H. A. Majid, M. K. Abd Rahim, M. R. Hamid, and M. F. Ismail, "Frequency reconfigurable microstrip patch-slot antenna with directional radiation pattern," *Progress In Electromagnetics Research*, vol. 144, pp. 319–328, 2014.
- [111] H. A. Majid, M. K. A. Rahim, M. R. Hamid, and M. F. Ismail, "Frequency and pattern reconfigurable slot antenna," *IEEE transactions on antennas and propagation*, vol. 62, no. 10, pp. 5339–5343, 2014.
- [112] S. Sharma and C. C. Tripathi, "Frequency reconfigurable u-slot antenna for sdr application," *Progress In Electromagnetics Research Letters*, vol. 55, pp. 129–136, 2015.
- [113] L. Han, C. Wang, X. Chen, and W. Zhang, "Compact frequency reconfigurable slot antenna for wireless applications," *IEEE Antennas and Wireless Propagation Letters*, vol. 15, pp. 1795–1798, 2016.
- [114] G. Srivastava and A. Mohan, "Compact mimo slot antenna for uwb applications," *IEEE Antennas and Wireless Propagation Letters*, vol. 15, pp. 1057–1060, 2016.
- [115] R. Karimian, H. Oraizi, S. Fakhte, and M. Farahani, "Novel f-shaped quad-band printed slot antenna for wlan and wimax mimo systems," *IEEE Antennas and Wireless Propagation Letters*, vol. 12, pp. 405–408, 2013.

- [116] S. Soltani, P. Lotfi, and R. D. Murch, "A port and frequency reconfigurable mimo slot antenna for wlan applications," *IEEE Transactions on Antennas and Propagation*, vol. 64, no. 4, pp. 1209–1217, 2016.
- [117] <http://www.skyworksinc.com>, "Smv123x series: Hyperabrupt junction tuning varactors," *Skyworks Solutions SMV 123X datasheet*, 2012.
- [118] K. K. Kishor and S. V. Hum, "A pattern reconfigurable chassis-mode mimo antenna," *IEEE Transactions on Antennas and Propagation*, vol. 62, no. 6, pp. 3290–3298, June 2014.
- [119] K. Kishor and S. Hum, "A reconfigurable chassis-mode mimo antenna," *7th European Conference on Antennas and Propagation (EuCAP)*, pp. 1992–1996, April 2013.
- [120] K. K. Kishor and S. V. Hum, "A Two-Port Chassis-Mode MIMO Antenna," *IEEE Antennas and Wireless Propagation Letters*, vol. 12, no. , pp. 690-693, 2013.
- [121] A. Araghi and G. Dadashzadeh, "Oriented Design of an Antenna for MIMO Applications Using Theory of Characteristic Modes," *IEEE Antennas and Wireless Propagation Letters*, vol. 11, no. , pp. 1040-1043, 2012.
- [122] H. Li, R. Ma, J. Chountalas, and B. K. Lau, "Characteristic mode based pattern reconfigurable antenna for mobile handset," in *2015 9th European Conference on Antennas and Propagation (EuCAP)*, May 2015, pp. 1–4.



- [123] R. Martens, E. Safin and D. Manteuffel, "Selective excitation of characteristic modes on small terminals," *IEEE 5th European Conference on Antennas and Propagation (EUCAP)*, Rome, pp. 2492-2496, 2011.
- [124] R. Martens, E. Safin and D. Manteuffel, "Inductive and capacitive excitation of the characteristic modes of small terminals," *IEEE Loughborough Antennas & Propagation Conference*, Loughborough, pp. 1-4, 2011.
- [125] R. Martens and D. Manteuffel, "Systematic design method of a mobile multiple antenna system using the theory of characteristic modes," *IET Microwaves Antennas & Propagation*, vol. 8, no. 12, pp. 887-893, Sept. 2014.
- [126] K. A. Obeidat, B. D. Raines, R. G. Rojas and B. T. Strojny, "Design of Frequency Reconfigurable Antennas Using the Theory of Network Characteristic Modes," *IEEE Transactions on Antennas and Propagation*, vol. 58, no. 10, pp. 3106-3113, Oct. 2010.
- [127] K. A. Obeidat, B. D. Raines and R. G. Rojas, "Antenna design and analysis using characteristic modes," *IEEE Antennas and Propagation Society International Symposium*, pp. 5993-5996, 2007.
- [128] K.-F. Lee, S. L. S. Yang, and A. A. Kishk, "Dual- and multiband U-slot patch antennas," *IEEE Antennas Wireless Propagation Letters*, vol. 7, pp. 645-647, 2008.
- [129] E. Antonino-Daviu, M. Cabedo-Fabrés, M. Ferrando-Bataller, and V. M. R. Peñarrocha, "Modal analysis and design of band-notched UWB planar

- monopole antennas,” *IEEE Trans. Antennas Propag.*, vol. 58, no. 5, pp. 1457–1467, May 2010.
- [130] J.-S. Kuo and K.-L. Wong, “A compact microstrip antenna with meandering slots in the ground plane,” *Microw. Opt. Technol. Lett.*, vol. 29, no. 2, pp. 95–97, Apr. 2001.
- [131] P. C. Sharma and K. Gupta, “Analysis and optimized design of single feed circularly polarized microstrip antennas,” *IEEE Trans. Antennas Propag.*, vol. 31, no. 6, pp. 949–955, Nov. 1983.
- [132] K. Gosalia and G. Lazzi, “Reduced size, dual-polarized microstrip patch antenna for wireless communications,” *IEEE Trans. Antennas Propag.*, vol. 51, no. 9, pp. 2182–2186, Sep. 2003.
- [133] M.-C. Tang, R. W. Ziolkowski, and S. Xiao, “Compact hyper-band printed slot antenna with stable radiation properties,” *IEEE Trans. Antennas Propag.*, vol. 62, no. 6, pp. 2962–2969, Jun. 2014.
- [134] P. Li, J. Liang, and X. Chen, “Study of printed elliptical/circular slot antennas for ultrawideband applications,” *IEEE Trans. Antennas Propag.*, vol. 54, no. 6, pp. 1670–1675, Jun. 2006.
- [135] Y. F. Liu, K. L. Lau, Q. Xue, and C. H. Chan, “Experimental studies of printed wide-slot antenna for wide-band applications,” *IEEE Antennas Wireless Propag. Lett.*, vol. 3, no. 1, pp. 273–275, Dec. 2004.

- [136] W. S. Chen, "A novel broadband design of a printed rectangular slot antenna for wireless communications," *Microwave Journal.*, vol. 49, no. 1, pp. 122–130, Jul. 2006.
- [137] S.-W. Qu, C. Ruan, and B.-Z. Wang, "Bandwidth enhancement of wide-slot antenna fed by CPW and microstrip line," *IEEE Antennas Wireless Propag. Lett.*, vol. 5, pp. 15–17, 2006.
- [138] S.-W. Qu, J.-L. Li, J.-X. Chen, and Q. Xue, "Ultrawideband striploaded circular slot antenna with improved radiation patterns," *IEEE Trans. Antennas Propag.*, vol. 55, no. 11, pp. 3348–3353, Nov. 2007.
- [139] J.-Y. Jan and J.-W. Su, "Bandwidth enhancement of a printed wide-slot antenna with a rotated slot," *IEEE Trans. Antennas Propag.*, vol. 53, no. 6, pp. 2111–2114, Jun. 2005.
- [140] S. Weigand, G. H. Huff, K. H. Pan, and J. T. Bernhard, "Analysis and design of broad-band single-layer rectangular U-slot microstrip patch antennas," *IEEE Trans. Antennas Propag.*, vol. 51, no. 3, pp. 457–468, Mar. 2003.
- [141] V. Natarajan and D. Chatterjee, "An empirical approach for design of wide-band, probe-fed, U-slot microstrip patch antennas on single-layer, infinite, grounded substrates," *ACES J.*, vol. 18, no. 3, pp. 191–200, Nov. 2003.
- [142] H. G. Akhavan and D. Mirshekar-Syahkal, "Characteristics of fundamental and first higher-order modes of microstrip-fed slot antennas," *International Conf. on Antennas and Propag.*, vol.1, 1997.

- [143] K. Y. Kabalan, A. El-Hajj and R. F. Harrington, "Characteristic mode analysis of a slot in a conducting plane separating different media," *IEEE Trans. Antennas Propag.*, vol. 38, no. 4, pp. 476-481, Apr 1990.
- [144] A. El-Hajj, K. Y. Kabalan and R. F. Harrington, "Characteristic modes of a slot in a conducting cylinder and their use for penetration and scattering, TE case," *IEEE Trans. Antennas Propag.*, vol. 40, no. 2, pp. 156-161, Feb 1992.
- [145] K. Y. Kabalan, A. El-Haji and R. F. Harrington, "Characteristic modes of a slot in a conducting cylinder and their use for penetration and scattering, TM case," *IEE Proceedings H - Microwaves, Antennas and Propag.*, vol. 139, no. 3, pp. 287-291, June 1992.
- [146] A. El-Hajj, K. Y. Kabalan and R. F. Harrington, "Characteristic mode analysis of electromagnetic coupling through multiple slots in a conducting plane," *IEE Proceedings H - Microwaves, Antennas and Propag.*, vol. 140, no. 6, pp. 421-425, Dec. 1993.
- [147] E. Antonino-Daviu, M. Cabedo-Fabrés, M. Sonkki, N. Mohamed Mohamed-Hicho and M. Ferrando-Bataller, "Design Guidelines for the Excitation of Characteristic Modes in Slotted Planar Structures," *IEEE Trans. Antennas Propag.*, vol. 64, no. 12, pp. 5020-5029, Dec. 2016.
- [148] A. Ghalib, R. Hussain and M. S. Sharawi, "Characteristic Modes of Circular Slot Antennas Etched on a Finite Ground Plane," *IEEE Inter. Symposium*

- on Antennas and Propag. (APSURSI)*, San Diego, California, USA, 2017.
- [149] N. M. Mohamed-Hicho, E. Antonino-Daviu, M. Cabedo-Fabrés and M. Ferrando-Bataller, "Characteristic modes in slot antennas etched in a finite ground plane," *IEEE Inter. Symposium on Antennas and Propag. (APSURSI)*, Fajardo, pp. 7-8, 2016.
- [150] N. M. Mohamed-Hicho, E. Antonino-Daviu, M. Cabedo-Fabrés, J. P. Ciafarini and M. Ferrando-Bataller, "On the interaction of Characteristic Modes in slot antennas etched on finite ground planes," *10th European Conference on Antennas and Propagation (EuCAP)*, Davos, pp. 1-5, 2016.
- [151] M. Honkala, A. Lehtovuori, E. Raninen and P. Ylä-Oijala, "Effect of shape deformation of a patch antenna on its characteristic modes," *URSI International Symposium on Electromagnetic Theory (EMTS)*, pp. 690-693, 2016.
- [152] M. M. Elsewe and D. Chatterjee, "Modal analysis of patch slot designs in microstrip patch antennas," *IEEE/ACES International Conference on Wireless Information Technology and Systems (ICWITS) and Applied Computational Electromagnetics (ACES)*, Honolulu, pp. 1-2, 2016.
- [153] A. Ghalib and M. S. Sharawi, "Excitation Shape and Placement Effects on Natural Radiating Modes," *IEEE Inter. Symposium on Antennas and Propag. (APSURSI)*, San Diego, California, USA, 2017.

- [154] Y. Chen and C. F. Wang, "Characteristic-Mode-Based Improvement of Circularly Polarized U-Slot and E-Shaped Patch Antennas," *IEEE Antennas Wireless Propag. Lett.*, vol. 11, no. , pp. 1474-1477, 2012.
- [155] M. Khan and D. Chatterjee, "Characteristic Mode Analysis of a Class of Empirical Design Techniques for Probe-Fed, U-Slot Microstrip Patch Antennas," *IEEE Trans. Antennas Propag.*, vol. 64, no. 7, pp. 2758-2770, July 2016.
- [156] M. Khan and D. Chatterjee, "Performance optimization of multiple U-Slot antennas using theory of characteristic modes," *IEEE International Symposium on Phased Array Systems and Technology (PAST)*, Waltham, pp. 1-7, 2016.
- [157] F. H. Lin; Z. N. Chen, "Low-Profile Wideband Metasurface Antennas Using Characteristic Mode Analysis," *IEEE Trans. Antennas Propag.*, Feb, 2017.
- [158] J. P. Ciafardini, E. A. Daviu, M. C. Fabr s, N. M. Mohamed-Hicho, J. A. Bava and M. F. Bataller, "Crossed-slot antenna array design for an Incoherent Scatter Radar and characteristic modes analysis," *10th European Conference on Antennas and Propagation (EuCAP)*, Davos, pp. 1-5, 2016.
- [159] H. Arai and K. Takahashi, "Bi-directional pattern of two-notch antenna by characteristic modes analysis," *European Conf. on Antennas and Propag. (EuCAP)*, Davos, pp. 1-2, 2016.

- [160] R. Hussain, A. Ghalib and M. S. Sharawi, "Annular Slot-Based Miniaturized Frequency-Agile MIMO Antenna System," *IEEE Antennas and Wireless Propagation Letters*, vol. 16, pp. 2489-2492, 2017.
- [161] A. Ghalib, R. Hussain and M. S. Sharawi, "Low profile frequency agile MIMO slot antenna with TCM characterization," *11th European Conference on Antennas and Propagation (EUCAP)*, Paris, pp. 2652-2655, 2017.
- [162] A. Ghalib and M. S. Sharawi, "Effects of actual antenna excitation on natural radiation modes," *11th European Conference on Antennas and Propagation (EUCAP)*, Paris, pp. 3467-3470, 2017.
- [163] G. Zhai, Z. N. Chen, and X. Qing, "Enhanced isolation of a closely spaced four-element mimo antenna system using metamaterial mushroom," *IEEE Transactions on Antennas and Propagation*, vol. 63, pp. 3362–3370, Aug 2015.
- [164] D. K. Ntaikos and T. V. Yioultis, "Compact split-ring resonator-loaded multiple-input-multiple-output antenna with electrically small elements and reduced mutual coupling," *IET Microwaves, Antennas Propagation*, vol. 7, pp. 421–429, April 2013.
- [165] C. C. Hsu, K. H. Lin, and H. L. Su, "Implementation of broadband isolator using metamaterial-inspired resonators and a t-shaped branch for mimo antennas," *IEEE Transactions on Antennas and Propagation*, vol. 59, pp. 3936–3939, Oct 2011.

- [166] C.-Y. Lui, Y.-S. Wang, and S.-J. Chung, "Two nearby dual-band antennas with high port isolation," in *2008 IEEE Antennas and Propagation Society International Symposium*, pp. 1–4, July 2008.
- [167] Y. Wang and Z. Du, "A wideband printed dual-antenna with three neutralization lines for mobile terminals," *IEEE Transactions on Antennas and Propagation*, vol. 62, pp. 1495–1500, March 2014.
- [168] A. Diallo, C. Luxey, P. L. Thuc, R. Staraj, and G. Kossiavas, "Study and reduction of the mutual coupling between two mobile phone pifas operating in the dcs1800 and umts bands," *IEEE Transactions on Antennas and Propagation*, vol. 54, pp. 3063–3074, Nov 2006.
- [169] S. Soltani and R. D. Murch, "A compact planar printed mimo antenna design," *IEEE Transactions on Antennas and Propagation*, vol. 63, pp. 1140–1149, March 2015.
- [170] A. C. K. Mak, C. R. Rowell, and R. D. Murch, "Isolation enhancement between two closely packed antennas," *IEEE Transactions on Antennas and Propagation*, vol. 56, pp. 3411–3419, Nov 2008.
- [171] R. R. Ramirez and F. D. Flaviis, "A mutual coupling study of linear and circular polarized microstrip antennas for diversity wireless systems," *IEEE Transactions on Antennas and Propagation*, vol. 51, pp. 238–248, Feb 2003.



- [172] B. Wu and K. M. Luk, "A 4-port diversity antenna with high isolation for mobile communications," *IEEE Transactions on Antennas and Propagation*, vol. 59, pp. 1660–1667, May 2011.
- [173] H. Kim and S. Kahng, "Design of a compact four MIMO handset antenna structure," *Microwave Journal*, vol. 59, no. 4, pp. 162-174, 2016.
- [174] S. Kahng, J. Jeon, J. Anguera, and T. Park, "A compact MIMO antenna using CRLH configuration double-layered folded ring radiations with planar mushroom decoupling structure," *IEEE Antennas Propagation Magazine*, vol. 57, no. 4, pp. 123-130, Apr. 2015.
- [175] K. Wei, J. Li, L. Wang, Z. Xing, and R. Xu, "S-shaped periodic defected ground structures to reduce microstrip antenna array mutual coupling," *Electronics Letters*, vol. 52, no. 15, pp. 1288–1290, 2016.
- [176] C. M. Luo, J. S. Hong, and L. L. Zhong, "Isolation enhancement of a very compact uwb-mimo slot antenna with two defected ground structures," *IEEE Antennas and Wireless Propagation Letters*, vol. 14, pp. 1766–1769, 2015.
- [177] R. Anitha, V. P. Sarin, P. Mohanan, and K. Vasudevan, "Enhanced isolation with defected ground structure in mimo antenna," *Electronics Letters*, vol. 50, no. 24, pp. 1784–1786, 2014.
- [178] M. S. Sharawi, A. B. Numan, M. U. Khan, and D. N. Alofi, "A dual-element dual-band mimo antenna system with enhanced isolation for mobile termi-

- nals,” *IEEE Antennas and Wireless Propagation Letters*, vol. 11, pp. 1006–1009, 2012.
- [179] J. Ren, W. Hu, Y. Yin, and R. Fan, “Compact printed mimo antenna for uwb applications,” *IEEE Antennas and Wireless Propagation Letters*, vol. 13, pp. 1517–1520, 2014.
- [180] Y. S. Chen and C. P. Chang, “Design of a four-element multiple-input-multiple-output antenna for compact long-term evolution small-cell base stations,” *IET Microwaves, Antennas Propagation*, vol. 10, no. 4, pp. 385–392, 2016.
- [181] C. Y. Chiu, C. H. Cheng, R. D. Murch, and C. R. Rowell, “Reduction of mutual coupling between closely-packed antenna elements,” *IEEE Transactions on Antennas and Propagation*, vol. 55, pp. 1732–1738, June 2007.
- [182] R. Hussain and M. S. Sharawi, “Planar meandered-f-shaped 4-element reconfigurable multiple-input-multiple-output antenna system with isolation enhancement for cognitive radio platforms,” *IET Microwaves, Antennas Propagation*, vol. 10, no. 1, pp. 45–52, 2016.
- [183] M. Ikram, R. Hussain, A. Ghalib, and M. S. Sharawi, “Compact 4-element mimo antenna with isolation enhancement for 4g lte terminals,” in *2016 IEEE International Symposium on Antennas and Propagation (APSURSI)*, pp. 535–536, June 2016.

- [184] M. Ikram, R. Hussain, O. Hammi, and M. S. Sharawi, "An l-shaped 4-element monopole mimo antenna system with enhanced isolation for mobile applications," *Microwave and Optical Technology Letters*, vol. 58, no. 11, pp. 2587–2591, 2016.
- [185] R. Saleem, M. Bilal, K. B. Bajwa, and M. F. Shafique, "Eight-element uwb-mimo array with three distinct isolation mechanisms," *Electronics Letters*, vol. 51, no. 4, pp. 311–313, 2015.
- [186] H. Li, Y. Tan, B. K. Lau, Z. Ying and S. He, "Characteristic Mode Based Tradeoff Analysis of Antenna-Chassis Interactions for Multiple Antenna Terminals," *IEEE Transactions on Antennas and Propagation*, vol. 60, no. 2, pp. 490-502, Feb. 2012.
- [187] H. Li, B. K. Lau, Z. Ying and S. He, "Decoupling of Multiple Antennas in Terminals With Chassis Excitation Using Polarization Diversity, Angle Diversity and Current Control," *IEEE Transactions on Antennas and Propagation*, vol. 60, no. 12, pp. 5947-5957, Dec. 2012.
- [188] H. Li, J. Xiong, Z. Ying and S. L. He, "Compact and low profile co-located MIMO antenna structure with polarisation diversity and high port isolation," *IEEE Electronics Letters*, vol. 46, no. 2, pp. 108-110, January 2010.
- [189] H. Li, B. K. Lau, Y. Tan, S. He and Z. Ying, "Impact of current localization on the performance of compact MIMO antennas," *IEEE 5<sup>th</sup> European*

- Conference on Antennas and Propagation (EUCAP)*, Rome, pp. 2423-2426, 2011.
- [190] H. Li, B. K. Lau and Z. Ying, "Optimal multiple antenna design for compact MIMO terminals with ground plane excitation," *IEEE International Workshop on Antenna Technology (iWAT)*, Hong Kong, pp. 218-221, 2011.
- [191] S. K. Chaudhury, W. L. Schroeder and H. J. Chaloupka, "MIMO antenna system based on orthogonality of the characteristic modes of a mobile device," *2<sup>nd</sup> International ITG Conference on Antennas*, Munich, pp. 58-62 2007.
- [192] I. Szini, A. Tatomirescu and G. F. Pedersen, "On Small Terminal MIMO Antennas, Harmonizing Characteristic Modes With Ground Plane Geometry," *IEEE Transactions on Antennas and Propagation*, vol. 63, no. 4, pp. 1487-1497, April 2015.
- [193] B. Yang and J. J. Adams, "Systematic Shape Optimization of Symmetric MIMO Antennas Using Characteristic Modes," *IEEE Transactions on Antennas and Propagation*, vol. 64, no. 7, pp. 2668-2678, July 2016.
- [194] R. Martens, J. Holopainen, E. Safin, J. Ilvonen and D. Manteuffel, "Optimal Dual-Antenna Design in a Small Terminal Multiantenna System," *IEEE Antennas and Wireless Propagation Letters*, vol. 12, no. , pp. 1700-1703, 2013.
- [195] M. Bouezzeddine and W. L. Schroeder, "Design of a Wideband, Tunable Four-Port MIMO Antenna System With High Isolation Based on the Theory

- of Characteristic Modes,” *IEEE Transactions on Antennas and Propagation*, vol. 64, no. 7, pp. 2679-2688, July 2016.
- [196] Q. Wu, W. Su, Z. Li and D. Su, “Reduction in Out-of-Band Antenna Coupling Using Characteristic Mode Analysis,” *IEEE Transactions on Antennas and Propagation*, vol. 64, no. 7, pp. 2732-2742, July 2016.
- [197] I. Vasilev and B. K. Lau, “On User Effects in MIMO Handset Antennas Designed Using Characteristic Modes,” *IEEE Antennas and Wireless Propagation Letters*, vol. 15, no. , pp. 758-761, 2016.
- [198] A. Ghalib and M. S. Sharawi, “TCM Analysis of Defected Ground Structures for MIMO Antenna Designs in Mobile Terminals,” *IEEE Access*, vol. 5, pp. 19680-19692, 2017.
- [199] A. Ghalib and M. S. Sharawi, “Analyzing DGS behavior for a MIMO antenna system using theory of characteristic modes,” *IEEE Middle East Conference on Antennas and Propagation (MECAP)*, Beirut, pp. 1-4, 2016.
- [200] L. Qiu, K. Xiao, S. L. Chai, H. Y. Qi and J. J. Mao, “A Double-Layer Shaped-Beam Traveling-Wave Slot Array Based on SIW,” *IEEE Transactions on Antennas and Propagation*, vol. 64, no. 11, pp. 4639-4647, Nov. 2016.
- [201] H. Gharibi and F. H. Kashani, “Design of a Compact Circularly Polarized Dual-Mode Monopulse Cavity-Backed Substrate Integrated Waveguide Antenna,” *IEEE Antennas and Wireless Propagation Letters*, vol. 14, no. , pp. 519-522, 2015.

- [202] N. Ashraf, O. Haraz, M. A. Ashraf and S. Alshebeili, "28/38-GHz dual-band millimeter wave SIW array antenna with EBG structures for 5G applications," *International Conference on Information and Communication Technology Research (ICTRC)*, Abu Dhabi, pp. 5-8, 2015.
- [203] O. Caytan et al., "Half-Mode Substrate-Integrated-Waveguide Cavity-Backed Slot Antenna on Cork Substrate," *IEEE Antennas and Wireless Propagation Letters*, vol. 15, no. , pp. 162-165, 2016.
- [204] Y. Zhao and K. M. Luk, "Dual Circular-Polarized SIW-Fed High Gain Scalable Antenna Array for 60 GHz Applications," *IEEE Transactions on Antennas and Propagation*, vol. PP, no. 99, pp. 1-1, 2018.
- [205] Q. Zhu, K. B. Ng and C. H. Chan, "Printed Circularly Polarized Spiral Antenna Array for Millimeter-Wave Applications," *IEEE Transactions on Antennas and Propagation*, vol. 65, no. 2, pp. 636-643, 2017.
- [206] D. Kim, M. Zhang, J. Hirokawa and M. Ando, "Design and Fabrication of a Dual-Polarization Waveguide Slot Array Antenna With High Isolation and High Antenna Efficiency for the 60 GHz Band" *IEEE Transactions on Antennas and Propagation*," vol. 62, no. 6, pp. 3019-3027, June 2014.
- [207] M. Li and K. Luk, "Low-Cost Wideband Microstrip Antenna Array for 60-GHz Applications" *IEEE Transactions on Antennas and Propagation*," vol. 62, no. 6, pp. 3012-3018, June 2014.

- [208] C. Liu, Y. X. Guo, X. Bao and S. Q. Xiao, "60-GHz LTCC Integrated Circularly Polarized Helical Antenna Array," *IEEE Transactions on Antennas and Propagation*, vol. 60, no. 3, pp. 1329-1335, March 2012.
- [209] Y. Li and K. M. Luk, "A 60-GHz Wideband Circularly Polarized Aperture-Coupled Magneto-Electric Dipole Antenna Array," *IEEE Transactions on Antennas and Propagation*, vol. 64, no. 4, pp. 1325-1333, April 2016.
- [210] A. Nafe, F. A. Ghaffar, M. F. Farooqui and A. Shamim, "A Ferrite LTCC-Based Monolithic SIW Phased Antenna Array," *IEEE Transactions on Antennas and Propagation*, vol. 65, no. 1, pp. 196-205, Jan. 2017.
- [211] H. Choe and S. Lim, "Millimeter-Wave Continuous Transverse Stub (CTS) Antenna Array Using Substrate Integrated Waveguide (SIW) Technology," *IEEE Transactions on Antennas and Propagation*, vol. 62, no. 11, pp. 5497-5503, Nov. 2014.
- [212] Y. J. Cheng et al., "Substrate Integrated Waveguide (SIW) Rotman Lens and Its Ka-Band Multibeam Array Antenna Applications," *IEEE Transactions on Antennas and Propagation*, vol. 56, no. 8, pp. 2504-2513, Aug. 2008.
- [213] J. Pourahmadazar and T. A. Denidni, "Multi-beam tapered slot antenna array using substrate integrated waveguide Rotman lens," *European Radar Conference (EuRAD)*, Paris, pp. 425-428, 2015,
- [214] P. Loghmannia, M. Kamyab, M. Ranjbar Nikkhah and R. Rezaiesarlak, "Miniaturized Low-Cost Phased-Array Antenna Using SIW Slot Elements,"

- IEEE Antennas and Wireless Propagation Letters*, vol. 11, pp. 1434-1437, 2012.
- [215] L. Wu, A. J. Farrall and P. R. Young, "Substrate Integrated Waveguide Switched Beam Antenna," *IEEE Transactions on Antennas and Propagation*, vol. 63, no. 5, pp. 2301-2305, May 2015.
- [216] Y. Cai, Y. Zhang, C. Ding and Z. Qian, "A Wideband Multilayer Substrate Integrated Waveguide Cavity-Backed Slot Antenna Array," *IEEE Transactions on Antennas and Propagation*, vol. 65, no. 7, pp. 3465-3473, July 2017.
- [217] S. J. Park, D. H. Shin and S. O. Park, "Low Side-Lobe Substrate-Integrated-Waveguide Antenna Array Using Broadband Unequal Feeding Network for Millimeter-Wave Handset Device," *IEEE Transactions on Antennas and Propagation*, vol. 64, no. 3, pp. 923-932, March 2016.
- [218] B. Cao, H. Wang and Y. Huang, "W-Band High-Gain TE<sub>220</sub>-Mode Slot Antenna Array With Gap Waveguide Feeding Network," *IEEE Antennas and Wireless Propagation Letters*, vol. 15, pp. 988-991, 2016.
- [219] P. Kumar, A. Kedar and A. K. Singh, "Design and Development of Low-Cost Low Sidelobe Level Slotted Waveguide Antenna Array in X-Band," *IEEE Transactions on Antennas and Propagation*, vol. 63, no. 11, pp. 4723-4731, Nov. 2015.
- [220] A.W. Rudge, K. Milne, A. D. Olver and P. Knight, *The handbook of Antenna Design*. Peter Peregrinus Ltd., London, UK, 1983.



- [221] Y. Chen and C.-F. Wang, "Electrically small UAV antenna design using characteristic modes," *IEEE Trans. Antennas Propag.*, vol. 62, no. 2, pp. 535–545, Feb. 2014.
- [222] Y. Chen and C.-F. Wang, "HF band shipboard antenna design using characteristic modes," *IEEE Trans. Antennas Propag.*, vol. 63, no. 3, pp. 1004–1013, Mar. 2015.
- [223] T.-Y. Shih and N. Behdad, "Bandwidth enhancement of platform mounted HF antennas using the characteristic mode theory," *IEEE Trans. Antennas Propag.*, vol. 64, no. 7, pp. 2648–2659, Jul. 2016.
- [224] C. Rowell and E. Y. Lam, "Mobile-phone antenna design," *IEEE Antennas Propag. Mag.*, vol. 54, no. 4, pp. 14–34, Aug. 2012.
- [225] L. Qiu, K. Xiao, S. L. Chai, H. Y. Qi and J. J. Mao, "A Double-Layer Shaped-Beam Traveling-Wave Slot Array Based on SIW," *IEEE Transactions on Antennas and Propagation*, vol. 64, no. 11, pp. 4639-4647, Nov. 2016.
- [226] J. F. Xu, W. Hong, P. Chen and K. Wu, "Design and implementation of low sidelobe substrate integrated waveguide longitudinal slot array antennas," *IET Microwaves, Antennas & Propagation*, vol. 3, no. 5, pp. 790-797, August 2009.
- [227] L. Jin, R. M. Lee and I. D. Robertson, "Analysis and design of a slotted waveguide antenna array using hollow substrate integrated waveguide," *European Radar Conference (EuRAD)*, Paris, pp. 401-404, 2015.

- [228] Randy L.Haupt, *A Computatuvinal Approach*, USA: Wiley, 2010
- [229] Robert E. Collin, *Antennas and Radiowave Propagation*, New York: McGraw Hill, 1985
- [230] S. Clauzier, S. M. Mikki, A. Shamim, and Y. M. M. Antar, "A new method for the design of slot antenna arrays: Theory and experiment," *10th European Conference on Antennas and Propagation (EuCAP), IEEE*, pp 1–5, 2016.

# Vitae

- Name: Asim Ghalib
- Nationality: Pakistani
- Date of Birth: 05 April 1989
- Email: *asimghalib@gmail.com*
- Current Address: P.O. Box 8247, King Fahd University of Petroleum and Minerals, Dhahran 31261, Saudi Arabia.
- Permanent Address: House 140, Street 03, Sector K-4, Phase 3, Hayatabad, Peshawar, Pakistan.
- Telephone: (+966) 596 284 321; (+92) 305 919 1818
- Received Bachelor of Science (B.Sc.) in Electrical Engineering from University of Engineering and Technology, Peshawar, Pakistan in 2011.
- Received Master of Science (M.Sc.) in Electrical Engineering from University of Engineering and Technology, Peshawar, Pakistan in 2014.
- Completed Ph.D. in Electrical Engineering from King Fahd University of Petroleum and Minerals, Dhahran, Saudi Arabia in May 2018.

# LIST OF PUBLICATIONS

## Journal Publications

1. A. Ghalib and M. S. Sharawi, "TCM Analysis of Defected Ground Structures for MIMO Antenna Designs in Mobile Terminals," in *IEEE Access*, vol. 5, pp. 19680-19692, 2017.
2. R. Hussain, A. Ghalib and M. S. Sharawi, "Annular Slot-Based Miniaturized Frequency-Agile MIMO Antenna System," in *IEEE Antennas and Wireless Propagation Letters*, vol. 16, pp. 2489-2492, 2017.
3. A. Ghalib and M. S. Sharawi, "Analyzing antenna effects on mobile chassis currents using theory of Characteristic modes," *Microwave and Optical Technology Letters*, Wiley, March 2018.
4. A. Ghalib and M. S. Sharawi, "Analysis of Slot based radiators using TCM and its application in MIMO Antennas," submitted to *International Journal of RF and Microwave Computer-Aided Engineering*, May 2018.
5. A. Ghalib and M. S. Sharawi, "Chassis Modal changes due to Antenna elements using TCM," submitted to *IEEE Antenna and Wireless Propagation Letters*, March 2018.

6. A. Ghalib and M. S. Sharawi, "Substrate integrated waveguide (SIW) based 5G antenna" Under preparation for IEEE Transactions on Antenna and Propagations, 2018.

## **International Conferences**

1. A. Ghalib, M. S. Sharawi, H. Attia and Raj Mittra, "Broadband Substrate integrated waveguide slotted array antenna at mm-wave bands," submitted to IEEE International Microwave Workshop Series on 5G hardware and System technologies, Dublin, Ireland, 2018
2. A. Ghalib and M. S. Sharawi, "Effect of Antenna Element Placement on Chassis Modes" IEEE International Symposium on Antennas and Propagation (APS/URSI 2018), Boston, Massachusetts, USA, July 2018.
3. A. Ghalib and M. S. Sharawi, "MIMO Antenna Elements Effect on Chassis Modes" IEEE International Symposium on Antennas and Propagation (APS/URSI 2018), Boston, Massachusetts, USA, July 2018.
4. A. Ghalib, R. Hussain and M. S. Sharawi, "Characteristic modes of circular slot antennas etched on a finite ground plane," 2017 IEEE International Symposium on Antennas and Propagation & USNC/URSI National Radio Science Meeting, San Diego, CA, pp. 167-168,2017.
5. A. Ghalib and M. S. Sharawi, "Excitation shape and placement effects on natural radiating modes," 2017 IEEE International Symposium on Anten-

- nas and Propagation & USNC/URSI National Radio Science Meeting, San Diego, CA, pp. 165-166, 2017.
6. A. Ghalib and M. S. Sharawi, "Effects of actual antenna excitation on natural radiation modes," 2017 11th European Conference on Antennas and Propagation (EUCAP), Paris, pp. 3467-3470, 2017.
  7. A. Ghalib, R. Hussain and M. S. Sharawi, "Low profile frequency agile MIMO slot antenna with TCM characterization," 2017 11th European Conference on Antennas and Propagation (EUCAP), Paris, pp. 2652-2655, 2017.
  8. A. Ghalib and M. S. Sharawi, "Analyzing DGS behavior for a MIMO antenna system using theory of characteristic modes," 2016 IEEE Middle East Conference on Antennas and Propagation (MECAP), Beirut, pp. 1-4, 2016.
  9. A. Ghalib and M. S. Sharawi, "A comparison between the antenna current green function and theory of characteristic modes," 2016 IEEE Middle East Conference on Antennas and Propagation (MECAP), Beirut, pp. 1-4, 2016.
  10. A. Ghalib, S. Clauzier, M. S. Sharawi and Y. M. M. Antar, "A slotted waveguide based MIMO antenna system for wireless access points," 2016 IEEE International Symposium on Antennas and Propagation (APSURSI), Fajardo, pp. 1459-1460, 2016.
  11. M. Ikram, R. Hussain, A. Ghalib and M. S. Sharawi, "Compact 4-element MIMO antenna with isolation enhancement for 4G LTE terminals," 2016

IEEE International Symposium on Antennas and Propagation (APSURSI),  
Fajardo, pp. 535-536, 2016.